The Dissertation Committee for Brian William Mulligan certifies that this is the approved version of the following dissertation:

A compact circumstellar shell model as a source of high velocity features in Type Ia supernovae

Committee:

John Craig Wheeler, Supervisor

Volker Bromm

Milos Milosavljevic

Edward L. Robinson

Jozsef Vinko

A compact circumstellar shell model as a source of high velocity features in Type Ia supernovae

by

Brian William Mulligan

Dissertation
Presented to the Faculty of the Graduate School of
The University of Texas at Austin
in Partial Fulfillment
of the Requirements
for the degree of
Doctor of Philosophy

The University of Texas at Austin
August, 2018

Dedicated to Dennis W. Mulligan, and Dorothy and Ralph “Ned” Noonan.

Acknowledgements

There are many people to thank who have influenced and contributed to this work. Firstly to my advisor, Craig Wheeler, for his support in many forms in my time in graduate school. My committee, Volker Bromm, Milos Milosavljevic, Rob Robinson, and Jozsef Vinko, for many suggestions, discussions, encouragement, and, most of all, their patience. G. Howie Marion, Jeffrey Silverman, and Kaicheng Zhang for their efforts and discussion that has gone into this work. Mark McCormick and Doene Demirgoez for many discussions about science over beers and kofta, and providing my inspiration and motivation to finally pursue a doctorate degree. Jeremy Johnson for many years of friendship, helping me through difficult times, and providing some occasional mental distractions over the last seven years. Jane Pamperin for many years of odd and interesting conversations, introducing me to so many people over the years, and helping me further a love for the outdoors. Sean Noonan for helping develop and cultivate my interest in science, astronomy, and computers, especially the many years in the basement 'lab.' Jennifer Rios for being going above and beyond in her support for me in the last two years. Melissa Lefebvre for many smiles, laughs, and Packer game updates over the years. My graduate school cohort (Kyle Kaplan, Marshall Johnson, Emma Yu, Keaton Bell, Thomas Gomez, Andrew Riddle, Inh Jee, Yi-Kuan Chang) for friendship and assistance in making the transition to living in Austin. My many other friends who I have met through graduate school and who have been helpful and supportive through this journey, in particular Joel Green, Chris Lindner, Kevin and Cori Gullickson, Briana Indahl, Jacob and Sarah Hummel, and Rachael Livermore. Tom Montemayor for volleyball, boats, and Tomaritas. Churro, Walle, and Frankie for their love and affection. The many coffee shops around town that have helped me stay caffeinated and sane while writing the papers included in this dissertation, especially Buzzmill Coffee and the owners and staff. Live Oak Brewery, St. Elmo Brewing Company, and Hops and Grain Brewing and their respective staffs for providing liquid encouragement during my time in Austin. Crown and Anchor Pub and the staff for providing a place for camaraderie and relaxation. My parents, sister, and extended family who have encouraged and supported me throughout my life. Finally to all of my other friends and family who have made it possible for me to be here today.

This work was supported in part by NSF grant AST-1109801, the University of Texas Graduate School Continuing Fellowship, and the University of Texas Graduate School Summer Fellowship. The Texas Advanced Computing Center (TACC) at the University of Texas at Austin provided HPC resources that have contributed to the research results reported within this work.

A compact circumstellar shell model as a source of high velocity features in Type Ia supernovae

by

Brian William Mulligan, Ph.D.
The University of Texas at Austin, 2018

SUPERVISOR: John Craig Wheeler

High-velocity features (HVF) of Type Ia supernovae are found in calcium, silicon, iron, and other elements. These features are observed only at early epochs — generally within the first one to three weeks after the supernova explodes. These features can provide insight into the cause of the supernova or the composition of the system prior to the explosion. We consider a model in which the HVF are the result of an interaction between the supernova and compact circumstellar shell. Hydrodynamic simulations of the interaction are performed, and synthetic spectra are generated using SYN++ from the results of the simulation to explore the effect of the shell and interaction. Of the masses, sizes, and density profiles of the shell that we consider, only density profiles that have a steep gradient at the outer edge may be ruled out based on the shape and evolution of the Ca II near-infrared feature. The observed features of SN 2011fe are then fit using these models, finding that the mass of the shell is not well constrained, but the velocity of the feature near peak brightness is better explained by a shell with a mass of 0.005 $M_\odot$. I describe a method to estimate the calcium abundance in supernova or shell material based on the results of the fit assuming purely radiative excitation and ionization, and simultaneously solving the excitation- and ion-states for a given element. Possible compositions of the shell and ejecta are explored using TARDIS for spectral synthesis, considering shells that consist of a solar abundance of metals within a hydrogen, helium, or carbon and oxygen substrate, as well compositions based upon a helium envelope detonation. The material in the shell is more likely to contain a Solar or super-Solar abundance of calcium; the substrate within which this calcium lies is not detectable using spectra.

Contents

List of Tables

List of Figures

Chapter One: Introduction

For millennia, humankind has assumed that, other than planets and the occasional comet, the stars in the sky were fixed and unchanging. There were some hints that this was not true – occasional 'guest' stars that would appear. The oldest known occurrence of this was in 185 CE, when Chinese astronomers recorded a new star that appeared and remained for several months. Until the Tycho Brahe made a record of such an event in 1572, these events have been sporadically recorded by cultures around the world simply as the appearance, and perhaps location in the sky, of such stars. Brahe, and soon thereafter, Johannes Kepler, recorded the appearance of new stars and carefully documented not just their location but also their brightness (Brahe, 1572; Kepler, 1606).

At the time of their appearance, the appearance of these new stars was not understood. By the 20th century, our understanding of physics and astronomy advanced such that these events could be recognized as supernovae, the extreme end-point of the evolution of some stars wherein most of all of a star is unbound through an explosive release of energy. We have identified two general mechanisms by which stars can explode. The first is stars with a mass eight times that of the Sun ($M_\odot$) and larger exhaust the available nuclear fuel in the core of the star, leading in at least some cases to a collapse and explosive rebound, expelling the outer layers of the star as well as large quantities of newly synthesized heavy elements near the former core of the star (Zwicky, 1938). The second is via a compact stellar remnant, known as a white dwarf, that acquires a total mass of 1.4 $M_\odot$, eventually resulting in an explosion that completely destroys the star and also releases large quantities of intermediate-mass elements, including silicon, calcium, sulfur, magnesium, and iron (Hoyle & Fowler, 1960a).

These latter types of supernovae are known as Type Ia supernovae (SN Ia), identifiable by a lack of evidence of hydrogen and helium, and strong evidence of silicon, in their spectra. In the latter half of the 20th century, SN Ia were recognized as important in helping to understand the history of the Universe. Because they are thought to always have the same mass when they explode, they are expected to always release the same total amount of energy. By knowing the luminosity and apparent brightness

of these events when they are seen in the sky, we can deduce their distance from the Solar System, allowing fine calibration of the expansion of the Universe and accurate mapping of the structure of the Universe. In the 1990's, use of these events to measure the history of expansion led to the discovery of 'dark energy', an unknown and invisible source of energy that accelerates the expansion of the Universe (Riess et al., 1998; Perlmutter et al., 1999).

In addition to cosmological interests, SN Ia produce approximately a 0.5 $M_\odot$ of silicon, sulfur, and iron when they explode (c.f. Seitenzahl et al., 2013). These elements are distributed into the galaxy by the explosion, where they are incorporated into future generations of stars. Understanding the details of these explosions can help provide a better understanding of the history of our and other galaxies (Tsujimoto & Shigeyama, 2012).

In order to calibrate the use of the explosions for purposes of cosmology and galactic archaeology, it is important that the details of the cause of the explosion and the process by which the explosion occurs be understood. One of the steps in coming to this understanding involves identifying what the system looked like prior to the explosion. This work represents one step in attempting to understand the appearance of the system and subsequent cause of the explosion by probing the details the observations of SN Ia in the first few days and weeks after the explosion.

1.1 SN Ia

Type Ia (SN Ia) supernovae are those that lack evidence of hydrogen and helium and show strong evidence of silicon in their spectra. Their luminosity increases over the first ∼18–20 days after the explosion, reaching a peak of $\sim 10^9$ times the brightness of the sun, then fading over the subsequent months (Elias et al., 1981; Branch, 1986; Harkness et al., 1987; Wheeler & Harkness, 1990).

The lack of hydrogen and helium features in the spectra is interpreted to be the result of the progenitor being a compact degenerate star (i.e. a white dwarf) composed of carbon and oxygen (Hoyle & Fowler, 1960a; Bloom et al., 2012). The observed silicon is the result of fusion of the carbon and oxygen that produces intermediate mass elements up to nickel. The cause of the fusion and subsequent explosion is explained by accumulation of material onto the progenitor white dwarf from either merger with

a companion white dwarf or accretion from a main sequence or post-main sequence stellar companion. Once the star reaches the a mass near the Chandrasekhar limit, $\sim$1.4 $M_\odot$, the pressure that prevents collapse is overcome, leading to the compaction and heating of the core that is necessary to begin the fusion of carbon and oxygen. The final cause of the detonation that unbinds the star is ill-understood (Hillebrandt & Niemeyer, 2000).

The progenitor system of such supernovae have never been observed prior to the explosion, so deduction of the origin of the supernova must occur through simulation and modeling of the system to explain the observed luminosity and spectra and their evolution after the explosion occurs. The light and spectra at the earliest epochs, i.e. within the first days or weeks after the explosion, can provide insight to what the system consists of prior the the explosion.

How the white dwarf accumulates mass and reaches the Chandrasekhar limit is determined by the progenitor system. The system is generally expected to consist of two stars: the white dwarf that explodes (the primary star) and another, unspecified star (the companion star). If the companion is a main sequence or post-main sequence (i.e. red giant) star, the mass is donated to the primary via Roche lobe overflow that occurs either as the companion star expands during later evolutionary stages or due to the stars getting sufficiently close to one another due to drag or gravitational radiation (Whelan & Iben, 1973). If the progenitor system is two white dwarfs, then the mass is donated from the companion to the primary through a merger, most likely resulting from inspiral due to gravitational radiation (Iben & Tutukov, 1984).

Some of the material that is being donated to the primary may exist in an envelope or shell just prior to explosion. While the shell itself is swept up by the ejecta of the explosion, it may be observable through kinematic or radiative effects after the explosion. Specifically, such an envelope may slow the outer layers of the supernova ejecta through hydrodynamic interaction, and may be observable via absorption lines produced as light from the supernova passes through the shell. Because the shell lay outside of the supernova prior to the explosion, the material in such a shell will be accelerated to very high velocities after interaction with the explosion.

1.2 Spectra of SN Ia and high-velocity features

Only a small fraction of SN Ia have been observed in the first few weeks after the explosion, and of those, only a smaller fraction have spectra at the earliest epochs. While more recent searches for SN Ia, largely driven by a desire to improve the precision of cosmological measurements, have greatly increased the number of SN Ia caught at early times, there are still only ~ 100 of these events available in the Open Supernova Catalog (as of this writing) that have spectra in the first week after the explosion (Guillochon et al., 2017). The lack of such observations is due to the limited availability of telescope time and the difficulty of obtaining useful spectra from these transient, faint events.

The first early epoch spectra of SN Ia were obtained in the 1990s. SN 1994D was observed starting at -12 d before peak brightness, corresponding to $\sim 6 - 8$ d after the explosion (Hatano et al., 1999). This event was noteworthy for the presence of Ca II and Fe II moving faster than is typically expected of ejecta of SN Ia, with velocities $>$ 20,000 km s^{-1} at -12 d; this was the first time such high velocity material was observed. The presence of absorption features suggesting of fast-moving material have been dubbed "high-velocity features" (HVF), contrast with the absorption features, dubbed "photospheric-velocity features" (PVF) expected from the ejecta. Such features have been observed in hundreds of SN Ia since this initial discovery (Wang et al., 2003; Thomas et al., 2004; Mazzali et al., 2005b; Quimby et al., 2006; Parrent et al., 2012; Marion et al., 2013; Childress et al., 2013a, 2014; Maguire et al., 2014; Silverman et al., 2015; Zhao et al., 2015, 2016).

The HVF fade and slow down over the course of the first weeks after the explosion, typically becoming undetectable by a few days after peak brightness of each supernova. Spectropolarimetry reveal the HVF are polarized by $\sim 0.1 - 1$ %, suggesting that the material that is causing the features is clumpy rather than isotropic (Wang et al., 2003; Wang & Wheeler, 2008; Patat et al., 2009). There are three proposed sources of such features: excitation or ionization effects in the outer layers of the ejecta that cause an enhancement in the presence of Ca II and other ions in which HVF appear (Blondin et al., 2013), clumps of material enriched in calcium, iron, etc. that are ejected during the process of the explosion (Mazzali et al., 2005b; Tanaka et al., 2006), or material that was not part of the supernova itself but has been swept up by the ejected material (Gerardy et al., 2004).

Identifying which of these models explains HVF will lead to a better understanding of SN Ia and, more generally, of physics and / or cosmology. HVF that are a result of ionization or excitation effects could lead to better understanding of those processes, radiation transport, and the internal structure of SN Ia. If the HVF are a result of ejected material, a better understanding of the physics of the explosion can result. Finally, if the HVF are material that is swept up by the explosion, then the properties of such material can give a better picture of what the progenitor system consisted of prior to the explosion.

It is this latter model that we investigate in the following works. We consider a circumstellar shell with a mass ≤ 0.02 $M_{\odot}$ of gas that surrounds the supernova prior to the explosion. Such shells have previously been investigated and have been shown to produce HVF in SN Ia, but those studies have not considered the evolution of the HVF as the material expands. We consider only shells that are compact such that the interaction between the shell and supernova is complete within seconds of the explosion occurring; this ensures that the swept up material has sufficient time to cool before the supernova is observed and prevents production synchrotron radiation or excess blue or UV radiation that would occur if the interaction between the ejecta and the swept up material is ongoing for hours, days, or weeks after the explosion.

In Chapter 2 we provide further information on HVF in SN Ia and investigate the evolution of the velocity and strength of such features. In Chapter 3 we develop hydrodynamic simulations between SN Ia and a circumstellar shell, devise a method to generate synthetic spectra from the results of those simulations, then constrain some of the parameters of the shell based upon those results. In Chapter 4 we use the models developed in Chapter 3 to the well observed SN Ia, SN 2011fe, seeking determine whether the supernova-shell interaction model can produce the observed spectra and evolution of the PVF and HVF. In Chapter 5 we use the spectral generation software TARDIS to produce synthetic spectra using the supernova-shell interaction models, again comparing those spectra to SN 2011fe, as an attempt to constrain the composition of the shell. In Chapter 6 we discuss a method to derive the abundance of individual elements in the shell based on the methods described in Chapter 4. Finally, we conclude our results in Chapter 7.

Chapter Two: High-Velocity Features of Calcium and Silicon in the Spectra of Type Ia Supernovae

2.1 Prelude

Significant portions of this chapter have been published previously as Silverman et al. (2015). It is presented here largely as detailed background on the evolution of HVF in SN Ia up to and just beyond peak brightness. While the bulk of the effort in this work is that of Jeffrey Silverman and the other authors, this author was involved in the interpretation and analysis of the results, and contributed some writing and a graph to the conclusion.

2.2 Introduction

Observations of Type Ia supernovae (SNe Ia) led to the discovery of the accelerating expansion of the Universe (Riess et al., 1998; Perlmutter et al., 1999) and have been extremely useful as a way to accurately measure cosmological parameters (e.g., Suzuki et al., 2012; Betoule et al., 2014; Rest et al., 2014). The cosmological utility of SNe Ia as precise distance indicators relies on the fact that their luminosity can be standardised. Phillips (1993) was the first to convincingly show that the light-curve decline rate of most SNe Ia is well correlated with luminosity at peak brightness, a connection now known as the "Phillips relation."

SNe Ia arise from the thermonuclear explosion of C/O white dwarfs (WDs; e.g., Hoyle & Fowler, 1960b; Colgate & McKee, 1969; Nomoto et al., 1984; Nugent et al., 2011; Bloom et al., 2012), but beyond that basic statement, we still lack a detailed understanding of the progenitor systems and explosion mechanisms of SNe Ia (see Howell 2011 and Maoz et al. 2014 for further information). In general, the two leading progenitor scenarios are the single-degenerate (SD) channel, when the WD accretes matter from a nondegenerate companion star (e.g., Whelan & Iben, 1973), and the double-degenerate (DD) channel, which is the result of the merger of two WDs (e.g., Iben & Tutukov, 1984; Webbink, 1984).

Detailed spectroscopic studies of large collections of low-redshift SNe Ia have been undertaken in the past (e.g., Barbon et al., 1990; Branch & van den Bergh, 1993; Nugent et al., 1995; Hatano et al., 2000; Folatelli, 2004; Benetti et al., 2005; Bongard et al., 2006; Hachinger et al., 2006; Bronder et al., 2008; Foley et al., 2008; Branch et al., 2009; Wang et al., 2009b; Walker et al., 2011; Nordin et al., 2011; Blondin et al., 2011; Konishi et al., 2011; Foley & Kasen, 2011; Silverman et al., 2012b), and have focused mainly on "photospheric-velocity features" (PVFs), which are absorption features with minima indicating typical photospheric (i.e., bulk ejecta) velocities (usually $\sim$9000–15, 000 km s^{-1} near B-band maximum brightness). These features are formed at the outer edge of the optically–thick portion of the ejecta; thus, most absorption features in the spectra of SNe Ia should be PVFs. However, some recent work has focused on carefully identifying and characterising so-called "high-velocity features" (HVFs), which are spectral features that have minima indicating significantly higher velocities than typical photospheric velocities (i.e., 6000–13, 000 km s^{-1} larger than PVFs, e.g., Mazzali et al., 2005b; Maguire et al., 2012a; Folatelli et al., 2013; Childress et al., 2014; Maguire et al., 2014).

In addition to these extensive samples, many studies of individual SNe Ia have presented evidence for HVFs (e.g., Hatano et al., 1999; Li et al., 2001a; Gerardy et al., 2004; Thomas et al., 2004; Wang et al., 2009a; Foley et al., 2012a; Parrent et al., 2012; Silverman et al., 2012c; Childress et al., 2013b; Marion et al., 2013; Maund et al., 2013; Pereira et al., 2013; Silverman et al., 2013b) and have shown that they appear strongest in early-time spectra and weaken with time (as the PVFs strengthen). Previous work has also shown that HVFs are most often seen in the Ca II H&K (hereafter CaHK), Si II 6355 Å, and Ca II NIR triplet (hereafter CaNIR) features, though they are sometimes also present in other features as well (e.g., Parrent et al., 2012; Marion et al., 2013). Furthermore, the line-forming regions of the PVFs and HVFs appear to be physically distinct and substantially asymmetric, based in part on numerous spectropolarimetric observations (e.g., Leonard et al., 2005; Wang et al., 2003, 2006; Chornock & Filippenko, 2008; Patat et al., 2009; Maund et al., 2013).

It has been suggested that the velocity of the CaHK feature is correlated with light-curve width (e.g., Maguire et al., 2012a) and that HVFs are responsible for this relationship. However, Foley (2013) claims that Si II λ3858 usually dominates the CaHK profile and is actually the cause of the observed correlation. Recently, Childress et al. (2014) examined HVFs of CaNIR in 58 low-redshift SNe Ia with

spectra within 5 d of B-band maximum brightness and found that the existence and strength of HVFs is (positively) correlated with light-curve width and uncorrelated with SN colour. They also find that the existence and strength of the CaNIR HVFs are anticorrelated with Si II 6355 Å (photospheric) velocity. These results are confirmed by Maguire et al. (2014), who studied a different dataset, consisting of 258 low-redshift SNe Ia with spectra earlier than 5 d after maximum brightness. This study finds that ∼80 per cent (60–70 per cent) of SNe Ia at epochs earlier than 5 d before (after) maximum show evidence for HVFs of CaNIR, and that these features have velocities that are ∼7000 km s^{-1} faster than the PVFs seen in the same spectra.

Despite the recent interest in HVFs, an explanation of the physical origin of these features and how they might be related to SN Ia progenitors and their environments is still lacking. Interaction with circumstellar material (CSM) is one of the leading proposed causes of HVFs, which could arise from the SN ejecta sweeping up (or otherwise interacting with) a clumpy CSM, or a torus or shell of CSM (e.g., Kasen et al., 2003; Wang et al., 2003; Gerardy et al., 2004; Mazzali et al., 2005b; Tanaka et al., 2006; Patat et al., 2009). Alternatively, HVFs could arise naturally from the SN Ia explosion mechanism itself, such as from helium detonations in WD envelopes (e.g., Shen & Moore, 2014). No matter what the origin of HVFs, it seems likely that an abundance or density enhancement at high velocity (i.e., large radius in homologously expanding SN Ia ejecta) must be present (e.g., Mazzali et al., 2005b; Tanaka et al., 2008), though perhaps ionisation effects play a role as well (Blondin et al., 2013).

In this work, we explore a large dataset of low-redshift ($z < 0.1$), low-resolution, optical and NIR SN Ia spectra observed earlier than 5 d before maximum brightness (described in Section 2.3), a subset of which was studied by Childress et al. (2014). In these data we carefully search for and measure the profiles of HVFs and PVFs of CaHK, Si II 6355 Å, and CaNIR (discussed in detail in Section 2.4). The temporal evolution of these features, and how their velocities and strengths correlate with each other and other observables, are described in Section 2.5. We summarise our conclusions in Section 2.6.

2.3 Dataset

The majority of the SN Ia spectra used in this study come from the Berkeley SN Ia Program (BSNIP) and have been published in BSNIP I (Silverman et al., 2012a). Most of these data were obtained with the Shane 3 m telescope at Lick Observatory using the Kast double spectrograph (Miller & Stone, 1993). The typical wavelength coverage of 3300–10, 400 Å (with resolutions of ∼11 and ∼6 Å on the red and blue sides, respectively) allows us to observe the CaHK and CaNIR features simultaneously. All objects have $z < 0.1$ with a median redshift of 0.02.

We require that each SN Ia have a well-determined date of maximum brightness so that we can assign an age to each spectrum. In this work, we only investigate spectra obtained earlier than 5 d after maximum brightness. Note that this is a superset of what was studied by Childress et al. (2014), who only used BSNIP spectra *within* 5 d of maximum. We removed objects which do not follow the "Phillips relation" *a priori*, including the extremely peculiar SN 2000cx (e.g., Li et al., 2001a), SNe Iax (e.g., Li et al., 2003; Jha et al., 2006b; Foley et al., 2013), and super-Chandrasekhar-mass objects (e.g., Howell et al., 2006; Scalzo et al., 2010; Silverman et al., 2011). A handful of the remaining spectra had signal-to-noise ratios (S/N) that were too low to reliably measure any spectral features or did not cover the wavelengths any of the three features under investigation (CaHK, Si II 6355 Å, and CaNIR). After all of these cuts, 226 spectra of 169 SNe Ia remained.

To this sample, we added low-resolution optical spectra obtained using the Marcario Low-Resolution Spectrograph (LRS; Hill et al., 1998) on the 9.2 m Hobby-Eberly Telescope (HET) at McDonald Observatory and the Robert Stobie Spectrograph (RSS; Nordsieck et al., 2001) on the 11.1 m by 9.8 m Southern African Large Telescope (SALT), and low-resolution NIR spectra obtained using SpeX (Rayner et al., 2003) on the NASA Infrared Telescope Facility (IRTF). Applying the same cuts as for the BSNIP sample, this yielded 128 spectra of 48 SNe Ia that covered at least the CaNIR feature. Most of these data are unpublished and will appear in upcoming works (e.g., Marion et al., in preparation), although a handful of these spectra have appeared in previous publications (e.g., Quimby et al., 2006; Marion et al., 2009; Parrent et al., 2011). There are 11 SNe Ia with spectra in both this sample and BSNIP.

We also include in the current study 91 published spectra of 5 extremely well-

observed SNe Ia: SNe 2009ig (Marion et al., 2013), 2011by[1] (Silverman et al., 2013a), 2011fe (Vinkó et al., 2012; Parrent et al., 2012), 2012cg (Silverman et al., 2012c; Marion et al., 2012), and 2012fr (Childress et al., 2013b; Zhang et al., 2014). This yields a total of 445 spectra of 210 SNe Ia that we analyse herein. Table A.1 lists the names and phases of the spectra for each object. Note that all results discussed in Section 2.5 are consistent with what is found when using just the BSNIP sample alone. Thus, adding the other spectra into the current study does not bias any of our findings, yet it adds statistical weight and significance to the results.

To better characterise the objects in our sample, we attempt to classify each SN Ia using a variety of classification schemes. We consider an object "spectroscopically normal" if it is classified as "Ia-norm" by the SuperNova IDentification code (SNID; Blondin & Tonry, 2007) as implemented in BSNIP I (Silverman et al., 2012a). Other "SNID Types" used in this work include "Ia-91bg" (e.g., Filippenko et al., 1992a; Leibundgut et al., 1993), which represent typically underluminous SNe Ia, and "Ia-91T" (e.g., Filippenko et al., 1992b; Phillips et al., 1992) and "Ia-99aa" (e.g., Li et al., 2001b; Strolger et al., 2002; Garavini et al., 2004), which together represent typically overluminous SNe Ia.

Using the expansion velocity of the Si II 6355 Å feature, Wang et al. (2009b) classified spectroscopically "normal" SNe Ia within 5 d of maximum brightness as either "normal velocity" (N) or "high velocity" (HV), with a velocity cutoff of 11, 800 km s^{-1} at maximum brightness. While a sharp distinction between the two "Wang Types" may not exist (e.g., Silverman et al., 2012b), we nonetheless utilise this classification scheme for illustrative purposes. Note that an individual SN Ia can be classified as N or HV, and each of its spectra may have PVFs, HVFs, or both. In other words, the Wang Type is used to classify a SN Ia, while the presence or absence of PVFs and HVFs is determined for each spectrum.

Another spectral classification scheme often used in SN Ia research was first introduced by Branch et al. (2006). Using the pseudo-equivalent widths (pEWs) of Si II 6355 Å and Si II λ5750 in spectra near maximum brightness, they divide their spectral sample into four different groups: core normal (CN), broad line (BL), cool (CL), and shallow silicon (SS). This classification scheme is not used in the current work because it is effectively equivalent to a combination of SNID Types and Wang

[1]Note that there are also spectra of SN 2011by in the aforementioned HET/SALT/IRTF sample.

Types (CN = N, BL = HV, CL = Ia-91bg, SS = Ia-91T/99aa).

Benetti et al. (2005) used the rate of decrease of the Si II 6355 Å expansion velocity before and near maximum brightness to define the velocity gradient, $\dot{v}$. Adopting these values, they separated their SN Ia sample into three subclasses, or "Benetti Types." High velocity gradient (HVG) and low velocity gradient (LVG) objects are normal-luminosity or overluminous SNe Ia with $\dot{v} \geq 70$ km s^{-1} d^{-1} and $\dot{v} < 70$ km s^{-1} d^{-1}, respectively. The third subclass (FAINT) have moderately large velocity gradients, but are underluminous ($\Delta m_{15}(B) \gtrsim 1.6$ mag). All three of the aforementioned classifications are listed for each object in Table A.1.

Photometric information was obtained from published sources, when available. This includes the date of B-band maximum for each object, as well as light-curve width (characterised by $\Delta m_{15}(B)$) and $(B-V)_0$ colour (the observed $B-V$ colour of the SN at B-band maximum brightness). For the BSNIP data, this information came from Jha et al. (2006a), Hicken et al. (2009), and Ganeshalingam et al. (2010). Photometric information for the HET, SALT, and IRTF data were obtained from a variety of sources (Quimby et al., 2006; Ganeshalingam et al., 2010; Stritzinger et al., 2011; Maguire et al., 2012a; Hicken et al., 2012; Silverman et al., 2013a). As for the five well-studied objects, their spectroscopic and photometric references are listed above. About two-thirds of the objects in this study have published $\Delta m_{15}(B)$ and $(B-V)_0$ values, and these are also presented in Table A.1.

2.4 Measurement Procedure

The measurement procedure used in this study is implemented in `IDL` and based in part on the one utilised extensively in BSNIP II (Silverman et al., 2012b). It is briefly described by Silverman et al. (2013b), but the description of our procedure herein is more in-depth. Each spectrum is first deredshifted (adopting the redshift listed in NED) and corrected for Milky Way (MW) reddening using values from Schlegel et al. (1998). Each of the three features measured (CaHK, Si II 6355 Å, and CaNIR) is then investigated individually.

For each feature, a local minimum in the spectrum is found, and the first local, relatively broad maxima are recorded to the left and right of this minimum. Note that the local maximum to the right of the minimum often corresponds to the peak

of the P-Cygni profile. A concave downward quadratic function is fit to these local maxima, and the peaks of these parabolas are considered the endpoints of the spectral feature. These endpoints were visually inspected for every feature measured, and in about one-third of cases one or both of the endpoints were clearly incorrect, either still within the feature profile or very far from it. In these cases, the endpoints were chosen manually.

The two endpoints for each feature are then connected with a straight line, and this becomes the pseudo-continuum (black, dotted lines in Fig. 2.1). The continuum flux at each pixel is then subtracted from the observed flux, yielding the background-subtracted spectrum used in the procedure described below. This step is sometimes referred to as flattening the spectra and was used previously in BSNIP II (Silverman et al., 2012b). One might instead *divide* the observed flux at each pixel by the continuum flux, though our tests indicate that this alternative approach does not significantly change the derived fit parameters; the values differ only at the few-percent level.

For each feature, the local minimum is found (when fitting only one velocity component, either PVF *or* HVF) or two separate local minima are found (when fitting two velocity components simultaneously, i.e., a PVF *and* HVF). These minima are then used as initial estimates in a nonlinear least-squares fitting routine that fits the entire profile between the two endpoints with either one or two velocity components. Each component consists of one (for Si II 6355 Å), two (for CaHK, left column of Figure 2.1), or three (for CaNIR, right column of Figure 2.1) Gaussian functions and contains three free parameters. The relative separations of the Ca II lines come from their rest wavelengths, while their relative strengths come from their gf-weights[2]. We are thus operating in the optically thin limit, an assumption which has been shown in previous work using similar spectral feature fitting methods to not strongly affect the results (Childress et al., 2014; Maguire et al., 2014; Pan et al., 2015).

For CaNIR and Si II 6355 Å, two fits were attempted for each profile: a one-component fit (PVF *or* HVF) and a two-component fit (both HVF *and* PVF). For CaHK, however, the possible presence of Si II λ3858 (e.g., Foley, 2013) complicates matters. Thus, we attempt four fits for each CaHK profile: a one-component fit (PVF *or* HVF), a two-component fit (both HVF *and* PVF), a different two-component fit

[2]`http://www.nist.gov/pml/data/asd.cfm`.

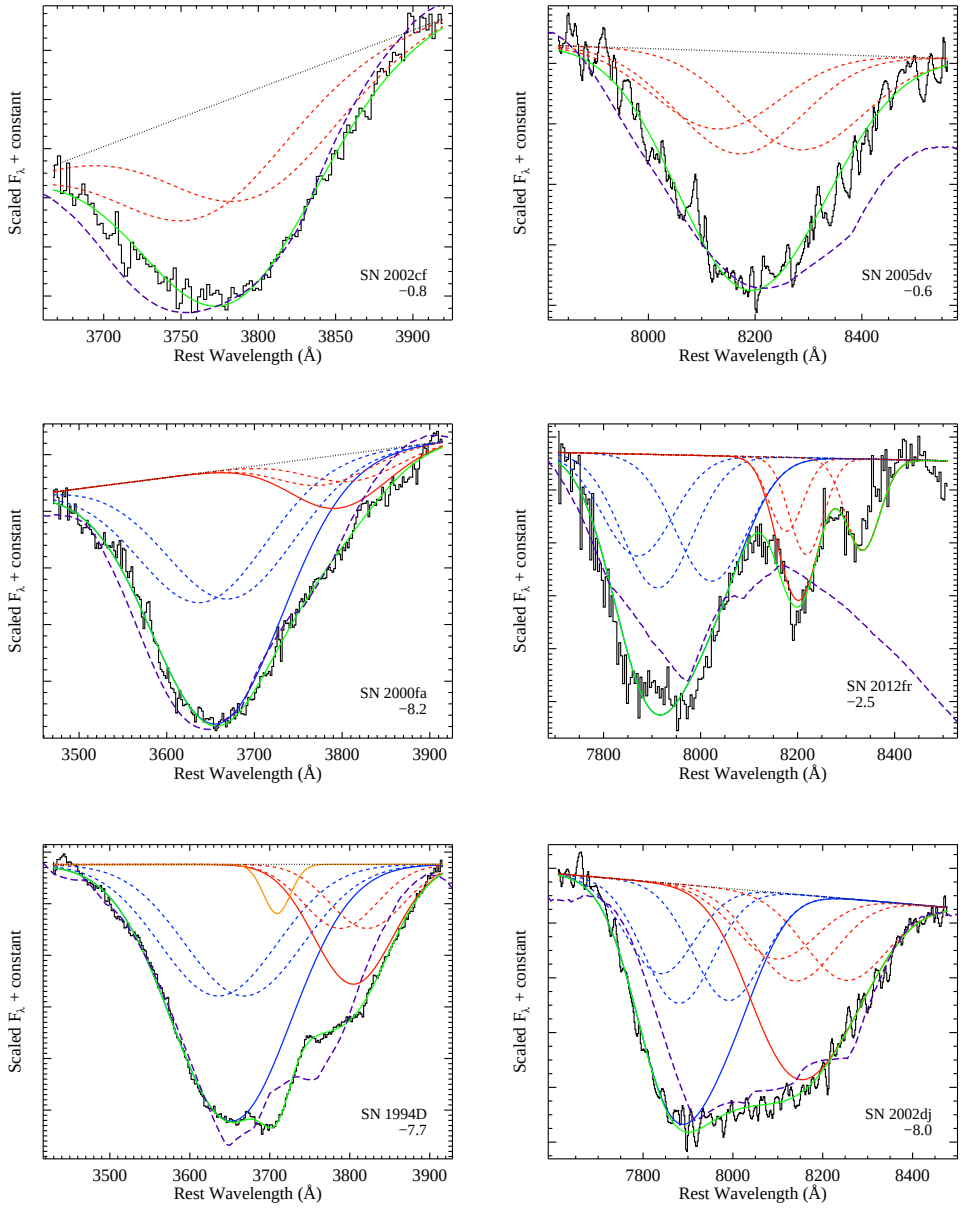

Figure 2.1: Fits to CaHK (*left column*) and CaNIR (*right column*) showing PVFs (*red*) and HVFs (*blue*, where required). Individual Gaussian components are *short-dashed* and their sum is *solid*. Also shown are the sum of the total fit (*green*), the data (*black, solid*), the linear continuum (*black, dotted*), and a SYNAPPS (Thomas et al., 2011a) fit (*purple, long-dashed*). Si II λ3858 is also required in the *bottom-left* fit (*orange, solid*). Each spectrum is labeled with its object name and age relative to B-band maximum brightness.

(PVF *or* HVF, but with a single component of Si II λ3858 included), and a three-component fit (both HVF *and* PVF, but with a single component of Si II λ3858 included). Each fit is then visually inspected, and in extreme cases where the fits do not match the data well, the initial estimates of local minima are changed and the fit is redone. As mentioned above, some spectra, mostly ones with low S/N, did not yield any acceptable fit.

While the *relative* separations and strengths of the spectral features are fixed as mentioned above, we do not impose any other constraints on the fit parameters. This differs from what was done by Maguire et al. (2014), who required that the CaNIR PVF velocities be within 25 per cent of the Si II 6355 Å velocity and that the CaNIR HVF velocities be at least 2000 km s^{-1} faster than the Si II 6355 Å velocity.

To decide which combination of fit components best represents the data, a variety of methods were used. All fits of a given spectral profile were visually inspected and the best fit was chosen via "χ-by-eye." This choice was then compared to the reduced-χ^2 value and the Bayesian information criterion (BIC) value for each fit. In the vast majority of cases, all three methods agreed unanimously. In the few cases where there was serious disagreement, we erred on the side of trusting fits with fewer parameters.

Once a best fit was chosen for each profile, the Gaussian fit parameters were used to calculate a velocity using the relativistic Doppler equation and a pEW (e.g., Garavini et al., 2007; Silverman et al., 2012b) for each component of the fit. These values (and their uncertainties) for CaHK, Si II 6355 Å, and CaNIR are listed in Tables A.2, A.3, A.4, respectively. The formal uncertainty of the Gaussian fits indicates that the typical velocity error is $\sim$60 km s^{-1}. The minima of the spectral fits, however, are only accurate to a few Å, which implies a velocity uncertainty more like $\sim$200–400 km s^{-1}. This measurement uncertainty increases for weaker features. A few examples of Ca II "best fits" are displayed in Figure 2.1.

2.4.1 Ambiguous CaHK Fits

As mentioned above, the CaHK feature overlaps with the Si II λ3858 feature, which can affect the observed spectral profile (e.g., Foley, 2013). This was seen in our data, as many spectra were fit equally well (in a reduced-χ^2 sense) by both a HVF and a PVF of CaHK, and Si II λ3858 and a PVF of CaHK. To break this degeneracy, we

exploited the fact that the majority of the spectra studied herein include both the CaHK and CaNIR features in the same observation. We assumed that if a spectrum showed a HVF of CaNIR (based on the method outlined above), then it should also have a HVF of CaHK (and vice versa). In the two ambiguous cases where the spectra did not cover the CaNIR feature, we found that the inferred Si II λ3858 velocity was significantly larger than the Si II 6355 Å velocity in the same observations, and thus we identify those profiles as containing HVFs of CaHK (instead of Si II λ3858).

To test our assumption that a HVF of CaNIR implies a HVF of CaHK, we temporarily changed all of our Si II λ3858 identifications to HVFs of CaHK. This led to large differences in the velocities of the HVFs of CaHK and the HVFs of CaNIR in the same spectrum ($\sim$5000 km s^{-1}, as opposed to the more typical value of $\sim$500 km s^{-1}; see below). It also led to relatively small differences between the velocities of the HVFs and PVFs of CaHK in the same spectrum ($\sim$5500 km s^{-1}, as opposed to the average of $\sim$9000 km s^{-1}; again, see below). Therefore, it seems that our identifications of Si II λ3858 are correct. Furthermore, we also compare the velocity of Si II λ3858 (when we detect it) with that of Si II 6355 Å in the same spectra and find the typical difference to be $\sim$600 km s^{-1}, consistent with previous work on velocities of various Si II spectral features (e.g., Silverman et al., 2012b).

The opposite test to the one described above was also performed. Namely, we temporarily changed all of our HVFs of CaHK to Si II λ3858. After doing this, the average Si II λ3858 velocity was found to be $\sim$15, 000 km s^{-1}, and on average about 2600 km s^{-1} faster than the Si II 6355 Å velocity in the same observation. Thus, these inferred Si II λ3858 velocities are too high to be real and so our HVF CaHK identifications appear to be correct.

Another way to visualise this is shown in Figure 2.2. There we plot the velocity of Si II 6355 Å versus the velocity of CaHK. The open points are PVFs of CaHK while the filled points are HVFs of CaHK, as determined using our method described above. The dotted line is the one-to-one line and shows that PVFs of CaHK are slightly faster than Si II 6355 Å at low Si II velocities and comparable at higher Si II velocities. The dashed line is the cutoff between HVFs and PVFs used by Foley (2013); the classifications from his study mostly match those in this work. Finally, the solid line represents Si II λ3858 at the same velocity as Si II 6355 Å, if our HVFs of CaHK were actually misidentified Si II. Thus, if a solid point fell directly on this line, the velocity of our measured HVF of CaHK would match that of Si II 6355 Å if

it were actually Si II λ3858.

The fact that most of the filled points lie above this line implies that our identification of HVFs of CaHK is correct and that if those features were actually Si II λ3858, then their velocities would be significantly higher than that of Si II 6355 Å in the same spectra (as discussed above). Finally, we note that our inferred velocities of the HVFs of CaHK and CaNIR are highly correlated, as are the velocities of the PVFs of CaHK and CaNIR, as well as the velocities of Si II λ3858 and Si II 6355 Å. This once again supports our spectral identifications.

2.4.2 Ambiguous Si II 6355 Å Fits

When applying the aforementioned fitting algorithm to the Si II 6355 Å feature, we discovered that a single Gaussian (plus linear background) fits most spectral profiles quite well. However, as has been seen previously (e.g., Silverman et al., 2012b), the stronger Si II 6355 Å profiles appear non-Gaussian and look more Lorentzian in shape (though these are mostly at greater than 3 d past maximum brightness, well after HVFs of Si II 6355 Å usually disappear; e.g., Marion et al., 2013). In addition, two Gaussian profiles (i.e., both a HVF and a PVF) fit nearly every observation very well, both via visual inspection as well as in a reduced-χ^2 sense. Thus, to decide whether one or two components were present in a given profile, other factors must be considered.

Some of the HVF+PVF fits to Si II 6355 Å had the difference in velocity between the two components less than 4500 km s^{-1}. This is significantly smaller than the smallest difference between Ca II HVFs and PVFs (i.e., $\sim$6000 km s^{-1}; see Section 2.5.3) and our fitting algorithm is not capable of reliably distinguishing between two components that are so close to each other in velocity space (see Section 2.4.3.1). Thus, we are unable to say with confidence that two components are present and in these cases we prefer the one-component fit. Other HVF+PVF fits to Si II 6355 Å indicated a velocity of the PVF of $\lesssim$ 9000 km s^{-1}, which is never seen at these epochs in the "relatively normal" SNe Ia used herein (e.g., Silverman et al., 2012b). Therefore, we regard these fits as unreliable as well, and we instead use the one-component fit for these data.

After removing the unphysical two-component fits mentioned above, we find that there are nearly no reliable two-component fits where the measured HVF velocity is

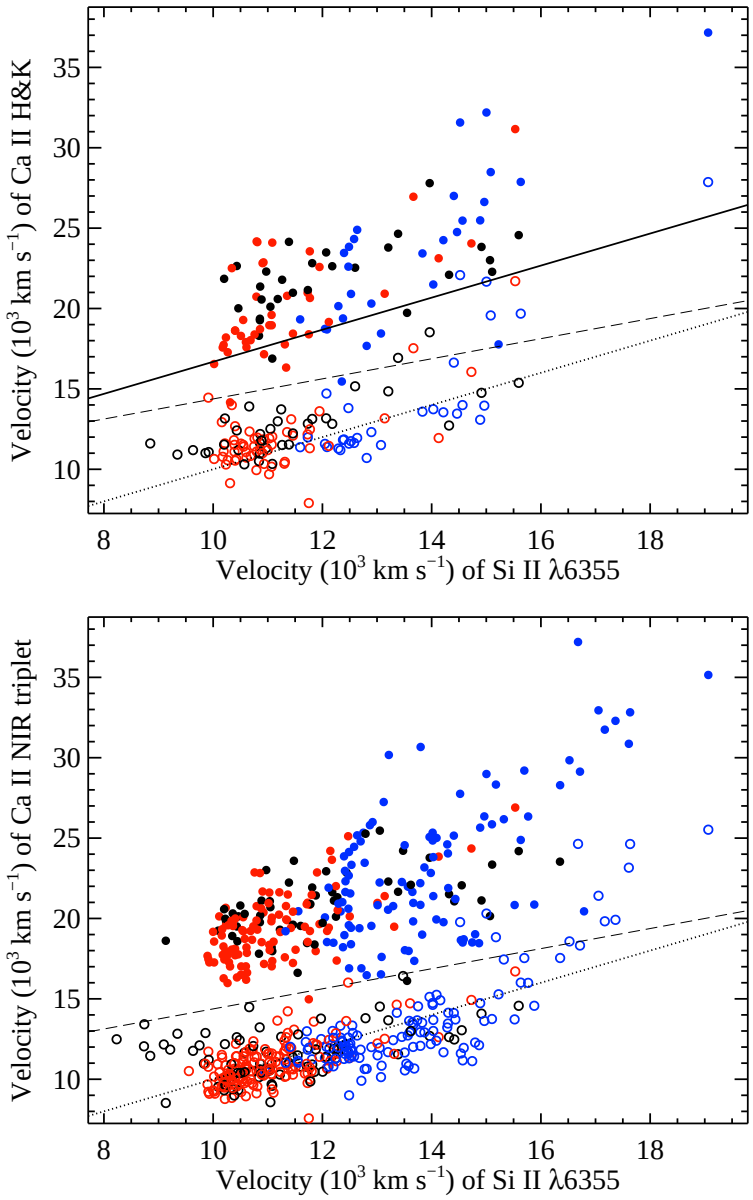

Figure 2.2: The velocity of CaHK (*top*) and CaNIR (*bottom*) versus the velocity of Si II 6355 Å. Open points are PVFs of Ca II and filled points are HVFs of Ca II. Blue points are HV objects, red points are N objects, and black points are objects without a Wang Type. The dotted line is the one-to-one line; the dashed line is the cutoff between HVFs and PVFs used by Foley (2013). The solid line in the top panel represents Si II λ3858 at the same velocity as Si II 6355 Å, if our HVFs of CaHK were actually misidentified Si II. Since most of the filled points in the top panel lie above the solid line, it is unlikely that they are actually Si II λ3858, and thus they are probably HVFs of CaHK, as our assumption implies.

less than 16, 500 km s^{-1}. Thus, our analysis indicates that HVFs of Si II 6355 Å always remain above ∼16, 500 km s^{-1}, consistent with previous work (e.g., Marion et al., 2013). Hence, we make the assumption that for a two-component (i.e., HVF+PVF) fit of Si II 6355 Å to be preferred over a one-component fit, the inferred HVF velocity must be larger than 16, 500 km s^{-1}.

Under this assumption, our measured PVF velocities of Si II 6355 Å are consistent with previous measurements of the same data (Silverman et al., 2012b; Childress et al., 2014). Figure 2.3 shows this by plotting the Si II 6355 Å velocities for the 201 spectra in the current study (on the abscissa) that were also analysed in BSNIP II (Silverman et al., 2012b, on the ordinate). Filled points represent spectra for which only one velocity component is detected in the current work. Pairs of open points connected with a horizontal line represent spectra for which both a PVF and a HVF velocity are measured in this work, with the left endpoint representing the PVF and the right endpoint representing the HVF. The "×" along each line segment represents the pEW-weighted mean of the Si II 6355 Å PVF and HVF velocities for that spectrum. The dotted line is the one-to-one line.

For velocities less than about 16, 000 km s^{-1}, only the PVF velocity was measured in BSNIP II, whether or not a HVF was actually present in the Si II 6355 Å profile. There are 11 spectra in which we detect two components herein that fall into this category, and all of them have relatively weak HVFs (which were simply missed by the fitting algorithm used in BSNIP II). For Si II 6355 Å velocities that are greater than ∼16, 000 km s^{-1}, BSNIP II typically measured the pEW-weighted mean of the Si II 6355 Å PVF and HVF velocities. The 8 spectra which have both a HVF and PVF component that are in this category were mostly observed at early times when the PVF velocity was high and the pEW of the HVF was large. This likely caused the two components to be severely blended and thus the pEW-weighted mean of the two velocities was measured in BSNIP II. Finally, when considering only spectra with one component, the BSNIP II velocities and those measured in the current work are consistent.

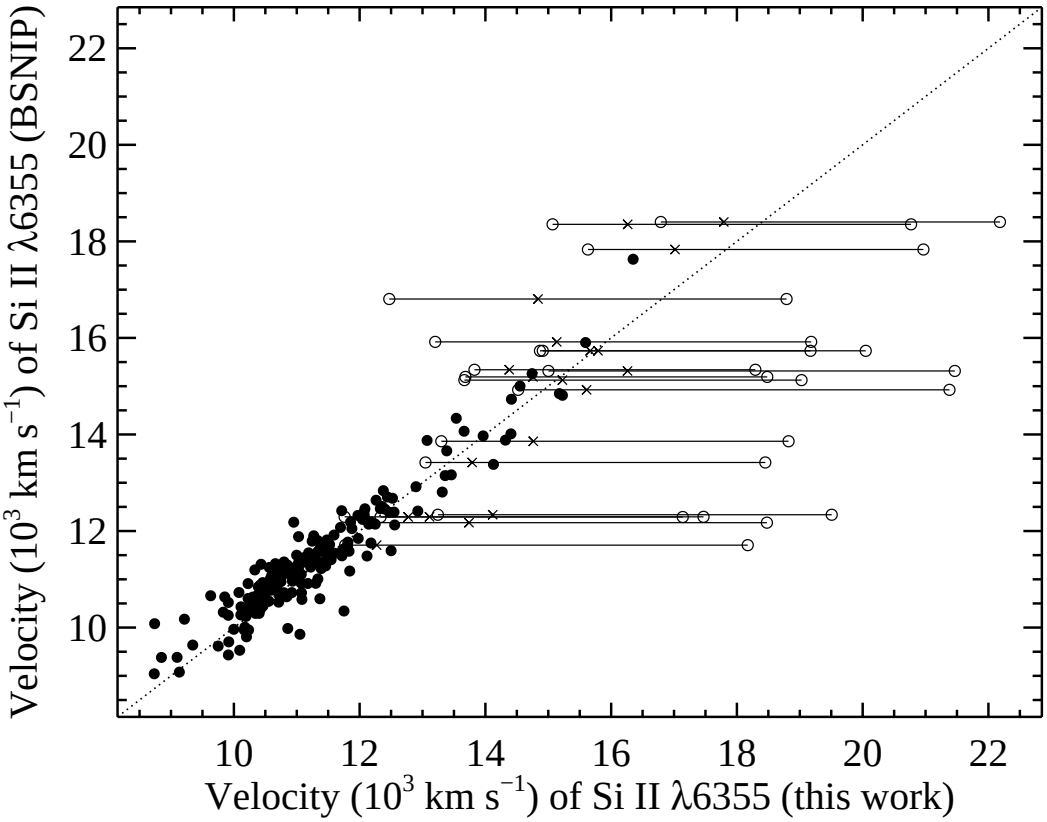

Figure 2.3: Si II 6355 Å velocities for the 201 spectra in the current study (on the abscissa) that were also analysed in BSNIP II (Silverman et al., 2012b, on the ordinate). Filled points are spectra with one velocity component. Open points connected with a horizontal line are spectra with two velocity components; the left endpoint is the PVF, the right endpoint is the HVF, and the "×" is the pEW-weighted mean of the Si II 6355 Å PVF and HVF velocities for that spectrum. The dotted line is the one-to-one line.

2.4.3 Checks of the Fitting Procedure

2.4.3.1 Synthetic Data

To test the limits of our fitting algorithm, we constructed synthetic spectral profiles with a variety of Gaussian input parameters. The first test varied only the separation in velocity/wavelength space between the two components (i.e., HVFs and PVFs). We started with representative values of PVF and HVF velocities and widths from our fit to one of our relatively high-S/N spectra (SN 2002dj, $t = -8$ d). The velocity of the PVF was held constant at its value from the fit to the actual data ($\sim$14, 600 km s^{-1}), while the velocity of the HVF component was varied. Random noise was also added to the Gaussian functions to more closely resemble real data.

The HVF velocities tested ranged from the original value from the fit to the data ($\sim$24, 200 km s^{-1}) down to $\sim$17, 700 km s^{-1}, in steps of 500 km s^{-1}. This allowed us to create 13 synthetic spectra with velocity differences between the HVF and PVF of 9600–3100 km s^{-1}. We then applied our spectral fitting algorithm as outlined above to these synthetic data. For all spectra with velocity separations greater than or equal to 4500 km s^{-1}, our fitting procedure preferred a two-component profile, while spectra with separations in velocity below this value were better fit by a one-component CaNIR profile. Thus, it seems that our fitting algorithm is able to "resolve" distinct PVF and HVF components when they are separated by greater than about 4500 km s^{-1}. As we will show below, the smallest velocity difference between HVFs and PVFs seen in our data is $\sim$5000 km s^{-1}. Therefore, it seems unlikely that nature produces HVFs and PVFs with velocity separations of less than about 5000 km s^{-1}; otherwise, our algorithm would probably have detected them.

A similar test was performed by varying the depth of the HVF, while holding the depth of the PVF constant (along with the width and velocity of both components). The difference in velocity between the HVF and PVF used in this test was $\sim$9000 km s^{-1}, which is typical for our dataset (see below). The depth of the HVF was varied such that we tested depth ratios (HVF depth divided by PVF depth) of 1–0.05, in steps of 0.05. Two-component fits to the CaNIR profile (i.e., HVF+PVF) were preferred in spectra where the ratio of depths was greater than 0.1. Thus, if there is a HVF whose depth is less than about 10 per cent that of the PVF, or vice versa, we will likely be unable to detect it using our fitting algorithm. The smallest finite ratio between the strengths of HVFs and PVFs of Ca II that we measure in

our data is about 0.12 (see below). Therefore, nature *may* produce HVFs that are so weak compared to their PVFs (or vice versa) that our algorithm cannot detect them.

2.4.3.2 SYNAPPS Fits

As another check to our spectral measurement technique, we use the spectrum-synthesis code SYNAPPS (Thomas et al., 2011a). SYNAPPS (and its modeling kernel `SYN++`) is derived from SYNOW (Fisher et al., 1997), which can compute spectra of SNe in the photospheric phase using the Sobolev approximation (Sobolev, 1960; Castor, 1970; Jeffery, 1989). By varying many parameters automatically and simultaneously, SYNAPPS can find an optimum fit to an input spectrum via χ^2-minimisation. SYNAPPS assumes that spectral lines are formed via resonance scattering above a sharp photosphere. The location of this photosphere (in velocity space) is defined by the $v_{\rm ph}$ parameter, and the ejecta are assumed to be in homologous expansion at a photospheric temperature defined by the $T_{\rm phot}$ parameter.

For each input ion, the minimum and maximum velocity of the line-forming region are defined by the $v_{\rm min}$ and $v_{\rm max}$ parameters, respectively. In cases where $v_{\rm min} \gtrsim v_{\rm ph}$, the line-forming region is considered "detached" from the photosphere; by definition, this is the case for all HVFs. Each input ion also requires a value for the optical depth of a "reference line, " $\tau_{\rm ref}$ (usually the strongest optical line), an e-folding velocity width of the optical-depth profile above the photosphere, v_e, and an excitation temperature, $T_{\rm exc}$.

SYNAPPS was used to fit 11 spectra that were chosen semirandomly to represent various CaHK and CaNIR profile shapes (i.e., differing relative strengths of HVFs, PVFs, and Si II λ3858). Each fit used ions that are typically found in SNe Ia (i.e., O I, Ca II, Mg II, Si II, S II, and Fe II); some fits also included Si III, Fe III, or Ti II. SYNAPPS was also allowed to include a "detached" version of Ca II, representing the HVFs. Some of these fits can be seen in Figure 2.1 as the purple, long-dashed curves.

In general, the SYNAPPS fits match well with our Gaussian fits to the data in that the spectral shapes agree, and when our fitting algorithm detects a HVF, it is also required in the SYNAPPS fit (and vice versa). Note that the SYNAPPS fits were not intended to perfectly match the entire spectral range covered by the data; they were used mainly to identify and disentangle the HVF and PVF components

of the CaHK and CaNIR features. The sum of the Gaussian fits used herein tend to reproduce the details of the profile better than the SYNAPPS fits, as the latter appear to be "smoothed out" and are unable to match the smaller-scale features in the data.

Given the uncertainties of the measured velocities using our fitting algorithm and the degeneracy in the SYNAPPS fits between input velocity and $\tau_{\rm ref}$, the velocities derived using the two methods are consistent within $\sim 2\sigma$ (i.e., $\sim$1200 km s^{-1}). The largest disagreement in the velocities comes when the PVFs are weak. In these cases, there are large uncertainties in the SYNAPPS parameters, and one can change the value of $\tau_{\rm ref}$ a small amount to force the velocity of the PVFs to match what is measured using our fitting algorithm.

As for the measured strengths of the features as characterised by their pEWs, the SYNAPPS fits and the measurements from our fitting algorithm are roughly consistent, but not as close to each other as the velocities of the features. This is possibly caused by the uncertainty associated with the $\tau_{\rm ref}$ parameter in the SYNAPPS fits. Furthermore, SYNAPPS indicates that the Si II λ3858 feature is always present in the observations, but is only noticeably strong in spectra where our fitting algorithm required it to be included in the Gaussian fits. In conclusion, while both SYNAPPS and our spectral feature fitting algorithm have their distinct pros and cons, their general agreement (especially regarding the existence of HVFs) is encouraging.

2.4.4 Comparisons to Previous Measurements

Marion et al. (2013) present a detailed study of the well-observed Type Ia SN 2009ig, specifically focusing on HVFs of various ions in the pre- and near-maximum-brightness spectra. This study is one of the very few that seriously investigates HVFs of Si II 6355 Å (as we also do in this work). To compare and contrast with SN 2009ig, they also discuss HVFs in a handful of other objects. To derive the velocities, Marion et al. (2013) fit Gaussians to the cores of the features without removing the continuum. They inspect the positions of the derived minima visually and then calculate the velocity and uncertainty of HVFs and PVFs in CaHK, Si II 6355 Å, and CaNIR.

The dataset used herein includes 16 of their spectra of SN 2009ig, as well as 16 spectra of 9 other SNe Ia studied by Marion et al. (2013). For the 7 (27) spectra present in both samples that include the CaHK (CaNIR) feature, we find that both

the HVF and PVF velocities are consistent at the 2–3σ level, with a nearly constant offset of $\sim$1400 km s^{-1} ($\sim$900 km s^{-1}) between the two studies. Similar results are found for the Si II 6355 Å feature, where the average offset in the HVF velocity is $\sim$1100 km s^{-1} (for 8 spectra) and in the PVF velocity is $\sim$400 km s^{-1} (for 14 spectra). We detect about half the number of HVFs of Si II 6355 Å as Marion et al. (2013), likely owing to the different fitting algorithms employed in the two studies. Finally, we note that the offsets are such that the HVF velocities measured herein tend to be higher than those of Marion et al. (2013), while the PVF velocities tend to be lower, thus leading to the current study finding larger velocity differences between the two components.

Childress et al. (2014), as mentioned above, studied HVFs of CaNIR in a relatively large sample of SNe Ia spectra near maximum brightness, which represents a subset of the sample used herein. They used two Gaussians to fit each CaNIR profile and assumed equal strength in each of the triplet components. Childress et al. (2014) also forced a minimum velocity difference between the HVFs and the PVFs in a given spectrum of 2000 km s^{-1}, and required that the velocity and width of the PVFs be within 10 per cent of those of the Si II 6355 Å feature in the same spectrum. As described in Section 2.4, our fitting algorithm does not impose such strict limits on the fit parameters.

The measured Si II 6355 Å PVF (CaNIR HVF and PVF) velocities of the 56 spectra that are in both datasets are consistent at the 1–2σ level, with typical offsets of $\sim$300 km s^{-1} ($\sim$500 km s^{-1}). These offsets are such that the velocities measured herein tend to be larger than those reported by Childress et al. (2014). They also measure pEWs for the Si II 6355 Å PVFs and the CaNIR PVFs and HVFs. These values are consistent with what we measure at the 2–3σ level (offsets of $\sim$9 Å), and once again our values tend to be larger than those of Childress et al. (2014). These relatively minor differences are likely caused by the assumption of optically thin (this work, see above) versus optically thick (Childress et al., 2014) spectral features.

2.5 Results & Analysis

2.5.1 The Existence of HVFs in CaHK and CaNIR

Using the aforementioned algorithm, we calculate the pEW and expansion velocities of HVFs and PVFs for the CaHK and CaNIR features; these are listed in Tables A.2 and A.4, respectively. For CaHK, we fit a total of 126 spectra of 84 SNe Ia; 5 of these spectra have HVFs only, 12 have PVFs only, 79 have both HVFs and PVFs present, 15 have PVFs and a Si II λ3858 feature, and 15 have both HVFs and PVFs, in addition to Si II λ3858. On the other hand, we fit the CaNIR feature in a total of 382 spectra of 192 SNe Ia; 16 of these spectra have HVFs only, 105 have PVFs only, and 261 have both HVFs and PVFs present.

There are eight SNe Ia in the sample that exhibit only HVFs in their earliest spectra; most of these observations are earlier than 7 d before maximum brightness. We have multiple spectra of three of these objects, and all three eventually develop PVFs. Childress et al. (2013b) found evidence for HVFs, but not PVFs, in their earliest spectra of SN 2012fr, consistent with what is found herein using the same observations. On the other hand, Marion et al. (2013) detected HVFs, but *not* PVFs, in early-time spectra of SN 2009ig, while we *do* detect PVFs (as well as HVFs) in the same data. Note that Maguire et al. (2014) found no spectra with only HVFs in their sample.

SN Ia spectra tend to evolve from having only HVFs (in $\sim$4 per cent of cases), to having both HVFs and PVFs (in the majority of spectra, i.e., $\sim$65–75 per cent), to having only PVFs (in $\sim$20–30 per cent of the observations). This generic picture of spectra changing with time (HVFs$\rightarrow$HVFs+PVFs$\rightarrow$PVFs) is consistent with what has been seen in previous work (e.g., Childress et al., 2013b; Marion et al., 2013). As mentioned above, spectra with only HVFs are seen almost exclusively at very early times. Spectra with only PVFs are seen as early as $\sim$12 d before maximum brightness and as late as 5 d past maximum (which are the oldest spectra included in the current study). Data that show both HVFs and PVFs simultaneously are observed at all epochs studied herein ($-16 < t < 5$ d), implying that there is evidence of some SNe Ia showing HVFs at epochs as late as 5 d past maximum brightness, though most HVFs are gone by about 5 d *before* maximum.

When considering the entire dataset studied herein, we find that $\sim$67 per cent

of all objects show HVFs in at least one spectrum. This is almost exactly the same percentage that was found by Maguire et al. (2014). When looking at only early-time observations ($t \lesssim -4$ d), $\sim$91 per cent of the objects show evidence of HVFs, which is consistent with, but slightly higher than, what was found previously (83 per cent, Maguire et al., 2014).

Of the SNe Ia for which we fit the CaHK or CaNIR features, $\sim$28 per cent of them are HV objects, consistent with the overall SN Ia population (e.g., Wang et al., 2009b; Silverman et al., 2012b). Of the SNe Ia with a known Wang Type, 77 per cent (71 per cent) of HV objects show HVFs of CaHK (CaNIR), while 70 per cent (62 per cent) of N objects shows HVFs of CaHK (CaNIR). Similarly, (SNID Type) Ia-norm objects contain HVFs of CaHK 78 per cent of the time and HVFs of CaNIR 70 per cent of the time, and all 10 Ia-91T/99aa objects in our dataset show HVFs of Ca II. Given the number of SNe Ia in each category, these percentages are all mutually consistent. On the other hand, only 1 out of 17 Ia-91bg objects show HVFs of Ca II. This significant dearth of HVFs in underluminous SNe Ia (i.e., Ia-91bg objects) has been noticed in previous work as well (Maguire et al., 2012a; Childress et al., 2014; Maguire et al., 2014).

The entire BSNIP dataset averages $\sim$2 spectra per object (Silverman et al., 2012a), and since these data make up the bulk of the sample used herein, there are not many objects for which we have multiple spectra. Thus, we are only able to determine a Benetti Type for a handful of the objects studied in this work. For those SNe Ia with a Benetti Type, 62 per cent (72 per cent) of HVG objects show HVFs of CaHK (CaNIR), while 85 per cent (82 per cent) of LVG objects shows HVFs of CaHK (CaNIR). Only 1 of 8 SNe Ia with a Benetti Type of FAINT (i.e., underluminous objects) contained HVFs. These numbers are consistent with what was found above using Wang and SNID Types, given the association of HV/N/Ia-91bg objects with HVG/LVG/FAINT objects (e.g., Silverman et al., 2012b).

A possible bias leading to the above result is that we do not have any spectra of Ia-91bg (or FAINT) objects at epochs earlier than 3 days before maximum brightness. Thus, perhaps, Ia-91bg/FAINT objects have HVFs, but they disappear earlier than in other SN Ia subtypes. We reject this idea in part because at $t = -3$ d, about half of all SNe Ia show HVFs, and this is also the same epoch when HVFs and PVFs tend to be about equal in strength (see Section 2.5.2). Conversely, 6 of the 9 objects that show only PVFs at $t < -3$ d are spectroscopically somewhat similar to SN 1991bg

or have relatively narrow light curves and thus appear to be border cases between Ia-norm and Ia-91bg. The remaining 3 objects in this category all have their earliest spectra at $t \approx -6$ d, so HVFs could have been present at earlier times, but have faded by the time our spectra were obtained.

We further investigate whether the apparent lack of HVFs in Ia-91bg/FAINT objects is an observational bias by determining the typical epoch at which HVFs "disappear." This was done by taking each object with more than 1 spectrum in our dataset and fitting a line to the strength of the HVF relative to the PVF (see Section 2.5.2) versus time in order to find the epoch at which the relative strength of the HVF drops below our detection threshold of 0.1 (see Section 2.4.3.1); we refer to this as the "epoch of disappearance." This epoch is then compared to the light-curve width (i.e., $\Delta m_{15}(B)$) in order to search for any relationship between peak luminosity and the epoch of disappearance.

In the current sample, there were 26 SNe Ia with known $\Delta m_{15}(B)$ values and for which we were able to determine an epoch of disappearance. The latter for these objects is about $t = -1$ d to $t = +0.5$ d. When comparing the epoch of disappearance to $\Delta m_{15}(B)$, we find a large amount of scatter. The epoch of disappearance may decrease with increasing $\Delta m_{15}(B)$, but the slope of the linear fit is consistent with 0. Using our best linear fit to the data, we find the epoch of disappearance to be about -1.0 d for $\Delta m_{15}(B)$ values of 1.4–1.6 mag (e.g., Ganeshalingam et al., 2010, typical for Ia-91bg/underluminous objects).

There are no objects classified as Ia-91bg in this work with spectra obtained earlier than 3 d before maximum brightness. However, according to the above analysis, Ia-91bg spectra obtained earlier than $\sim$1 d before maximum *should* show HVFs. Thus, Ia-91bg objects (equivalently, Benetti FAINT objects or SNe Ia with narrow light curves) seem to *never* show HVFs, while all other SN Ia subtypes studied herein (HV, N, Ia-norm, Ia-91T/99aa, LVG, and HVG objects) *always* show HVFs (in spectra obtained earlier than $\sim$6 d before maximum). Owing to there being relatively few Ia-91bg objects in our sample, however, there is a small possibility that they may have HVFs at epochs earlier than about 3 d before maximum, but these features would have to disappear even earlier than one would expect based on the rest of our dataset.

2.5.2 Ca II pEWs

The pEWs of CaHK and CaNIR for both HVFs and PVFs are listed in Tables A.2 and A.4, respectively. The temporal evolution of these pEWs is displayed in Figures 2.4, 2.5, and 2.6. Open symbols represent PVFs while filled symbols represent HVFs. Blue points are high-velocity (HV) objects, red points are normal-velocity (N) objects, and black points are objects for which we could not determine a Wang Type. Squares are Ia-norm objects, stars are Ia-91bg objects, triangles are Ia-91T/99aa objects, and circles are objects which do not have a SNID Type.

At all epochs there is large scatter in the pEWs of HVFs and PVFs for both Ca II features. For $t \gtrsim -9$ d, the pEWs of the HVFs tend to decrease with time while those of the PVFs tend to increase with time, as expected. One specific counterexample to this is SN 2009ig, which has stronger PVFs than HVFs at the very earliest times, but quickly evolves to have the HVFs dominate the profile (until $t \approx -6$ d; see also Marion et al., 2013). The typical epoch at which the strengths of the HVFs and PVFs of the Ca II features are equal is about 4 d before maximum brightness. That being said, individual SNe Ia achieve equal HVF and PVF strength at a range of epochs ($-8 < t < 2$ d), which matches what has been found previously (Marion et al., 2013).

HV objects tend to have strong HVFs at the earliest times, but they decrease in strength relatively quickly, leading to somewhat weak HVFs in HV objects near maximum brightness. The latter part of this result has been seen previously (Childress et al., 2014; Maguire et al., 2014), but at a much stronger level than what is found in the current study. We attribute this difference not only to the epochs studied (the previous works only used spectra within 5 d of maximum brightness), but also to the fact that these prior studies contained too few HV objects (∼13 per cent of their sample, versus 28 per cent herein; Childress et al., 2014; Maguire et al., 2014). This difference is discussed in more detail in Section 2.5.4.

While Ia-91bg objects never show HVFs, they do exhibit some of the largest pEWs of PVFs. On the other hand, Ia-91T/99aa objects always show HVFs, but the pEWs of their PVFs and HVFs are some of the lowest values seen in Figures 2.4, 2.5, and 2.6. These results have been found previously and are relatively unsurprising since strong (weak) absorption features are a defining characteristic of Ia-91bg (Ia-91T/99aa) objects (Silverman et al., 2012b; Folatelli et al., 2013; Childress et al., 2014).

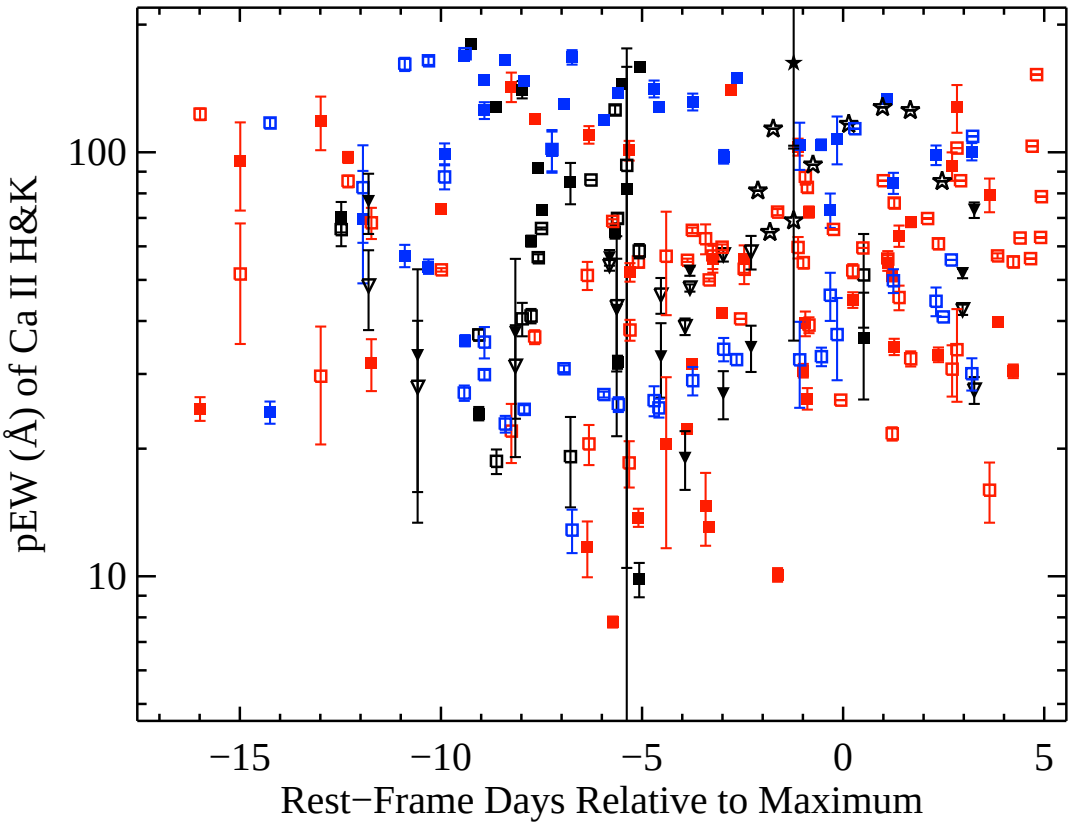

Figure 2.4: The CaHK pEWs versus time. The vertical error bars are the median absolute deviation in each bin. Open symbols are PVFs; filled symbols are HVFs. Blue points are HV objects, red points are N objects, and black points are objects without a Wang Type. Squares are Ia-norm, stars are Ia-91bg, triangles are Ia-91T/99aa, and circles are objects without a SNID Type. There is large scatter in the pEWs of HVFs and PVFs at all epochs, though the pEWs of HVFs (PVFs) tend to decrease (increase) with time.

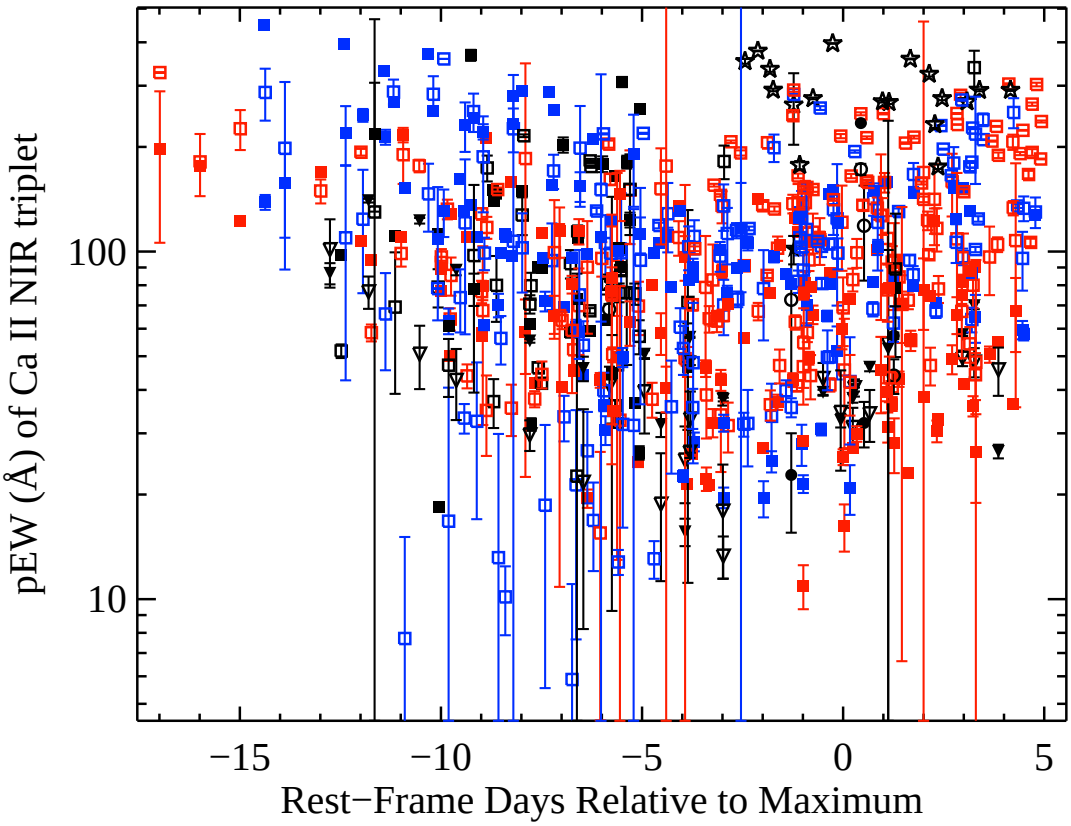

Figure 2.5: The CaNIR pEWs versus time. The vertical error bars are the median absolute deviation in each bin. Colours and shapes of data points are the same as in Figure 2.4. There is large scatter in the pEWs of HVFs and PVFs at all epochs, though the pEWs of HVFs (PVFs) tend to decrease (increase) with time.

To investigate the *relative* strength of HVFs to PVFs, Childress et al. (2014) defined $R_{\rm HVF}$ as the ratio of pEW of the HVF of CaNIR to the pEW of the PVF of CaNIR. In this work, we define $R_{\rm CaHK}$ and $R_{\rm CaNIR}$ as the ratios of pEWs of the HVFs to the PVFs of CaHK and CaNIR, respectively. Note that spectra with only PVFs have a ratio of identically zero, while spectra with only HVFs have an undefined ratio. The values of $R_{\rm CaHK}$ and $R_{\rm CaNIR}$ are listed in Tables A.2 and A.4, respectively.

The ratios found herein span a range of 0–20, though most are less than 4. This is much larger than what was measured by Childress et al. (2014), who do not find ratios larger than $\sim$2. The difference is likely caused by the smaller epoch range studied in Childress et al. (2014); they only use spectra within 5 d of maximum. When

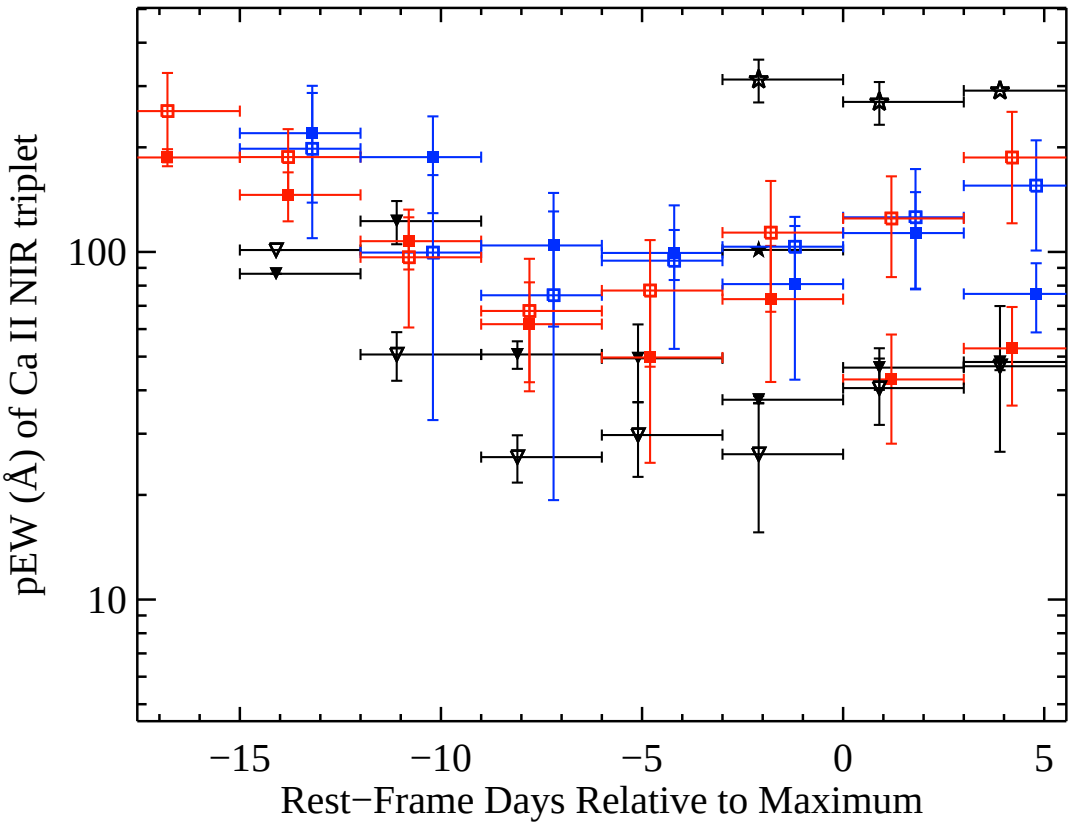

Figure 2.6: The median CaNIR pEW in time bins of 3 d for objects that are classified as Ia-91bg, Ia-91T/99aa, HV, or N (shifted slightly from bin centre for clarity). The horizontal error bars represent the width of each bin while the vertical error bars are the median absolute deviation in each bin. Colours and shapes of data points are the same as in Figure 2.4. There is large scatter in the pEWs of HVFs and PVFs at all epochs, though the pEWs of HVFs (PVFs) tend to decrease (increase) with time.

considering only spectra from these epochs in the current work, we find that most of the ratios are less than 2.5, with only 4 spectra falling above this value. Thus, our $R_{\rm CaNIR}$ values are consistent with those in Childress et al. (2014). While one might expect $R_{\rm CaHK}$ to be correlated with $R_{\rm CaNIR}$, we find that this is not true. One explanation is that the CaHK and CaNIR absorption strengths depend on temperature in different ways and the material that is responsible for the HVFs is likely at a different temperature than the photospheric material (e.g., Childress et al., 2014). In addition, the values of $R_{\rm CaHK}$ might be skewed slightly by the presence of weak Si II λ3858 absorption, though we find that this is likely a relatively small contamination (see Section 2.5.5 for more).

2.5.3 Ca II Velocities

The expansion velocities of HVFs and PVFs for the CaHK and CaNIR features are listed in Tables A.2 and A.4, respectively. Figure 2.7 shows the temporal evolution of the CaHK (top) and CaNIR (bottom) velocities. Colours and shapes of data points are the same as in Figure 2.4; measurement uncertainties are comparable to the size of the data points. The black dashed line represents the best-fitting natural exponential function to all of the PVF velocities, while the blue and red dashed lines use only HV and N objects, respectively. Similarly, the black dotted line is the best-fitting natural exponential function to all of the HVF velocities, and the blue and red dotted lines use only HV and N objects, respectively.

For any given object, all of the measured velocities tend to decrease with time, as expected and as seen in previous work (e.g., Silverman et al., 2012b). Furthermore, in a given spectrum, the difference in velocity between the CaHK and CaNIR features (for both PVFs and HVFs) is typically $\sim$500 km s^{-1}. The exponential fits in Figure 2.7 show that in general, for both Ca II features, the HVFs (dotted lines) and PVFs (dashed lines) of HV objects start out with higher velocities than the N objects, and their velocities decrease more quickly with time. Consequently, the HV and N objects have similar HVF and PVF velocities near maximum brightness. This may not be surprising (i.e., that HV objects have higher velocities), but we note that the Wang Type classification is based on the near-maximum-brightness velocity of Si II 6355 Å, and not the Ca II features.

Furthermore, we find that Ia-norm and Ia-91bg objects have consistent PVF ve-

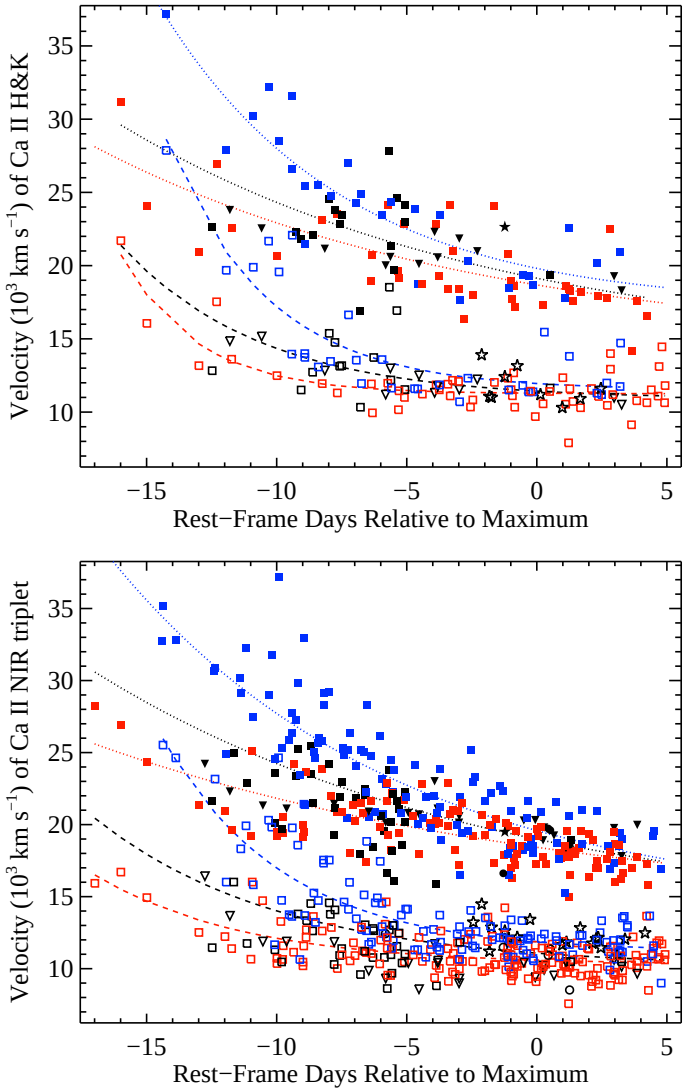

Figure 2.7: The CaHK (*top*) and CaNIR (*bottom*) velocities versus time. Colours and shapes of data points are the same as in Figure 2.4. Measurement uncertainties are comparable to the size of the data points. The black, blue, and red dashed lines are natural exponential function fits to PVF velocities of all objects, HV objects only, and N objects only, respectively. The black, blue, and red dotted lines are natural exponential function fits to HVF velocities of all objects, HV objects only, and N objects only, respectively. Note the gap between the HVF and PVF points, especially for $t \gtrsim -5$ d; this minimum difference between HVF and PVF velocities appears to be real and not merely a measurement artifact.

locities (recall that only a single Ia-91bg object shows a HVF), while Ia-91T/99aa objects have significantly lower HVF and PVF velocities. The Ia-91T/99aa objects also show a much slower decrease in their velocities with time, so once again the velocities become consistent with the rest of the sample by maximum brightness. As for the Benetti Types, HVG objects tend to start with higher velocities and decrease their velocities more quickly, as compared to LVG objects, consistent with the behaviour of the Wang HV and N objects above.

These results are somewhat different than what was seen in the early-time Ca II velocities reported in BSNIP II (Silverman et al., 2012b), but the studies are consistent for data closer to maximum brightness. This is likely due to strong HVFs of Ca II in early-time spectra being blended with PVFs and biasing the measurements in BSNIP II. The velocities presented herein more accurately reflect the actual spectral profiles and expansion velocities present in the data since we carefully take into account the (possible) presence of HVFs in each observation.

In order to show how the velocities of a few individual objects evolve with time, in Figure 2.8 we plot a subset of the data displayed in the bottom panel of Figure 2.7. Figure 2.8 shows only CaNIR velocities of objects for which we have more than seven spectra.[3] All of the PVF (HVF) velocities of a given object are connected with a dashed (solid) line. This sample of eight objects includes the five extremely well-observed SNe Ia mentioned above (SNe 2009ig, 2011by, 2011fe, 2012cg—the lone Ia-91T/99aa object in the figure, and 2012fr), in addition to SNe 2006X, 2010kg, and 2011ao. The above conclusions for the entire sample appear to also hold for this subset. Namely, HV objects tend to have faster HVFs and PVFs and their velocities decrease more quickly with time than N objects.

In both panels of Figure 2.7 and in Figure 2.8, there is a noticeable gap between the HVF and PVF points, especially for $t \gtrsim -5$ d. We further investigate this gap by calculating the difference in velocity between the HVFs and PVFs in a given spectrum for all observations where both components are observed. The temporal evolution of this separation for CaHK (CaNIR) is shown in top (bottom) panel of Figure 2.9.

Both Ca II features, in all subtypes, show a large range of values for the velocity separation at all epochs, but the difference tends to decrease with time. In fact, a linear fit to the data indicates a decrease at the 4σ level (7σ level) for CaHK (CaNIR)

[3]SN 2009ig is the only object in our dataset with more than seven spectra where we are able to fit CaHK. Thus, we did not make a plot corresponding to Figure 2.8 for CaHK.

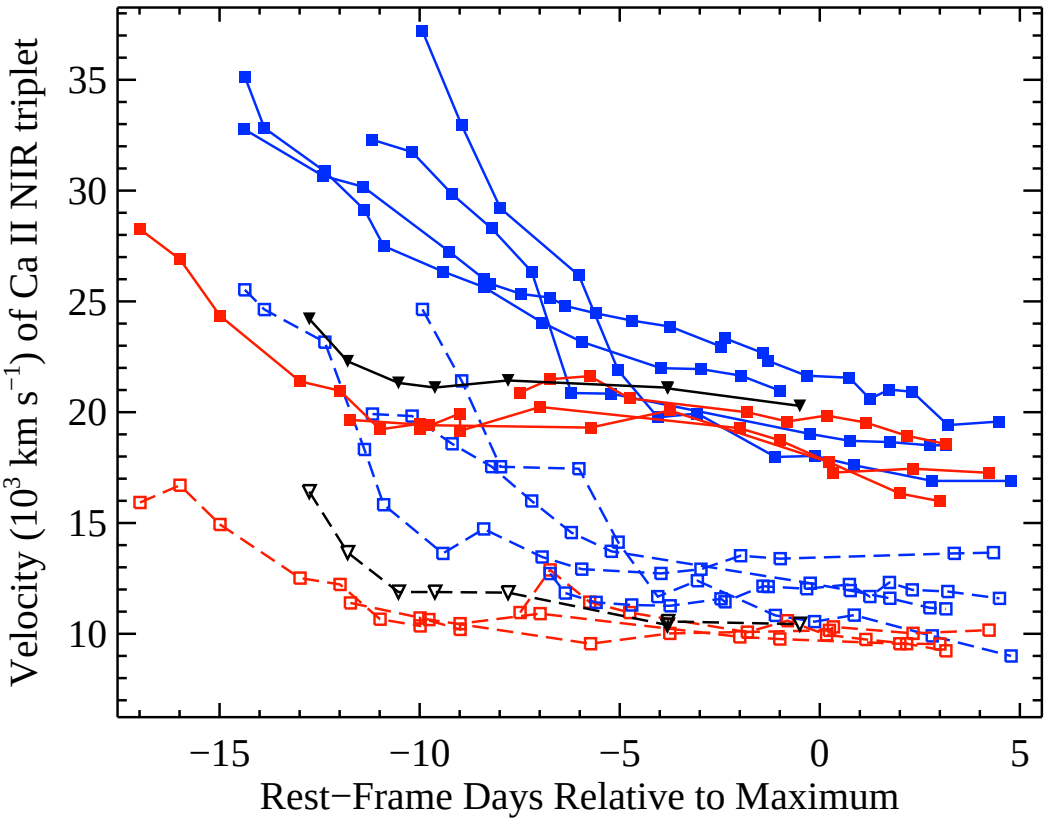

Figure 2.8: The CaNIR velocities versus time for the eight SNe Ia for which we have more than seven spectra (see main text for the list of objects). All PVF (HVF) velocities of a given object are connected with a dashed (solid) line. Colours and shapes of data points are the same as in Figure 2.4. Measurement uncertainties are comparable to the size of the data points.

from ∼11, 000 km s^{-1} to ∼8000 km s^{-1}. The typical velocity separation for both Ca II features is ∼9000 km s^{-1}, slightly higher than the 7000 km s^{-1} value found by Maguire et al. (2014), and all of the SN Ia subtypes studied herein have consistent typical velocity differences. No velocity differences are detected in the present study less than 5000 km s^{-1}, consistent with Marion et al. (2013). In fact, the vast majority of the velocity differences are greater than 6000 km s^{-1}, significantly larger than the minimum separation that our fitting algorithm is able to "resolve" (see Section 2.4.3.1). Thus, the gaps between the HVFs and PVFs in Figures 2.7 and 2.8 appear to be real.

While Figure 2.9 plots the velocity difference between HVFs and PVFs in a given spectrum, we also investigated the velocity separations for a given object at all epochs.

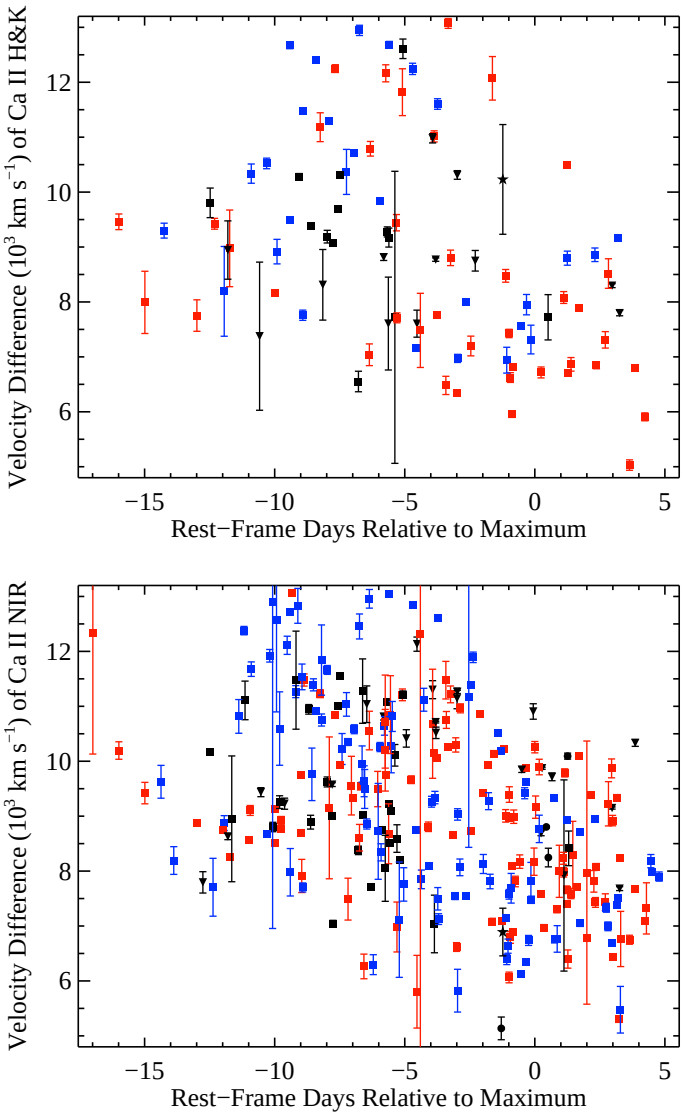

Figure 2.9: The temporal evolution of the difference in velocity between HVFs and PVFs of CaHK (*top*) and CaNIR (*bottom*). Colours and shapes of data points are the same as in Figure 2.4. Note that three of these objects have early-time PVFs with higher velocities than their later-time HVFs.

To do this, each object's maximum PVF velocity, usually from the earliest spectrum of the object in question, was compared to its minimum HVF velocity (usually from the latest spectrum of the object in question). The vast majority of objects, ∼96 per cent, have all of their HVF velocities larger than all of their PVF velocities (i.e., the minimum HVF velocity is larger than the maximum PVF velocity).

In contrast, there are five objects with a measured PVF velocity that is larger than the lowest HVF velocity. Four of these objects (SNe 2002bo, 2006X, 2009ig, and 2010kg) show some of the fastest photospheric velocities ever observed in SNe Ia (e.g., Benetti et al. 2004; Wang et al. 2008; Marion et al. 2013; Silverman et al., in preparation, respectively) and are thus all classified as HV objects. There are many other HV objects in the current sample, however, that do not show a PVF velocity larger than their lowest HVF velocity. Perhaps this is caused by the fact that we do not have sufficiently early spectra for these other HV objects to show such a fast PVF. The fifth object in this category is SN 2011fe, which was spectroscopically observed at extremely early epochs (e.g., Parrent et al., 2012). It is interesting to note that all five of these objects also show evidence for a HVF of Si II 6355 Å in their earliest epochs. Although, once again, a handful of other objects show HVFs of Si II 6355 Å but do not have any PVF velocities that are larger than their lowest HVF velocity (see Section 2.5.6).

2.5.4 HVFs of Ca II Compared to Other Observables

In order to connect our analysis of HVFs to possible SN Ia progenitors and environments, we compare the absolute strengths (pEWs), relative strengths ($R_{\rm CaHK}$ and $R_{\rm CaNIR}$), and velocities measured herein to other observables. Using the photometric information discussed at the end of Section 2.3, we find no correlation between $(B-V)_0$ and the pEWs of the HVFs or the PVFs of CaHK and CaNIR at any epoch. The latter was also seen by Childress et al. (2014) for their low-reddening ($-0.15 < (B-V)_0 < 0.15$ mag), near maximum-brightness (within 5 d of maximum) sample. There is also no significant correlation between $(B-V)_0$ and $R_{\rm CaHK}$ or $R_{\rm CaNIR}$ at any epoch, again consistent with Childress et al. (2014).

The so-called "Phillips relation" correlates the light-curve decline rate of SNe Ia with their luminosity at peak brightness (Phillips, 1993). Faster-declining SNe Ia tend to be underluminous and are also often spectroscopically Ia-91bg objects. In contrast,

slow-declining objects are usually overluminous and are of the Ia-91T/99aa subtype. Figure 2.10 compares $R_{\rm CaHK}$ (top) and $R_{\rm CaNIR}$ (bottom) to the light-curve decline rate, characterised by the $\Delta m_{15}(B)$ parameter. For objects with multiple spectra, the median R value for a given object is plotted in the figure.[4] The dashed vertical line at $\Delta m_{15}(B) = 1.6$ mag represents a typical cutoff between normal-declining and fast-declining objects (e.g., Ganeshalingam et al., 2010). The dotted vertical line at $\Delta m_{15}(B) = 1.4$ mag is a more conservative fast-declining cutoff. The horizontal dashed line at $R = 1$ represents where the pEWs of the HVFs and the PVFs are equal.

Both $R_{\rm CaHK}$ and $R_{\rm CaNIR}$ possibly show an overall decrease with $\Delta m_{15}(B)$, though the range of observed R values definitely decreases at higher values of $\Delta m_{15}(B)$. The overluminous and normal luminosity objects ($\Delta m_{15}(B) < 1.6$ mag) exhibit a wide range of R values, from identically 0 (i.e., no HVFs) to $\sim$7. On the other hand, the underluminous SNe Ia ($\Delta m_{15}(B) > 1.6$ mag) almost all have R values that are 0, and the very few that are nonzero are all less than 1. A Kolmogorov-Smirnov (KS) test indicates that $R_{\rm CaHK}$ and $R_{\rm CaNIR}$ values for normal and slow-declining objects are statistically different than those of the fast-declining objects ($p = 0.007$ and $p = 10^{-5}$ for CaHK and CaNIR, respectively).

These results still hold true even if the "fast-declining cutoff" is more conservative ($\Delta m_{15}(B) = 1.4$ mag), with KS tests indicating significant differences in $R_{\rm CaHK}$ and $R_{\rm CaNIR}$ values above and below this cutoff ($p = 10^{-5}$ and $p = 5 \times 10^{-8}$, respectively). This is consistent with what was seen in Section 2.5.1 when SNID Type was used instead of light-curve decline rate (i.e., Ia-91bg objects often show fast-declining light curves). Furthermore, the results presented here match those of Maguire et al. (2012a), Childress et al. (2014), and Maguire et al. (2014).

Figure 2.11 displays the PVF velocity of Si II 6355 Å versus $R_{\rm CaNIR}$ for spectra obtained earlier than 5 d before maximum brightness (top) and later than 5 d before maximum (bottom); a similar plot using $R_{\rm CaHK}$ is not shown but is qualitatively similar, though with fewer data points. Once again, the median values of both $R_{\rm CaNIR}$ and Si II 6355 Å velocity for a given object are used for SNe Ia with multiple spectra in each epoch range. The dashed vertical line at 11, 800 km s^{-1} in each panel represents the cutoff between N and HV objects while the horizontal dashed line at

[4]Here, and elsewhere, when using the median R value, we note that the results are unchanged when we instead use the mean R value or the R value from the earliest, latest, or closest-to-maximum brightness spectrum in our sample.

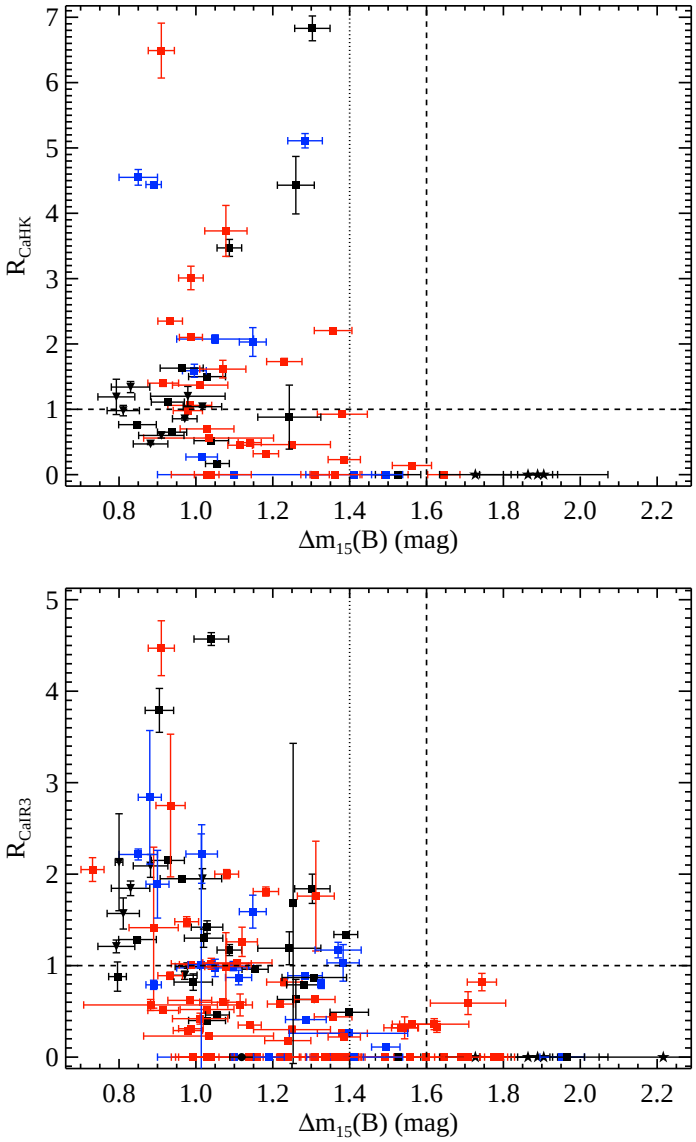

Figure 2.10: $R_{\rm CaHK}$ (*top*) and $R_{\rm CaNIR}$ (*bottom*) versus light-curve decline rate ($\Delta m_{15}(B)$). The median R value of a given object is used for objects with multiple spectra. The dashed vertical line is a typical cutoff between normal- and fast-declining objects; the dotted vertical line is a more conservative cutoff. The horizontal dashed line is where the pEWs of the HVFs and PVFs are equal. Colours and shapes of data points are the same as in Figure 2.4.

$R = 1$ represents where the pEWs of the HVFs and the PVFs are equal.

Aside from the Ia-91bg objects (i.e., the stars in Figure 2.11), which we have shown almost never contain HVFs, there is a large range of $R_{\rm CaNIR}$ values at all Si II 6355 Å velocities in both age ranges. Thus, we find no correlation between these two parameters and no significant difference in $R_{\rm CaNIR}$ (or $R_{\rm CaHK}$) values for N versus HV objects. This is inconsistent with Childress et al. (2014) and Maguire et al. (2014), both of which find that HV objects do not show HVFs. On the contrary, we find many HV objects with relatively strong HVFs at all epochs, represented by blue points in the upper-right quadrants of the panels in Figure 2.11. Compare this to the bottom panel of Figure 5 in Childress et al. (2014) and the left panel of Figure 6 in Maguire et al. (2014), both of which lack objects in the upper-right quadrant.

Our results are unchanged even if we restrict our sample only to spectra within 5 d of maximum brightness (top panel of Figure 2.11), in order to match the epochs studied in the two aforementioned works. Thus, this discrepancy is likely caused by the fact that Childress et al. (2014) and Maguire et al. (2014) have too few HV objects in their datasets. As mentioned in Section 2.5.1, ∼28 per cent of the objects studied herein are HV objects, which matches the overall SN Ia population (e.g., Wang et al., 2009b; Silverman et al., 2012b). On the other hand, only ∼13 per cent of the objects studied by Childress et al. (2014) and Maguire et al. (2014) were HV. This difference in sample demographics likely led to the inconsistency discussed above.

Many other SN Ia observables were compared to $R_{\rm CaHK}$ and $R_{\rm CaNIR}$, but almost none showed any significant correlation. For completeness, we list here the parameters investigated. Some normal SNe Ia are found to exhibit C II absorption features in their early-time spectra (e.g., Parrent et al., 2011; Thomas et al., 2011b; Folatelli et al., 2012; Silverman & Filippenko, 2012). This C is likely unburned fuel from the progenitor WD. No difference in $R_{\rm CaHK}$ ($R_{\rm CaNIR}$) is found for objects with or without C II absorption features when investigating 107 (252) spectra, consistent with what was found by Maguire et al. (2014).

Narrow Na I D absorption features have been found to be preferentially blueshifted (relative to the host galaxy's rest frame) in SNe Ia (e.g., Sternberg et al., 2011; Foley et al., 2012b; Maguire et al., 2013). When using 40 spectra that have the shift of these features measured, we find no difference in R values of objects with blueshifted versus redshifted Na I D lines. The rise time of a SN Ia light curve is usually calculated by extrapolating early-time photometry backward in time to a flux of zero. Using rise

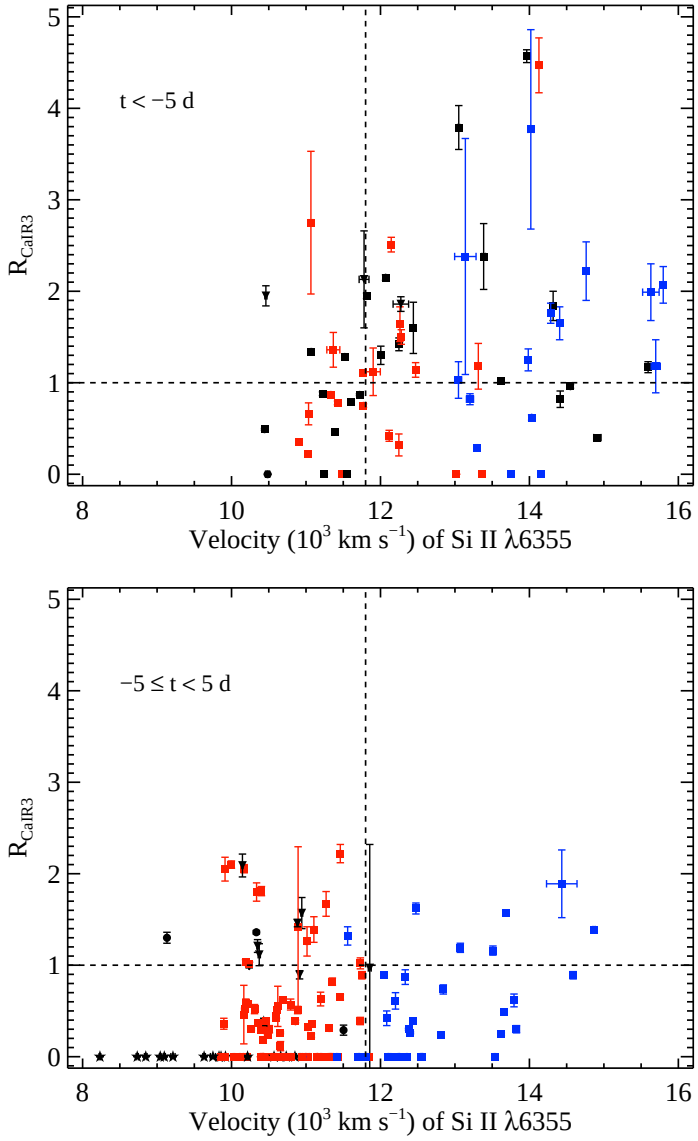

Figure 2.11: $R_{\rm CaNIR}$ versus Si II 6355 Å (PVF) velocity for spectra obtained earlier than 5 d before maximum brightness (*top*) and later than 5 d before maximum (*bottom*). The median R value and velocity of a given SN Ia are used for objects with multiple spectra in each epoch range. The dashed vertical line in each panel are the cutoffs between N and HV objects. The horizontal dashed line in each panel are where the pEWs of the HVFs and PVFs are equal. Colours and shapes of data points are the same as in Figure 2.4.

times of 74 objects published by Ganeshalingam et al. (2011), we find no correlation with $R_{\rm CaHK}$ or $R_{\rm CaNIR}$.

Concentrating now on late-time spectra of SNe Ia, we compare the R values calculated herein to nebular velocities — that is, the average of the [Fe II] λ7155 and [Ni II] λ7378 velocities (Maeda et al., 2010). The nebular velocity has been found to correlate with the velocity gradient near maximum brightness, as well as the near-maximum ejecta velocity (i.e., PVF velocity) (e.g., Maeda et al., 2010; Silverman et al., 2013a), neither of which were seen to correlate with the strengths of HVFs in the current work. Thus, it is unsurprising that the nebular velocity is unrelated to $R_{\rm CaHK}$ and $R_{\rm CaNIR}$ for 22 and 47 spectra, respectively.

On the other hand, the full-width at half-maximum intensity (FWHM) of the [Fe III] λ4701 feature, which is detected in many SN Ia nebular spectra, is somewhat correlated with $R_{\rm CaHK}$ and $R_{\rm CaNIR}$ (Pearson r value of $\sim$0.6). This is consistent with previous work which found the FWHM of this feature to be anticorrelated with $\Delta m_{15}(B)$ (e.g., Silverman et al., 2013a), and we have shown above that $R_{\rm CaHK}$ and $R_{\rm CaNIR}$ are also anticorrelated with $\Delta m_{15}(B)$.

For 242 spectra, we compared $R_{\rm CaHK}$ and $R_{\rm CaNIR}$ to host-galaxy type, as listed in NED. SNe Ia in E/S0 hosts are found to have significantly lower R values than those found in Sa/Sb/Sc/Sd/Irr hosts. We note that this result was also seen by Pan et al. (2015). There is a well-established connection between early-type hosts and underluminous SNe Ia, and late-type hosts and normal/overluminous SNe Ia (e.g., Hamuy et al., 1995; Sullivan et al., 2006; Pan et al., 2014), so this finding is completely consistent with the aforementioned result that underluminous, Ia-91bg objects show relatively weak (or nonexistent) HVFs.

We searched for correlations between the SN Ia observables mentioned above and the velocities of the Ca II HVFs and PVFs, but found no significant results. Our analysis indicates that Ca II velocities (both the HVFs and PVFs) are uncorrelated with $(B-V)_0$, $\Delta m_{15}(B)$, the presence or absence of C II absorption, the relative Doppler shift of narrow Na I D absorption, light-curve rise time, nebular velocity, FWHM of [Fe III] λ4701, and host-galaxy type.

2.5.5 Si II λ3858

The Si II λ3858 absorption feature has been discussed in multiple sections above, but here we summarise our results regarding it. Foley (2013) claim that Si II λ3858 usually dominates the CaHK profile, but the findings of both Childress et al. (2014) and Maguire et al. (2014) are inconsistent with this conclusion. We agree with the latter two works, as outlined below. As discussed in Section 2.4.1, the only extra assumption we made in order to determine whether Si II λ3858 was present in a given spectrum was as follows: if a spectrum showed a HVF of CaNIR, then it should also have a HVF of CaHK, and vice versa. This broke the degeneracy between Si II λ3858 (PVF) absorption and CaHK HVF absorption.

We tested this assumption by supposing Si II λ3858 was never present. This led to velocity differences between HVFs of CaHK and CaNIR of $\sim$5000 km s^{-1} (instead of the more typical value of $\sim$500 km s^{-1}) and velocity differences between CaHK HVFs and PVFs of $\sim$5500 km s^{-1} (as opposed to the median value of $\sim$9000 km s^{-1}). The assumption was further investigated by assuming that Si II λ3858 was *always* present (instead of HVFs of CaHK). This again yielded inconsistent results, namely the Si II λ3858 velocities were $\sim$2600 km s^{-1} faster than the Si II 6355 Å velocities in a given spectrum (compared to the more typical value of $\sim$600 km s^{-1}, e.g., Silverman et al., 2012b). Note that this was previously shown graphically in Figure 2.2. Thus, our assumption seems to be valid.

Si II λ3858 is detected in the CaHK profile in $\sim$24 per cent (30/126) of the spectra fit, and half of these also show evidence for a HVF of CaHK. These spectra represent $\sim$27 per cent (23/84) of the SNe Ia in the current dataset. When Si II λ3858 is detected, its pEW is $\sim$70 Å smaller than that of Si II 6355 Å in the same spectrum, which represents a factor of $\sim$6 (see Section 2.5.7). This difference in strength is larger than expected given typical SN Ia photospheric temperatures and the gf-weights of the two Si II lines.[5] While weak absorption from Si II λ3858 may actually be present in a higher percentage of the data, our fitting algorithm is unable to detect such a feature. Furthermore, no evidence of a HVF of Si II λ3858 is detected in any of the observations.

Figure 2.12 shows the temporal evolution of the velocity of the Si II λ3858 absorption feature (using the same epoch range as previous temporal evolution figures

[5] `http://www.nist.gov/pml/data/asd.cfm`.

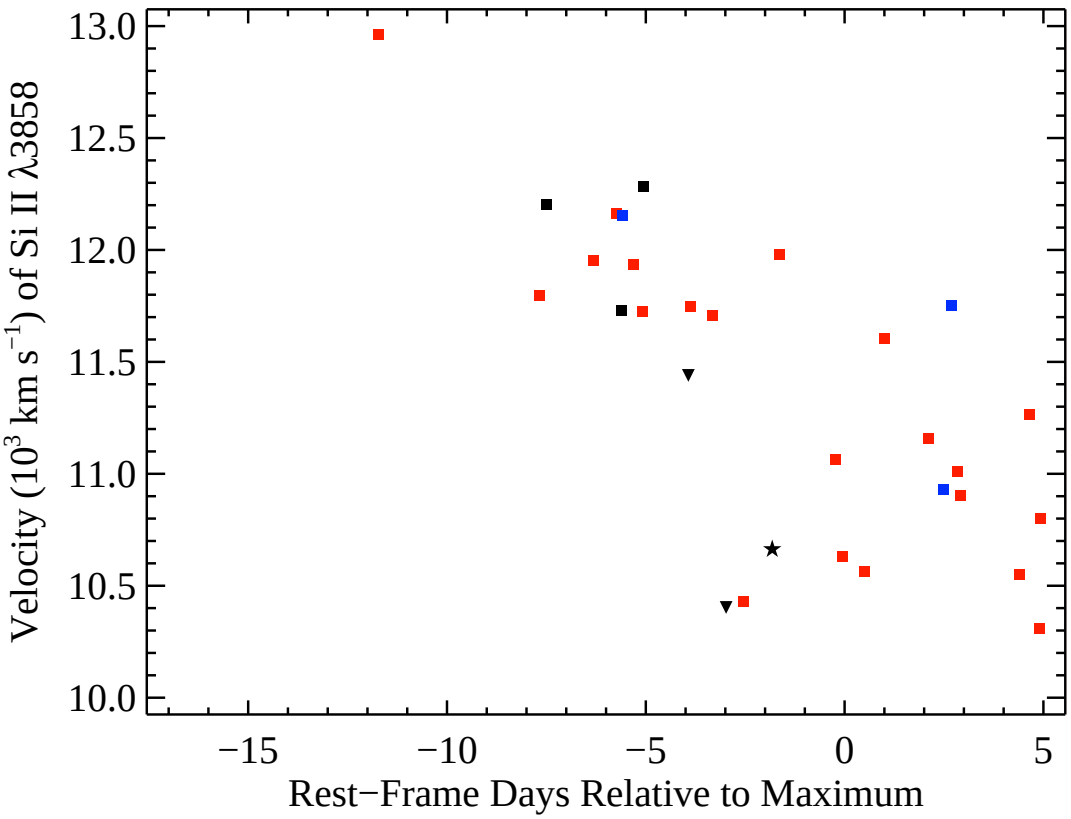

Figure 2.12: The Si II λ3858 velocity versus time. Colours and shapes of data points are the same as in Figure 2.4. Measurement uncertainties are comparable to the size of the data points.

in this work, and adopting the same data-point colours and shapes as in Figure 2.4). The Si II λ3858 feature is detected mostly at epochs later than 8 d before maximum brightness (there is one detection at $t \approx -12$ d) and, as expected, the velocities tend to decrease with time. The detection of Si II λ3858, as well as the strength (i.e., pEW) and velocity of the feature when detected, are uncorrelated with any of the aforementioned SN Ia classification schemes (i.e., SNID Type, Wang Type, and Benetti Type), as well as any of the other SN Ia observables mentioned in Section 2.5.4 (except, of course, the Si II 6355 Å PVF velocity). Another possible exception is that Si II λ3858 might be detected more frequently in N objects, as opposed to other subtypes, though the relatively small total number of detections makes this result rather weak.

2.5.6 The Existence of HVFs in Si II 6355 Å

Using the algorithm described in Section 2.4, the pEWs and expansion velocities were calculated for both HVFs and PVFs of Si II 6355 Å; the values are listed in Table A.3. HVFs of Si II 6355 Å have rarely been carefully studied previously, with Marion et al. (2013) representing one of the most detailed works on the subject. In the present study, Si II 6355 Å was fit in a total of 422 spectra of 208 SNe Ia; 2 of these spectra have only HVFs, 326 have only PVFs, and 94 have both HVFs and PVFs detected. SN 2012fr is the only object in our sample with spectra showing only HVFs of Si II 6355 Å, and this is found for only the two earliest spectra (14.4 and 14.0 d before maximum brightness). As mentioned in Section 2.5.1, this is consistent with an in-depth study of this object which found HVFs of CaNIR and Si II 6355 Å but no PVFs in these spectra (Childress et al., 2013b).

Like the Ca II features, SNe Ia tend to evolve from having only Si II 6355 Å HVFs, though this is seen only in one object and at very early times, to having both HVFs and PVFs, to having only PVFs, which is what is seen in the majority of the spectra, ∼77 per cent. Spectra with only Si II 6355 Å PVFs are detected as early as 15 d before maximum and as late as 5 d past maximum (i.e., the oldest spectra in the current study), while spectra with both HVFs and PVFs are observed at all epochs studied ($-16 < t < 5$ d).

Unlike the Ca II features, however, HVFs of Si II 6355 Å are somewhat rare in SN Ia spectra. Only ∼16 per cent of all SNe Ia studied herein show evidence for Si II 6355 Å HVFs in at least one spectrum (compared to ∼67 per cent for HVFs of CaHK and CaNIR). In early-time observations ($t \lesssim -5$ d), ∼32 per cent of objects have detectable HVFs of Si II 6355 Å, much lower than the ∼91 per cent of objects that exhibit HVFs of Ca II at these early epochs.

All spectra obtained earlier than 11 d before maximum brightness contain HVFs of Si II 6355 Å, while they are seen in 21 spectra of 7 SNe Ia for $t > -5$ d. This latter result is inconsistent with Childress et al. (2014), who find no HVFs of Si II 6355 Å at these epochs. The difference is likely caused by the larger dataset used herein, as well as by differences in the spectral fitting algorithms used. The low detection rate of HVFs of Si II 6355 Å could be explained by an inherent rarity of HVFs of Si II 6355 Å, the possibility that they disappear at very early times, or some combination of both.

As when fitting the Ca II features, we find that ∼29 per cent of the objects for which we fit the Si II 6355 Å feature are HV objects, again consistent with the overall SN Ia population (e.g., Wang et al., 2009b; Silverman et al., 2012b). Furthermore, only 8 objects had their Wang Type changed when using the PVF velocity calculated in this work as compared to previous work (e.g., Silverman et al., 2012b), and all of these SNe Ia had velocities that were near the cutoff between HV and N objects. For the SNe Ia with a Wang Type, 33 per cent of HV objects contain HVFs of Si II 6355 Å, while only 6 per cent of N objects show HVFs of Si II 6355 Å. This dramatic difference has never been convincingly seen before, although it was previously suggested by Tanaka et al. (2008), and is significantly different than the HVFs of Ca II which are found in similar percentages of HV and N objects. This result may be surprising since one might expect PVFs with higher velocities to be blended more severely with any possible HVF, and thus one might be biased *against* finding distinct HVFs of Si II 6355 Å in HV objects.

Much like Ca II, however, HVFs of Si II 6355 Å are found in similar numbers of Ia-norm and Ia-91T/99aa objects (14 per cent and 19 per cent, respectively) while no HVFs are seen in Ia-91bg objects. As mentioned previously, the BSNIP dataset (which represents the bulk of the sample studied herein) is not well suited to velocity-gradient measurements or Benetti Type classifications. That being said, we report our results here for completeness, though note the relatively low numbers of objects involved. We find no HVFs of Si II 6355 Å in FAINT objects, consistent with Ia-91bg objects having no HVFs. On the other hand, 29 per cent of LVG objects and 27 per cent of HVG objects show evidence for HVFs of Si II 6355 Å. This is somewhat different than the aforementioned predominance of Si II 6355 Å HVFs in HV objects and the relative lack of them in N objects. However, given the relatively small number of SNe Ia for which we can measure a reliable Benetti Type, these percentages are formally consistent with the results found when using Wang Types.

2.5.7 Si II 6355 Å pEWs

The pEWs of Si II 6355 Å are listed in Table A.3 and their temporal evolution is displayed in Figure 2.13. Like the Ca II features, there is significant scatter in the pEWs of the HVFs and PVFs of Si II 6355 Å. In addition, the HVF pEWs tend to decrease with time while the PVF pEWs typically increase with time. As discussed

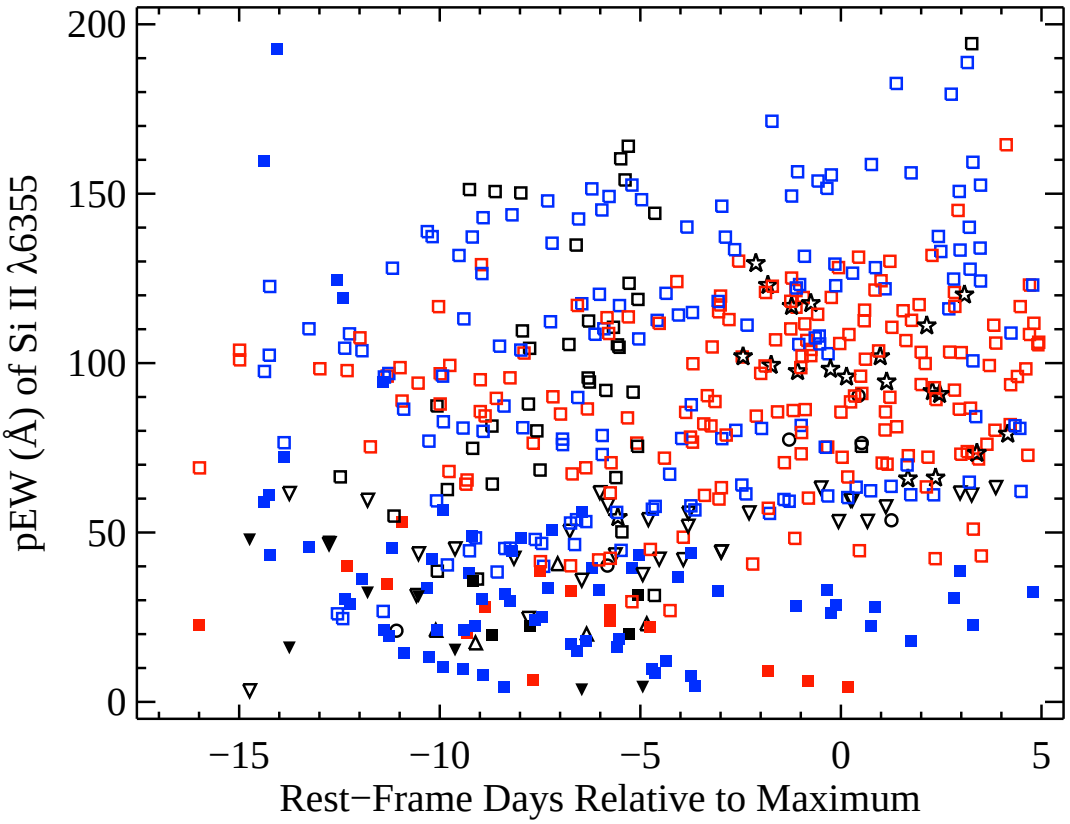

Figure 2.13: The Si II 6355 Å pEWs versus time. Colours and shapes of data points are the same as in Figure 2.4. Measurement uncertainties are comparable to the size of the data points.

above, HVFs of Si II 6355 Å disappear at much earlier epochs than either Ca II feature. The strengths (i.e., pEWs) of HVFs and PVFs are seen to be equal for CaHK and CaNIR for $-8 < t < 2$ d, while this is achieved for Si II 6355 Å $\sim$11 d before maximum brightness. In fact, there are only 5 spectra in which the pEW of the Si II 6355 Å HVF is larger than that of the Si II 6355 Å PVF, and all of these were obtained at $t < -11$ d. In spite of this, moderately strong HVFs of Si II 6355 Å are observed in a handful of objects through $t \approx -6$ d and in some objects through $t \approx 5$ d, and these are almost exclusively HV objects.

As mentioned in Section 2.5.6, HV objects tend to show HVFs of Si II 6355 Å significantly more often than N objects, and, according to Figure 2.13, on average they exhibit stronger HVFs than N objects when detected in both subtypes at the

same epoch. Similar to the Ca II pEWs, though not quite as extreme, Ia-91bg objects have relatively large pEWs of Si II 6355 Å PVFs but no HVFs, and Ia-91T/99aa objects have relatively low pEWs of both Si II 6355 Å PVFs and HVFs.

Analogous to the Ca II features, we define $R_{\rm Si}$ as the ratio of pEWs of the HVFs to the PVFs of Si II 6355 Å.[6] Once again, spectra with only PVFs are defined to have a ratio of zero, while spectra with only HVFs have an undefined ratio; the values of $R_{\rm Si}$ are listed in Table A.3. For nearly all spectra studied herein, $R_{\rm Si} < 1$. There are five spectra whose ratio is larger than unity, and they represent the earliest spectral observations of SNe 2012cg and 2012fr (Silverman et al., 2012c; Childress et al., 2013b, respectively). Note that SN 2012fr was also the sole object in this work found to have spectra showing HVFs of Si II 6355 Å *without* PVFs.

2.5.8 Si II 6355 Å Velocities

The measured PVF and HVF velocities of the Si II 6355 Å feature are listed in Table A.3, and Figure 2.14 shows the temporal evolution of these velocities. As in Figure 2.7, the black dashed line is the best-fitting natural exponential function to all Si II 6355 Å PVF velocities, while the blue and red dashed lines use only HV and N objects, respectively. The black dotted line is the best-fitting natural exponential function to all Si II 6355 Å HVF velocities, and the blue and red dotted lines use only HV and N objects, respectively.

Like the Ca II features, the measured velocities (both PVFs and HVFs) of a given object tend to decrease with time. The exponential fits in Figure 2.14 show that, again as seen in the Ca II features, the HVFs (dotted lines) and PVFs (dashed lines) of HV objects start out with higher velocities than the N objects and likely decrease their velocity more quickly with time. For Si II 6355 Å, however, the HVF and PVF velocities of the HV objects are almost always larger than those of the N objects at a given epoch. This is by construction, at least for the PVF velocities, since the PVF Si II 6355 Å velocity is how a Wang Type is assigned to a given object.

Ia-91bg objects are found to have the lowest Si II 6355 Å velocities, with Ia-91T/99aa objects having slightly larger velocities. N objects have slightly larger

[6]Note that $R_{\rm Si}$ defined here is unrelated to the so-called "Si II ratio, " $\Re$(Si II), which was defined by Nugent et al. (1995) as the ratio of the depth of the Si II λ5972 feature to the depth of the Si II 6355 Å feature.

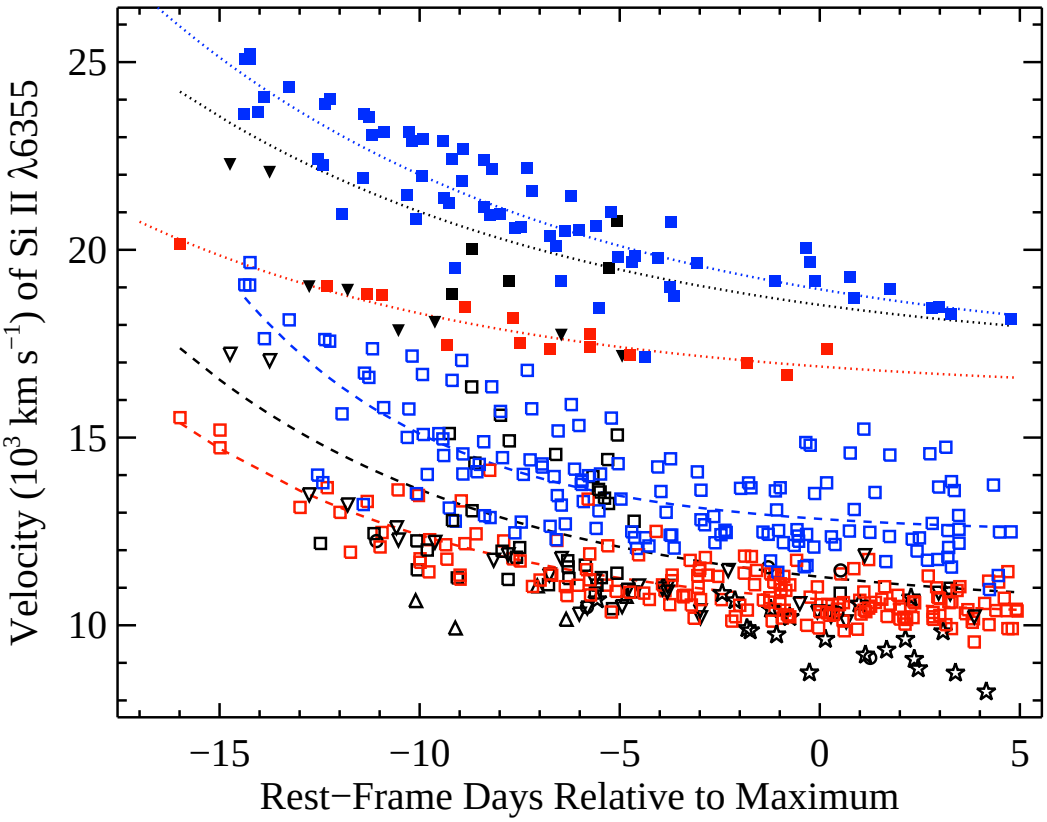

Figure 2.14: The Si II 6355 Å velocities versus time. Colours and shapes of data points are the same as in Figure 2.4. Measurement uncertainties are comparable to the size of the data points. Like Figure 2.7, the black, blue, and red dashed lines are natural exponential function fits to PVF velocities of all objects, HV objects only, and N objects only, respectively. The black, blue, and red dotted lines are natural exponential function fits to HVF velocities of all objects, HV objects only, and N objects only, respectively.

velocities than that and, of course, HV objects exhibit the highest velocities. This is consistent with previous Si II 6355 Å velocity studies (e.g., Silverman et al., 2012b).

Only Si II 6355 Å velocities of objects for which we have more than seven spectra are shown in Figure 2.15 (thus, this is a subset of what is displayed in Figure 2.14). As in Figure 2.8, the PVF (HVF) velocities of a given object are connected with a dashed (solid) line. The nine objects plotted in Figure 2.15 include the five extremely well-observed SNe Ia mentioned above (SNe 2009ig, 2011by, 2011fe, 2012cg — the lone Ia-91T/99aa object in the Figure — and 2012fr), in addition to SNe 1994D, 2006X, 2010kg, and 2011ao. The aforementioned conclusions once again hold for this subset: HV objects have faster HVFs and PVFs at all epochs, and they likely decrease more quickly with time than N objects.

As with the Ca II features, the Si II 6355 Å feature shows a distinct gap between HVF and PVF velocities. This gap is most noticeable for $t \gtrsim -6$ d. Once again, the difference in velocity between the HVFs and PVFs in a given spectrum is calculated. While this difference tends to decrease with time, there is a very large amount of scatter at all epochs, similar to the CaNIR feature. The typical velocity separation for Si II 6355 Å is $\sim$6000 km s^{-1}, slightly less than what was found for the Ca II features (i.e., $\sim$9000 km s^{-1}). No velocity differences are found less than 4200 km s^{-1}, and most are greater than 5000 km s^{-1}. These values are somewhat larger than the minimum separation resolvable by our fitting algorithm (see Section 2.4.3.1), so as was the case for CaNIR, the gap between the Si II 6355 Å HVFs and PVFs is likely real.

As was done for the Ca II features, the velocity separations for a given object at all epochs were investigated for Si II 6355 Å. Again, each object's maximum PVF velocity, usually from the earliest spectrum of the object in question, was compared to its minimum HVF velocity, usually from the latest spectrum of the object in question. All objects studied herein have all of their HVF velocities larger than all of their PVF velocities (i.e., the minimum HVF velocity is larger than the maximum PVF velocity).

2.5.9 HVFs of Si II 6355 Å Compared to Other Observables

As with the Ca II features, we compare the $R_{\rm Si}$ values of the Si II 6355 Å feature to other SN Ia observables. The SN colour is being characterised in this work using the observed $B-V$ colour at B-band maximum brightness, with only a correction for MW

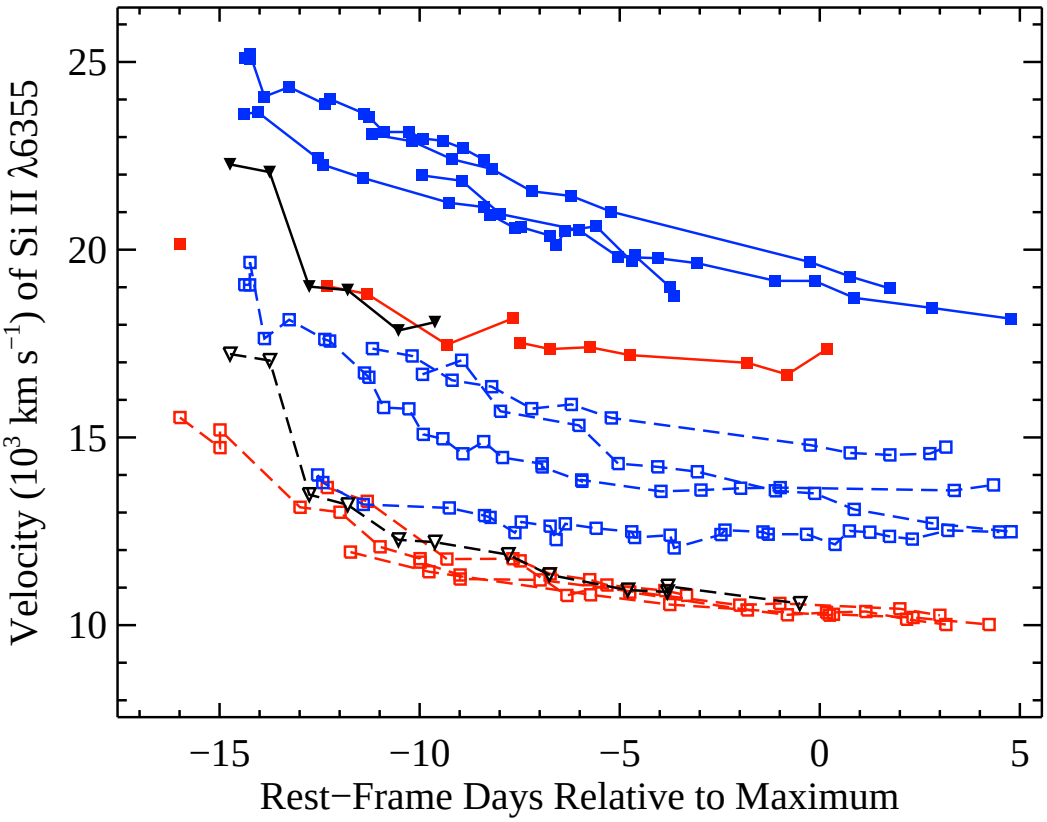

Figure 2.15: The Si II 6355 Å velocities versus time for the nine SNe Ia for which we have more than seven spectra (see main text for the list of objects). All PVF (HVF) velocities of a given object are connected with a dashed (solid) line. Colours and shapes of data points are the same as in Figure 2.4. Measurement uncertainties are comparable to the size of the data points.

reddening (Schlegel et al., 1998) having been applied. Thus, there are many objects in the sample that have large (i.e., red) values of $(B-V)_0$ caused by reddening from their host galaxy. When ignoring highly reddened objects ($(B-V)_0 > 0.4$ mag; e.g., Foley et al., 2011), the mean $R_{\rm Si}$ value is more than twice as large for objects with $(B-V)_0 > 0$ mag as compared to objects with $(B-V)_0 < 0$ mag (∼0.037 and ∼0.016 mag, respectively). Both of these values are quite close to $R_{\rm Si} = 0$, since there are relatively few objects that show HVFs of Si II 6355 Å; thus, this result is of somewhat low significance. If correct, however, it indicates that $R_{\rm Si}$ is larger for intrinsically redder SNe Ia, which are also found to show larger Si II 6355 Å velocities

(e.g., Foley et al., 2011; Milne et al., 2014).

Like the Ca II features, no HVFs of Si II 6355 Å are found in fast-declining SNe Ia, while normal- and slow-declining objects show a range of $R_{\rm Si}$ values (from identically 0 to $\sim$0.5). In fact, no object with $\Delta m_{15}(B) > 1.45$ mag show HVFs of Si II 6355 Å, and the difference in $R_{\rm Si}$ values above and below this cutoff is statistically significant. These findings are consistent with the results discussed in Section 2.5.6 where SNID Type was used instead of light-curve decline rate.

As also seen in Section 2.5.6, the majority of the Si II 6355 Å HVFs are found in HV objects. Another way to present this result is shown in Figure 2.16, which displays the (PVF) velocity of Si II 6355 Å versus $R_{\rm Si}$. The median values (of both $R_{\rm Si}$ and Si II 6355 Å velocity) are used for objects with multiple spectra. The dashed line at 11, 800 km s^{-1} represents the cutoff between N and HV objects.

The typical value of $R_{\rm Si}$ that we measure increases with Si II 6355 Å velocity, although there are only a handful of objects with $R_{\rm Si} \neq 0$. Of these SNe Ia that show HVFs of Si II 6355 Å, three are N objects, while two are Ia-91T/99aa and five are unclassified objects. On the other hand, 13 are HV objects, while HV objects make up less than 30 per cent of the current dataset. Also note that the five unclassified objects with HVFs of Si II 6355 Å are all found to have velocities greater than 11, 800 km s^{-1}, and are thus *likely* HV objects. About half of the highest-velocity objects (i.e., Si II 6355 Å velocity greater than 14, 000 km s^{-1}) show HVFs of Si II 6355 Å; compare this to the entire dataset, in which only $\sim$16 per cent of objects show HVFs of Si II 6355 Å.

As mentioned in Section 2.5.4, C II absorption features are sometimes found in early-time optical spectra of SNe Ia, likely coming from unburned progenitor WD material (e.g., Parrent et al., 2011; Thomas et al., 2011b; Folatelli et al., 2012; Silverman & Filippenko, 2012). For 288 spectra, we find a statistically significant difference in values of $R_{\rm Si}$ for objects with versus without C II absorption features. The mean $R_{\rm Si}$ value for SNe Ia with detected C II is $\sim$0.011, while the mean $R_{\rm Si}$ value for those without C II is nearly twice as large ($\sim$0.019). This implies that objects lacking C II absorption features also show stronger HVFs. Consistent with this finding, and previous results in the current work, HV objects have also been shown to lack C II absorption (e.g., Silverman & Filippenko, 2012).

Other SN Ia observables were also compared to $R_{\rm Si}$, but none of them showed any significant correlation. As was done for the Ca II feature, we list the observables

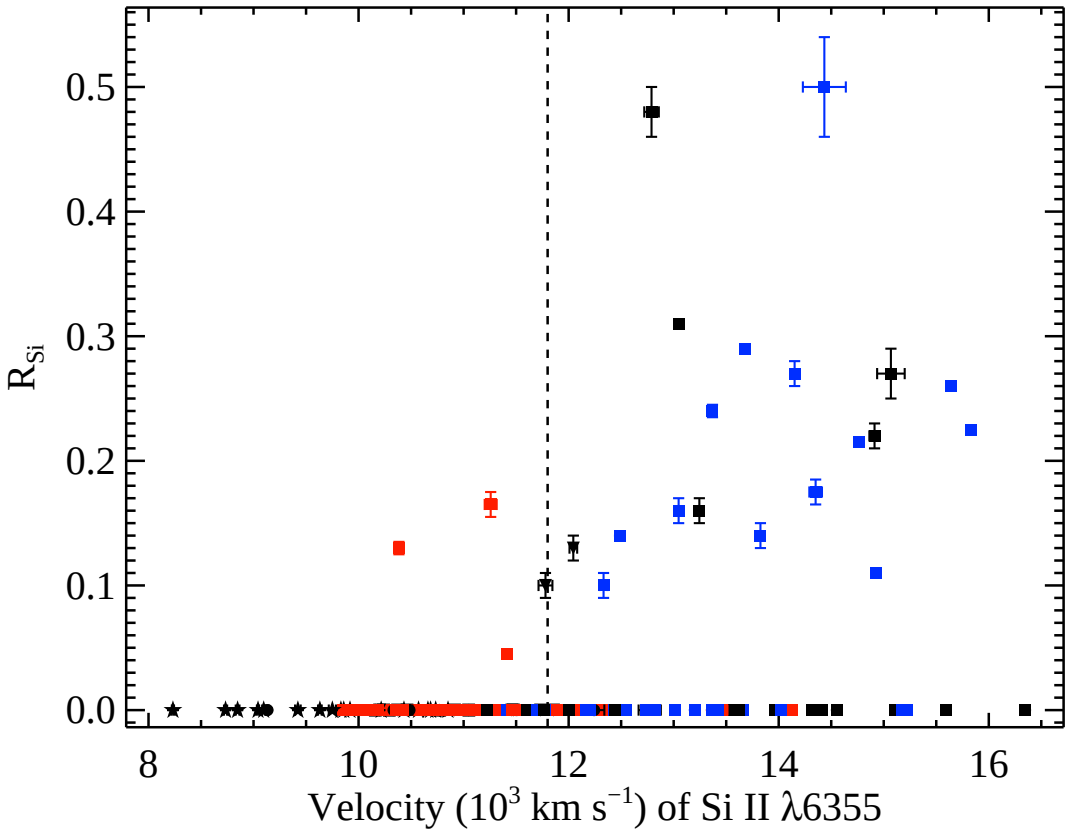

Figure 2.16: $R_{\rm Si}$ versus Si II 6355 Å (PVF) velocity. The median R value and velocity are used for objects with multiple spectra. The dashed line is the cutoff between N and HV objects. Colours and shapes of data points are the same as in Figure 2.4.

investigated for completeness. No difference in $R_{\rm Si}$ values is found for objects with blueshifted versus redshifted narrow Na I D absorption lines when using 47 spectra. Similarly, no correlation is found between $R_{\rm Si}$ and the light-curve rise times of 43 of the objects published by Ganeshalingam et al. (2011), the nebular velocity (of 17 objects), or the FWHM of the [Fe III] λ4701 feature (of 17 objects). Finally, the host-galaxy type (as reported in NED) is related to the value of $R_{\rm Si}$ for 287 spectra in the same way as $R_{\rm CaHK}$ and $R_{\rm CaNIR}$; objects in E/S0 hosts tend to have lower R values than those found in other galaxy types.

In summary, Si II 6355 Å HVFs are never found in slow-declining (i.e., Ia-91bg/FAINT) objects, as is the case with HVFs of CaHK and CaNIR. Unlike the HVFs of Ca II, however, HVFs of Si II 6355 Å are relatively rare overall, yet there are

significantly more HV objects with Si II 6355 Å HVFs as compared to any other SN Ia subtype. Furthermore, we find that objects showing strong HVFs of Si II 6355 Å also tend to have redder optical colours at maximum brightness and lack C II absorption in their early-time spectra. This connection between photospheric velocity, ultraviolet (UV)/optical colour near maximum, and C II absorption have all been recognised in previous works mentioned above, but the addition of the association between HV objects and relatively strong HVFs of Si II 6355 Å is new and unique to the current work. We also note the possibility that HV objects preferentially occur in the inner regions of their host galaxies (Wang et al., 2013; Pan et al., 2015).

As discussed above and in Wang et al. (2009b), the Wang Type classifications, and thus the correlations in the previous paragraph, only apply to "typical" SNe Ia. These objects make up ∼70 per cent of the SN Ia population (Li et al., 2011), are spectroscopically "normal" (e.g., according to SNID), and usually have $\Delta m_{15}(B) = 1.1 \pm 0.3$ mag (e.g., Ganeshalingam et al., 2010). For such objects, there seems to be an observational dichotomy, or, more likely, a continuous distribution of multiple observables that are mutually correlated. Table 2.1 presents this dichotomy, or rather, the extremes of this continuous distribution. In essence, we find that a "typical" SN Ia with a relatively large near-maximum photospheric velocity, which would lead to classification as a HV object, will likely lack early-time C II absorption, tend to have relatively red UV/optical colours near maximum brightness, will show relatively strong HVFs of Si II 6355 Å, and may be found in the inner regions of its host galaxy.

Table 2.1: Correlated Observables of "Typical"[a] SNe Ia

Observable	HV objects	N objects	Example Reference(s)
Si II 6355 Å (PVF) velocity near maximum	$> 11,800$ km s^{-1}	$< 11,800$ km s^{-1}	Wang et al. (2009b)
Early-time C II absorption features	No	Yes	Silverman & Filippenko (2012)
UV/optical colours near maximum	Red	Blue	Foley et al. (2011); Milne et al. (2014)
HVFs of Si II 6355 Å	Strong	Weak/None	**This Work**
Location within host galaxy	Inner ∼70 per cent?	Everywhere?	Wang et al. (2013); Pan et al. (2015)

[a]"Typical" SNe Ia are objects that are spectroscopically "normal" (e.g., according to SNID) and usually have $\Delta m_{15}(B) = 1.1 \pm 0.3$ mag (e.g., Ganeshalingam et al., 2010); thus, they can be assigned a Wang Type.

2.6 Conclusions

We have conducted the most detailed study of HVFs performed to date, using a sample of 445 low-resolution optical and NIR spectra at epochs up to 5 d past maximum brightness of 210 low-redshift SNe Ia that follow the "Phillips relation." By fitting a series of Gaussian functions, we are able to determine whether a given spectrum shows evidence for HVFs of CaHK, Si II 6355 Å, or CaNIR, as well as measure the velocities and pEWs of the PVFs and HVFs of these three spectral features. Our measured values are consistent with previous studies of HVFs (e.g., Marion et al., 2013; Childress et al., 2014), and our detection, or lack thereof, of HVFs also matches spectral fits produced via SYNAPPS.

In general, SNe Ia are found to have HVFs with no corresponding PVFs at the earliest epochs and these features weaken and slow down with time. PVFs appear later and grow stronger with time, while also slowing down. HVFs and PVFs of CaHK, Si II 6355 Å, and CaNIR are found (in at least some objects) at nearly all epochs studied herein. SNe Ia with faster PVFs tend to have faster HVFs.

About two-thirds of all objects in the current sample show HVFs of Ca II. For objects with spectra obtained earlier than ∼4 d before maximum brightness, ∼91 per cent show HVFs, and the remaining ∼9 per cent all seem to be underluminous / Ia-91bg / FAINT objects. This connection between the relative strength of Ca II HVFs and luminosity has also been seen in previous work (Maguire et al., 2012a; Childress et al., 2014; Maguire et al., 2014). Our analysis further indicates that Si II λ3858 is detectable in the CaHK profile of ∼24 per cent of spectra, implying that it does not usually dominate the spectral profile in this wavelength range.

We also investigate HVFs of Si II 6355 Å, a relatively unexplored area of research, but see Marion et al. (2013) for one of the best previous studies of Si II 6355 Å HVFs. As with the Ca II features, no HVFs of Si II 6355 Å are found in underluminous / Ia-91bg / FAINT objects. On the other hand, Si II 6355 Å HVFs are much rarer than their Ca II counterparts, and are detected in only ∼16 per cent of the objects in the current sample. Even at early times ($t < -5$ d), HVFs of Si II 6355 Å are seen in only ∼32 per cent of SNe Ia.

Despite their rarity, Si II 6355 Å HVFs are observed about one-third of the time in HV objects, compared to only 5–10 per cent of the time in all other SN Ia subtypes. We also find that stronger HVFs of Si II 6355 Å are associated with a lack of

C II absorption at early times and relatively red UV/optical colours near maximum brightness. These new-found connections, in conjunction with previous work, led to Table 2.1, which presents a list of correlated parameters that likely constitute a continuous distribution of SN Ia observables.

Future SN Ia models should utilise the empirical relations and observational constraints set forth in this and previous work regarding HVFs. For example, if HVFs arise purely from an opacity effect, then a stronger line (i.e., one with a larger pEW) would form at a larger radius in the SN photosphere. Assuming homologous expansion, this would correspond to a larger observed velocity for the HVFs of a stronger line.

Using the measurements of HVFs of Si II 6355 Å and CaNIR discussed above, 94 per cent of all spectra have $R_{\rm Si} < R_{\rm CaNIR}$, while the remaining $\sim$6 per cent are consistent with equality. Thus, all HVFs of CaNIR are consistent with being stronger, relative to their PVFs, than those of Si II 6355 Å. In $\sim$80 per cent of observations, HVFs of CaNIR have larger velocities than HVFs of Si II 6355 Å, with $\sim$5 per cent consistent with equality. The remaining $\sim$15 per cent of spectra, where Si II 6355 Å HVFs are significantly faster than CaNIR HVFs, include SNe Ia with some of the fastest Si II 6355 Å velocities ever observed (e.g., SNe 2006X and 2010kg; Wang et al. 2008; Silverman et al., in preparation, respectively). Thus, CaNIR is stronger and also faster than Si II 6355 Å, except in these extremely high-velocity objects, and so the HVFs of Si II 6355 Å and CaNIR *could* be caused primarily by opacity effects in most SNe Ia.

While opacity may play a role, an abundance or density enhancement or an ionisation change at high velocity (i.e., large radius) is likely required to produce detectable HVFs. Gerardy et al. (2004) showed that a model in which SN ejecta collide with a circumstellar shell can yield observed velocities of the CaNIR HVF feature. Mulligan & Wheeler (2015, in preparation) show that the evolution in time of the PVF and HVF profiles, and the nearly constant velocity gap between the two sets of features, can be reproduced by a model of the interaction between SN Ia ejecta and a circumstellar shell of small mass contained within a few tenths of a solar radius near the exploding WD. Figure 2.17 shows the evolution of the CaNIR PVF and HVF velocities as open and filled circles, respectively, for a shell with mass 0.005 $M_{\odot}$. Also shown in the figure (as open and filled squares, respectively) are the PVF and HVF velocities measured herein for SN 2011fe.

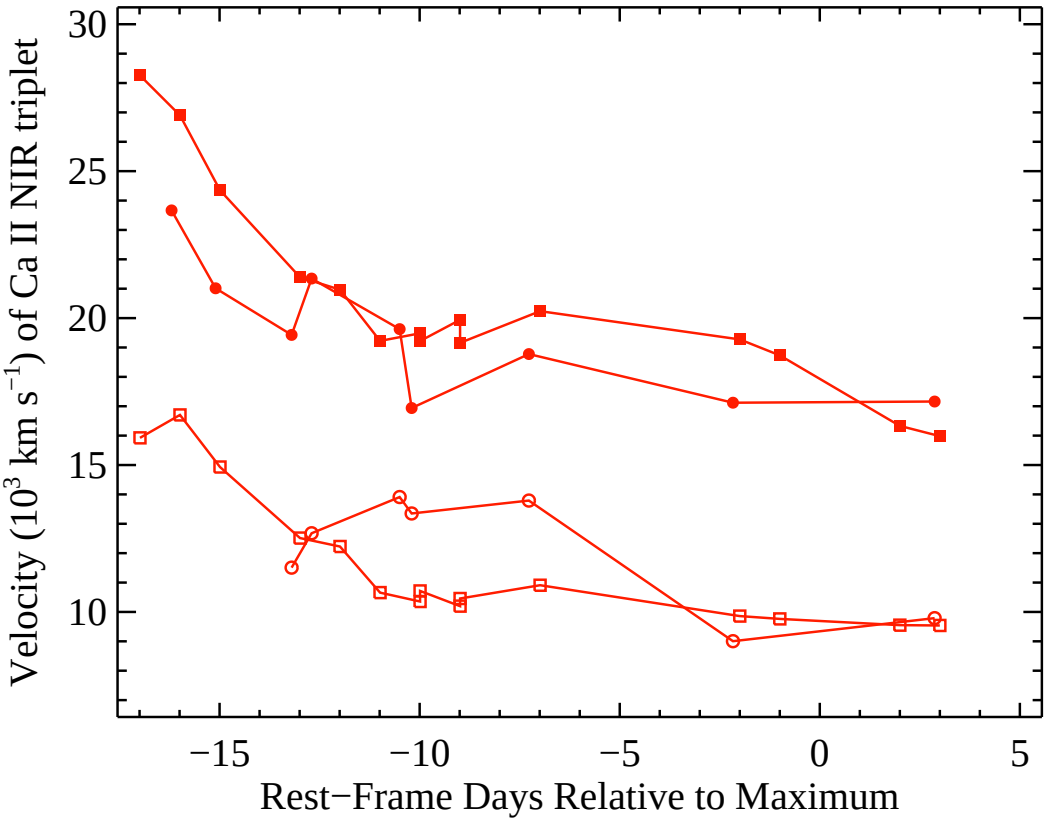

Figure 2.17: The measured CaNIR velocities of SN 2011fe from the current work (squares) and model CaNIR velocities from Mulligan & Wheeler (2015, in preparation; circles). Open points are PVFs and filled points are HVFs.

The model PVF velocities match quite well the measured values from the current work at early times and near maximum brightness, though in between these times they are slightly higher than the data indicate. The model HVF velocities match fairly well at most epochs, but are sometimes slightly slower than the measured values. Prior to about 13 d before maximum brightness the photosphere is at the contact discontinuity, below the shell, and thus only the HVF is seen in the model. At later times, the photosphere moves deeper into the ejecta, allowing the PVF to be observed, but the CSM shell still has enough optical depth to yield HVFs. The evolution of the features in the model is caused by the receding velocity of the photosphere and the free expansion of the higher-velocity shell material that leads to weaker absorption in the HVFs (Mulligan & Wheeler 2015, in preparation).

The current work now stands as an observational benchmark against which theoretical models of SNe Ia can be compared. Any successful model of a normal or overluminous SN Ia that follows the"Phillips relation" must naturally produce HVFs of Ca II since they are found so ubiquitously and at a range of pre- and near-maximum-brightness epochs. On the other hand, models of underluminous / Ia-91bg objects should never produce Ca II HVFs. Furthermore, based on spectropolarimetric observations, the HVFs of Ca II should also show polarisation, distinct from any polarisation present in the PVFs (e.g., Leonard et al., 2005; Wang et al., 2003, 2006; Chornock & Filippenko, 2008; Patat et al., 2009; Maund et al., 2013). Similarly, HVFs of Si II 6355 Å should be occasionally produced in N and overluminous/Ia-91T/99aa objects, never produced in underluminous / Ia-91bg objects, and preferentially more often (but still somewhat rarely) produced in HV objects. It is now clear that the detection and characterisation of HVFs is yet one more piece of the SN Ia puzzle.

Chapter Three: High-Velocity Features in Type Ia Supernovae from a Compact Circumstellar Shell

3.1 Prelude

Significant portions of this chapter have been published previously as Mulligan & Wheeler (2017). In this chapter, we develop the hydrodynamic simulations for the supernova interacting with a shell and consider the possible parameter space for the shell, namely the mass, size, and density profile of the shell, the explosion model that is used for the supernova itself, and the equation of state that is used within the simulation. The core concept of a supernova interacting with a shell was that of J. Craig Wheeler. The development of the methodology for hydrodynamic simulation and related parameter space, the methodology of generating limited synthetic spectra to explore the parameter space, performing the simulations, and developing software for the simulation and subsequent analysis, modification of SYN++, and the writing of the article were the work of this author. Discussion and analysis was generally a joint work between J. Craig Wheeler and this author. All figures in this work were generated using software written by this author.

3.2 Introduction

Type Ia supernovae (SN Ia) provide a fundamental tool for our understanding of the history of the universe. SN Ia are 'standardizable candles' used to explore the expansion of the universe as well as the chemical enrichment of galaxies (Riess et al., 1998; Perlmutter et al., 1999; Tsujimoto & Shigeyama, 2012). The configuration of the progenitor system and the cause of the explosion remain elusive, although observations of SN 2011fe within about a day after the explosion have shown it to be a compact system (Nugent et al., 2011; Bloom et al., 2012; Piro & Nakar, 2014). Since the progenitor of a SN Ia has never been observed, we must rely on *ex post facto* information to glean the nature of the system and explosion. The light curve and spectral features observed at the earliest times, within the first days or weeks

after the explosion, can reveal unique signatures of the explosion or the results of interaction between the supernova and its immediate environment. Spectroscopy of SN Ia in these first weeks reveals high-velocity features (HVF) in Ca II and Si II (Hatano et al., 1999; Parrent et al., 2012; Marion et al., 2013). The HVF have a velocity $\gtrsim$25,000 km s^{-1} at 15-18 days before B-band maximum (Bmax) that slows to a plateau of about 18,000 km s^{-1} by Bmax. The photospheric feature also starts at high velocity and recedes to lower velocities over the same interval, but the HVF consistently remain $\gtrsim$7,000 km s^{-1} faster than the photospheric velocity features (PVF) (Marion et al., 2013; Maguire et al., 2014; Silverman et al., 2015). Ca II HVF appear in over 90 per cent of normal SN Ia (Mazzali et al., 2005b; Childress et al., 2014; Maguire et al., 2014; Silverman et al., 2015) and show significant polarization (Wang et al., 2003), indicating that the material has a high covering factor and is asymmetric.

Suggestions for the source of the high-velocity material include plumes of partially burned ejecta (Wang et al., 2003), a surface detonation of He (Mazzali et al., 2005a), or interaction with a circumstellar medium (CSM) with a total mass of high-velocity material of about 0.02 $M_\odot$ and a solar abundance of metals (Gerardy et al., 2004; Quimby et al., 2006). Understanding the source of the high-velocity material will give insight to the nature of the progenitor system or mechanism by which the explosion is initiated; both of these are necessary to control the systematics in the use of SN Ia as cosmological probes.

Gerardy et al. (2004) have previously shown that a circumstellar shell (CSS) model with solar abundance will produce HVF, however their result focused on the epoch near Bmax, at which time the HVF velocity is asymptotic and the feature is fading. Gerardy et al. (2004) also considered interaction with an extended r^{-2} wind, though this is disfavored because of excess radiation emitted throughout the interaction. Here we investigate the interaction of ejecta with compact CSSs with a range of masses and initial structures with no underlying assumption regarding the composition of the shell material. The compactness of the CSS (< 1 $R_\odot$) ensures that no extra luminosity will be visible during times in which SN Ia have been observed. We consider the observational signatures of these models beginning 1 d after explosion and continuing past Bmax. Here we focus on techniques, dynamics, and spectral synthesis, and study parameters related to the simulation: explosion model, equation of state, and initial conditions in the shell.

In §3.3 we describe the hydrodynamic methods used; the models are described in §3.3.1. In §3.4 we discuss the methods used for generating synthetic spectra from the hydrodynamic results. We present the results, comparing the effects of mass and geometry of the shell and choice of equation of state in §3.5. In §3.5.4 we provide a summary of the results and a discussion of the implications.

3.3 Hydrodynamics

The hydrodynamic simulation is performed using FLASH 4.1 (Fryxell et al., 2000) with 1-D spherical geometry and multipole gravity. We use both the Helmholtz and gamma-law equation of states (EOS) (Timmes & Swesty, 2000). The Helmholtz EOS is more appropriate for density or temperature applications wherein the material is fully ionized, as occurs in the interior of the recently exploded white dwarf as well as in the strong shocks that occur when supernova ejecta interact with a circumstellar shell. The Helmholtz EOS is limited to a density $\geq 10^{-10}$ g cm^{-3} and temperature $\geq 10,000$ K, restricting its use to only the first few tens of seconds after the explosion occurs. The gamma-law EOS is better suited for low-temperature or low-density applications. Unfortunately the two EOS do not have a simple overlap, so we have chosen to use each individually in order to bracket the pressures and temperatures occurring in the material. The choice of EOS for each simulation is shown in Table 3.1. We compare the effects of the choice of EOS in §3.5.2.2. A more comprehensive Helmholtz-like EOS that accounts for partial ionization and a much lower density and temperature floor is required to fully understand the true evolution of this and other supernovae in the first minutes after the explosion.

Our simulation volume is limited to 10^{12} cm, large enough such that no material escapes from the volume during the simulation. The minimum resolution is 4.18×10^6 cm per zone and maximum resolution equal to the entire volume. The adaptive mesh refinement feature of FLASH is used to set the resolution of any given block during simulation, with pressure used to determine when refinement is required. The multispecies unit is used to track H, He^3, He^4, C^{12}, O^{16}, Mg^{24}, Si^{32}, and Ni^{56}. The length of simulation is typically 50s, when a cell reaches the Helmholtz temperature or density floor or until the AMR unit reached a limit for the maximum number of blocks per node.

Table 3.1: List of models tested, with the parameters used in or resulting from the simulation.

Model ID	Explosion Model[a]	EOS[b]	Shell Mass ($M_\odot$)	Shell Geometry[c]	Shell Inner Radius ($R_\odot$)	Shell Outer Radius ($R_\odot$)	Ejecta:Shell Normalization Factor Ratio[e] $\frac{\mathcal{R}^E_{\text{Si Group}}}{\mathcal{R}^S}$
10	a	H	...	...	...	...	...
17	c	H	...	...	...	...	...
18	b	H	...	...	...	...	...
41	c	γ	0.008	RS	0.010	0.297	6.761
45	c	γ	0.012	RS	0.010	0.297	3.903
49	c	γ	0.010	RS	0.010	0.297	5.233
53	c	γ	0.020	RS	0.010	0.297	2.784
54	c	γ	0.005	T	0.010	0.297	45.54
55	c	γ	0.005	G	0.008[d]	0.728[d]	12.42
56	c	γ	0.005	S	0.010	0.297	44.90
57	c	γ	0.005	RS	0.010	0.297	9.979
61	c	γ	0.003	RS	0.010	0.297	22.46
64	c	H	0.005	RS	0.010	0.297	15.15
70	c	γ	0.005	RS	0.007	0.040	14.82
71	c	γ	0.005	RS	0.007	0.080	10.82
72	c	γ	0.005	RS	0.007	0.120	12.23
73	c	γ	0.005	RS	0.007	0.500	9.924
74	c	γ	0.005	RS	0.007	1.000	7.879
80	b	γ	0.005	RS	0.010	0.297	3.866
81	a	γ	0.005	RS	0.010	0.297	23.53

[a] (Gamezo et al., 2005)
[b] H = Helmholtz. γ = gamma-law
[c] T = top-hat. G = Gaussian. S = sawtooth. RS = reverse sawtooth
[d] For the Gaussian model, the listed inner and outer radii are the radius at 1 e-folding from the center.
[e] See Sec. 3.4.

3.3.1 Supernova and Circumstellar Shell Models

We use the delayed-detonation models of Gamezo et al. (2005) for the supernova, maintaining the resolution of the original models with a maximum radius of 0.0076 $R_\odot$ resolved into 128^3 zones and use spherical averaging to reduce the model from 3-D to 1-D. The model provides C, O, Mg group (mostly Ne, Mg), Si group (mostly Si, S, Ar, Ca), and Fe group (Ti, Fe, Co, Ni) abundances for each zone. The three models differ in the delay between deflagration and detonation, the location of the detonation, and the total energy released. Model `b` is off-center detonation, while models `a` and `c` have a central detonation; models `a` and `b` have 1.62 s delay between the deflagration and detonation, while model `c` has a 1.51 s delay. Models `a` and `b` result in a final total energy of about 1.3×10^{51} erg; model `c` has a final energy of 1.6×10^{51} erg (Gamezo et al., 2005).

The resulting 1-D model is not designed to produce the best fit to the overall spectral evolution of a typical SN Ia, but instead to be representative of the evolution. We have tried some of our shell models with Gamezo et al. (2005) explosion models `a`, `b`, and `c`, and find that explosion model `a` will produce weak features for intermediate mass elements at all times (see §3.5.1 for Ca II), with or without a shell; explosion models `b` and `c` result in synthetic spectra that are broadly representative of SN Ia spectra. In future work we will utilize 3-D models to explore the nature of the HVF and will employ those models for which the 1-D version provide a better match to the full spectral evolution of the PVF and HVF. As we will see below, even these rather roughly constructed 1-D models lead to new insights and new issues regarding the HVF.

For the CSS models we use a range of masses between 0.001 – 0.1 $M_\odot$ and radii between 0.04 – 2 $R_\odot$. We consider four density profiles for the shell:

$$\rho^{\rm S}(r) = \begin{cases} \rho_{\rm r} & {\rm top-hat}, |\Delta r_{\rm c}| \leq \frac{\Delta r}{2} \\ \rho_{\rm r} \left(\frac{\Delta r_{\rm O}}{\Delta r}\right) & {\rm sawtooth}, |\Delta r_{\rm c}| \leq \frac{\Delta r}{2} \\ \rho_{\rm r} \left(1 - \frac{\Delta r_{\rm O}}{\Delta r}\right) & {\rm reverse-sawtooth}, |\Delta r_{\rm c}| \leq \frac{\Delta r}{2} \\ \rho_{\rm c} e^{-\frac{2(\Delta r c)^2}{r_e}} & {\rm Gaussian, all}\ r \\ 0 & {\rm Elsewhere} \end{cases} \tag{3.1}$$

where r is the radius, $r_{\rm c}$ is the radius at the center of the shell, $\Delta r_{\rm c} \equiv r_{\rm c} - r$, $\Delta r_{\rm O} \equiv r_{\rm O} - r$, where $r_{\rm O}$ is the radius at the outer edge of the shell, Δr the width of

the shell, r_e is the e-folding factor for the Gaussian model, and $\rho_{\rm r}$ is a density selected to achieve the desired mass for the given inner and outer radii. A temperature and density floor are applied corresponding to the CSM values (as described below) for all models (i.e. $\rho(r) = \max(\rho^{\rm S}(r), 10^{-9}\,{\rm g\ cm^{-3}})$). The mass, density structure, and inner and outer radii of the shell for each model considered here are specified in Table 3.1. For hydrodynamic purposes only we assume a hydrogenic shell with solar abundance of metals. The total He is also solar, but we enhance the He^3 by 10 per cent in the shell to act as a tracer.

For computational purposes, all zones that are within neither the ejecta nor the shell are given a CSM with density 10^{-9} g cm^{-3} and a temperature of 20,000 K, selected to fit within the range of both the Helmholtz and Gamma-law EOS in FLASH.

3.4 Spectral synthesis

We post-process the simulation data in order to generate synthetic spectra at selected epochs. While there are a variety of 1-D LTE and nLTE radiative transfer codes available for generating spectra, nearly all of these codes require an abundance profile for the ejecta and other material to be specified. Since the abundances of the shell (or the HVF material) are unknown, we use SYN++ (Thomas et al., 2011a) because it allows direct control of the Sobolev optical depth of individual ions. We have modified SYN++[1] to accept an arbitrary Sobolev optical depth profile for each ion,

$$\tau_{k,j} = S_j(t)\mathcal{G}_{k,j}, \tag{3.2}$$

where index j refers to a particular ion (e.g. j = Ca II), and index k refers to a velocity index, $S_j(t)$ is a time-dependent scalar, and $\mathcal{G}_j$ is a normalized optical depth profile for a given ion ($\mathcal{G}_{k,j}$ is the value of $\mathcal{G}_j$ at velocity index k). Typically in SYNOW or SYN++, $\mathcal{G}_{k,j} = e^{-(v_k - v_{\rm j,ref})/v_{j,e}}$, where $v_{\rm j,ref}$ is the reference velocity, and $v_{j,e}$ is the e-folding length in velocity space (the `aux` parameter), and $S_j(t) = 10^{\mathcal{T}_j}$, where $\mathcal{T}_j$ is the `log_tau` parameter. The construction of a normalized optical depth profile for $\mathcal{G}_{k,j}$, as described below. In this paper, we assume for illustration that

$$S_j(t) = S_{j,1}(t/1\ {\rm d})^{-2}, \tag{3.3}$$

[1]The modified version of SYN++ is publicly available on github.com in repository `astrobit/es`.

where $S_{j,1}$ is the peak optical depth at 1 d after explosion. This scaling of $S_j(t)$ assumes that the optical depth simply scales with the density in free expansion. The time dependance of the optical depth is likely not t^{-2} due to ionization and thermal effects; we discuss this further in §3.5.4. The choice of 1 d as the point of reference is selected for simplicity. To distinguish between quantities for the shell and ejecta, we will use superscript S to denote the shell, and E to denote the ejecta; hence $\tau^{\rm S}_{k,j}$ would designate the optical depth of velocity index k for ion j for the shell. Within SYN++, the optical depth for a specific line of an ion is

$$\tau_{k,j,l} = \tau_{k,j} \frac{f_l}{f_{ref}} e^{-(E_l - E_{ref})/(k_B T_{exc})}, \tag{3.4}$$

where f_l is the oscillator strength of the line, f_{ref} is the oscillator strength of the reference line, E_l is the energy of the lower level of the line, $E_{\rm ref}$ the energy of the lower level of the reference line, and T_{exc} is the excitation temperature. For Ca II, the K line ($\lambda = 3934$ Å, $f_{\rm ref} = 1.42$, $E_{\rm ref} = 0$ eV) is used as the reference line.

We determine the minimum and maximum velocities for the line opacity profile based on the minimum and maximum zone velocities from the simulation data, then create 2048 velocity bins with each bin having the same width in velocity space. We generate $\mathcal{G}_{k,j}$ by post-processing the simulation results to extract the radial distribution of density, composition, and velocity for the ejecta and shell. Because zone velocities are not unique in space due to reverse shocks resulting from the ejecta-CSS interaction and CSS-CSM interaction, the $\mathcal{G}_{k,j}$ for a given velocity must be summed over several zones. We generate $\mathcal{G}_{k,j}$ for the ejecta and shell individually, identifying each based upon composition of the material from the simulation: the supernova ejecta contain no hydrogen, and the CSS and CSM contain hydrogen with solar abundance of metals, with the CSS containing enhanced He^3. For the spectral synthesis we neglect all cells that contain CSM.

For the ejecta, we define

$$\mathcal{G}^{\rm E}_{k,j} = \frac{1}{\mathcal{R}^E_G} \sum_{r:v(r)=v_k} X^{\rm E}_G(r) \rho^{\rm E}(r), \tag{3.5}$$

where the sum is over all zones with velocity v_k, $\rho^{\rm E}(r)$ is the total mass density in the zone at the end of the simulation, v is the velocity within a zone, v_k is the velocity at which optical depth is being measured, and $X^{\rm E}_G(r)$ is the abundance by mass of the element group G in the zone (G refers to the element group information from

Gamezo et al. (2005), i.e C, O, Mg, Si, or Fe, of which ion j is a member). We define a normalization constant

$$\mathcal{R}_G^E = \max(X_G^{\rm E}(r)\rho(r)) \tag{3.6}$$

to force the peak value of $\mathcal{G}_{k,j}^{\rm E}$ to be near unity. This normalization is chosen because both the ejecta and shell material are expected to produce a spectral feature at some epoch after the explosion, and the physical parameters such as ion state, abundance (for the shell), and temperature are not known. The effects of these physical parameters on optical depth are degenerate; by this definition of $\mathcal{G}_{k,j}^{\rm E}$ the parameters are effectively folded into the value of $S_{j,1}^{\rm E}$; see below for further explanation.

While we have specified solar abundance for shell and CSM in the hydrodynamic simulation, we do not know the abundances of the shell. Thus, instead of including abundance information for the shell in $\mathcal{G}_{k,j}^{\rm S}$, we choose

$$\mathcal{G}_{k,j}^{\rm S} = \frac{1}{\mathcal{R}^S} \sum_{r:v(r)=v_k} \rho^{\rm S}(r), \tag{3.7}$$

where

$$\mathcal{R}^S = \max(\rho^{\rm S}(r)), \tag{3.8}$$

and other terms are as above.

We can relate the optical depth for ion j used to generate our spectra to the Sobolev optical depth for a given velocity (with index k)

$$\tau_{k,j,ul}(t) = \frac{\pi e^2}{m_{\rm e} c} f_{ul} \lambda_{ul} e^{-E_l/k_B T_{k,j}} n_{k,j}(t) \frac{{\rm d}r}{{\rm d}v}_k, \tag{3.9}$$

where f_{ul} is the oscillator strength, λ_{ul} is the wavelength of the line, E_l is the energy of the lower state, $T_{k,j}$ is the effective temperature of the ion, $\frac{{\rm d}r}{{\rm d}v}|_k$ is the velocity gradient at velocity index k (assuming that the material is in free expansion, then $\frac{{\rm d}r}{{\rm d}v}|_k = t$), and $n_{k,j}(t)$ is the number density of the ion at a given time. The latter can be rewritten as $n_{k,j} = m_i^{-1} F_{k,j} X_{k,i} \rho_k \ell (t/t_{\rm ref})^{-3}$, where m_i is the mass of the element i (of which j is an ion), $F_{k,j}$ is the fraction of element i in the j ion state, $X_{k,i}$ is the abundance of the element, ρ_k the mass density at a given velocity at the reference time $t_{\rm ref}$, ℓ is an effective coverage factor, and t is time.

If we relate Eq. 3.2, Eq. 3.4 and Eq. 3.9 for the ejecta and shell then, invoking Equations 3.5 through 3.8, we can define

$$\mathcal{G}_{k,j}^{\rm E} = \frac{X_{k,G}^{\rm E} \rho_k^{\rm E}}{\mathcal{R}_G^E}, \tag{3.10}$$

and

$$\mathcal{G}^{\rm S}_{k,j} = \frac{\rho^{\rm S}_k}{\mathcal{R}^S}. \tag{3.11}$$

Then

$$S^{\rm E}_j(t) = \chi_{ul} m_i^{-1} e^{-\frac{E_l}{k_B}\left(\frac{1}{T^{\rm E}_{k,j}} - \frac{1}{T^{\rm E}_{exc}}\right)} \frac{f_{ref}}{f_l} \times F^{\rm E}_{k,j} \ell^{\rm E} \frac{X^{\rm E}_{k,i}}{X^{\rm E}_{k,G}} \mathcal{R}^E_G \left(\frac{t}{t_{\rm ref}}\right)^{-2} t_{\rm ref} \tag{3.12}$$

and

$$S^{\rm S}_j(t) = \chi_{ul} m_i^{-1} e^{-\frac{E_l}{k_B}\left(\frac{1}{T^{\rm S}_{k,j}} - \frac{1}{T^{\rm S}_{exc}}\right)} \frac{f_{ref}}{f_l} \times F^{\rm S}_{k,j} \ell^{\rm S} X^{\rm S}_i \mathcal{R}^S \left(\frac{t}{t_{\rm ref}}\right)^{-2} t_{\rm ref}, \tag{3.13}$$

where $\chi_{ul} = (\pi e^2)/(m_{\rm e} c) f_{ul} \lambda_{ul}$ and $X^{\rm E}_{k,i}/X^{\rm E}_{k,G}$ is the ratio of abundance of element i to that of group G to which it belongs. These expressions explicitly include the excitation state, ion state, clumpiness factors, abundances, and normalization constant in $S_{j,1}$. There is an implicit time dependence within the ion fraction ($F_{k,j}$) and excitation temperature ($T_{k,j}$) for each of these values. The $t_{\rm ref}$ term is the time at which the density term is normalized and is the same for both $S^{\rm S}_j(t)$ and $S^{\rm E}_j(t)$. The method we use for normalizing $\mathcal{R}^E_G$ or $\mathcal{R}^S$ can be performed at any time, but the ratio $\mathcal{R}^E_G/\mathcal{R}^S$ is time-independent provided that each is selected at the same epoch, as they are normalization factors for the hydrodynamic results. We have selected $t_{\rm ref} = 1$ d for simplicity.

In this study, we focus on the Ca II near-infrared triplet (CaNIR), because the high-velocity feature in this particular triplet is strong and very common (unlike the Si II HVF), persists until or after Bmax, and does not seem to blend with other features (unlike the Ca II H & K HVF). We assume scalar factors of $S^{\rm E}_{Ca\ {\rm II},1} = 10^{3.5}$ for the ejecta and $S^{\rm S}_{Ca\ {\rm II},1} = 10^4$ for the shell. We have assumed an excitation temperature of $10,000$ K, consistent with typically assumed photosphere temperatures. From Eqs. 3.2 and 3.4, the choices of scalar $S_{Ca\ {\rm II},1}$, in combination with the effect of the excitation temperature, result in a value of $\tau_{\lambda\lambda 8542}$ $\sim$70 for the shell and $\sim$20 for the ejecta at the velocities at which $\mathcal{G}_k$ is normalized. These values are selected to achieve a pseudo-equivalent width (pEW) for CaNIR that is near observed values at a few days after the explosion and again near Bmax. We note that the choice of $S_{Ca\ {\rm II},1}$ scales inversely with excitation temperature to achieve the same optical depth. For example, a choice of ($T_{exc} = 10,000$ K, $S^{\rm S}_{Ca\ {\rm II},1} = 10^4$) and ($T_{exc} = 20,000$ K, $S^{\rm S}_{Ca\ {\rm II},1} = 10^{3.6}$) both yield the results presented here. Hence, the pEW

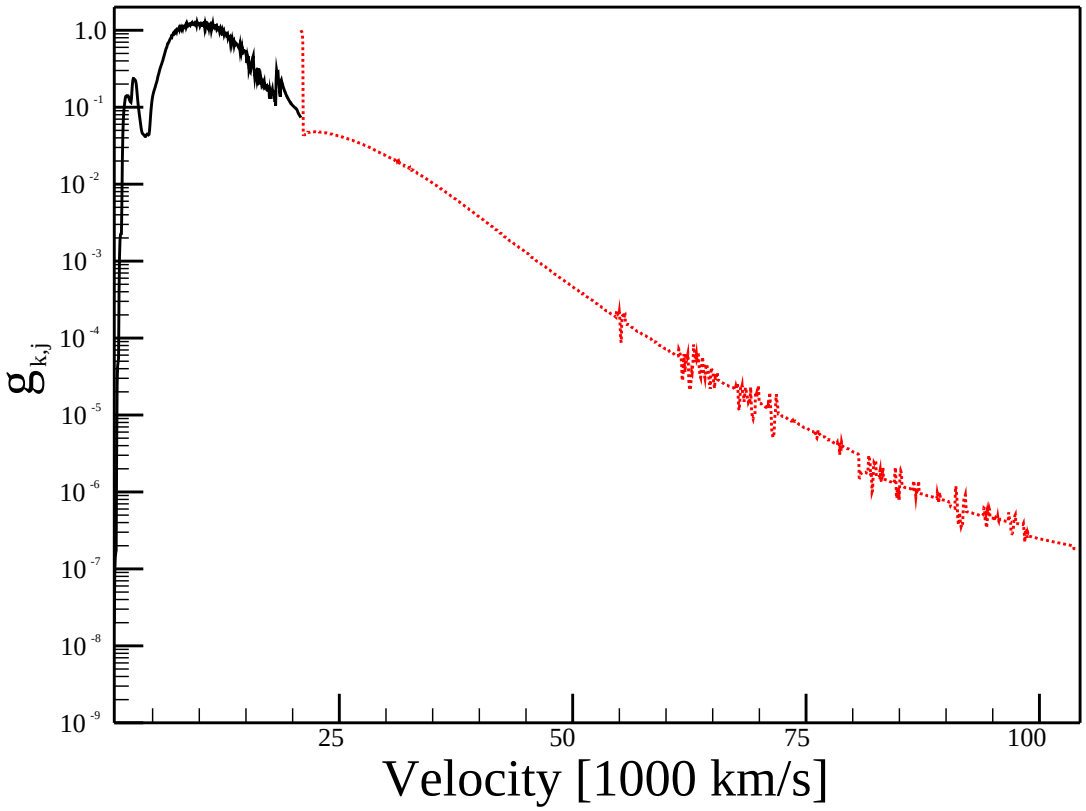

Figure 3.1: Normalized line optical depth profile ($\mathcal{G}_{k,j}$) for Si group elements for the model with a shell of mass 0.005 $M_\odot$ and outer radius 0.3 $R_\odot$ (model # 57), with the ejecta (black, solid) and shell (red, dashed) components separated. The small scale density irregularities in the shell are due to numerical artifacts relating to the mesh refinement and can be reduced with higher resolution simulation. The noise tends to lie at low optical depths so it generally does not have an effect on the generated spectra. There is a density enhancement in the shell at the contact discontinuity ($\sim$20,000 km s^{-1}), and another at the reverse shock in the ejecta ($\sim$18,000 km s^{-1}).

presented here are not dependent on the excitation temperature so long as the scalars $S_{Ca\ \mathrm{II},1}$ are modified appropriately.

In order to determine the velocity of the photosphere (PS) to provide to SYN++ for each model at each selected epoch, we assume a gray opacity. While free-free scattering is the source of opacity in the interior of the ejecta, the scattering in the outer layers where the spectral features form is dominated by electron scattering. The

total continuum optical depth at a given radius is then

$$\tau_{\rm PS} = \sigma_{\rm e} \left(\frac{t_{\rm ref}}{t} \right)^3 \sum_{r=R}^{R_{\rm max}} \sum_i \sum_{j=1}^{\min(Z_i, N_{\rm max})} j \rho(r) m_i^{-1} X_i \delta r(t), \tag{3.14}$$

where $\sigma_{\rm e}$ is the Thompson cross-section, m_i and Z_i are the mass and atomic number of element i, respectively, $N_{\rm max}$ is the maximum ionization state for all elements, $\delta r(t) \propto \delta v(r) t$ the width of a zone at a given epoch, and all other terms are as described above. We then define the PS velocity at $v(r)$ such that $\tau_{\rm PS} = 0.66$. Note that because $\delta r(t)$ is linearly proportional to t, the overall trend in time is $\tau_{\rm PS} \propto t^{-2}$. We find that a choice of $N_{\rm max} = 3$ produces an evolution of the photosphere that is in reasonable agreement with that observed in typical SN Ia in most models (i.e. initial velocity ∼25,000 km s^{-1}, dropping to about 10–15,000 km s^{-1} by Bmax). This prescription results in a photosphere that lies within the shell at early times, which may present issues concerning the appearance of PS Si II during this phase (see §3.5.4 for discussion). The PS velocities used for each model are shown in Table 3.2. A choice of lower $N_{\rm max}$ has little effect on the velocity of the photosphere in the first days after the explosion but results in a velocity near 7,000 km s^{-1} for most models near the epoch of Bmax.

3.5 Results

We generated synthetic spectra at one-day intervals from 1 to 25 days after explosion for shells with a range of masses between 0.001 $M_\odot$ and 0.02 $M_\odot$ as enumerated in Table 3.1. The mass and geometry of the shell, choice of explosion model, and choice of equation of state each may affect the resulting Sobolev optical depth profiles.

We employ two methods to compute the pEW for each model. The first, used by many in the community (c.f. Childress et al., 2014; Silverman et al., 2015; Zhao et al., 2015), assumes the continuum to be a line extended between a point on the blue side of the feature of interest to the P Cygni peak; the pEW is then measured by integrating the difference between this pseudo-continuum and the actual measured flux across the feature. We use the point at which the flux in our synthetic spectra is 1 per cent below the continuum as the blue edge and the P Cygni peak, as measured by the peak flux redward of the feature minimum, as the red edge. We hereafter refer to this method as the "P Cygni method."

Table 3.2: Photosphere velocity in 1,000 km s^{-1} for $N_{max} = 3$ for days 1 – 12 after explosion

	Day after explosion											
Model	1	2	3	4	5	6	7	8	9	10	11	12
10	11.6	11.3	11.0	10.8	10.6	10.4	10.2	10.1	9.9	9.8	9.7	9.6
17	28.1	24.4	22.1	20.5	19.2	18.2	17.2	16.3	15.6	14.9	14.3	13.7
18	19.0	17.4	16.5	15.9	15.5	15.1	14.8	14.6	14.5	14.3	14.2	14.1
41	37.3	31.1	27.1	23.7	20.6	18.9	18.2	17.5	17.0	16.8	15.7	14.9
45	37.2	31.4	27.9	25.1	22.7	20.5	18.2	17.5	16.9	16.3	15.9	16.0
49	37.3	31.3	27.6	24.6	21.9	19.4	18.2	17.5	16.9	16.4	16.4	15.4
53	36.8	31.3	28.2	26.0	24.1	22.4	20.8	19.4	17.9	16.4	16.0	15.5
54	38.7	28.3	22.5	20.7	19.8	19.3	18.0	16.9	16.0	15.2	14.6	14.0
55	34.7	27.9	23.5	21.1	20.2	20.1	18.6	17.3	16.3	15.5	14.8	14.1
56	37.5	32.6	27.3	21.6	19.7	18.3	17.6	17.2	16.7	15.7	15.0	14.3
57	37.2	30.2	25.3	20.9	19.9	19.0	18.5	17.9	16.7	15.8	15.0	14.3
61	36.5	28.3	22.4	21.1	20.2	19.6	18.2	17.1	16.1	15.3	14.7	14.0
64	38.0	30.8	25.4	20.5	19.2	18.4	17.8	18.0	16.8	15.8	15.1	14.4
70	37.7	30.6	25.5	20.9	19.7	18.9	18.3	17.8	16.7	15.7	15.0	14.3
71	37.5	30.3	25.3	20.9	19.8	19.0	18.4	17.9	16.7	15.8	15.0	14.3
72	37.4	30.3	25.3	20.9	19.8	19.0	18.4	17.9	16.7	15.8	15.0	14.3
73	37.1	30.1	25.2	20.9	19.8	19.0	18.4	17.9	16.7	15.8	15.0	14.3
74	36.3	29.5	24.9	20.7	19.6	18.8	19.5	18.0	16.8	15.8	15.0	14.3
80	28.9	24.2	21.1	18.5	16.2	15.0	14.8	14.6	14.4	14.2	14.1	14.0
81	20.5	17.4	15.6	14.2	13.0	11.9	10.9	10.0	9.4	9.3	9.3	9.2

The second method to determine pEW uses the flux from the actual continuum produced by SYN++ for the synthetic spectra. In this case, the pEW is measured between 6000 Å and the wavelength at which there is more emission than absorption on the red side of the feature (i.e. the wavelength at which the flux is greater than the continuum). We hereafter refer to this method as the "absorption pEW method."

In order to compare our synthetic data with actual SN Ia, we consider a subset of data from Silverman et al. (2015). Figure 3.2 shows the trend of pEW for those supernovae for which data are available prior to −10 d. The mean trend, shown in black, is the average of observations that are within 0.5 day of each other; e.g. any data between −1.5 d and −0.5 d are assumed to be at −1 d. We have excluded SN 2006X and SN 2010kg from the mean as those supernovae have a pEW that is about

Table 3.2: (cont.) Photosphere velocity in 1,000 km s^{-1} for $N_{\max} = 3$ for days 13 - 24 after explosion

	Day after explosion											
Model	13	14	15	16	17	18	19	20	21	22	23	24
10	9.5	9.4	9.3	9.2	9.1	9.1	9.0	8.9	8.8	8.7	8.7	8.6
17	13.2	12.7	12.3	11.8	11.5	11.1	10.7	10.4	10.1	9.8	9.5	9.2
18	13.9	13.7	13.5	13.3	13.1	12.8	12.5	12.1	11.8	11.4	11.1	10.7
41	14.2	13.6	13.0	12.5	12.0	11.6	11.2	10.8	10.4	10.1	9.7	9.4
45	15.1	14.3	13.6	13.0	12.4	11.9	11.5	11.1	10.7	10.3	9.9	9.6
49	14.6	13.9	13.3	12.7	12.2	11.7	11.3	10.9	10.5	10.2	9.8	9.5
53	15.0	14.6	14.2	14.6	13.7	13.0	12.4	11.9	11.4	10.9	10.5	10.1
54	13.4	12.9	12.4	12.0	11.6	11.2	10.8	10.5	10.1	9.8	9.5	9.2
55	13.6	13.0	12.6	12.1	11.7	11.2	10.9	10.5	10.2	9.9	9.6	9.2
56	13.7	13.2	12.7	12.2	11.8	11.3	11.0	10.6	10.2	9.9	9.6	9.3
57	13.7	13.2	12.7	12.2	11.8	11.3	11.0	10.6	10.2	9.9	9.6	9.3
61	13.5	13.0	12.5	12.0	11.6	11.2	10.8	10.5	10.2	9.8	9.5	9.2
64	13.7	13.2	12.7	12.2	11.8	11.3	11.0	10.6	10.3	10.0	9.7	9.4
70	13.7	13.2	12.7	12.2	11.8	11.3	11.0	10.6	10.2	9.9	9.6	9.3
71	13.7	13.2	12.7	12.2	11.8	11.3	11.0	10.6	10.2	9.9	9.6	9.3
72	13.7	13.2	12.7	12.2	11.8	11.3	11.0	10.6	10.2	9.9	9.6	9.3
73	13.7	13.2	12.7	12.2	11.8	11.3	10.9	10.6	10.2	9.9	9.6	9.3
74	13.7	13.2	12.7	12.2	11.8	11.3	11.0	10.6	10.2	9.9	9.6	9.3
80	13.8	13.8	13.8	13.5	13.2	12.9	12.6	12.3	11.9	11.6	11.2	10.9
81	9.2	9.1	9.1	9.1	9.0	9.0	8.9	8.9	8.8	8.8	8.8	8.9

2-3 times larger than the other supernovae included. In the plots of pEW that utilize the P Cygni method generated from our synthetic spectra, we include the mean trend line from these observations. To place these data on the same plot as our results we assume that Bmax occurs 18 days after the explosion.

In order to determine the apparent velocity of the feature, we assume the three lines that make up the CaNIR triplet to each produce a Gaussian of the same width and a relative depth that is scaled only by the relative strength of the line,

$$\mathcal{F}(\lambda) = C(\lambda) + \mathcal{F}_0 \mathcal{N} \left(h_1 e^{-\frac{(\lambda/r_1 - \lambda_0)^2}{2\sigma^2}} + h_2 e^{-\frac{(\lambda - \lambda_0)^2}{2\sigma^2}} + h_3 e^{-\frac{(\lambda/r_3 - \lambda_0)^2}{2\sigma^2}} \right), \tag{3.15}$$

where λ_0 is the wavelength at which the central component is strongest, $C(\lambda)$ is the continnum at a given wavelength, $\mathcal{F}_0$ is the depth of the feature at λ_0, $\mathcal{N}$ is

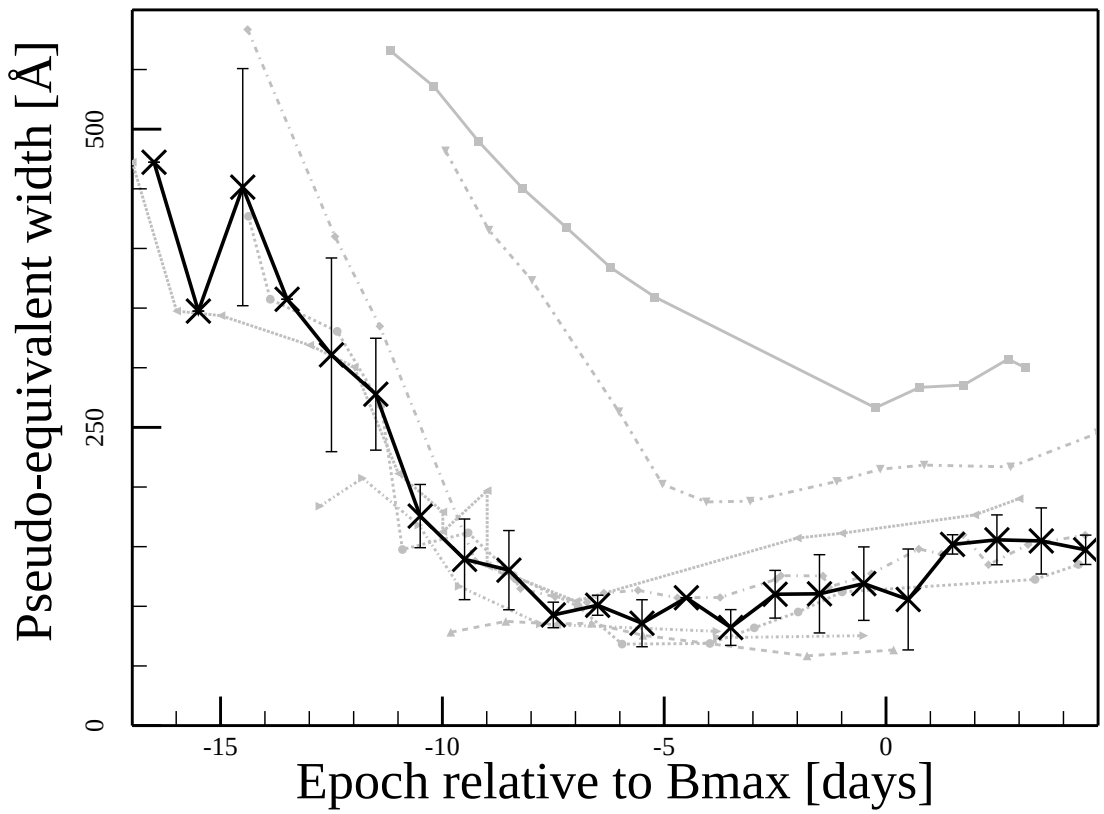

Figure 3.2: Pseudo-equivalent width of a subset of SN Ia from Silverman et al. (2015). gray lines are individual supernovae: SN2006X (Line: solid; Symbol: square), SN2009ig (Line: short dash; Symbol: circle), PTF10bjs (Line: long dash; Symbol: up triangle), SN2010kg (Line: long dash - short dash; Symbol: down triangle), SN 2011fe (Line: dotted; Symbol: left triangle), SN2012cg (Line: short dash - dotted; Symbol: right triangle), SN2012fr (Line: long dash - dotted; Symbol: diamond). Black line and 'X' symbols are the mean, excluding SN2006X and SN2010kg. SN 2006X and SN 2010kg are excluded from the mean due to their having a pEW 2-3 times as large as the others at all epochs. The uncertainties for the individual supernovae are not shown to avoid clutter, but tend to be significantly smaller than the scatter between different supernovae. Data used in this plot can be found in Table A4 of Silverman et al. (2015).

a normalization factor such that $\mathcal{F}(\lambda_0) = \mathcal{F}_0 + C(\lambda_0)$, $h_1 = 160$, $h_2 = 170$, and $h_3 = 130$ are the relative strengths of the three components of the triplet, $r_1 = 1.014$ and $r_3 = 0.995$ are the ratio of wavelengths of the red and blue components of the triplet, respectively, to the wavelength of the central line, and σ is the width of the feature. We perform a least-square fit to determine the parameters λ_0, $\mathcal{F}_0$, and σ for each feature. We allow for both single parameter set and double parameter set fitting (i.e. $\mathcal{F}(\lambda) = \mathcal{F}_a(\lambda) + \mathcal{F}_b(\lambda)$, where $\mathcal{F}_a$ and $\mathcal{F}_b$ have independent parameter sets λ_0, $\mathcal{F}_0$, and σ.) We choose the better of the fits (i.e. single or double parameter set), then compute the velocity(s) using

$$v = c\frac{(z^2 - 1)}{(z^2 + 1)}, \tag{3.16}$$

where $z \equiv (\lambda_0/\lambda_b - 1)$, and $\lambda_b = 8542.09$ Å is the rest wavelength of the central component of the CaNIR triplet.

We note that this method of fitting Gaussians to any feature is more likely to result in two parameter sets being a better fit than a single parameter set, especially as any given spectral feature is non-Gaussian. The depth of the weaker Gaussian can act as some degree of discriminant upon the appropriateness of the two parameter set fit: if the depth of the weaker Gaussian set is very small compared to that of the stronger set, if the weaker Gaussian is unusually wide, or if the evolution of the weaker set is stochastic, then the weaker component is more likely to be an artifact of fitting with six free parameters rather than three. This can have implications for detection of HVF at later epochs, or detection of a PVF at early epochs. We reject double parameter set fits that have opposing signs of the amplitude components ($\mathcal{F}_0$) or when the weaker component has an amplitude less than 5 per cent of the stronger component and the width of the weaker component is twice that of the stronger component.

We show an example of these two methods of measuring the pEW and generating a Gaussian fit in Figure 3.3.

In the subsections below we investigate the effect of choice of EOS, explosion model, and each parameter of the shell on the evolution of the shape, pEW, and velocity of the CaNIR feature.

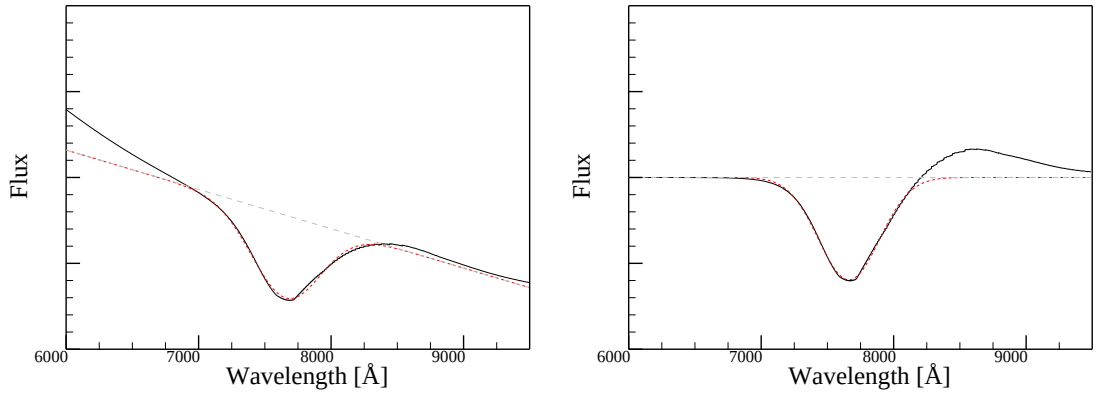

(a) P Cygni method

(b) Absorption method

Figure 3.3: The two methods for determining the pEW and subsequent fitting of a Gaussian set to the CaNIR feature for the model with a shell of mass 0.005 $M_\odot$ and outer radius 0.3 $R_\odot$ (model # 57) at 1 day after the explosion. Shown are the synthetic spectrum (black, solid), chosen continuum (cyan, long-dash), and Gaussian fit (red, short-dash). The reported pEW is the integral of the difference between the continuum and the flux. In Figure 3.3a the flux includes that of the continuum, while in Figure 3.3b the data have been normalized by the continuum prior to plotting. The feature has been fit by a single parameter set ($\mathcal{F}_0 = 0.47, \lambda_0 = 7633.73$ Å, σ =250.2 Å) for the P Cygni method, and a double parameter set ($\mathcal{F}_a : \mathcal{F}_0 = 0.59, \lambda_0 = 7639.05$ Å, $\sigma = 222.24$ Å; $\mathcal{F}_b : \mathcal{F}_0 = -0.034, \lambda_0 = 8228.68$ Å, σ =40.75 Å) for the absorption method. The opposing signs of the $\mathcal{F}_0$ components of the two parameter set Gaussian suggest that the $\mathcal{F}_b$ component is an artifact of using more free parameters for the fit rather than evidence of a second feature.

3.5.1 Supernova-Only model

Before examining the effect of the shell, we will begin with exploring the spectra that result from only the explosion models in order to illustrate a spectrum without a shell and high-velocity LGR.

Figure 3.4 shows the normalized line optical depth ($\mathcal{G}_{k,j}$) profiles of the three supernova models of Gamezo et al. (2005) with no surrounding shell included. It reveals that the bulk of Ca in model # 10 (explosion model `a`) lies below the photosphere at all times before Bmax, which will result in weak Ca features. Model #s 17 (explosion model `c`) and 18 (explosion model `b`) have similar velocities for the peak optical depth of the Ca, but model # 17 has Si group elements extending out to much larger velocities. If a solar abundance of Ca were added within unburned regions at high

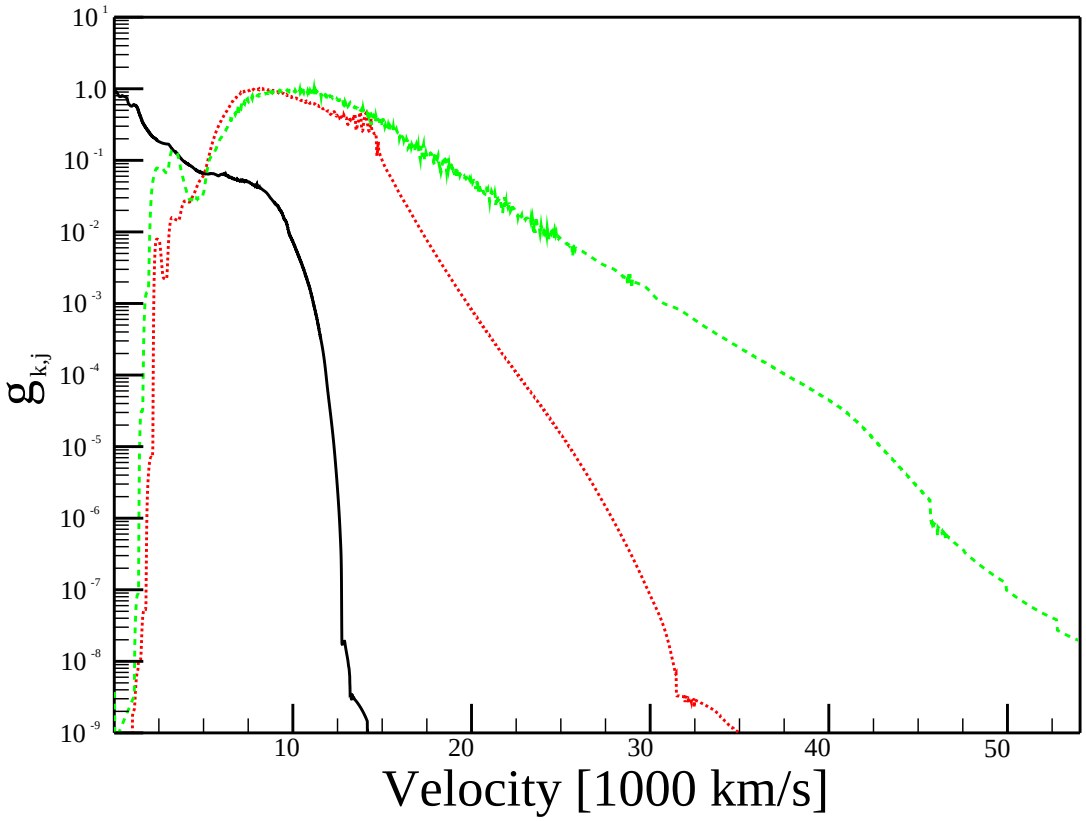

Figure 3.4: The normalized optical depth profile ($\mathcal{G}_{k,j}$) for Si group elements for the Gamezo et al. (2005) explosion models without a shell. Plots show case `a` (model # 10, black, solid), case `b` (model # 18, red, short dash), and case `c` (model # 17, green, long dash). Explosion model `a` results in a weak feature because the Si group elements are located below the photosphere. Explosion models `b` and `c` have similar velocities and profiles near the peak opacity, but model `c` has Si group elements at higher velocities.

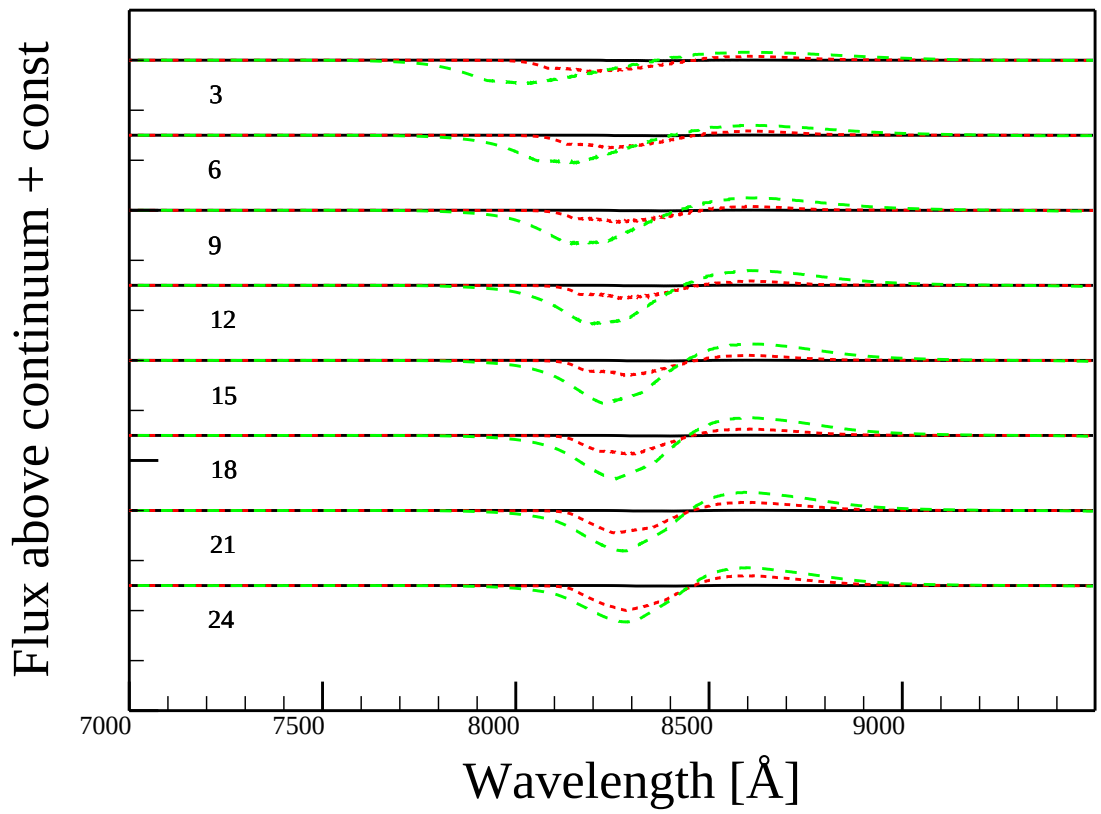

Figure 3.5: Evolution of the shape of the CaNIR feature for the Gamezo et al. (2005) explosion models with no shell. Plots show case `a` (model # 10, black, solid), case `b` (model # 18, red, short dash), and case `c` (model # 17, green, long dash). Labels on the left indicate the number of days after the explosion. The feature in model `a` is extremely weak (pEW ∼0.1 Å) for the selected optical depth scalar $S^{\rm E}_{Ca\ {\rm II},1}$.

velocities, it would result in $\mathcal{G}^{E}_{k,{\rm SiG}} \lesssim 10^{-6}$. Using the scalar $S^{\rm E}_{Ca\ {\rm II},1} = 10^{3.5}$ this results in $\tau^{E}_{Ca\ {\rm II}} \lesssim 10^{-2.5}$, thus a solar abundance of Ca in the unburned regions of the ejecta would have no impact on the spectrum. A larger value of $S^{\rm E}_{Ca\ {\rm II},1}$ for the higher velocity region would require increased Ca II fraction or a higher excitation temperature relative to the regions with freshly synthesized Ca, which is extremely unlikely.

Figure 3.5 shows spectra generated from these three explosion models. Model # 10, as expected, has an extremely weak CaNIR feature for the chosen scalar factor $S^{\rm E}_{Ca\ {\rm II},1}$. While a much larger choice of scalar can produce a stronger feature for this

model, the individual components of the CaNIR feature do not blend due to the limited quantity of Ca at velocities faster than ∼12,000 km s^{-1}. Model # 17 tends to produce a feature with a minimum at a shorter wavelength (i.e. higher velocity) than that of model # 18, especially in the two weeks immediately after the explosion. Model # 17 also produces a stronger feature at all epochs due to the more extended LGR. Some substructure can be seen in the model # 18 features; this structure is a result of the knee at about 15,000 km s^{-1} in the optical depth profile of Figure 3.4.

3.5.2 EOS and explosion model

Before considering the effects of the shell parameters we consider the effect of the explosion model and the equation of state used in the simulation on the resulting spectra, pseudo-equivalent width, and velocity profile of the CaNIR feature.

3.5.2.1 Explosion model

Figure 3.8 shows the evolution of the CaNIR feature in a shell interaction model highlighting the effect of the underlying explosion model while holding the parameters of the shell fixed. The result is similar to that of the models without a shell in that model # 57 (explosion model `c`) produces the deepest feature at all times and model # 81 (explosion model `a`) produces the weakest feature. When the shell is included, the depth of the feature is enhanced at early epochs, particularly within the first ∼12 d, due to absorption within the shell. After about 15 d, there is also a feature near 8000 Å and structure near 7800 Å due to the shell just forward of the contact discontinuity and the reverse shock in the ejecta, respectively, that do not appear in the models without a shell.

The velocity trend is shown in Figure 3.7. Prior to 11 d after the explosion, all three models tend to show, with a few exceptions, only a single velocity component. The velocity of this single component is more in line with the PVF in observed SN Ia for model #s 80 and 81 (explosion models `b` and `a`, respectively). The velocity evolution of model # 57 is consistent with HVF during this phase. Between 11 d and 18 d after the explosion, model #s 57 and 80 both show a two-component fit, with one component consistent with HVF and the other with PVF. At 19 d and later after the explosion, model # 80 continues to show some HVF-like components, while model # 57 shows only a PVF-like component. Model # 81 has a stochastic second

component, which is more likely to be an artifact of fitting an equation with more free parameters rather than truly a second feature. Overall, the velocity evolution of model # 57 is more consistent with that observed in SN Ia. The velocity of the feature is governed by a combination of the choice of photosphere velocity as well as the distribution of Ca within either the ejecta or shell and is not affected by the choice of scalar. The similarity of the lower velocity components of models 57 and 80 at 11 d and later after the explosion is due to the similarity in distribution of Ca in velocity space within the ejecta at velocities below 15,000 km s^{-1}. The presence of a photosphere-like component for model # 80 prior to 11 d is due to the photosphere in that model lying at a sufficiently low velocity that Ca in the ejecta can have a substantial contribution, unlike model # 57, in which the velocity of the photosphere lies above most of the Ca in the ejecta until about 8 d after the explosion. Once the photosphere is interior to the bulk of the Ca for either the ejecta or shell components, the velocity of those components are affected only by the distribution of Ca in velocity space; i.e. the $\mathcal{G}_{k,j}$ profile.

If the shell were clumpy, it would allow some light from the ejecta to leak through at early epochs, when the clumps are optically thick. In this event, a second, lower velocity component would be visible due to absorption within the ejecta. This may explain the identification of PVF at early epochs in observed SN Ia.

The difference between the pEW measurement methods shown in Figures 3.8a and 3.8b is notable: the method which uses the P Cygni peak as the continuum falsely suggests that the feature is growing in strength in the first few days for explosion model `c`, whereas the method in which the actual continuum is used reveals that the total pEW is decreasing monotonically with a knee as the photosphere recedes into the ejecta. The absorption method is not possible with actual spectra as the true continuum is not known, thus we do not compare it to data in Figure 3.8b and subsequent similar figures. The P Cygni method will overemphasize the strength of any particular feature; we urge caution in making use of this method in identifying multiple components of any particular feature or the depth of those components. We will discuss this concern further in §3.5.4.

The evolution of the pEW computed using the P Cygni method in these models does not precisely match the evolution of observed SN Ia. In the first few days after the explosions, the pEW in these models are between 50 Å and 200 Å less than the observed values. The maximum observed pEW of the CaNIR feature is 472 Å for

SN 2011fe at 17 d before Bmax (Silverman et al., 2015), the earliest available SN Ia spectrum to date. If the photosphere is below the contact discontinuity, a value of the scalar factor for the shell of $10^{3.5}$ results in a pEW of about 470 Å. For each 0.5 dex decrease in the scalar factor below $10^{3.5}$, the pEW decreases by about 100 Å. If the photosphere is at higher velocity than the contact discontinuity in the first days after the explosion, then increasing the scalar factor results in an increase in the pEW of about 50 Å for each 0.5 dex, thus requiring a substantially larger scalar factor (i.e. $S^{\mathrm{S}}_{Ca\ \mathrm{II},1} = 10^6$ at 1 d) to achieve the maximum value for SN 2011fe. A possibility that may mitigate the need for either a slower photosphere or a larger Ca optical depth is that the pEW measured in observed SN Ia is artificially enhanced because of the choice of continuum; we discuss this further in §3.5.4. In the period between 7 d and 20 d after the explosion, the model feature seems deeper than observed in typical SN Ia. The depth of the CaNIR feature during this epoch is largely determined by the choice of the scalar factor for the ejecta ($S^{\mathrm{E}}_{Ca\ \mathrm{II},1}$), though there is still some contribution from the shell. Choice of a slightly smaller $S^{\mathrm{E}}_{Ca\ \mathrm{II},1}$ parameter or a more rapid drop in the $S^{\mathrm{S}}_{Ca\ \mathrm{II}}$ parameter with time would improve the fit of the pEW evolution to the observed trend.

For the selected values of $S^{\mathrm{E}}_{Ca\ \mathrm{II},1}$ and $S^{\mathrm{S}}_{Ca\ \mathrm{II},1}$, explosion model c is most consistent with the observed trend in pEW and velocity evolution of SN Ia and is therefore used in all other models in this work.

3.5.2.2 Equation of State

The two EOS available in FLASH and used in these simulations do not fully reflect the conditions within the shell during and after interaction, nor in the ejecta at any time. The Gamma-law EOS assumes $T \propto E_i$, and $P \propto \rho E_i$, where T is the fluid temperature, E_i is the internal energy per unit mass and P is the fluid pressure. The Helmholtz EOS includes the effects of radiation and electrons, but assumes complete ionization. The gamma-law EOS tends to produce higher pressures and temperatures for a given density and energy state than does the Helmholtz EOS. As such, we consider these two EOS to bracket the true pressure and temperature conditions within the material. Figure 3.11 shows aspects of the evolution of the CaNIR feature for shell interaction models that have identical parameters other than choice of EOS (model #s 57 and 64). Figure 3.9 shows that the evolution of the shape of the feature

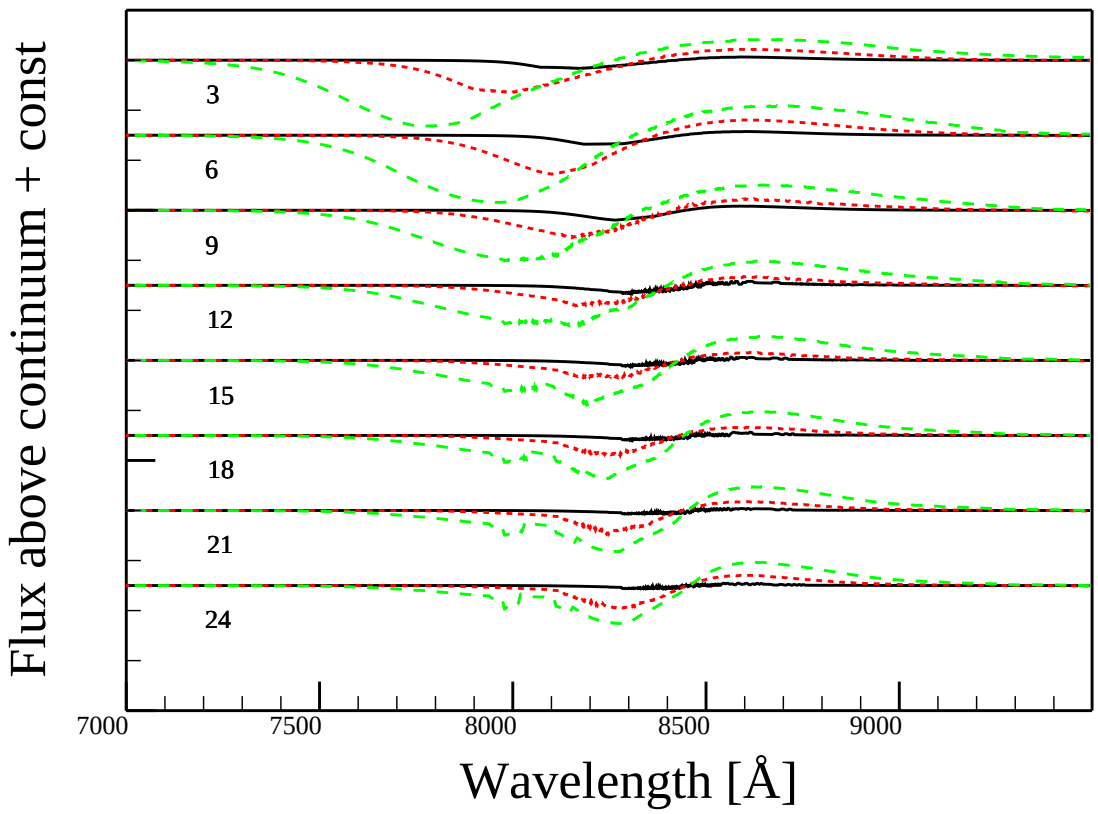

Figure 3.6: Evolution of shape of the CaNIR feature, demonstrating the difference between Gamezo et al. (2005) explosion models interacting with a shell with mass 0.005 $M_{\odot}$. Plots show case `a` (model # 81, black, solid), `b` (model # 80, red, short dash), and `c` (model # 57, green, long dash). Labels on the left indicate the number of days after the explosion.

is similar, though not identical, for these two EOS. The substructure visible in the spectrum between about 7950 Å and 8150 Å on day 12 and later is due to the density enhancement that occurs at the inner edge of the shell material as well as the reverse shock that is moving into the ejecta.

The velocity evolution shown in Figure 3.10 reveals that model # 64 (Helmholtz EOS) produces a higher apparent velocity by less than 5000 km s^{-1} compared to model # 57 (gamma-law EOS) prior to day 12. This is the result of the lower pressure in the Helmholtz EOS simulation producing lower velocities and more compact and higher density material. This difference is substantially smaller than the scatter

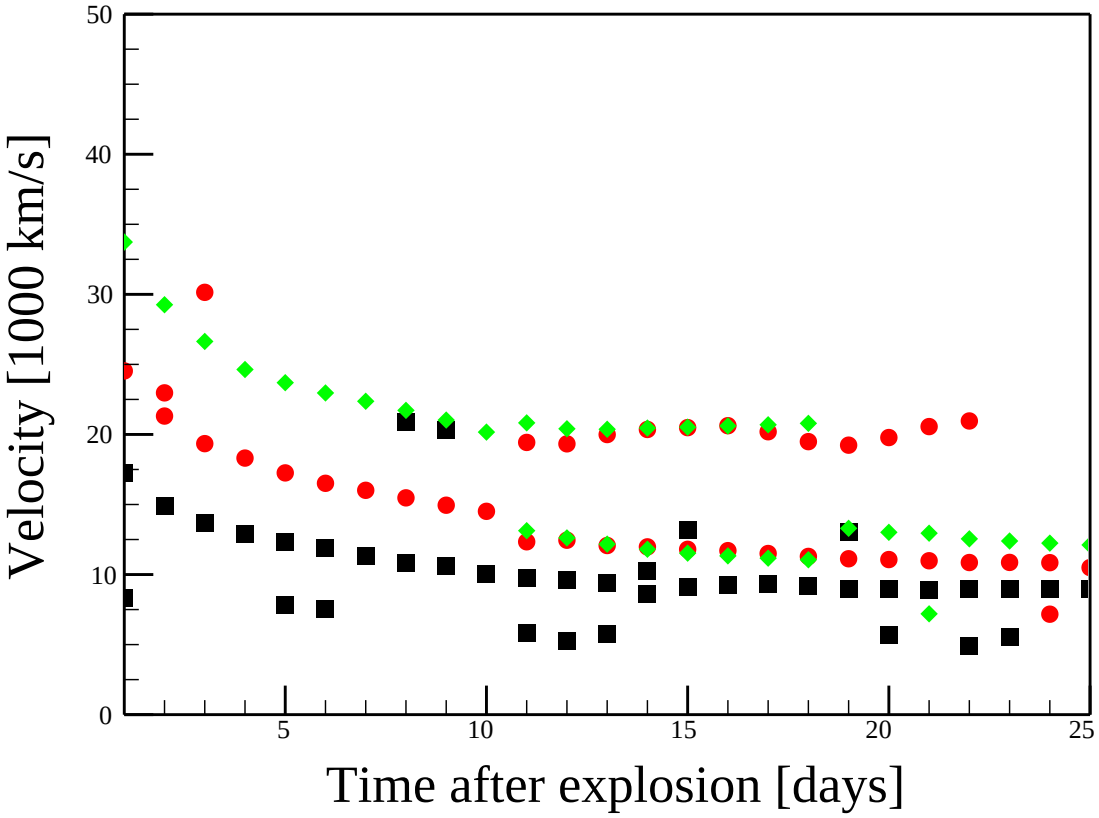

Figure 3.7: Evolution of velocity of the CaNIR feature, demonstrating the difference between Gamezo et al. (2005) explosion models interacting with a shell with mass 0.005 $M_{\odot}$. Plots show case `a` (model # 81, black, squares), `b` (model # 80, red, circles), and `c` (model # 57, green, diamonds). Model # 57 is most representative of the velocity evolution of observed SN Ia.

in HVF or PVF velocities between different SN Ia. Model # 64 shows a smooth transition between the high velocity dominated epoch (day 12 and earlier) to the low velocity dominated epoch (day 18 and later), unlike model # 57 that shows HVF and PVF that are similar to those observed in SN Ia. This is due to the CaNIR feature being slightly more flat blueward of the minimum of the feature in model # 80 than in model # 57, and thus reducing the need for a second Gaussian set to fit the feature.

Figures 3.11a and 3.11b show the evolution of the pEW of the feature using the two different methods of measurement. The differences between the two EOS are minor

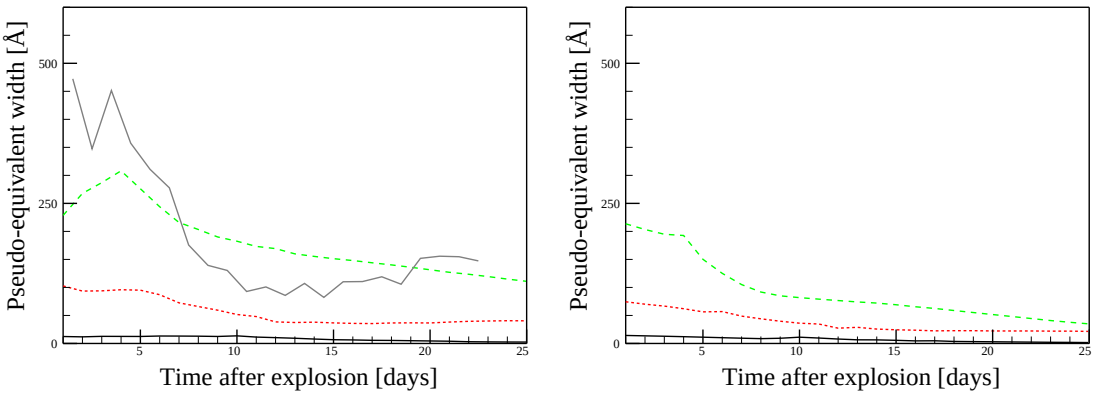

(a) pEW (P Cygni Method)

(b) pEW (Absorption Method)

Figure 3.8: Evolution of pEW of the CaNIR feature, using the P Cygni (3.8a) and absorption measurement (3.8b) methods (see §3.5), demonstrating the difference between Gamezo et al. (2005) explosion models interacting with a shell with mass 0.005 $M_\odot$. Plots show case `a` (model # 81, black, solid), `b` (model # 80, red, short dash), and `c` (model # 57, green, long dash). The solid, gray line in Figure 3.8a shows the observed trend in pEW of SN Ia measured by the P Cygni method from Silverman et al. (2015); see §3.5 and Figure 3.2 for details. Equivalent observational data are not available for the absorption method. The deviation between the observed and synthetically generated pEW at early times in Figure 3.8a is due to choice of scalar $S^{\rm S}_{Ca\ II,1}$, and at intermediate times by the time dependence of $S^{\rm S}_{Ca\ II}$ and the choice of $S^{\rm E}_{Ca\ II,1}$. Model # 57 is most representative of the pEW evolution of observed SN Ia.

for these cases: the simulation using Helmholtz EOS results in a larger pEW than does the simulation using the gamma-law EOS, by less than 50 Å. This difference is also less than the scatter between the pEW of observed SN Ia.

3.5.3 Shell parameters

In previous subsections we have reviewed how simulation parameters, rather than parameters of the shell model, affect the spectral feature. Here we consider the parameters specific to the shell: the density profile, size prior to interaction, and mass.

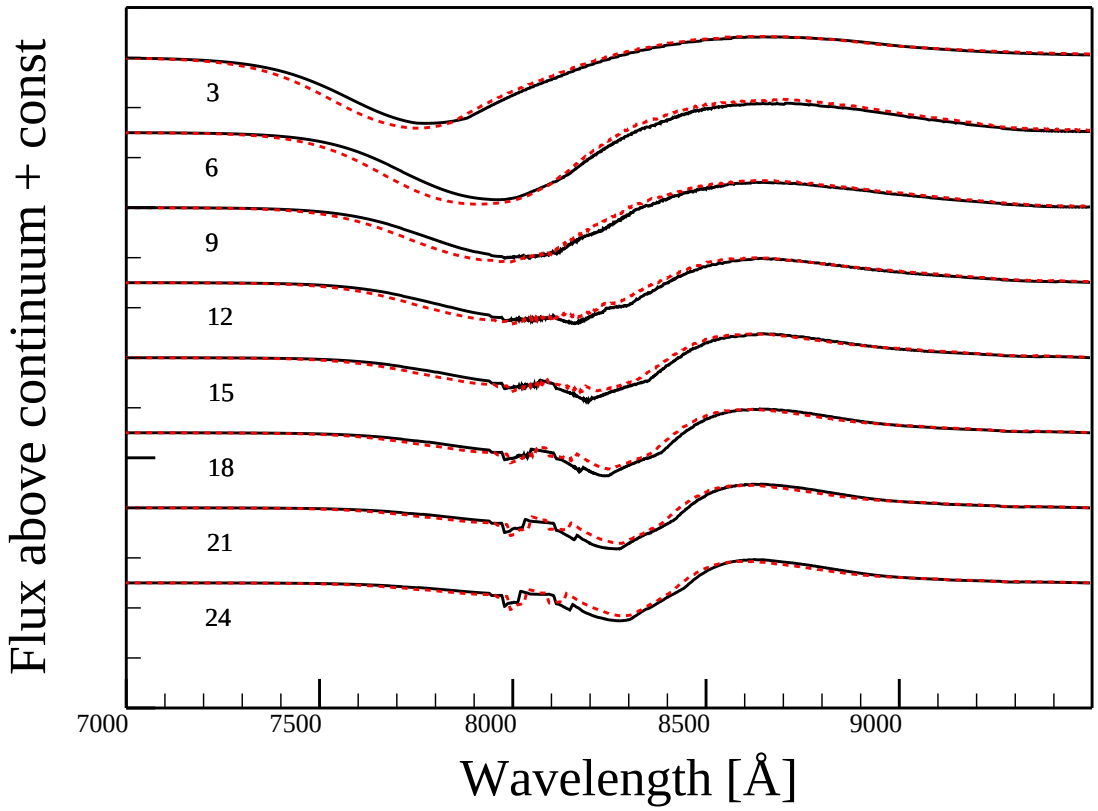

Figure 3.9: Evolution of shape of the CaNIR feature, demonstrating the difference between the use of the gamma-law and Helmholtz EOS in the simulations for a shell with mass 0.005 $M_{\odot}$. Plots show the gamma-law EOS (model # 57, black, solid) and Helmholtz EOS (model # 64, red, dashed). The CaNIR feature is stronger when using the Helmholtz EOS due to higher densities. Labels on the left indicate the number of days after the explosion.

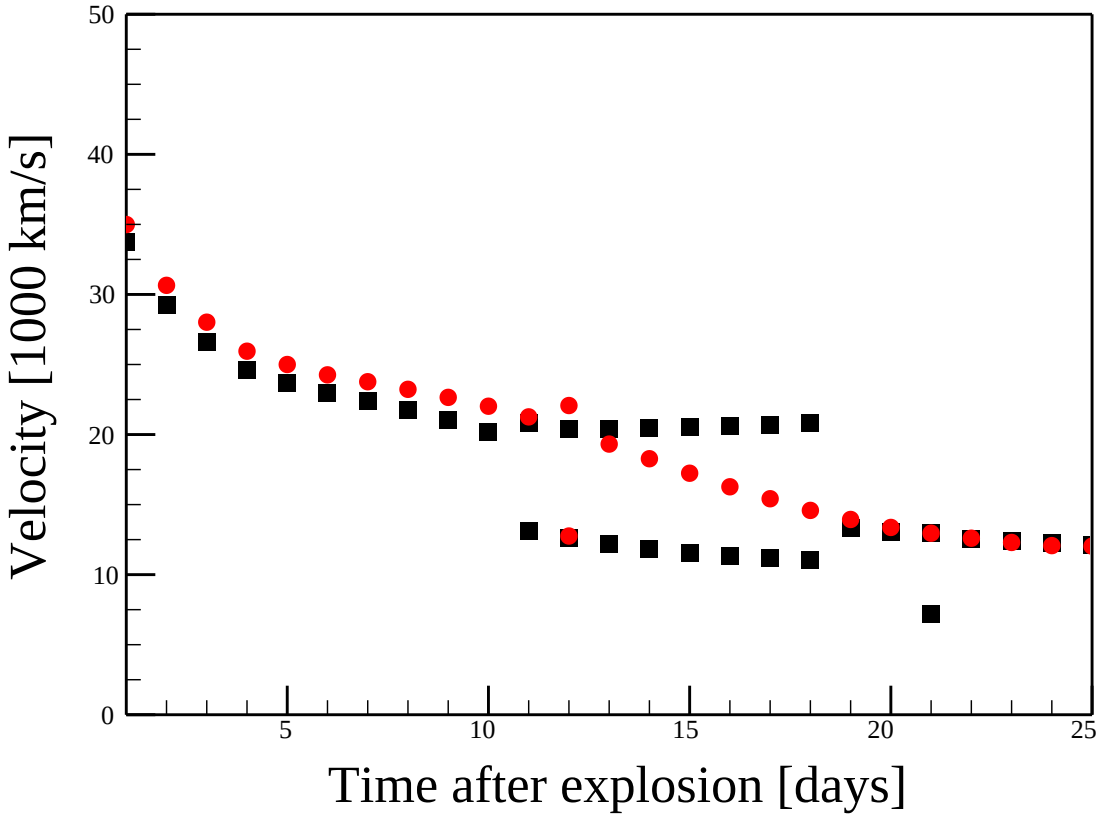

Figure 3.10: Evolution of velocity of the CaNIR feature, demonstrating the difference between the use of the gamma-law and Helmholtz EOS in the simulations for a shell with mass 0.005 $M_{\odot}$. Plots show the gamma-law EOS (model # 57, black, squares) and Helmholtz EOS (model # 64, red, circles). The CaNIR feature is stronger when using the Helmholtz EOS due to higher densities. The differences between the velocities of these models are within the range of scatter of observed SN Ia.

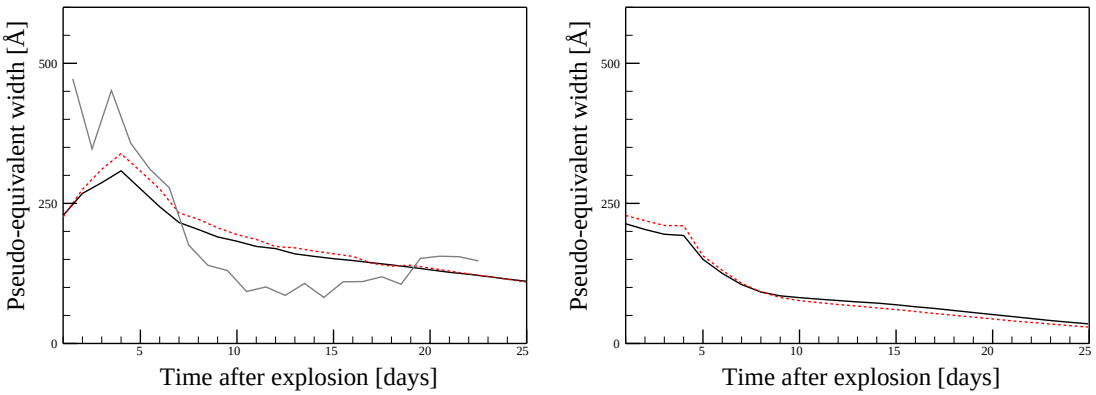

(a) P Cygni Method

(b) Absorption Method

Figure 3.11: Evolution of pEW of the CaNIR feature, using the P Cygni (3.11a) and absorption measurement (3.11b) methods (see §3.5), demonstrating the difference between the use of the gamma-law and Helmholtz EOS in the simulations for a shell with mass 0.005 $M_\odot$. Plots show the gamma-law EOS (model # 57, black, solid) and Helmholtz EOS (model # 64, red, dashed). The CaNIR feature is stronger when using the Helmholtz EOS due to higher densities. The solid, gray line in Figure 3.11a shows the observed trend in pEW of SN Ia measured by the P Cygni method from Silverman et al. (2015); see §3.5 and Figure 3.2 for details. Equivalent observational data are not available for the absorption method. The deviation between the observed range and synthetically generated pEW in Figure 3.11a may be due to the choice of or time dependance of scalars $S^{\mathrm{S}}_{Ca\ \mathrm{II},1}$ and $S^{\mathrm{E}}_{Ca\ \mathrm{II},1}$, or artificial enhancement of the feature in observed SN Ia (see §3.5.4). The differences between the pEW of these models are within the range of scatter of observed SN Ia.

3.5.3.1 Density profile of the shell

A comparison of line profiles for various initial density profiles of the shell is shown in Figure 3.12a for shell models with a mass of 0.005 $M_\odot$ and an outer radius of 0.3 $R_\odot$. Most differences occur in the first several days; Figure 3.12b shows the evolution in more detail over the first six days after the explosion. Model # 55 (Gaussian density profile) and model # 57 (reverse-sawtooth profile) tend to result in a similar shape of the feature. Model # 54 (top-hat profile) and model # 56 (sawtooth profile) tend to produce a flat bottom in the absorption feature in the first week after the explosion. The distinctive shape of the spectra generated from these latter two models is a result of a knee in $\mathcal{G}_{k,j}$. This knee is caused by the sharp discontinuity in the density profile prior to interaction at the outermost edge of the shell. The shape of the feature for

model #s 55 and 57 tend to be more consistent with the observed shape in SN Ia, however very few SN Ia spectra are available earlier than Bmax - 13 d that would allow probing these differences.

The pEW evolution is shown in Figures 3.13a and 3.13b. The largest variation between models in pEW occurs in the first 5 d after the explosion, where there is a difference of up to 100 Å. Once the feature is dominated by the absorption in the ejecta (after 10 d) the pEW and velocity evolution are effectively identical in all four models.

The velocity evolution is shown in Figure 3.14. Model # 56 results in a very distinctive velocity evolution that is initially rising over the first several days and a HVF near 27,000 km s^{-1} until about the time of Bmax. Such evolution has never been observed in any SN Ia, and thus suggests that the sawtooth profile with the sharp edge outward can be excluded from further consideration. Model # 54 shows a HVF that is slightly faster than observed SN Ia in the first week as well as near Bmax. Model #s 55 and 57 have a similar evolution though the HVF in model # 55 tends to persist longer than that of model # 57. Both have a velocity evolution that is generally consistent with observed SN Ia. For the remainder of this work, we use the reverse-sawtooth density profile as it is slightly more consistent with observations.

3.5.3.2 Outer radius of the shell

Figure 3.15 shows the effect of the initial outer radius of the shell on the resulting CaNIR feature. We consider shells with outer radius 0.04 $R_\odot$ (model # 70), 0.08 $R_\odot$ (model # 71), 0.12 $R_\odot$ (model # 72), 0.297 $R_\odot$ (model# 57), 0.5 $R_\odot$ (model # 73), and 1 $R_\odot$ (model # 74). The greatest variation occurs at early times (less than five days after the explosion), though some variation does persist though Bmax.

Figure 3.16 shows the evolution of the velocity of the feature for these models. The velocity differs by less than 2,000 km s^{-1} between most models at all times, with the exception being model # 57. Model # 57 tends to be slightly more smooth between 7800 Å and 8200 Å than the other models, which may explain the differing results in the Gaussian set fits. Only model # 57 consistently shows evidence of distinct PVF and HVF between 10 d and 18 d after the explosion, however this may be a failure of the fitting routine when attempting to fit the substructure near 8000 Å in model #s 70-74 rather than a true lack of a second component in these models.

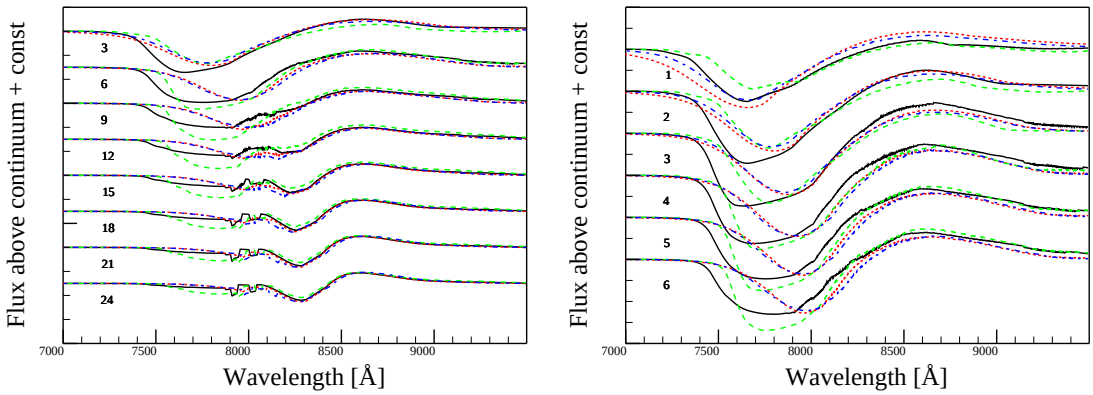

(a) Synthetic spectra

(b) Synthetic spectra, day 1-6

Figure 3.12: Evolution of the shape of the CaNIR feature, demonstrating the effect of the initial density profile of the shell for shells with mass 0.005 $M_\odot$. Plots show the 'top-hat' profile (model # 54, black, solid), 'Gaussian' profile (model # 55, red, short dash), 'sawtooth' profile with high density at the outer radius (model # 56, green, long dash), 'sawtooth' profile with high density at inner radius (model # 57, blue, long dash-short dash). The labels on the left of each figure indicate the number of days after the explosion.

The evolution of the pEW for these models is shown in figures 3.17a and 3.17b. The biggest difference between these models occurs in the first 5 to 10 days after the explosion. The variation is at most about 50 Å, which is within the typical range of scatter in pEW between SN Ia.

Because model # 57 tends to better produce distinct PVF and HVF, we adopt a shell radius of 0.297 $R_\odot$ for the remainder of this study.

3.5.3.3 Mass of the shell

Figure 3.18a shows the variation in the CaNIR feature for shells with mass 0.003 $M_\odot$ (model #61), 0.005 $M_\odot$ (model #57), 0.008 $M_\odot$ (model #41), 0.010 $M_\odot$ (model # 49), 0.012 $M_\odot$ (model # 45), and 0.020 $M_\odot$ (model # 53), each with outer radius 0.297 $R_\odot$ and using the reverse-sawtooth density profile. The effect of the mass of the shell tends to be significantly larger than any other parameter thus far considered. The overall shape of the feature is not affected by mass, though the location of the substructure due to the contact discontinuity and reverse shock is at longer wavelengths for higher mass shells, visible in Figure 3.18b. The substructure is also weaker for shells with

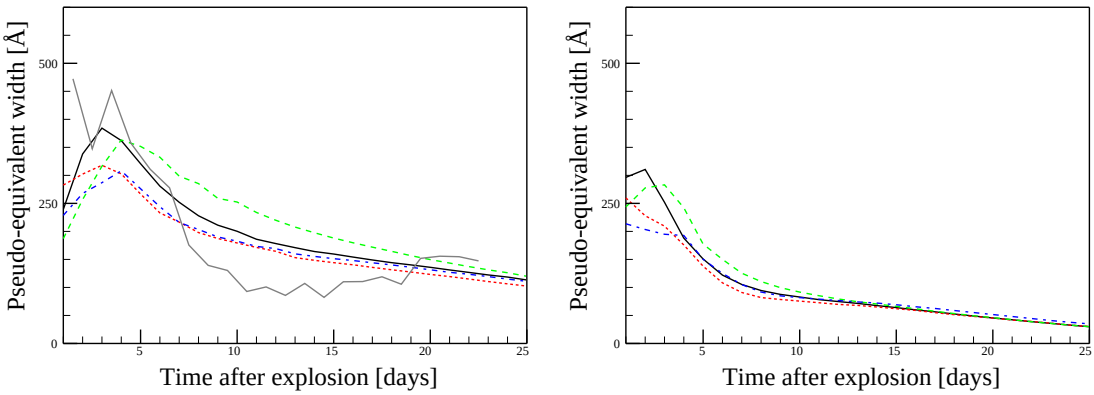

(a) pEW (P Cygni Method) (b) pEW (Absorbtion Method)

Figure 3.13: Evolution of pEW of the CaNIR feature, using the P Cygni (3.13a) and absorption measurement (3.13b) methods (see §3.5), demonstrating the effect of the initial density profile of the shell for shells with mass 0.005 $M_\odot$. Plots show the 'top-hat' profile (model # 54, black, solid), 'Gaussian' profile (model # 55, red, short dash), 'sawtooth' profile with high density at the outer radius (model # 56, green, long dash), 'sawtooth' profile with high density at inner radius (model # 57, blue, long dash-short dash). The solid, gray line in Figure 3.13a shows the observed trend in pEW of SN Ia measured by the P Cygni method from Silverman et al. (2015); see §3.5 and Figure 3.2 for details. Equivalent observational data are not available for the absorption method. The deviation between the observed range and synthetically generated pEW in Figure 3.13a may be due to the choice of or time dependance of scalars $S^{\rm S}_{Ca\ II,1}$ and $S^{\rm E}_{Ca\ II,1}$, or artificial enhancement of the feature in observed SN Ia (see §3.5.4).

higher mass for the specific choice of $S^{\rm S}_{Ca\ II,1}$.

The differences between models are most distinct in the evolution of the pEW, shown in Figures 3.19a (P Cygni method) and 3.19b (absorption pEW method). Shells with lower mass result in a stronger feature at an earlier time. Higher-mass models have a longer delay before the photosphere recedes below the contact discontinuity where the shell material is most dense and creates the strongest HVF. This reduces the pEW of the feature at earlier times. As noted in §3.5.2.2, a value of $S^{\rm S}_{Ca\ II,1} = 10^{3.5}$ is sufficient to explain the maximum observed pEW of SN 2011fe at 17 d before Bmax for model # 57 when the photosphere is below the contact discontinuity; this is also true for model # 61. Models having shells with mass larger than 0.005 $M_\odot$ require a larger value of the scalar to achieve the same pEW, increasing by

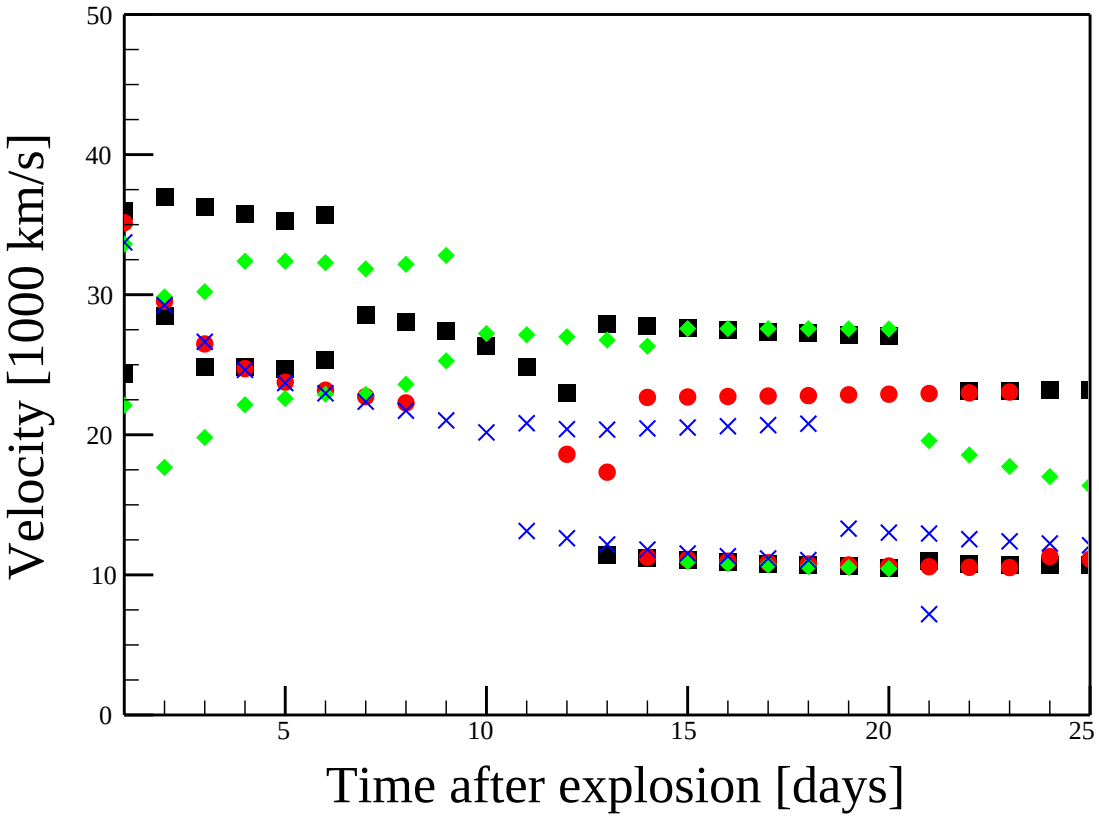

Figure 3.14: Evolution of the velocity of the CaNIR feature, demonstrating the effect of the initial density profile of the shell for shells with mass 0.005 $M_{\odot}$. Plots show the 'top-hat' profile (model # 54, black, squares), 'Gaussian' profile (model # 55, red, circles), 'sawtooth' profile with high density at the outer radius (model # 56, green, diamonds), 'sawtooth' profile with high density at inner radius (model # 57, blue, 'X's). The velocity evolution of model # 56 is inconsistent with observed SN Ia.

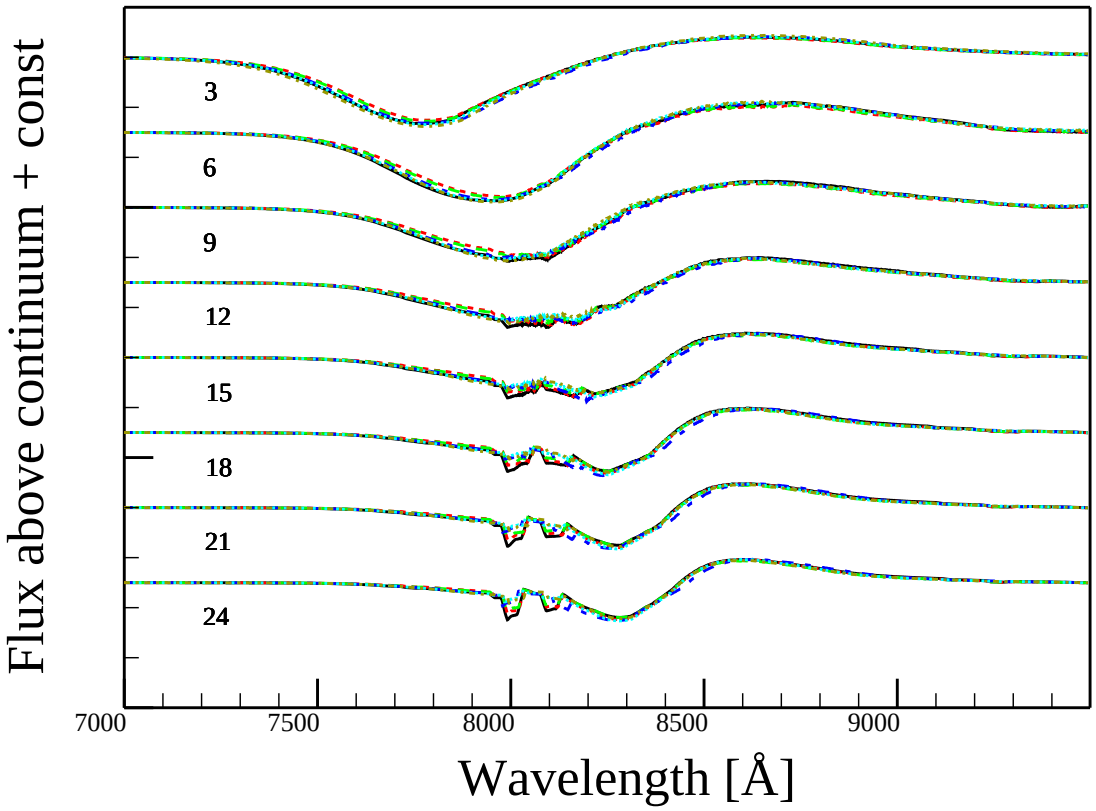

Figure 3.15: Evolution of shape of the CaNIR feature in shape, demonstrating the effect of the width of the shell, for a shell with mass 0.005 $M_\odot$. Plots show shells with outer radius 0.04 $R_\odot$ (model # 70, black, solid), 0.08 $R_\odot$ (model # 71, red, short dash), 0.12 $R_\odot$ (model # 72, green, long dash), 0.297 $R_\odot$ (model # 57, blue, long dash-short dash), 0.5 $R_\odot$ (model # 73, cyan, dotted), and 1 $R_\odot$ (model # 74, dark yellow, short dash-dot). Labels on the left indicate the number of days after the explosion.

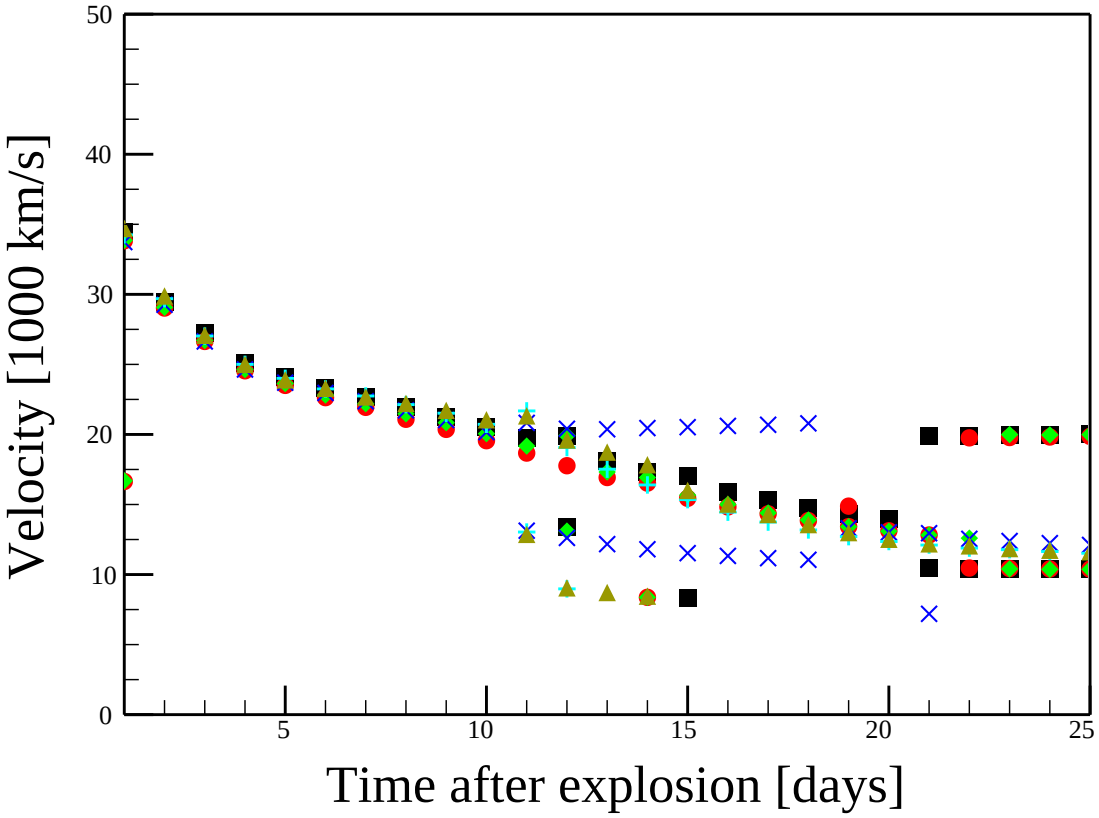

Figure 3.16: Evolution of velocity of the CaNIR feature demonstrating the effect of the width of the shell, for a shell with mass 0.005 $M_\odot$. Plots show shells with outer radius 0.04 $R_\odot$ (model # 70, black, squares), 0.08 $R_\odot$ (model # 71, red, circles), 0.12 $R_\odot$ (model # 72, green, diamonds), 0.297 $R_\odot$ (model # 57, blue, 'X's), 0.5 $R_\odot$ (model # 73, cyan, '+'s), and 1 $R_\odot$ (model # 74, dark yellow, triangles).

about 0.25 dex per 0.0025 $M_\odot$ increase in the mass of the shell.

We can individually measure the pEW of the shell and ejecta components by generating spectra with one of the components 'turned off' via setting the peak optical depth of the component to a very small value (e.g. $S^E_{Ca\ II,1} = 10^{-20}$ to generate a spectrum incorporating absorption from only the shell material), then measuring the pEW using one of the above methods. By doing so we can identify the time of transition from a shell-dominated feature to an ejecta-dominated feature. We show the time of transition from shell-dominated to ejecta-dominated absorption in Table 3.3. The uncertainties listed in the table reflect the change in the time of transition

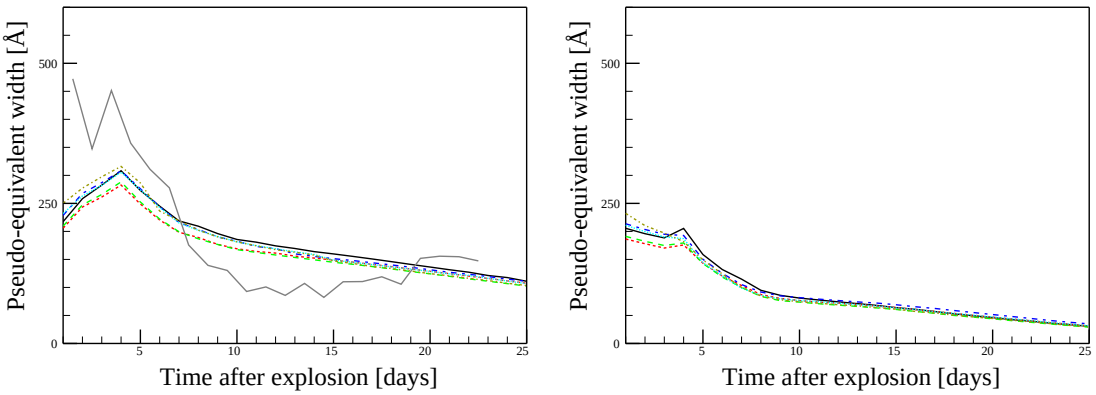

(a) pEW (P Cygni Method)

(b) pEW (Absorption Method)

Figure 3.17: Evolution of pEW of the CaNIR feature, using the P Cygni (3.17a) and aborption measurement (3.17b) methods (see §3.5), demonstrating the effect of the width of the shell, for a shell with mass 0.005 $M_\odot$. Plots show shells with outer radius 0.04 $R_\odot$ (model # 70, black, solid), 0.08 $R_\odot$ (model # 71, red, short dash), 0.12 $R_\odot$ (model # 72, green, long dash), 0.297 $R_\odot$ (model # 57, blue, long dash-short dash), 0.5 $R_\odot$ (model # 73, cyan, dotted), and 1 $R_\odot$ (model # 74, dark yellow, short dash-dot). The solid, gray line in Figure 3.17a shows the observed trend in pEW of SN Ia measured by the P Cygni method from Silverman et al. (2015); see §3.5 and Figure 3.2 for details. Equivalent observational data are not available for the absorption method. The deviation between the observed range and synthetically generated pEW in Figure 3.17a may be due to the choice of or time dependance of scalars $S^{\rm S}_{Ca\ II,1}$ and $S^{\rm E}_{Ca\ II,1}$, or artificial enhancement of the feature in observed SN Ia (see §3.5.4).

for a change of 1 dex in the Sobolev optical depths ($\tau^S_{Ca\ II}$ and $\tau^E_{Ca\ II,1}$). A change in the optical depths of the ejecta and shell have an approximately equal effect on the time of transition. The time of transition is not significantly affected by a steeper variation of the optical depth with time or a shallower variation of the optical depth of the ejecta with time, but will be significantly later (by ∼10 d) if the time dependence of the optical depth of the shell is much shallower (e.g. $\tau_{Ca\ II} \propto t^{-1}$) than that which we have used in this paper ($\propto t^{-2}$). Given that the P Cygni pEW of the synthetic CaNIR feature during the transitional phase is larger than the observed value, the time dependence is more likely to be steeper rather than shallower than we have assumed.

The time of transition occurs at a later epoch for shells of higher mass, suggesting

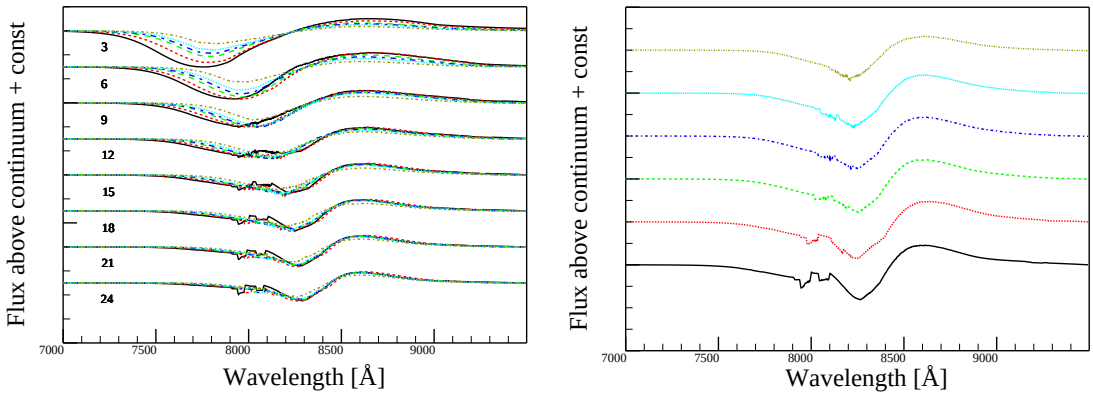

(a) Synthetic Spectra

(b) Synthetic Spectra at 18 d

Figure 3.18: Evolution of CaNIR feature in shape demonstrating the effect of the mass of the shell. Plots show shells with mass 0.003 $M_\odot$ (model # 61, black, solid), 0.005 $M_\odot$ (model # 57, red, short dash), 0.008 $M_\odot$ (model # 41, green, long dash), 0.01 $M_\odot$ (model # 49, blue, long dash-short dash), 0.012 $M_\odot$ (model # 45, cyan, dotted), 0.02 $M_\odot$ (model # 53, dark yellow, short dash-dot). Labels on the left of Figure 3.18a indicate the number of days after the explosion. The feature is deeper and has a bluer minimum for lower mass shells. Figure 3.18b makes visible the redward shift in the substructure (between 7900 Å and 8100 Å for the 0.003 $M_\odot$ shell, and between 8000 Å and 8200 Å for the 0.02 $M_\odot$ shell) due to increasing the mass of the shell. The substructure is a result of the contact discontinuity between the shell and ejecta and the reverse shock in the ejecta.

Table 3.3: Epoch of transition from a feature dominated by absorption in the shell to absorption in the ejecta.

Model #	Mass of Shell ($M_\odot$)	Epoch of Transition (Days after explosion)
61	0.003	8 ± 1
57	0.005	8 ± 1
41	0.008	10 ± 1
49	0.010	10 ± 1
45	0.012	11 ± 1
53	0.020	14 ± 1

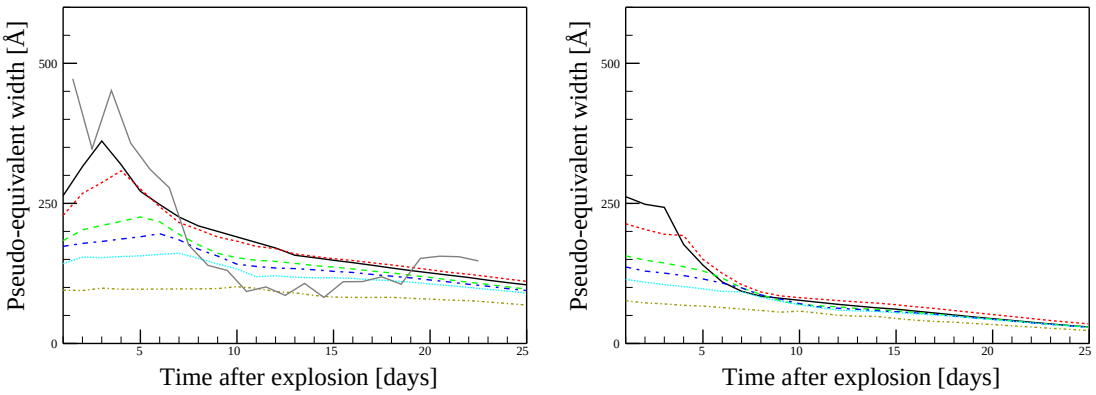

(a) pEW (P Cygni Method)

(b) pEW (Absorption Method)

Figure 3.19: Evolution of CaNIR feature in pseudo-equivalent width (pEW), using the P Cygni (3.19a) and absorption measurement (3.19b) methods (see §3.5), demonstrating the effect of the mass of the shell. Plots show shells with mass 0.003 $M_\odot$ (model # 61, black, solid), 0.005 $M_\odot$ (model # 57, red, short dash), 0.008 $M_\odot$ (model # 41, green, long dash), 0.01 $M_\odot$ (model # 49, blue, long dash-short dash), 0.012 $M_\odot$ (model # 45, cyan, dotted), 0.02 $M_\odot$ (model # 53, dark yellow, short dash-dot). The solid, gray line in Figure 3.19a shows the observed trend in pEW of SN Ia measured by the P Cygni method from Silverman et al. (2015); see §3.5 and Figure 3.2 for details. Equivalent observational data are not available for the absorption method. The mass of the shell strongly affects the pEW as well as the epoch at which the primary source of absorption transitions from the shell to the ejecta.

that the time of transition between stronger HVF to stronger PVF can be an indicator of the mass of the shell. The transition seems to occur between -14 d and -8 d (relative to Bmax) for Wang normal SN Ia (Silverman et al., 2015), suggesting a shell with a mass less than 0.012 ± 0.004 $M_\odot$. The earliest observed time of transition requires shells of mass or order 10^{-3} $M_\odot$, nearly an order of magnitude smaller than the 0.02 $M_\odot$ of Ca suggested in previous studies of Ca II HVF (Wang et al., 2003; Mazzali et al., 2005b; Quimby et al., 2006), though there is a significant amount of scatter in the observed epoch of transition of SN Ia. This scatter may be related to other parameters of the shell or differing masses of the shell for differing supernovae.

Figure 3.20 shows the velocity evolution of each of these models. Only the models with the lowest masses of shell, model #s 61 and 57 (0.003 and 0.005 $M_\odot$, respectively), show distinct HVF and PVF during the intermediate epochs. The shell material is still responsible for between 1/2 and 1/3 of the absorption even at late

times, so the lack of distinct HVF and PVF is more likely a failure of the fitting routine to match a Guassian set to the substructure near 8000 Å rather than a lack of two line generating regions in the other models. There is some difference between the velocities of model #s 57 and 61, though it tends to be less than the observed scatter in velocities of either HVF or PVF components of SN Ia. Model # 61 has an HVF component near Bmax that is slightly faster than observed SN Ia HVF, and thus probably is too low of a mass for the shell. Prior to 12 d after the explosion all models show a feature that is more consistent with the HVF and lack a PVF. A PVF may be found during this phase if there is light from the ejecta leaking through a clumpy shell, or due to an artifact of the pEW fitting method (see §3.5.4 for further discussion).

3.5.4 Discussion and analysis

We have shown the effect of EOS, explosion model, and the width, density profile, and mass of the shell on the resulting spectral evolution of the CaNIR feature. Of these, the mass of the shell has the strongest effect, demonstrating a marked difference in the time of transition between shell-dominated and ejecta-dominated absorption as well as the depth of the feature at early times. The width and initial density profile of the shell have a small effect on the pEW in the first week after the explosion, but are generally indistinguishable by the time of Bmax. Detection and spectra of supernovae in the first days after the explosion can reveal information about the density profile of the high-velocity material prior to interaction. The choice of EOS leads to a nearly identical evolution profile, but the Helmholtz EOS leads to a pEW that is about 50 Å larger than that of the Gamma-law EOS.

We have considered only the Gamezo et al. (2005) explosion models in this work; the choice of explosion model affects the layering and abundance profile of intermediate mass elements in the ejecta; this choice will have a strong effect near the time of and after Bmax, but will have limited impact on the appearance of the CaNIR feature at early times when it is dominated by absorption in the outer, higher-velocity layers, such as the shell presented in this work.

Of the shell models presented here, model # 57 ($0.005\ M_\odot, 0.297\ R_\odot$, and reverse-sawtooth initial density profile) is most consistent with the observed pEW and velocity evolution of an average SN Ia. This model, however, lacks distinct PVF at early times

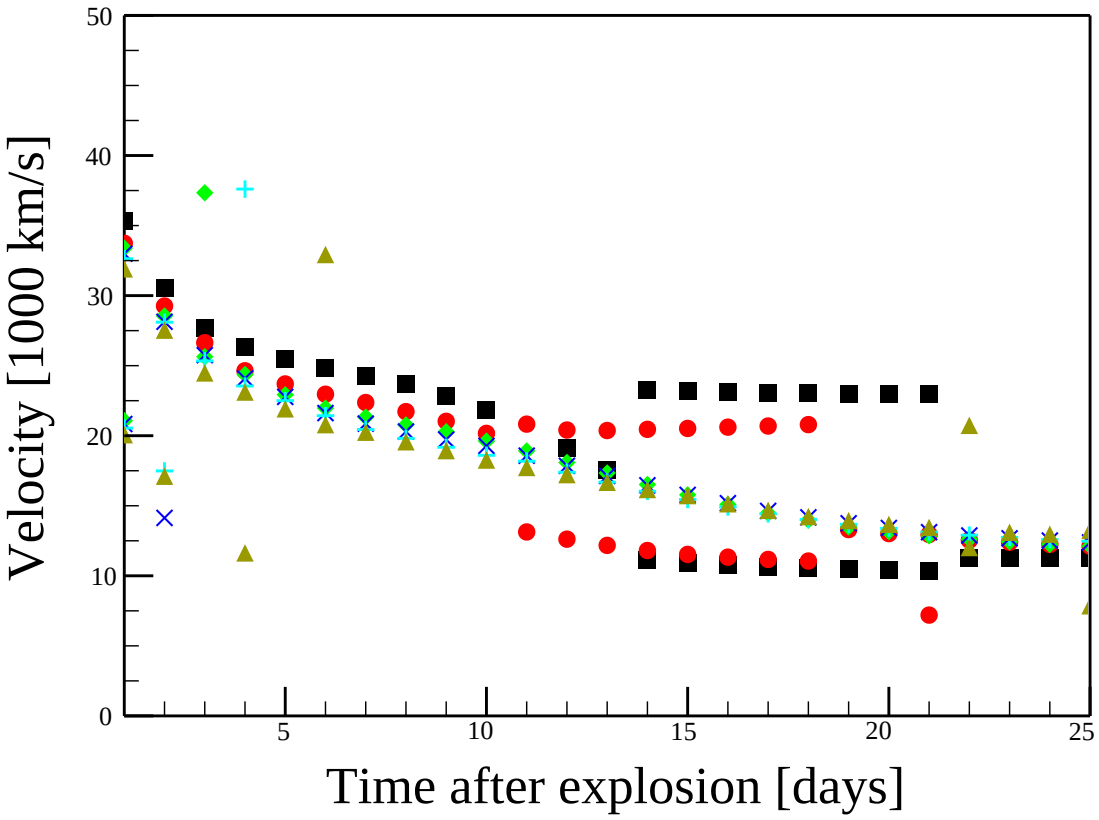

Figure 3.20: Evolution of CaNIR feature in velocity demonstrating the effect of the mass of the shell. Plots show shells with mass 0.003 $M_\odot$ (model # 61, black, squares), 0.005 $M_\odot$ (model # 57, red, circles), 0.008 $M_\odot$ (model # 41, green, diamonds), 0.01 $M_\odot$ (model # 49, blue, 'X's), 0.012 $M_\odot$ (model # 45, cyan, '+'s), 0.02 $M_\odot$ (model # 53, dark yellow, triangles). Only shells of mass 0.003 $M_\odot$ and 0.005 $M_\odot$ show separate PVF and HVF (with a few exceptions that are more likely to be artifacts of fitting). The lack of two features for most models may simply be due to the relative weakness of the substructure caused by the contact discontinuity in the models with higher mass shells for the choice of $S^{S}_{Ca\ II,1}$ (see Figure 3.18b).

(prior to 14 d after the explosion), and lacks distinct HVF at some time after Bmax (more than 21 d after the explosion).

The pEW for model #57 is about 100 Å low in the first 7 d after the explosion, meaning that the value chosen here for $S^{\rm S}_{Ca\ {\rm II},1}$ may be too low during this phase. Between 7 d and 20 d after the explosion, the pEW is too high by between 50 – 100 Å, suggesting that $S^{\rm S}_{Ca\ {\rm II},1}$ may be too large during this phase. In Eq 3.12 and 3.13 we have assumed that S declines as t^{-2} due only to the decreasing density as the material expands. This assumes that effective temperature, clumpiness, and ion state are constant in both the shell and ejecta from the time of explosion through Bmax. The assumption of constant clumpiness is reasonable, but ion state and effective temperature probably change over this period. Assuming that the ion state is more sensitive to radiative or thermal conditions, the rate of change of τ may be steeper than t^{-2} if the Ca is mostly in the Ca II state at early times, or shallower if the Ca tends to be more highly ionized than Ca II (i.e. mostly Ca III or Ca IV) after the interaction. The latter will allow for a larger optical depth in the shell at early times, leading to a much stronger feature. If the ion state and effective temperature are primarily determined by photo-ionization and photoexcitation, then the time dependence of the optical depth will depend on the rate of variation of the temperature of the photosphere. Assuming that the temperature of the photosphere varies slowly, this will result in only a small departure from the t^{-2} behavior.

The choice of continuum may artificially increase the pEW of the HVF or PVF when using the P Cygni method on observed SN Ia. Use of the P Cygni peak as the red side of the continuum may cause the PVF to appear larger than it really is. Our results also suffer from this effect, resulting in the difference between the pEW determined by the P Cygni and absorption measurement methods. The presence of the O I λ 7773 Å feature just blueward of the CaNIR feature can result in use of the P Cygni emission of O I as the apparent continuum, enhancing the apparent pEW of the HVF in observed SN Ia. The epoch at which this occurs will be dependent upon the location of the oxygen in the ejecta: if it is at higher velocity than the Ca II it will have a larger effect at earlier times. If it has a similar velocity to the Ca it will have a larger effect near Bmax. Our synthetic spectra do not include O I, so this effect could explain the discrepancy in the pEW compared to the observations at early epochs when the observations are affected by the presence of O I. This may also explain the need for a PVF at early epochs in observed SN Ia due to an apparent

broadening of the CaNIR feature by the effect of the O I.

The presence of the photosphere in the shell at early times inhibits absorption at the lower velocities of the material in the ejecta. One effect of this is that any absorption by Si must also occur in the shell and therefore the evolution of the pEW and velocity of Si features would be identical to that of the Ca at early times, assuming that Ca and Si in the shell are fully mixed (i.e. there is no abundance gradient for either Si or Ca in the shell). If the shell generally lacks Si, or the Si in the shell is not in the singly ionized state, this will result in a weak or non-existent Si II λ 6355 Å feature at early times, contrary to all observational evidence. A possible resolution to this is a clumpy shell, allowing light from the ejecta to escape. Given that the some HVF are polarized, this is certainly part of the explanation of why photospheric Si II can be observed even if the shell is optically thick.

An additional effect that would allow for Si features with little Si in the shell is a photosphere that lies at a velocity below that of the shell material. A lower velocity photosphere would also have the effect of increasing the strength of the Ca II absorption in the shell at early times. This is because the highest densities and largest Ca II optical depths occur near the contact discontinuity between the shell and ejecta. A lower photospheric velocity might be accomplished by using a self-consistent model for the ion state (and thus the electron scattering optical depth). In order to generate a self-consistent model, however, we would be required to specify a composition for the shell as well as provide a more complete radiative transfer model in the hydrodynamic simulation in order to account for radiative cooling. As this is a first attempt to characterize the composition and evolution of a shell, we leave these more comprehensive methods to future work.

The combination of a higher Ca II ion fraction than we have assumed, a time dependence of the ion state, a photosphere in the ejecta rather than shell, and the presence of the O I P Cygni peak combined can account for the discrepancy between the pEW measured for SN Ia by c.f. Silverman et al. (2015) and those generated using the methods and selected scalar factors in this paper. Fitting the spectra generated by the models presented here to observed CaNIR features of individual SN Ia will provide better indication of the time dependence of the optical depth and the velocity of the photosphere and hence of the nature of the HVF.

3.6 Conclusion

We have discussed a method of generating synthetic spectra from 1-D hydrodynamic simulations of the interaction between a Type Ia supernova and a nearby (less than a solar radius) circumstellar shell using a modified version of SYN++. We have used this method to generate a series of spectra comparing and contrasting the effects of equation of state, choice of explosion model, and width, initial density profile, and mass of the shell on the appearance and evolution of the Ca II near-infrared triplet (CaNIR) in the 25 days after the explosion. Of these parameters, the mass of the shell has the strongest effect, both determining the time of transition from absorption dominated by the material in the shell to being dominated by the material in the ejecta as well as the strength of the CaNIR feature in the first week after the explosion.

The range of masses of shell presented in this work have a time of transition that is consistent with that observed in Type Ia supernovae (SN Ia), between 8 and 14 days after the explosion (-10 to -4 days relative to Bmax, assuming Bmax occurs at 18 d after the explosion) and suggest that the mass of the shell is less than 0.012 ± 0.004 $M_\odot$ for supernovae with CaNIR high velocity features. The shell of mass 0.005 $M_\odot$, radius 0.297 $R_\odot$, and reverse-sawtooth initial density profile is the most consistent of the shells that we have evaluated in terms of the evolution of the velocity and pseudo-equivalent width (pEW) of the CaNIR feature of a sample of SN Ia. Individual supernovae may be fit better by shells having a different mass.

We used two different techniques to measure the pseudo-equivalent width (pEW) of the CaNIR feature: a method similar to that utilized by observers that considers an apparent continuum on the blue side of the feature and the P Cygni peak on the red side to establish the continuum across the feature (the "P Cygni method"), and another that uses the continuum generated by SYN++ (the "absorption pEW method"). Both methods reveal differences in evolution of the feature, but the P Cygni method tends to overestimate the actual pEW by 50 – 150 Å. When employed on observed spectra, the P Cygni method may utilize the P Cygni peak of the O I λ 7773 Å feature as the blue side of the continuum, which will further deepen the reported pEW. This may enhance the apparent strength of high-velocity features reported in the literature for SN Ia.

This study highlights the need for more spectra of Type Ia supernovae in the first several days after the explosion ($\sim$14 days or more prior to B-band maximum).

Further study is warranted in order to place better constraints on the total mass of material based on the pEW at early phases and the time of transition between an HVF-dominated to PVF-dominated feature. In future work we will consider the effect of the time-dependence and scale of the ion fraction and effective temperature of Ca II, as well as how unfiltered light from the ejecta can blend with light from the shell at early times, and whether this information can lead to insights into the composition of the high-velocity material. We will also extend our technique to include other spectral lines and to fit spectra to those observed in specific SN Ia.

Chapter Four: A Compact Circumstellar Shell as the Source of High-velocity Features in SN 2011fe

4.1 Prelude

Significant portions of this chapter have been published previously as Mulligan & Wheeler (2018). In this chapter, we make use of the models developed in the chapter 3 to generate synthetic spectra to match the observed spectral features of a well studied supernova, SN 2011fe. SN 2011fe was first observed within about 1 d after the explosion, and the first spectra were taken a few hours later. It is one of the best studied supernova and is thus a prime choice for investigating the evolution of HVF and aiding in distinguishing models. The development of the methodology for fitting synthetic spectral features to features in an observed supernova, the associated software created to interactively view and generate spectra, the software developed to generate spectra and fit them to observed features within a multi-dimensional parameter space, and writing the article are each work of this author. Discussion and analysis was generally a joint effort between J. Craig Wheeler and this author. All figures in this work were generated using software written by this author.

4.2 Introduction

Type Ia supernovae (SN Ia) represent an extreme end point of binary stellar evolution and a challenge to thermonuclear combustion physics. Their spectral and photometric characteristics are sufficiently uniform to allow them to be used as calibrated candles. Further study of SN Ia is important for a deeper understanding of binary stellar evolution, thermonuclear explosions, and to buttress the use of SN Ia as cosmological probes. A SN Ia progenitor has yet to be detected prior to the explosion, therefore it is necessary to use the information from the explosion itself to understand these systems. Photometry and spectroscopy of the system within the first days and weeks after the explosion are especially important, as the outermost layers have the strongest effect during this phase. SN 2011fe was fortuitously discovered within about a day

after the explosion (Nugent et al., 2011), and is among the nearest to the time of the explosion that a SN Ia has been observed.

In SN Ia observed before peak brightness, absorption features of calcium, silicon, and other elements are observed with two components: a high-velocity component with a velocity between 18,000–35,000 km s^{-1}, referred to as a high-velocity feature (HVF), and a lower-velocity component with a velocity consistently about 7,000 km s^{-1} slower than the HVF (Hatano et al., 1999; Wang et al., 2003; Thomas et al., 2004; Mazzali et al., 2005b; Quimby et al., 2006; Parrent et al., 2012; Marion et al., 2013; Childress et al., 2013a, 2014; Maguire et al., 2014; Silverman et al., 2015; Zhao et al., 2015, 2016). The lower-velocity component, typically referred to as the photospheric-velocity feature (PVF) is the strongest component at and after peak brightness. Both components slow over time, with the HVF reaching an asymptote of 17–23,000 km s^{-1} and the PVF reaching 8–15,000 km s^{-1} at about the time of peak brightness. The HVF is strongest, in terms of the pseudo-equivalent width (pEW), at the earliest epochs, fading away entirely by about one week after peak brightness. The PVF remains relatively constant in strength over all epochs over which the HVF is visible (Childress et al., 2014; Silverman et al., 2015).

The PVF is associated with either unburned carbon and oxygen or material that is synthesized during the explosion, and is reasonably well explained by existing explosion models. The HVF is distinct from the PVF and is a result of material that is physically separate from the material that causes the PVF. The HVF also exhibit a polarization of 0.1 – 1 per cent (Wang et al., 2003; Wang & Wheeler, 2008; Patat et al., 2009), implying that the material causing the HVF is clumpy or otherwise assymetric. The composition, structure, and source of the material that causes the HVF is unclear. Any model that explains these features must explain the polarization and the temporal evolution of the appearance of both the HVF and PVF. Explanatory models fall into three broad categories: material that is part of the 'normal' ejecta but has stronger absorption features due to enhanced populations of the ion- and atomic- state(s) responsible for the feature, material ejected at high velocity during the explosion, and material swept up by the ejecta after the explosion.

The first category, enhanced populations at high velocity, relies on a solar or near-solar abundance of metals in the outer layers that are not in local thermodynamic equilibrium. In this category of models there must be an enhancement of the population of the species responsible for the HVF compared to similarly enriched material at

slightly lower velocities. The evolution in velocity of the HVF in these models is due to the evolution in position of the population enhancement. The underlying cause of this shift is entirely dependent on the details of the physics of the excitation and ionization of the material. One challenge of this class of models is that there is no natural explanation for the population enhancements to be clumpy, thereby failing to explain the polarization of the HVF.

One set of delayed-detonation explosion models evaluated by Blondin et al. (2013) show that the models with the lowest density at the time of transition from deflagration to detonation will have a high-velocity Ca II near-infrared triplet (CaNIR) feature, though they predict a stronger than observed HVF component. These models were evaluated only near the time of bolometric maximum, so the temporal evolution and appearance at early epochs of the CaNIR feature for these models is not yet known.

The second category includes bullets of material that are ejected at high velocity during the detonation of the carbon and oxygen in the progenitor white dwarf. Such bullets could contain enhanced quantities of newly synthesized calcium, silicon, or other elements and can potentially explain the polarization of the HVF. This model would result in HVF at an early epoch that likely fade over time as the material expands. Testing this category of models requires hydrodynamic simulations of the explosion with sufficient resolution to capture any material ejected in this way. This category of models has not yet been evaluated.

The final set of models include interaction with a wind or an essentially static circumstellar medium. These models explain the HVF as the result of the density enhancement at the contact discontinuity, the clumpiness by Rayleigh-Taylor instability at the contact discontinuity, and velocity evolution by the slowing of the contact discontinuity as more material is swept up, the changing density of the material at the contact discontinuity as it expands, and evolving ion- and atomic- state populations in the material.

Gerardy et al. (2004) considered a simulation of the interaction between the ejecta and a wind, demonstrating that models with a total mass of swept up material of about 2–5 $\times$ 10^{-2} $M_{\odot}$ do show evidence of high-velocity features near the time of maximum light. The temporal evolution of the velocity and strength of the HVF in these models has not been evaluated. Models such as this involving an ongoing interaction with a wind or extended shell are now disfavored due to predicted radio

emission (Harris et al., 2016) during the interaction that has not been observed in SN 2011fe(Chomiuk et al., 2012).

Interaction with a radially compact shell allows for high-velocity material that does not produce excess radiation for more than an hour or two after the explosion. To detect the radiation produced by such an interaction would require very early observation of the supernova. Bloom et al. (2012) place constraints on the g-band flux of SN 2011fe at 3.92 h after the explosion, with the time of explosion extrapolated from the rising light curve. This constraint could be relaxed by a few days if there is a 'dark time' that occurs after the explosion (Piro & Nakar, 2013). A shell that is sufficiently compact could interact and cool sufficiently that it is not detectable even within the first few hours after the explosion. There are generally two possible sources for such a shell — a shell associated with accretion onto the progenitor white dwarf, or a shell of material ejected by a detonation on the surface of the white dwarf just prior to the explosion of the white dwarf itself (c.f. Shen et al. (2010) and references therein). The latter model will be nearly identical to the former so long as the material ejected in the surface detonation is moving sufficiently slowly that it is quickly overtaken by the outer edges of the ejecta from the final explosion.

In this work we consider compact ($R < \mathrm{R}_{\odot}$) circumstellar shells as a source of the CaNIR HVF in SN 2011fe. SN 2011fe provides one of the earliest detections of a SN Ia with associated spectra available to-date. We seek to evaluate the supernova–shell interaction models of Mulligan & Wheeler (2017) with a focus on the temporal evolution of the velocity, shape, and depth of the HVF. We fit spectra generated from the models to observational data of SN 2011fe from the earliest available epoch through to 9 d after B-band maximum. We seek to determine the plausibility of the supernova-shell interaction model, to identify the mass of this shell in SN 2011fe, and to understand how the opacity of the shell and ejecta evolve in the first weeks after the explosion.

4.3 Methods

4.3.1 Observational data

The observed spectra to which the models are fit were obtained through the Open Supernova Catalog (Guillochon et al., 2017). The sources of the observed spectra for

each epoch are listed in Table 4.1. We performed fits for data that are available in the first 4 days SN 2011fe was visible and include the CaNIR feature. This is the time period when HVF are strongest and PVF are weakest. After the first 4 days we use only data taken with the Hubble Space Telescope (HST) as these spectra have high signal-to-noise, there is no concern of telluric features and the data have a much larger wavelength range (< 3000 – >10000 Å) than any ground-based spectra. The latter is especially important for flux scaling, described below, and determination of the photospheric temperature. We refer to the observed specific flux from any given spectral data set as $F_\lambda^{\rm obs}$. Because the relative strength of the HVF is dependent upon the time elapsed since the explosion, we hereafter refer to time as that relative to the explosion, taken to be $t_{\rm exp}$ = MJD 55796.696 (Nugent et al., 2011). Before fitting, the spectra are shifted to the rest frame wavelength, then dereddened according to Cardelli et al. (1989) with corrections to the visual range from O'Donnell (1994). We adopt a value of E(B-V) = 0.0077 and a redshift of $z = 0.000804$ (Mazzali et al., 2014).

4.3.2 Supernova-shell interaction models

In Mulligan & Wheeler (2017) we reported the results of hydrodynamic simulations of the interaction bewteen a SN Ia and compact, circumstellar shells. The shells have a range of initial radii between 0.04 $R_\odot$ and 1 $R_\odot$, masses between 0.001 $M_\odot$ and 0.02 $M_\odot$, and different initial density profiles, equations of state, and underlying explosion models. We found that of these parameters, the mass of the shell has the largest effect on the velocity and equivalent width of the CaNIR feature while preserving shapes of the feature that are commensurate with those that are observed. In this work, we use supernova-shell interaction model numbers 17, 41, 45, 49, 57, and 61, representing a supernova without interaction (model 17), and those interacting with shells with mass 0.003 $M_\odot$ (model 61), 0.005 $M_\odot$ (model 57), 0.008 $M_\odot$ (model 41), 0.010 $M_\odot$ (model 49) and 0.012 $M_\odot$ (model 45). Each model has a shell with and initial outer radius of 0.3 $R_\odot$, uses Gamezo et al. (2005) delayed detonation model `c` for the explosion and ejecta with the gamma-law equation of state (excepting model 17, which uses a Helmholtz equation of state), and has a sawtooth density profile with the highest density at the edge closest to the explosion. Hereafter we refer to supernova-shell interaction models by the mass of the shell rather than model number

Table 4.1: Data sources, fit ranges, and flux scaling ranges by date of observation

Observation Date [MJD]	Phase[a] [days]	Time since explosion[b] [days]	Flux Scaling Range [Å]	Fit Range [Å]	SN 2011fe Data Sources
55797.86	-17.04	1.16	3900 – 9200	7680 – 8900	1, 5
55798.3	-16.6	1.6	3400 – 9300	7600 – 8600	1, 5
55799.26	-15.64	2.56	3290 – 9700	8000 – 8800	3, 5
55799.3	-15.6	2.6	3290 – 9700	7790 – 8700	2, 5
55801.17	-13.73	4.47	2700 – 16800	7930 – 8700	4, 5
55804.25	-10.65	7.55	2900 – 16800	7970 – 8750	4, 5
55807.38	-7.52	10.68	1780 – 16800	7930 – 8700	4, 5
55811.37	-3.53	14.67	1780 – 16800	7910 – 8750	4, 5
55814.39	-0.51	17.69	1780 – 16800	7930 – 8700	4, 5
55817.67	2.77	20.97	1700 – 16500	7940 – 8800	4, 5
55823.62	8.72	26.92	1740 – 10210	8000 – 8800	4, 5

[a] Relative to B-band maximum on MJD 55814.90 (Maguire et al., 2012b).
[b] Based on explosion at MJD 55796.696 (Nugent et al., 2011).
1: Nugent et al. (2011)
2: Parrent et al. (2012)
3: Pereira et al. (2013)
4: Mazzali et al. (2014)
5: Guillochon et al. (2017)

for clarity.

The models provide the spatially resolved density and velocity of the supernova and shell material, and, for the ejecta, the abundance of interesting elements (e.g. C, O, Si, etc.). The hydrodynamic data is used to produce a normalized, dimensionless density profile ($\mathcal{G}^c_{v,i}$) for each ion i and component c (i.e. the ejecta, E, and the shell, S) as a function of velocity (v). The profile is described over 2048 velocity bins spanning the range of velocity for all material for each model, and normalized by the spatial maximum of the total gas density (for the shell) or the density of a given element (for the ejecta).

4.3.3 Synthetic Spectra

In generating synthetic spectra, we are interested in only one absorbtion feature (CaNIR), which we presume to be unblended with any other features. In addition,

we do not assume an *a priori* composition of the material within the shell. As such, we use a modified version[1] of SYN++ (Thomas et al., 2011a) that allows for selection of individual ions and an arbitrary profile of optical depth versus velocity.

The optical depth at velocity v for ion i is given by

$$\tau_{v,i} = \sum_c \left(S_i^c \mathcal{G}_{v,i}^c \right), \tag{4.1}$$

where S_i^c is a scalar factor for each ion and component that may contribute to absorption within the supernova. The scalar factors are a proxy for elemental abundance, ion- and excitation-states, and line specific components of the line optical depths. When generating a spectrum with SYN++, the temperature and velocity of the photosphere must also be specified. These set the shape of the blackbody continuum and the minimum velocity in the profile ($\mathcal{G}_{v,i}$) that has an effect on the spectrum.

The spectra generated by SYN++ have a relative flux value between 0 – 1, whereas the observational data may be reported in counts $\sec^{-1}$ or erg $\sec^{-1}$ Å^{-1} cm^{-2}. We therefore scale the relative flux such that the total flux over some range of wavelengths matches the observed flux over the same range for a given observation. The resulting scaled synthetic flux is then

$$F_\lambda^{\text{syn}} = \left(\frac{\sum_\lambda F_\lambda^{\text{obs}}}{\sum_\lambda f_\lambda^{\text{syn}}} \right) f_\lambda^{\text{syn}}, \tag{4.2}$$

where f_λ^{syn} is the relative flux generated by SYN++, and the sums are over the flux scaling ranges listed in Table 4.1.

4.3.4 Fitting

We define the parameter space for fitting with four parameters: temperature and velocity of the photosphere (T_{PS} and v_{PS}) and the log of the scalar factors $S^{\text{E}}_{Ca\ \text{II}}$ and $S^{\text{S}}_{Ca\ \text{II}}$ for the ejecta and shell components, respectively. We collectively describe the parameters as vector $\boldsymbol{x} = [T_{\text{PS}}, v_{\text{PS}}, \log S^{\text{E}}_{Ca\ \text{II}}, \log S^{\text{S}}_{Ca\ \text{II}}]$. A starting point is chosen that has a reasonably good fit by eye, then a grid search and refinement is performed. At each step, the grid consists of a hypercube of 3^4 vertices in parameter space, i.e. 3 values for each parameter. The initial grid has a total range of $\boldsymbol{\Delta x} =$

[1]The modified version of SYN++ is publicly available on `github.com` in repository `astrobit/es`.

[10000 K, 5000 km s^{-1}, 0.4, 0.4]. After generating spectra at each vertex in the grid, we identify the vertex that minimizes the variance,

$$J = \frac{1}{2N} \sum_{\lambda=\lambda_{\rm min}^{\rm Fit}}^{\lambda_{\rm max}^{\rm Fit}} \left(F_\lambda^{\rm obs} - F_\lambda^{\rm syn}(\boldsymbol{x})\right)^2, \tag{4.3}$$

where N is the number of data points in the selected fitting range. The range of wavelengths over which each spectrum is fit are listed in Table 4.1. The fitting ranges include most of the P Cygni emission component on the red side of the feature and the identifiable blue side of the feature (including HVF), excluding regions potentially affected by P Cygni emission of the 7500 Å feature blue-ward of the CaNIR feature. The vertex with the best fit is then chosen as the next starting point and the size of the grid is halved. This process is iterated to a final grid size of $\boldsymbol{\Delta x}$ = [19 K, 10 km s^{-1}, 0.0008, 0.0008]. The use of variance to find the best fitting set of parameters and model does not fully capture the differences in shape of the feature; further, the use of an adaptively-refined grid search can result in an identification of a local, rather that global minima, although for this parameter space we find that the topography seems relatively smooth. We discuss these issues further in Appendix B.

4.4 Results and discussion

The variances of the fits by model and time after the explosion are listed in Table 4.2. No single model clearly has the best quality of fit over all epochs, but the model with no shell performs poorly prior to 8 d, when the feature is dominated by HVF. The fits between models with a shell are generally of similar quality, though the model with a shell of mass 0.005 M$_\odot$ tends to be the best fit at more epochs than any other model.

Table 4.2: Variance of fit by time since explosion and mass of the shell

Time Since Explosion [d]	Units	No Shell	0.003 $M_\odot$	0.005 $M_\odot$	0.008 $M_\odot$	0.010 $M_\odot$	0.012 $M_\odot$
1.16	10^{-33} erg^2 cm^{-4} sec^{-2}	19.42	6.92	7.00	7.04	7.10	7.22
1.60	10^{-3} counts^2 sec^{-2}	136.62	4.03	3.58	7.12	5.55	5.42
2.56	10^{-32} erg^2 cm^{-4} sec^{-2}	12.85	10.85	11.79	10.63	10.44	9.87
2.60	10^{-32} erg^2 cm^{-4} sec^{-2}	102.90	4.33	18.46	3.56	26.24	27.27
4.47	10^{-31} erg^2 cm^{-4} sec^{-2}	4.79	1.04	1.02	1.92	1.23	...
7.55	10^{-31} erg^2 cm^{-4} sec^{-2}	55.92	13.77	3.28	4.16	8.21	11.35
10.68	10^{-30} erg^2 cm^{-4} sec^{-2}	8.48	3.31	3.68	5.02	5.33	5.70
14.67	10^{-30} erg^2 cm^{-4} sec^{-2}	12.07	8.40	6.43	8.32	10.10	11.65
17.69	10^{-30} erg^2 cm^{-4} sec^{-2}	17.04	14.36	7.32	17.93	10.41	17.49
20.97	10^{-30} erg^2 cm^{-4} sec^{-2}	7.14	7.36	8.62	7.86	8.59	13.19
26.92	10^{-30} erg^2 cm^{-4} sec^{-2}	11.20	8.97	9.50	9.82	11.19	13.61

Figure 4.1 shows the velocity of the photosphere for each model as well as the velocity of the photosphere reported in Mazzali et al. (2014), determined using the W7 and WDD1 (Nomoto et al., 1984; Iwamoto et al., 1999) models. The photosphere velocity decreases monotonically for each model from about 4 days after explosion to about maximum light. There is a larger scatter among models in the velocity of the photosphere at early epochs (4 d and earlier). During this period, HVF are relatively strong and the fit is more dependent upon the material in the shell. After 8 d the CaNIR feature is dominated by absorption within the ejecta and thus the velocity of the photosphere is independent of the details of the shell. The photosphere lies within the shell in the first several days for the models with a shell of mass 0.008 $M_\odot$ or larger; in the shells of lower mass (0.003 $M_\odot$ and 0.005 $M_\odot$) the photosphere is in the ejecta at all times. This suggests that for shells of higher mass there could be broadband photometric signatures of the shell in the first several days after the explosion. Hydrodynamic simulations that include cooling effects are required to understand the temperature, and thus the luminosity, of the shell at these epochs. A broadband photometric signature will only occur for a period of minutes for shells of lower mass, satisfying the limits of Bloom et al. (2012), though there may be line emission for a longer period.

The temperature of the photosphere, shown in Figure 4.2, determines the specific flux and slope of the continuum in the vicinity of the CaNIR feature. These temperatures are about 4000 K lower than those found by Mazzali et al. (2014), that utilise a more complete set of spectral features, though the overall trend is similar. The ground-based data at 2.5 d and earlier have a smaller wavelength range over which the flux scaling can be done compared to the spectra obtained with HST. The variation in temperature at these epochs is because the flux scaling does not capture the effect of features in the near-ultraviolet or near-infrared.

As illustrated in Figure 4.3, the scalar factors ($\log S^c_{Ca\ II}$) arising from the fits tend to decrease until about the time of Bmax, then begin to increase. The shell component is weak after about 7 d, so the overall fit is weakly dependent on the scalar factor for the shell. The late-time increase in the scalar factor for the ejecta, however, may be an indicator that there is more calcium at lower velocities than there is in the explosion model. Alternatively, the relative strength of absorption may be changing because of an increasing population in the ejecta of the Ca II in the lower state of the CaNIR transition.

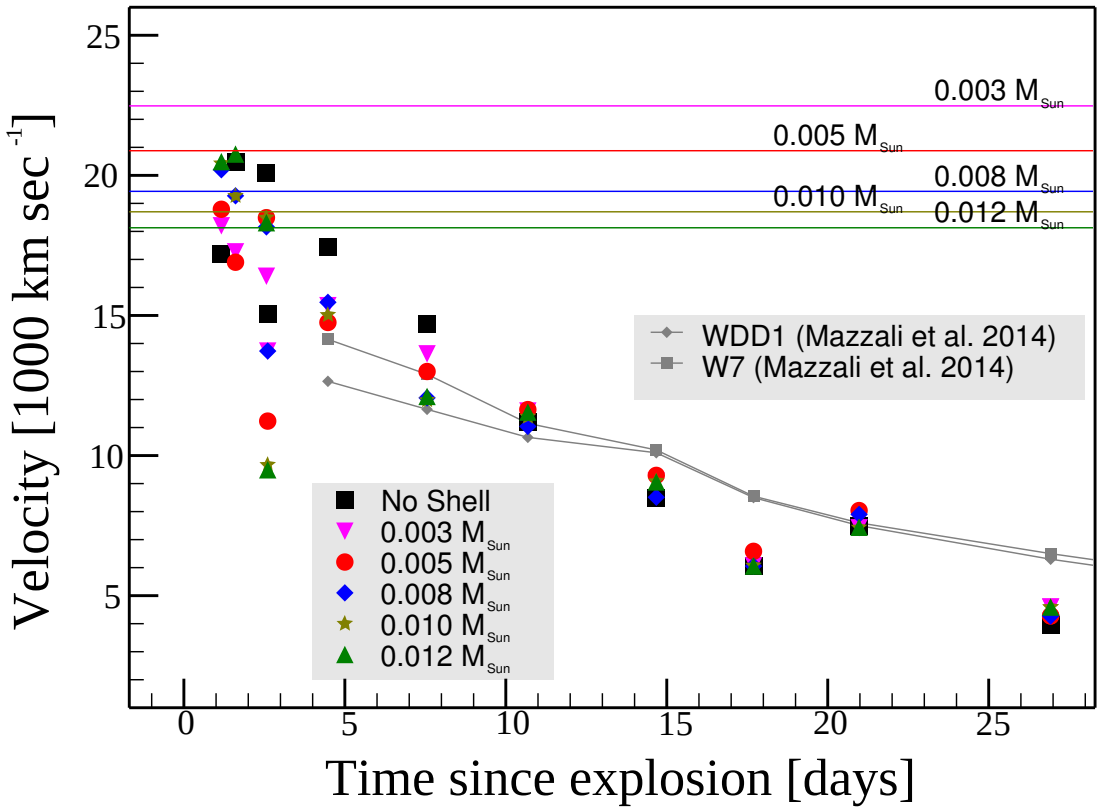

Figure 4.1: The evolution of the velocity of the photosphere for each model as well as the photosphere velocities as estimated in Mazzali et al. (2014) based on the W7 and WDD1 (Nomoto et al., 1984; Iwamoto et al., 1999) supernova models. For models with a shell, the velocity of the contact discontinuity is shown as colored lines, labelled just above each line. The photosphere is at lower velocity than the contact discontinuity at all epochs except for those of the highest mass shells. Uncertainties (not shown) are estimated to be less than 100 km s^{-1} for all points.

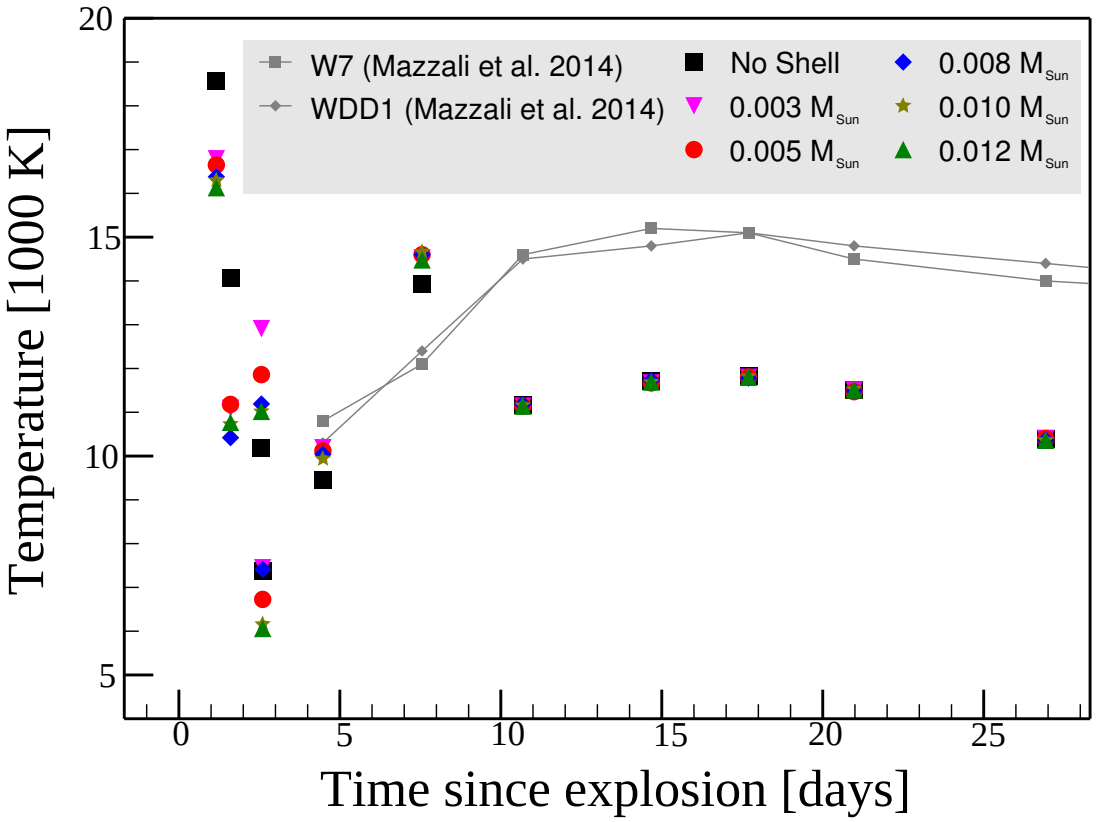

Figure 4.2: The evolution of the temperature of the photosphere, along with the photosphere temperatures estimated in Mazzali et al. (2014) based on the W7 and WDD1 (Nomoto et al., 1984; Iwamoto et al., 1999) supernova models. The photosphere temperatures are consistent with expected supernova photosphere temperatures, but tend to be about 4000 K cooler than those estimated in Mazzali et al. (2014). The scatter in the first four days is due to the limited range available for flux scaling (see §4.3.3). Uncertainties (not shown) are estimated to be less than 100 K for all points.

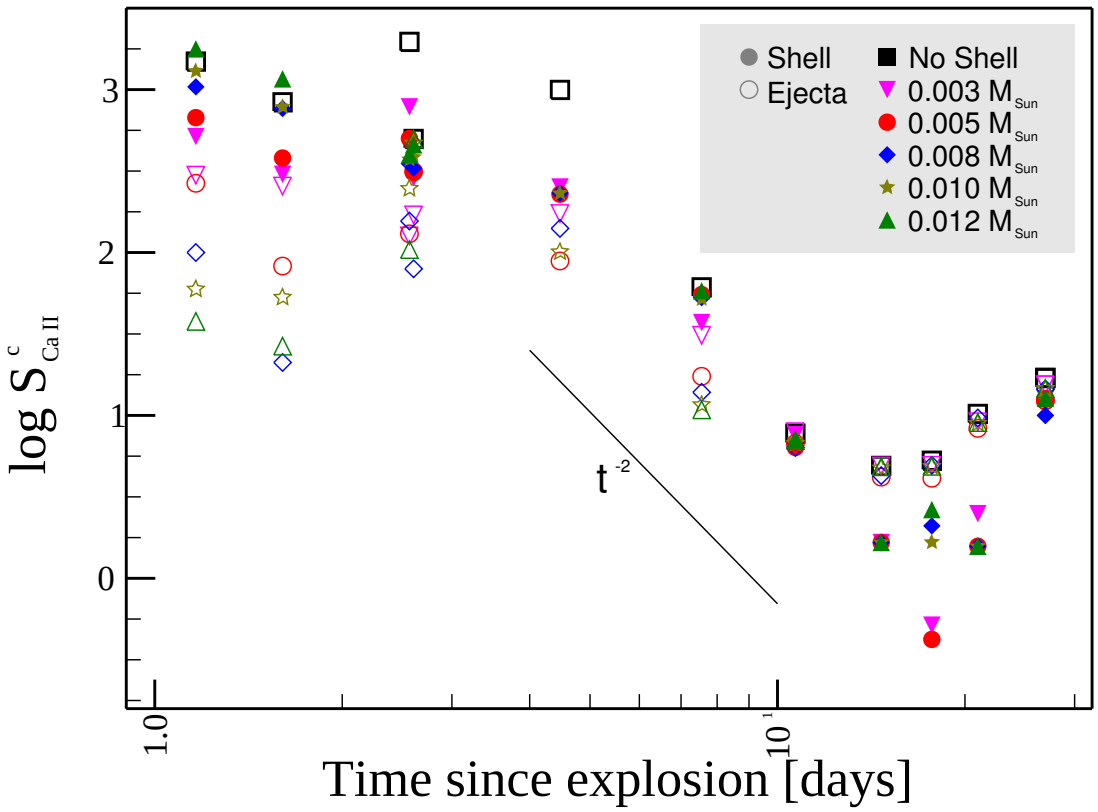

Figure 4.3: The evolution of the scalar factors $S^c_{Ca\ II}$ for each model. The t^{-2} trend in scalars expected for material in free expansion with constant ionization and excitation states is shown as a gray line. No individual models follow this trend for more than a few days. See §4.4 for further details and discussion. Uncertainties (not shown) are estimated to be less than 0.01 dex for all points.

For a gas in free expansion that has populations of all ionization and excitation states that vary slowly with respect to the expansion timescale, the scalar factors are expected to scale with density and decrease as t^{-2}. A line is given in Figure 4.3 to demonstrate the expected trend. None of these models follow a t^{-2} decline at any epoch, suggesting that the total populations of Ca II in the lower state of the CaNIR transition are changing or the opacity profile that we have used does not match the profile within the supernova. The latter may be due to a non-uniform distribution of Ca II in the shell (i.e. non-uniform abundance of calcium or variation of ionization or excitation state of calcium through the shell) and to differences between the structure

of the ejecta in the explosion model and that of the supernova.

Observed and synthetic spectra for all models at 1.6 d are shown in Figure 4.4. The fit to the observed feature for the spectrum generated with the model with no shell is very poor at this epoch, while the quality of fit for all models with a shell tend to be similarly good. Each panel in Figure 4.4 shows a decomposed synthetic spectrum revealing the relative contributions of the shell and ejecta components. The models with a shell of mass 0.008 $M_\odot$ or larger show only a continuum for the ejecta component indicating that only the shell has an effect on the CaNIR feature at this epoch, whereas the models with a shells of mass 0.003 $M_\odot$ or 0.005 $M_\odot$ show contributions from both the shell and ejecta components. This reflects that the photosphere lies within the shell at this epoch for the shells with highest mass, and that the photosphere is at lower velocity than the contact discontinuity for the lower mass models.

The temporal evolution of spectra is shown in Figure 4.5 for the shell of mass 0.005 $M_\odot$. These model spectra reveal that there is noticeable contribution from the shell through ∼10 d. The model with mass of 0.005 $M_\odot$ tends to reproduce the HVF at 8000 Å better than the other models due to the location of the contact discontinuity, though the feature in the synthetic spectra tends to be weaker than the observed HVF. At intermediate epochs (2 d – 7 d) the blue-ward side of the feature in the synthetic spectra is a poor match for the observed spectra. This may be due to P Cygni emission from the neighboring feature near 7500 Å contributing extra flux between ∼7500 – 8000 Å. Alternatively, a shell that does not have uniform distribution of Ca II could explain the discrepancy between the observed and synthetic features during these epochs. This may be the result of a different spatial distribution of calcium within the shell than we have assumed or by radiative effects (e.g. shadowing) resulting in more calcium in the lower states of the CaNIR transition at lower velocities.

4.4.1 Feature velocity evolution

The velocity of the components of the CaNIR feature are often determined by fitting it with a series of Gaussians (c.f. Zhao et al., 2015). The shape of the CaNIR feature, or any other absorption feature within a supernova spectrum, is dependent on the structure of the absorbing material. The shape is therefore complex and non-Gaussian. Fitting such a shape with multiple Gaussians can lead to falsely identifying compo-

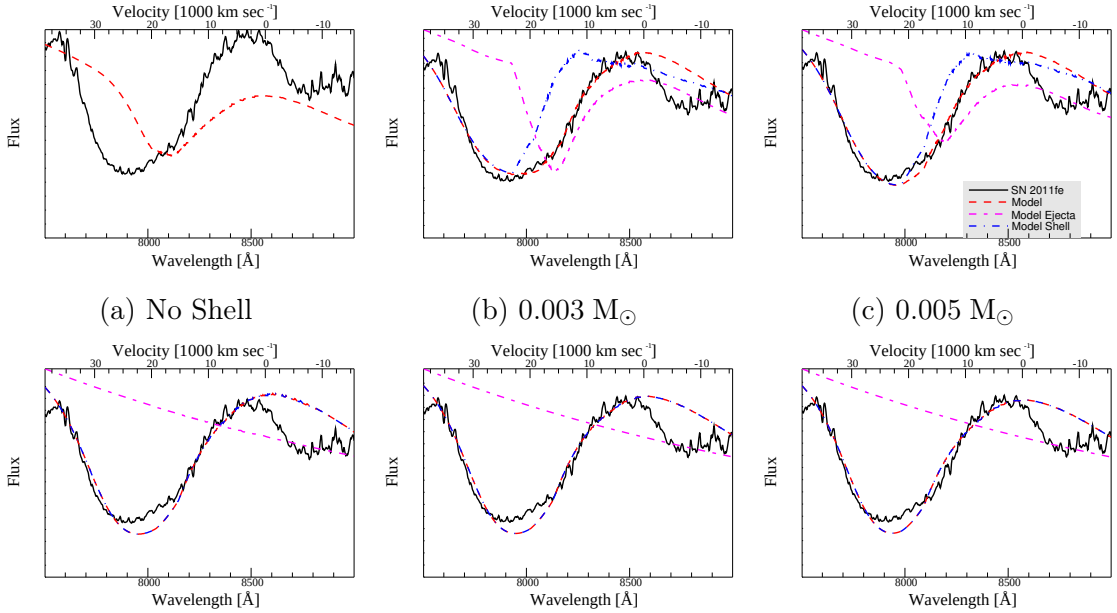

(a) No Shell (b) 0.003 $M_\odot$ (c) 0.005 $M_\odot$

(d) 0.008 $M_\odot$ (e) 0.010 $M_\odot$ (f) 0.012 $M_\odot$

Figure 4.4: Results of fitting the CaNIR feature for all models to SN 2011fe at 1.6 d. SN 2011fe spectra are shown in black and the generated spectrum from the model is shown in dashed red. SN 2011fe data sources are listed in Table 4.1. A legend is shown in Figure 4.4c. The shell with mass 0.005 $M_\odot$ has the best quality of fit (see Table 4.2) and the model without a shell is an extremely poor fit at this epoch. The velocity scale is based on the central component of the CaNIR triplet. The magenta long-dash–short-dash line shows the flux when the material in the shell is excluded, and the blue long-dash–dotted line shows the flux when the material in the ejecta is excluded. These demonstrate the relative contributions of the ejecta and shell components in each model. The ejecta has no effect on the shape of the feature at this epoch for models with a shell of mass 0.008 $M_\odot$ and larger.

nents that do not physically exist. Additionally, the continuum is not obvious in the UV and visible range of supernova spectra due to the density of P Cygni absorption and emission associated with those features. For the CaNIR feature, this can lead to use of the P Cygni emission of the nearby 7500 Å feature, as well as the P Cygni emission from CaNIR itself, as the blue and red sides of the continuum, respectively. This can further affect the apparent shape of the CaNIR feature, leading to falsely identified components.

Because we consider only absorption and related P Cygni emission from Ca II in this work, the synthetic spectra lack the 7500 Å feature so we cannot exactly

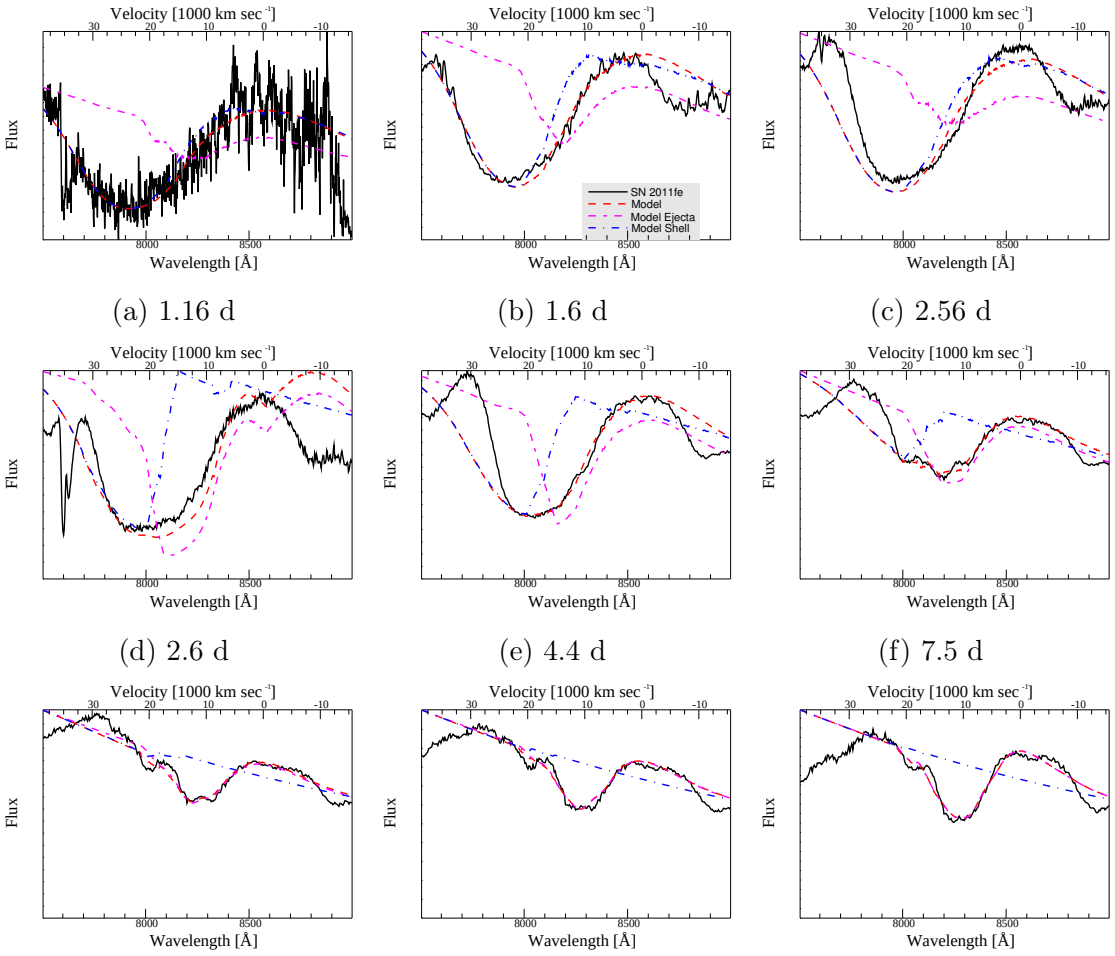

(a) 1.16 d (b) 1.6 d (c) 2.56 d

(d) 2.6 d (e) 4.4 d (f) 7.5 d

(g) 10.7 d (h) 14.7 d (i) 17.7 d

Figure 4.5: Evolution of the CaNIR feature in SN 2011fe comparing the observed data (black) and synthetic spectra generated from the model with a shell of 0.005 $M_{\odot}$ (red). Figure labels indicate time relative to the explosion. The magenta long-dash–short-dash line shows the flux when the material in the shell is excluded, and the blue long-dash–dotted line shows the flux when the material in the ejecta is excluded. These demonstrate the relative contributions of the ejecta and shell components in each model. There is some effect due to the material in the ejecta at all epochs, but the material in the shell has a larger effect through the first ∼2.5 d. The material in the shell has little direct effect on the feature at 10.7 d and later. The absorption feature near 7500 Å is presumed to be due to O I; it was neither generated nor included in the fitting range. SN 2011fe data sources are listed in Table 4.1. The velocity scale is based on the central component of the CaNIR triplet.

replicate the methods used on observed spectra. To emulate the observers' method, we use a continuum-flattened spectrum and identify the wavelength range over which absorption is greater than 1 per cent, thus avoiding the P Cygni emission. We then perform a Gaussian fit using the method of Zhao et al. (2015), allowing for either one or two sets of three Gaussians (three for the individual lines of the CaNIR feature, and one or two sets allowing for either a single component or PVF and HVF). Figure 4.6 shows the result of these fits. If a single component results in a lower variance than two components, only one is shown. Single components with a velocity greater than 15,000 km s^{-1} are designated as HVF. We show the velocities reported in Silverman et al. (2015) and the $v_{\rm min}$ values specified for fits with `SYANPPS` from Parrent et al. (2012) for comparison to the observed feature. The overall trend of all three are similar but there is scatter between the different methods and between models. It is particularly notable that the CaNIR feature generated from models of shells with higher mass (0.010 $M_\odot$ and 0.012 $M_\odot$) are best fit by two sets of Gaussians after $\sim$13 d, yet there is little to no contribution from these shells at those epochs. The additional Gaussian components at these epochs are due to the non-Gaussian shape of the feature, not to two physically distinct features.

4.4.2 Alternative single degenerate models

We used a Chandrasekhar mass, delayed-detonation supernova model for the work just summarized. An important category of SN Ia explosion models involve edge-lit double detonations whereby the explosion is triggered in a sub-Chandrasekhar white dwarf by the detonation of a thin layer of helium on the outside of a carbon/oxygen core. The required mass of helium is estimated to range from $\sim$0.05 – 0.1 $M_\odot$ (Fink et al., 2010; Woosley & Kasen, 2011), although the mass of helium might be considerably less if the helium is enriched with carbon and oxygen (Shen & Moore, 2014). In this latter case, if the helium is burned to a mixture of calcium, silicon, or iron group elements, and all energy is released into the kinetic energy of the envelope, the envelope will expand at 10,000$\pm$2,000 km s^{-1}. This is slow enough for the outer ejecta of the explosion to overtake the expanding envelope, leading to an interaction similar to that with the initially static shell considered here. While they need to be examined more quantitatively, such models might thus satisfy the properties of the shell needed to account for the HVF.

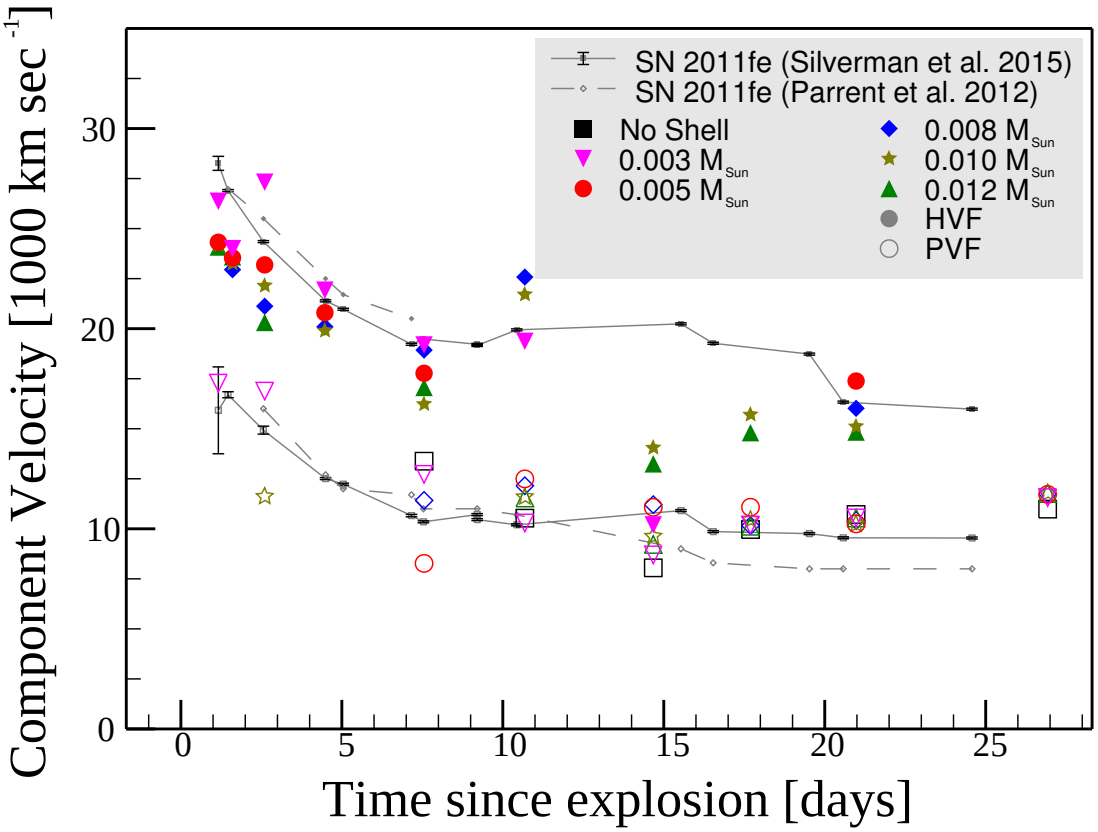

Figure 4.6: Evolution of the CaNIR feature velocity in SN 2011fe for each model based on Gaussian fitting, the minimum velocities ($v_{\rm min}$) for the PVF and HVF components of Parrent et al. (2012), and the PVF and HVF component velocities reported in Silverman et al. (2015). Lines are provided to guide the eye to the observed velocities and highlight the PVF and HVF components. The uncertainties of the observed velocities reflect only instrumental error and do not account for uncertainty in the selection of the continuum. Two-component fits of the synthetic spectra occur at later epochs despite there being little to no absorption within the shell at these times. In these cases the apparent HVF are a result of the non-Gaussian shape of the overall feature.

Our models also constrain progenitor models that predict, or are consistent with, very little circumstellar medium. Models in this category could be spin-up / spin-down models in which mass transfer has long since ceased (Di Stefano et al., 2011; Justham, 2011; Di Stefano & Kilic, 2012) or models in which isolated white dwarfs explode by pycnonuclear reactions (Chiosi et al., 2015). In the absence of a circumstellar medium, these models would not produce HVF by the mechanism modeled here.

4.5 Conclusion

We fit the observed Ca II near-infrared triplet (CaNIR) feature of SN 2011fe through 27 d after the explosion with synthetic spectra generated from models of Mulligan & Wheeler (2017) for Type Ia supernova that have interacted with compact shells with a mass between 0.003 $M_\odot$ and 0.012 $M_\odot$ and a model without a shell. The ejecta alone cannot explain the high-velocity features, and the model with a shell of mass 0.005 $M_\odot$ performs better than other shells for SN 2011fe at more epochs, though the variation in the quality of the fit is small between models that include a shell. In shells with a mass less than about 0.008 $M_\odot$, the photosphere lies within the shell only within the first minutes after the explosion and interaction, making such a shell difficult to detect photometrically.

The optical depth of neither the shell nor the ejecta follow the t^{-2} trend that is expected from freely-expanding material with a constant ionization and excitation state. This suggests that the state of the calcium is not constant or that the distribution of calcium in the lower states of the Ca II near-infrared transition within the ejecta and the shell of the supernova is not uniform or at least does not exactly match that of the models.

The velocity evolution of the CaNIR feature determined using Gaussian fits of the synthetic spectra demonstrate that the evolution broadly matches the observed evolution, though this method artificially generates high-velocity components due to an attempt to fit an inherently non-Gaussian feature with multiple Gaussians.

The composition and physical origins of the shells that we have considered remain to be determined. The presence of such a shell prior to the explosion is inconsistent with models that lack a circumstellar medium (CSM) or have an extended CSM such

as a wind. Such a shell might be consistent with some explosion models that invoke a surface detonation of a helium envelope around the progenitor or other models that include accretion onto the progenitor, though the accretion disc itself would be much less massive than the shells we have invoked. It may be possible to determine the source of the shell if its composition can be determined, an important issue we intend to pursue in future work.

Chapter Five: Synthetic spectra using TARDIS

5.1 Prelude

In previous chapters we evaluated how the spectra of SN Ia are affected by the presence of a circumstellar shell and the interaction between the supernova and the shell, and how well the resulting spectra match that of the well observed supernova SN 2011fe. We now attempt to understand the composition of the material within the shell by making use of TARDIS. TARDIS is software designed for spectral synthesis for supernovae that includes nLTE excitation and ionization effects, and requires explicit specification of the composition of all of the material within the supernova. We consider shells that consist of mostly hydrogen, helium, or carbon and oxygen, and a mix of metals, including calcium, based upon a Solar abundance. Over 300 total combinations of compositions for the shell and ejecta were considered, in addition to models that evaluate the effect of temperature, photospheric velocity, and luminosity of the supernova.

In this work, the majority of the writing is the work of this author. The methods were developed by this author in coordination with J. Craig Wheeler. The effort of generating the multitude of spectra that were considered was a joint effort between this author and Kaicheng Zhang. Analysis and discussion was a joint effort of J. Craig Wheeler, Kaicheng Zhang, and this author. The software developed for generating inputs into TARDIS based upon the hydrodynamic simulations and a selected photosphere velocity and temperature is the work of this author. All figures in this work were generated using software written by this author.

5.2 Introduction

Typical Type Ia supernovae (SN Ia) show high-velocity features (HVF) prior to maximum light that are separated from the photospheric-velocity features (PVF) by $\sim$7,000 km s^{-1} (Hatano et al., 1999; Wang et al., 2003; Thomas et al., 2004; Mazzali et al., 2005b; Quimby et al., 2006; Parrent et al., 2012; Marion et al., 2013; Childress

et al., 2013a, 2014; Maguire et al., 2014; Silverman et al., 2015; Zhao et al., 2015, 2016). Both the HVF and the PVF slow with time, but maintain this separation. The HVF are especially prominent in the near-infrared triplet of Ca II (CaNIR), but are also observed in Si II and other strong lines. The HVF exhibit a polarization of 0.1 – 1 per cent (Wang et al., 2003; Wang & Wheeler, 2008; Patat et al., 2009), requiring that the material that gives rise to the HVF be clumped or otherwise asymmetric.

Despite the near ubiquity of the HVF and their potential to reveal important information about the progenitor evolution or combustion physics, there is no accepted physical model. Proposed models fall into three broad categories: 1) material that is part of the "normal" ejecta but has stronger absorption features due to non-local thermodynamic equilibrium (nLTE) effects (Blondin et al., 2013), 2) material ejected at high velocity during the explosion (Mazzali et al., 2005b; Tanaka et al., 2006), and 3) material swept up by the ejecta after the explosion (Gerardy et al., 2004). Any cause of these features must explain the polarization and the temporal evolution of both the HVF and PVF.

Mulligan & Wheeler (2017), hereafter MW1, investigated the interaction between a model SN Ia and a compact circumstellar shell in an attempt to characterize the temporal behavior of the HVF in the CaNIR line. They employed a 1-D hydrodynamic simulation of the collision of the ejecta with shells of various mass from 0.003 – 0.02 $M_\odot$ to establish the density profile of the resulting collision and generated synthetic spectra assuming constant ion state and excitation temperature. The calcium abundance of the shell was taken to be a free parameter. They explored the effect of the equation of state, the explosion model, and the width, initial density profile and mass of the shell on the appearance and temporal evolution of the CaNIR line. They compared the evolution of the pseudo-equivalent width (pEW) of the CaNIR feature from their models to observational results from Silverman et al. (2015) and found that the mass of the shell must be less than 0.012 ± 0.004 $M_\odot$.

Mulligan & Wheeler (2018), hereafter MW2, used the models and techniques of MW1 to explore the evolution of the HVF and PVF in the CaNIR feature in the well-observed SN 2011fe. They concluded that the CaNIR feature is better explained by the supernova model interacting with a shell than the model without a shell, with a shell of mass 0.005 $M_\odot$ resulting in a somewhat better fit than shells of other masses. The evolution of the optical depth of CaNIR suggested that the ionization state of calcium within the ejecta and shell is not constant. MW2 noted that their model

line profiles were intrinsically non-Gaussian and discussed associated ambiguities in observational methods for determining the presence and the pEW of the HVF by fitting multiple Gaussian profiles to the line features. They concluded that the HVF or other components can be falsely identified.

The models of MW1 and MW2 were unable to constrain the abundance of calcium in the ejecta or shell nor the underlying substrate of the shell. The latter could plausibly be hydrogen, helium or a mixture of carbon and oxygen. In this work we make use of TARDIS (Kerzendorf & Sim, 2014) to generate synthetic spectra from a set of models of MW1 to explore constraints on all these factors, qualitatively comparing the generated spectra to the observed spectra of SN 2011fe at equivalent epochs after the explosion.

In Section 5.3, we describe the supernova-shell interaction models used for generating the synthetic spectra, the abundance models that are applied to the supernova ejecta and the shell, and the additional inputs required for TARDIS. In Section 5.4 we present the generated spectra for each model and compare those spectra to that of SN 2011fe and discuss the implications of the results. We conclude our results in Section 5.5.

5.3 Methods

5.3.1 Supernova-shell interaction models

We use the supernova-shell interaction models of MW1 as the source of velocity and density information for the supernova ejecta and the shell. These models make use of the Gamezo et al. (2005) delayed-detonation explosion model for the supernova itself, and surround the supernova with a compact (radius $\ll$ $R_\odot$) shell. The explosion model includes density, internal energy, and composition information for the supernova, though the composition is limited to groups rather than specific elements; e.g. silicon, sulfur, and calcium are all considered part of the silicon group. The explosion and shell data are used as starting conditions in a hydrodynamic simulation using FLASH. In the simulation, the shock is given time to propagate through the shell until both the shell and ejecta are expanding adiabatically.

In this work, we use only models #49, #53, and #57. Each model has a shell with an initial outer radius of 0.3 $R_\odot$, uses delayed detonation model `c` for the explosion

and ejecta with the gamma-law equation of state and has a saw-tooth density profile with the highest density at the edge closest to the explosion. Model #s 49 and 53 are used only for evaluation of the compositions of helium envelopes of SNe Ia of 0.01 and 0.02 $M_\odot$, respectively, described by Shen & Moore (2014). We have chosen model # 57, with a shell of mass 0.005 $M_\odot$, as a slightly better match to SN 2011fe, though the differences between the spectra resulting from different masses of the shall is small, and thus this model is generally representative of shells with a mass near 0.01 $M_\odot$. We hereafter refer to the shell models based upon the mass of the shell rather than the model number for clarity.

The hydrodynamic models provide density as a function of velocity that is then used as an input to TARDIS. The density is sampled at 256 points spanning the range of velocity of both the ejecta and shell. For the ejecta, the group composition from the Gamezo et al. (2005) model is used to provide a broad framework of the structure; the details of abundances for each element within each group are described in Section 5.3.2.

5.3.2 Compositions

For the composition of the ejecta, we use the group composition information that is given in the initial explosion model and the result of the hydrodynamic simulation of the interaction between the supernova and shell. In order to provide details of the individual elements of each group, we use the nucleosynthetic yields by mass of the delayed-detonation SN Ia explosion model N100 of Seitenzahl et al. (2013) for stable nuclides. We hereafter refer to this abundance model as "Seitenzahl-like." We find the relative abundance of each element within each group, then assume that the ratio holds for any areas in which elements within that group appear. The ratio of abundances for each element within the associated group are listed in Table 5.1. In addition to a pure Seitenzahl-like composition, we also consider composition models in which the calcium content is depleted. These models named as "N100$\pm X$," where $\pm X$ is the enhancement (+) or depletion (−) of calcium by X dex within the silicon group. For example, a Seitenzahl-like composition that is depleted by 1 dex in calcium would be named 'N100-1.' We note that the use of stable nuclides results in excess iron that should instead be in the form of cobalt and / or nickel at the epochs that we are considering. We have determined that this overabundance of iron does affect

Table 5.1: The abundance by mass fraction for stable nuclides within each nuclide group for the Seitenzahl et al. (2013) N100 model.

Group	Element	Mass Fraction within Group
C	C	1.0
O	O	1.0
Mg	F	2.2×10^{-9}
Mg	Ne	1.8×10^{-1}
Mg	Na	1.9×10^{-3}
Mg	Mg	7.8×10^{-1}
Mg	Al	3.4×10^{-2}
Si	Si	0.66×10^{-1}
Si	P	1.3×10^{-3}
Si	S	2.6×10^{-1}
Si	Cl	4.9×10^{-4}
Si	Ar	4.5×10^{-2}
Si	K	2.6×10^{-4}
Si	Ca	3.4×10^{-2}
Fe	Sc	2.5×10^{-7}
Fe	Ti	4.3×10^{-4}
Fe	V	1.6×10^{-4}
Fe	Cr	1.2×10^{-2}
Fe	Mn	1.1×10^{-2}
Fe	Fe	8.9×10^{-1}
Fe	Co	6.4×10^{-4}
Fe	Ni	8.9×10^{-2}
Fe	Cu	5.5×10^{-7}
Fe	Zn	3.7×10^{-6}
Fe	Ga	4.8×10^{-13}

the flux by a factor of $\sim$2 blueward of about 5000 Å, but does not otherwise change the results and conclusions presented here.

The composition of the material causing the HVF (i.e. the shell) is unknown, so we explore many possible models to identify those that look most similar to SN 2011fe. We base all compositions on the solar abundance of metals given in Asplund et al.

(2009). Allowing that the material in the shell may be the result of mass transfer from a white dwarf or otherwise stripped-envelope star, we also consider compositions in which hydrogen has been completely converted to helium and compositions in which all hydrogen and helium have been converted to carbon and oxygen. We refer to the primary constituent of each composition as the substrate and to this group of compositions as "solar-type." While the basis of each of the metal compositions is solar, we consider enhancement or depletion of calcium relative to a solar abundance. When referring to these abundance models, we name them by their substrate, basis composition, and calcium enhancement or depletion in dex. For example, a hydrogen substrate with solar abundance of metals and calcium enhanced by 2 dex is "H-Solar+2."

In addition to solar-type abundances, we also consider the abundances of helium envelopes that have undergone detonation just prior to the supernova explosion, as described by Shen & Moore (2014). We select envelopes with masses of 0.005, 0.01, and 0.02 $M_\odot$ and the subsequent yield after detonating around a 1 $M_\odot$ carbon-oxygen white dwarf. The masses of these envelopes span the estimated range of mass of the high-velocity material and are enhanced in silicon and / or calcium, offering a possible source of HVF. The compositions for these envelopes after detonation, derived from Shen & Moore (2014, Figure 11) are given in Table 5.2. When generating spectra with these abundance models, we use the models of MW1 with a shell of appropriate mass, i.e. for an envelope of mass 0.01 $M_\odot$, we use the MW1 model with a shell of mass 0.01 $M_\odot$. We note that the kinematics of a sub-Chandrasekhar mass detonation and subsequent interaction with the envelope would not match that of the Gamezo et al. (2005) delayed-detonation supernova interacting with the shells of MW1. We consider this a first approximation to the effect of the helium envelope upon the spectra; the velocity of the material within the remnants of the envelope are likely to have a lower velocity, and perhaps higher density, than the shell models of MW1.

Figures 5.1 and 5.2 show an example abundance as a function of mass and velocity, respectively, for an abundance model N100+0 for the ejecta and model H-Solar+0 for the shell. These figures demonstrate that, while the shell consists only of a small fraction of the mass of the supernova ejecta, it occupies a large range of velocities. For the shell with a mass of 0.005 $M_\odot$, the contact discontinuity lies at 20,880 km s^{-1}.

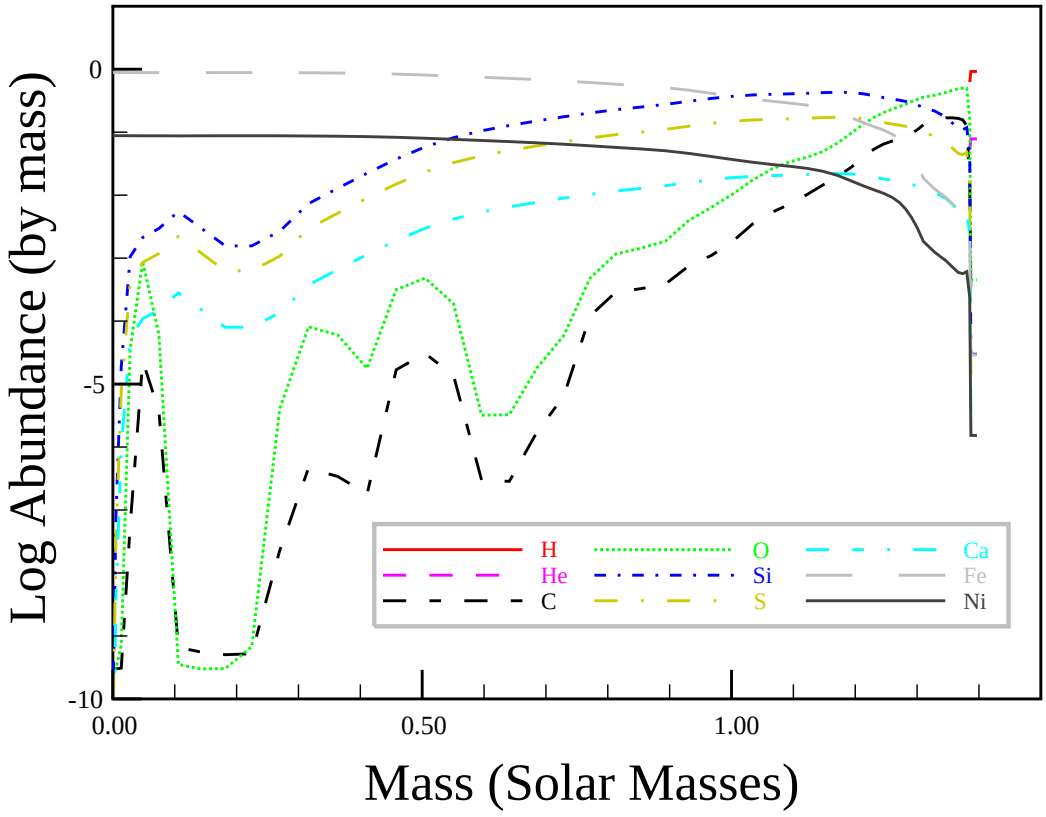

Figure 5.1: The abundance by mass fraction as a function of interior mass of the supernova ejecta and shell for a select set of elements, using the Gamezo et al. (2005) delayed-detonation explosion that has interacted with a shell of mass 0.005 $M_{\odot}$. This model incorporates the Seitenzahl et al. (2013) N100 model for ratios of individual elements within each nuclide group (N100+0), and a solar abundance for the material within the shell (H-Solar+0). Because we use the stable nuclides, iron is extremely enhanced within the supernova ejecta. A color figure is available online.

Table 5.2: Abundances by mass fraction for helium envelopes of mass 0.005, 0.01, and 0.02 $M_\odot$ from Shen & Moore (2014).

Name	Envelope Mass [$M_\odot$]	log X_{He}	log X_{Si}	log X_{Ca}	log X_{Ti}	log X_{Cr}	log X_{Fe}
S&M-M0.005	0.005	-0.11	-0.72	-∞	-∞	-∞	-∞
S&M-M0.01	0.01	-0.16	-2.61	-1.62	-4.16	-∞	-∞
S&M-M0.02	0.02	-0.24	-3.59	-0.82	-0.65	-1.74	-3.59

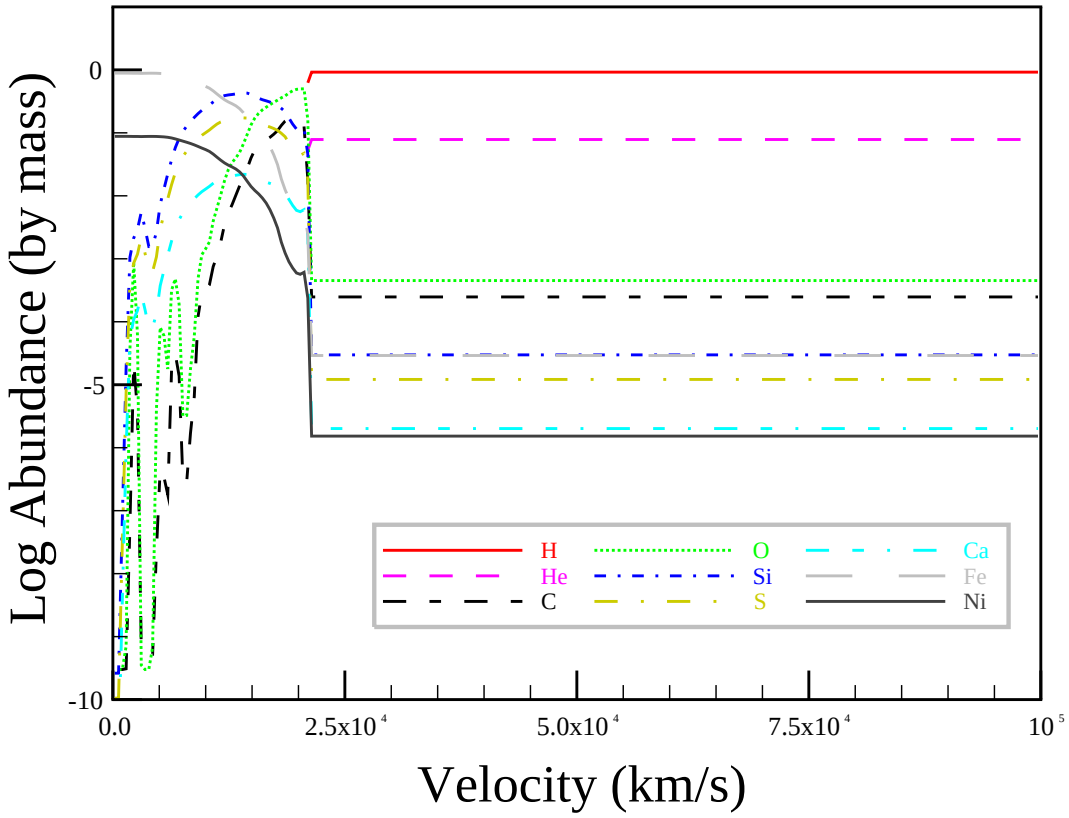

Figure 5.2: Similar to Figure 5.1, but as a function of velocity. The contact discontinuity between the ejecta and shell lies at 20,880 km s^{-1}. A color figure is available online.

5.3.3 Synthetic spectra

We use TARDIS to generate the synthetic spectra of the models described in Sec. 5.3.1 and using the composition described in Sec. 5.3.2. TARDIS is well suited for the particular problem explored in this paper that requires the computation of a large number of models to explore CaNIR HVF parameter space. TARDIS can only compute supernova atmospheres in spherical symmetry, and while the HVF problem surely requires departure from spherical symmetry, our current models are also restricted to that regime. Given that condition, TARDIS uses Monte Carlo (MC) methods to iterate to a self-consistent calculation of the radiation field and corresponding ionization and excitation and to compute a synthetic spectrum. The radiative transfer and associated physics can be treated with various levels of sophistication. While quite general, TARDIS was originally designed to be efficiently applied to SN Ia, as we do here. In their presentation of the TARDIS code, Kerzendorf & Sim (2014) note that of prominent species present in the atmospheres of SN Ia, silicon, sulfur, magnesium, and calcium, Ca II features are the least sensitive to the choice of excitation mode and are well represented by simple Boltzmann excitation levels. This also bodes well for the current study.

TARDIS does not simulate spectral evolution directly, but provides a "snapshot" at a given epoch, again a process well suited for the current problem where we study conditions at three specific epochs in the expansion of of the supernova. TARDIS accepts an arbitrary density profile that we provide with our shell interaction models and an arbitrary abundance profile that we vary in this study. The total luminosity is specified for the supernova; TARDIS iterates upon a photospheric luminosity that results in the desired total luminosity. We use the luminosity of SN 2011fe as reported by Pereira et al. (2013), using linear interpolation of the log of the luminosity at each epoch, resulting in luminosities of $\log(L/\ \mathrm{L}_\odot) = 7.81$ at 2 d, 8.62 at 5 d, and 9.19 at 9 d after the explosion.

TARDIS does not treat non-radiative energy sources such as radioactive decay and we neglect all such effects in this work. This means the photosphere must be external to the regions in which the majority of the luminosity is produced, a good approximation for the early phases we study here. The radiation field is injected at the inner boundary (the photosphere) with a blackbody temperature consistent with the luminosity adopted at that radius. For the photospheric velocity, we use

the photosphere velocities determined in MW2 for the model with a shell of mass 0.005 $M_\odot$, smoothed by a third-degree polynomial to reduce noise, resulting in a photospheric velocity of 16,470 km s^{-1} at 2 d after the explosion, 14,300 km s^{-1} at 5 d after the explosion, and 11,780 km s^{-1} at 9 d after the explosion. Finally, for the initial temperature estimates, we use the color indices of Zhang et al. (2016) to estimate the color temperature of the light. We select initial temperatures of 6325 K at 2 d after the explosion, 6676 K at 5 d after the explosion, and 7321 K at 9 d after the explosion. We acknowledge that the effective temperatures of SN Ia are not well identified by the color temperature, but in practice we find that the choices of the initial radiation temperatures have little effect on the final temperatures in TARDIS. The final radiation temperatures generated by TARDIS at the inner boundary are 11,100 – 11,800 K at 2 d, 11,600 – 12,100 K at 5 d, and 13,400 – 13,800 K at 9 d, with the ranges due to slight differences in .

We use TARDIS in the nebular mode for ionization and the dilute-LTE mode for excitation. Radiative rates are treated in the detailed mode and line interactions are treated in the macroatom mode. We use 10^5 packets for models during convergence, and 5×10^5 or 10^6 packets for each final spectrum. We have computed about 150 synthetic spectra using TARDIS in the course of this study. We find that each model requires several CPU-hours of computing time rather than the few minutes per spectrum described in Kerzendorf & Sim (2014). This is likely due to our use of detailed density and abundance models as inputs.

5.3.4 Reference spectra of SN 2011fe

We use spectra of SN 2011fe as a comparison at each epoch (2, 5, 9 d) in order to get a sense of the relative strength of observed features, mainly focused on the Ca II, Si II, and O I features. The spectra were acquired from Guillochon et al. (2017), dereddened according to Cardelli et al. (1989) with corrections to the visual range from O'Donnell (1994) using $E(B-V)$ of 0.0077, and shifted into the rest frame wavelength using a redshift of 0.000804. We assume an Nugent et al. (2011) explosion date of MJD 55796.696, and use the Nugent et al. (2011) spectrum taken on MJD 55798.2 as a reference at 2 d after the explosion, the Mazzali et al. (2014) spectrum taken on MJD 55801.17 as a reference at 5 d after the explosion, and the Parrent et al. (2012) spectrum taken on MJD 55805.2 as a reference at 9 d after

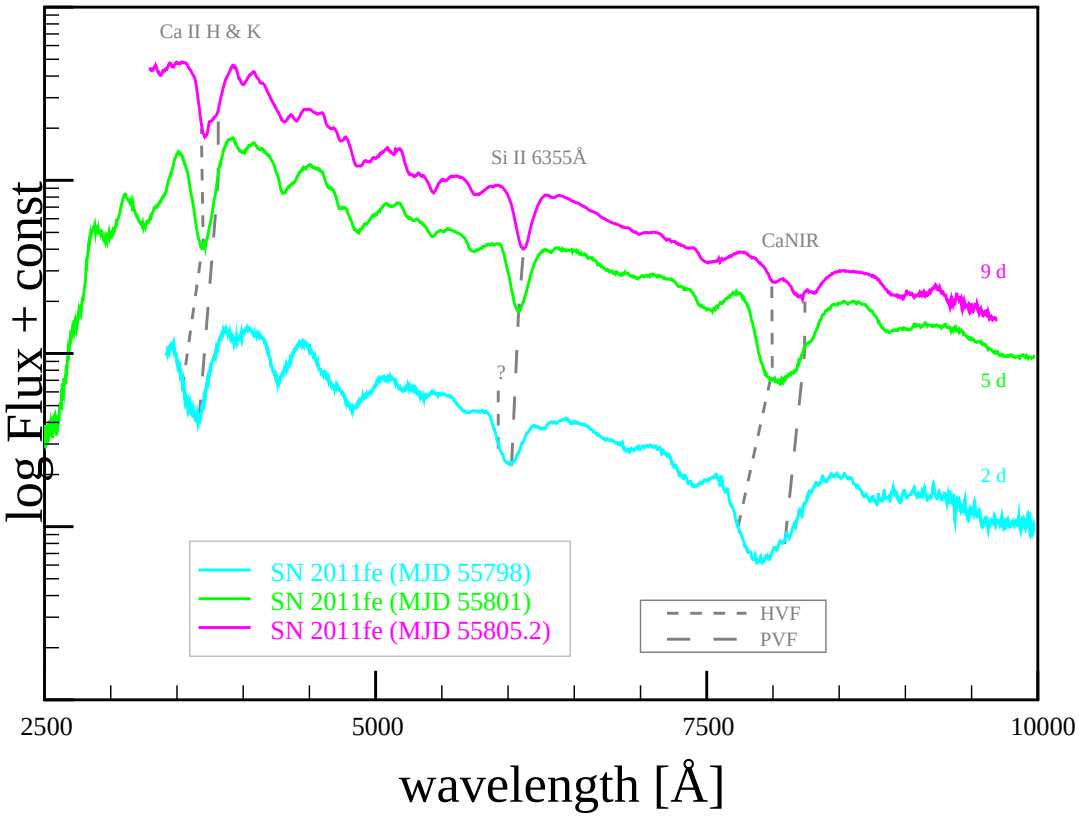

Figure 5.3: Spectra of SN 2011fe at the selected epochs, highlighting the Ca II H&K, Si II 6355 Å, and CaNIR features. Dashed lines highlight the evolution of the PVF and HVF. The time since the explosion is listed in the right side of the figure near each spectrum. A HVF in Si II near 5925 Å on MJD 55799, indicated with a question mark and line at MJD 79898, but HVF have not been identified at the later epochs that are shown here (Silverman et al., 2015). A color figure is available online.

the explosion. At each epoch, we scale the data such that it approximately matches the synthetic spectra, typically using the blue side of the Si II feature as the point of normalization. Figure 5.3 shows these spectra at each epoch, and highlights the Ca II H&K, Si II 6355 Å, and CaNIR HVF and PVF.

5.4 Results and discussion

We consider each abundance model for the shell and ejecta at three epochs: 2 d, 5 d, and 9 d after the explosion, spanning the range in which the high-velocity features of calcium are significant relative to the photospheric features. At each epoch, we consider the range of calcium abundance in the shell that may have an observable affect upon the spectrum. As described in the following sub-sections, we find that the solar-type composition models with a hydrogen substrate are broadly representative of the other solar-type models, and therefore use the hydrogen substrate only to demonstrate the effect of adjusting the calcium yield within the ejecta and to generate a "best" fitting model.

5.4.1 2 days after the explosion

5.4.1.1 Solar-type with hydrogen substrate

Figure 5.4 shows the spectra that result from abundance model N100+0 for the ejecta and the hydrogen substrate abundance models for the shell. Despite the shell in these abundance models containing mostly hydrogen, there is no evidence of hydrogen absorption or emission within the synthetic spectra, including in the mid- and far-infrared to 3 μm (not shown in the figure). The Ca II H&K feature is not affected by the calcium within the shell at this epoch. Figure 5.5 shows just the CaNIR feature for the hydrogenic shells. As the quantity of calcium within the shell increases, the feature gets deeper and broader toward the blue, while the P Cygni peak is enhanced. An enhancement of about 0.4 dex above solar abundance for calcium within the shell results in a better fit between the synthetic feature and the feature observed in SN 2011fe. An enhancement of 0.6 dex or more in calcium results in an excessively strong CaNIR feature.

There is an additional model absorption feature that appears near ∼8600 Å that has not been observed (or at least has not been observed to be as strong) in SN Ia and appears to get weaker with increasing calcium content in the shell. This feature will appear in nearly all spectra generated from the compositions that we consider. The apparent decrease in strength of this feature with increasing calcium within the shell is largely the result of increasing P Cygni emission as the CaNIR feature gets stronger. Fine tuning of the structure or composition of the ejecta would assist in

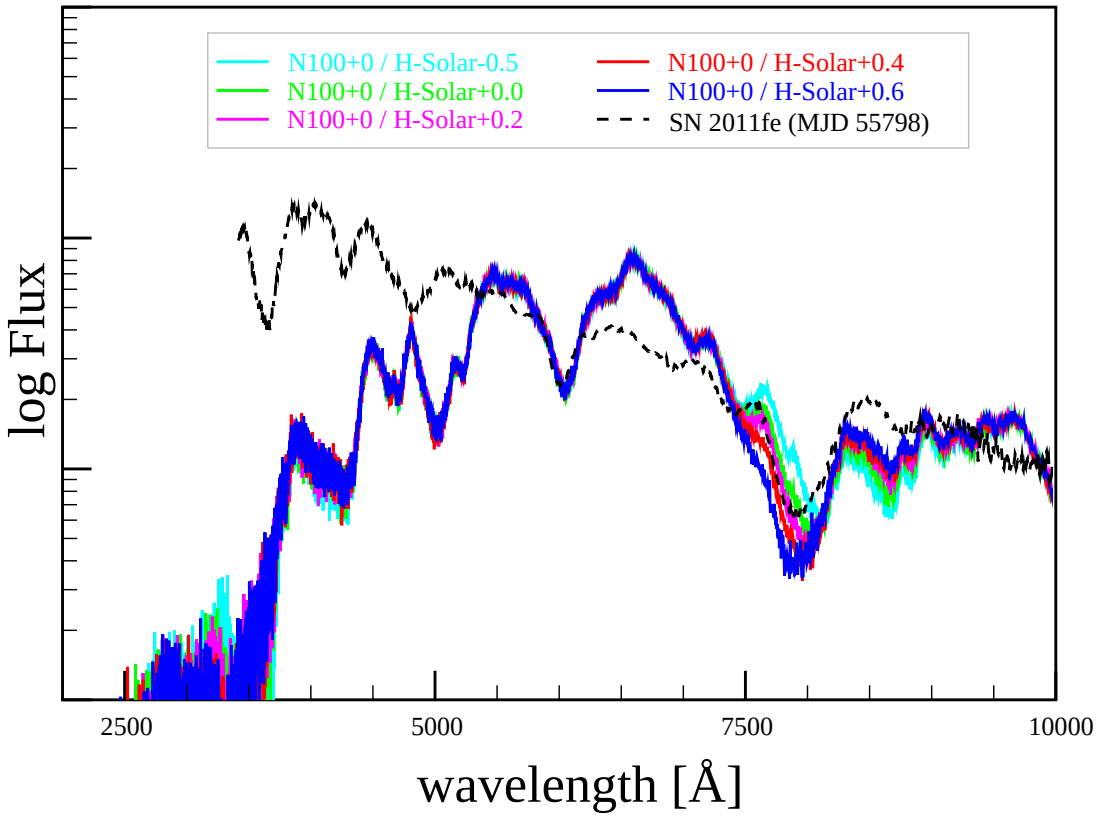

Figure 5.4: Synthetic spectra at 2 d after the explosion using a N100+0.0 abundance for the ejecta and solar-type abundances with a hydrogen substrate for the shell, with calcium depletion or enhancement ranging from -0.5 – +0.6 dex within the shell. The spectrum of SN 2011fe at MJD 55798.2 from Nugent et al. (2011) is shown in black for reference. Only the CaNIR feature is affected by the calcium abundance within the shell. There is no evidence of hydrogen absorption or emission features despite the large quantity of hydrogen within the shell. A color figure is available online.

improving the appearance of this feature but that is not the focus of this work.

Figure 5.6 shows the effect of calcium within the ejecta on the synthetic spectra, depleting the calcium yield relative to the Seitenzahl et al. (2013) N100 model with stable nuclides by -5 – 0 dex. Decreasing the calcium within the ejecta has an effect of slightly weakening the CaNIR feature, though increasing the flux of the related P Cygni peak. The effect of the ejecta upon the CaNIR feature is entirely on the red side of the feature, at wavelengths $\gtrsim$8000 Å. It is not clear that any one model of abundance in the ejecta results in a spectrum that is a better fit to the observed

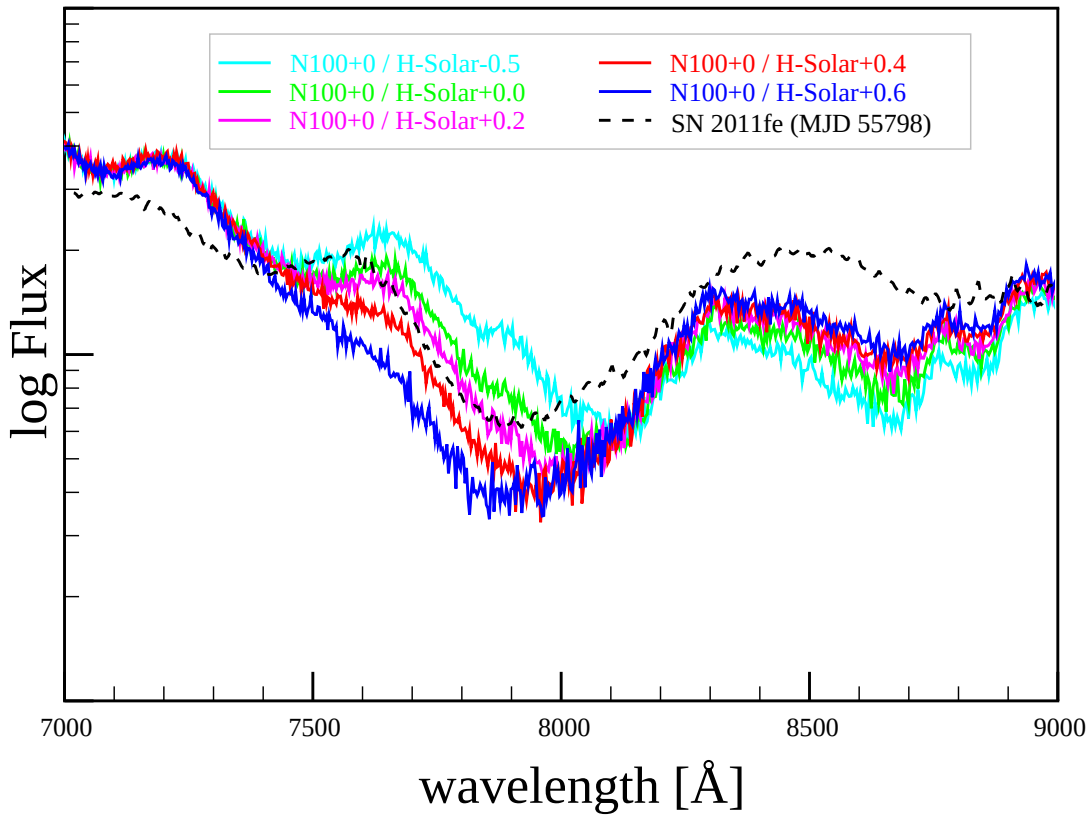

Figure 5.5: Similar to Figure 5.4; the N100+0.0 abundance for the ejecta and solar abundance within a hydrogen substrate for the shell at 2 d after the explosion, and focused on the CaNIR feature between 7000 – 9000 Å. From the shell that has less than a solar abundance of calcium we can see that the absorption within the ejecta (i.e. the PVF) may be too strong at this epoch when using the N100+0.0 model. The shell with only a solar abundance of calcium cannot explain the observed HVF component, but an enhancement of +0.2 – +0.4 dex above solar value of calcium within the shell, with the N100+0.0 composition for the ejecta, does reasonably well in fitting the observed feature. As the quantity of calcium within the shell increases, the feature gets deeper and broader toward the blue, while the P Cygni peak is enhanced. A color figure is available online.

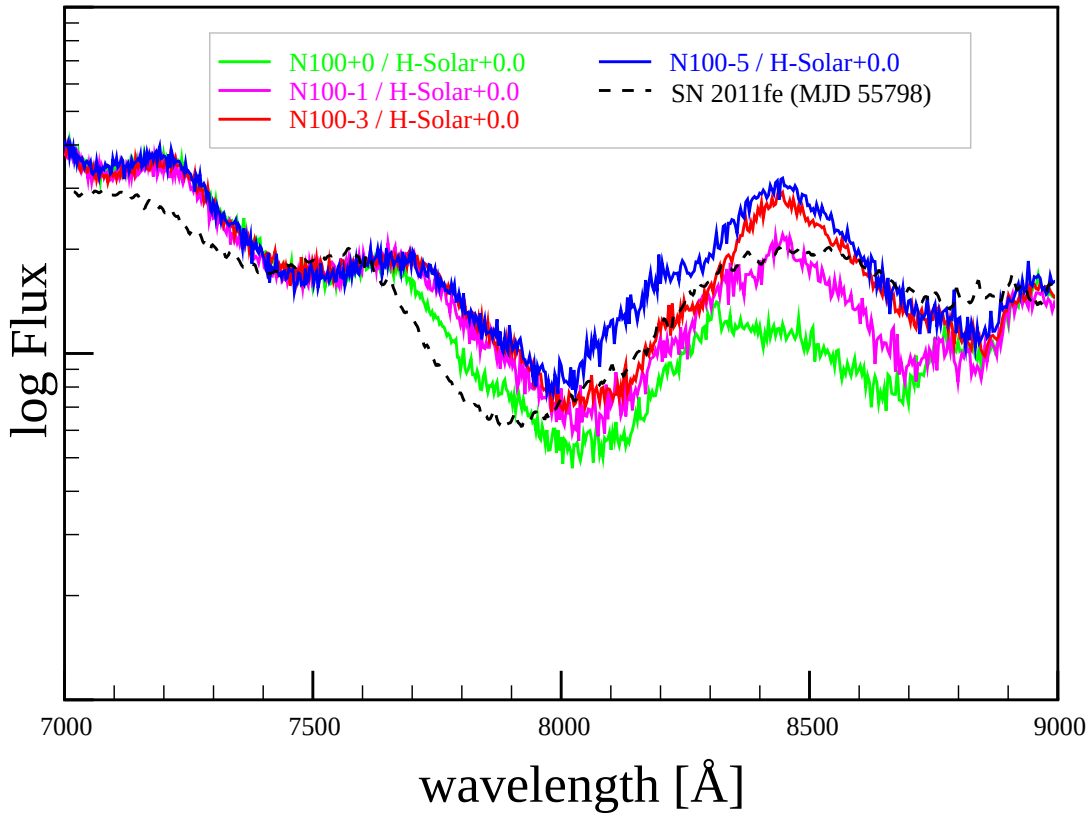

Figure 5.6: Like Figure 5.5 at 2 d after the explosion, but showing the effect of depletion of calcium within the ejecta with a solar abundance of calcium in the shell. The ejecta has a Seitenzahl-like composition, with calcium yield adjusted by -5 – 0 dex. Depletion of the calcium within the ejecta results in modest reduction in the strength of the CaNIR feature at this epoch. There is no clearly preferred calcium abundance within the ejecta at this epoch – a slight depletion of the calcium results in a better fit near 8400 Å, but stronger depletion results in a better fit near 8100 Å. A color figure is available online.

CaNIR feature at this epoch. Replacement of the calcium within the ejecta with silicon results in a slight enhancement of the Si II 6355 Å feature.

Figure 5.7 shows the result of an effort to produce a combination of ejecta and shell abundances to better match the observed CaNIR feature of SN 2011fe. We select a depletion of 2 dex of calcium relative to the Seitenzahl et al. (2013) N100 model with stable nuclides, and 0.4 dex of enhancement of calcium within the shell, relative to a solar value, based upon visual inspection of the results shown in Figures 5.5 and

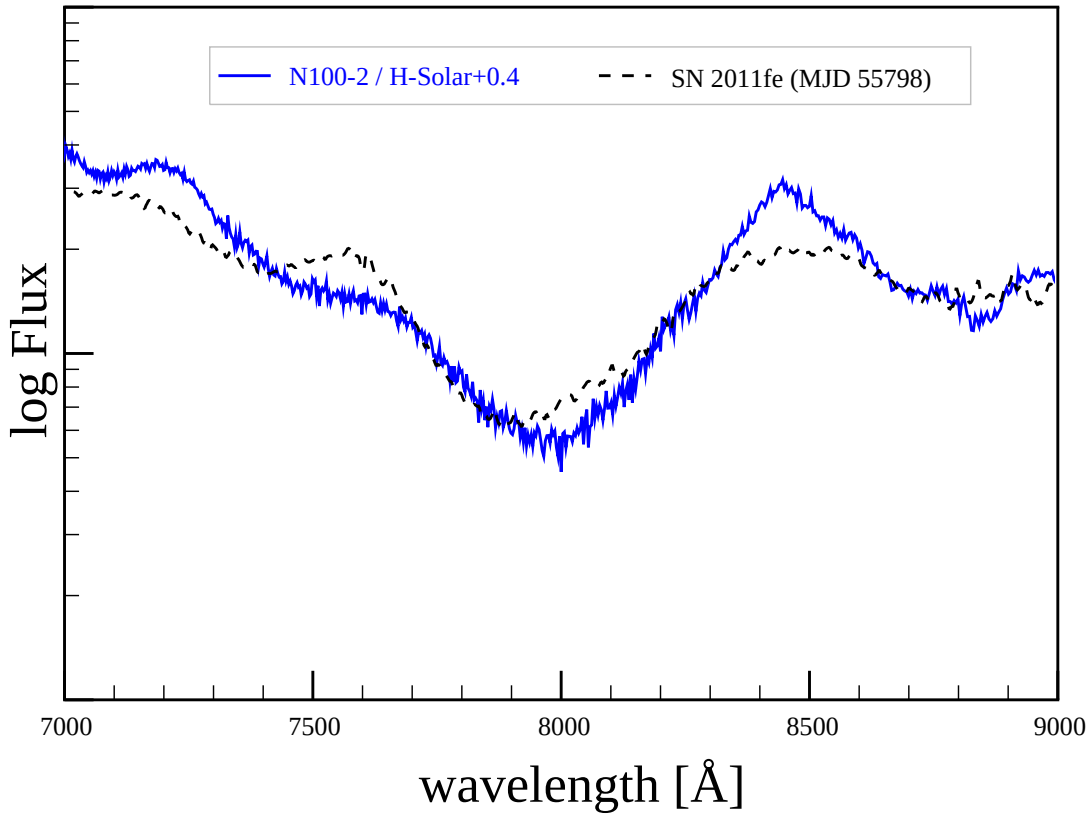

Figure 5.7: Same as Figure 5.5 at 2 d after the explosion, but for a model that represents a combination of depletion of calcium in the ejecta and enhancement of calcium in shell (-2 dex relative to the Seitenzahl et al. (2013) N100 model with stable nuclides, +0.4 dex above solar value in the shell) to better fit the observed CaNIR feature. The overall fit is reasonably good, through the P Cygni peak is slightly too strong and sharp, and the blue side of the CaNIR feature is slightly too round. A color figure is available online.

5.6. The Ca II H&K feature (not shown) is not affected by the choice of calcium within the ejecta or shell. This model captures the width and depth of the CaNIR feature reasonably well, though the peak of P Cygni emission is slightly too sharp and has slightly too much flux. The sharpness of the P Cygni peak may be in part due to the absorption feature near 8600 Å. The blue edge of the CaNIR feature is slightly too rounded relative to the observed feature.

5.4.1.2 Solar-type with helium substrate

Figure 5.8 shows the spectra that result from shells with a helium substrate, again using the N100+0 abundance model for the ejecta. A purely solar abundance of calcium in the shell is insufficient to generate the observed CaNIR HVF due to the calcium being more likely to be in a higher ionization state (e.g. Ca III) because of the higher ionization potential of helium and associated lower electron density in the gas. For He-Solar+0.0 model, the CaNIR feature is almost entirely photospheric, lacking evidence of a HVF. Calcium enhancement in the shell of 1 dex above solar levels produces a weak calcium HVF, but an enhancement of 2 dex above the solar value results in a very strong calcium feature. We have not attempted to generate a better fit for the shells with a helium substrate. We estimate that, for the N100+0 abundance model for the ejecta, a shell enhancement of about 1.3 dex will produce a reasonably good fit to the observed feature of SN 2011fe. Other than the CaNIR feature, the spectrum resulting from a shell with a helium substrate is identical to that of a shell with a hydrogen substrate, i.e. there are no helium absorption or emission features and the Ca II H&K feature is unaffected by calcium within the shell.

5.4.1.3 Solar-type with carbon-oxygen substrate

Figure 5.9 shows the spectra that result from shells with a carbon-oxygen substrate, again using the N100+0 abundance model for the ejecta. A purely solar abundance of calcium in the shell results in a feature that is similar to that observed in SN 2011fe. The models that include a carbon-oxygen substrate are nearly identical to those with a hydrogen substrate for the shell due to the similarity of ionization potential for hydrogen, carbon, and oxygen. Similar to the hydrogenic shell, a enhancement of about +0.4 dex of calcium in the shell relative to a solar abundance will result in a reasonably good fit to the observed feature of SN 2011fe. There is no evidence of any effect upon carbon or oxygen absorption features due to the carbon and oxygen in the shell at this epoch. In general, the spectrum resulting from the models with a carbon-oxygen substrate is similar to that of the models with a hydrogen substrate due to the ionization potentials of hydrogen, carbon, and oxygen being very similar.

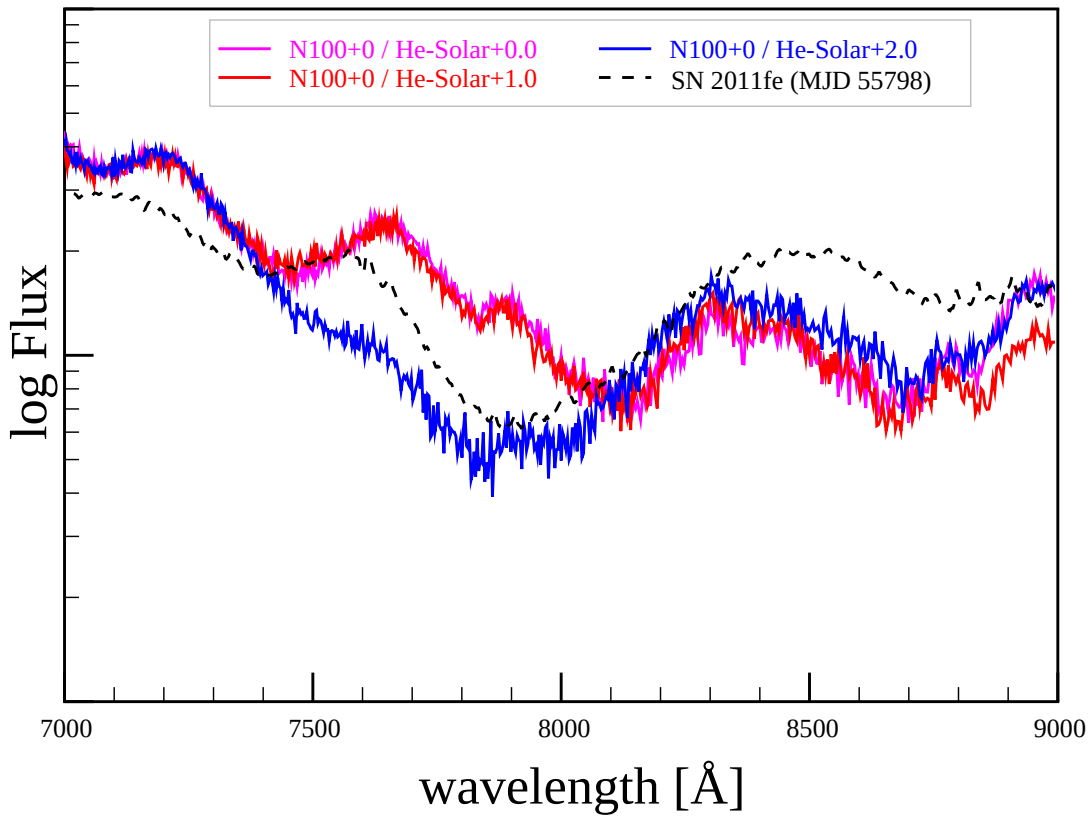

Figure 5.8: Like Figure 5.5 at 2 d after the explosion, but for a shell with a helium substrate and calcium enhancement in the shell ranging from 0 – +2 dex. At 0 – +1 dex enhancement above a solar abundance of calcium, there is little to no effect on the CaNIR feature. An enhancement of 2 dex results in an extremely strong and extended feature. The Ca II H&K feature is only weakly affected by the calcium within the shell at this epoch. The helium substrate requires more enhancement of calcium within the shell relative to that of the hydrogen (Figure 5.5) or carbon-oxygen (Figure 5.9) substrates. A color figure is available online.

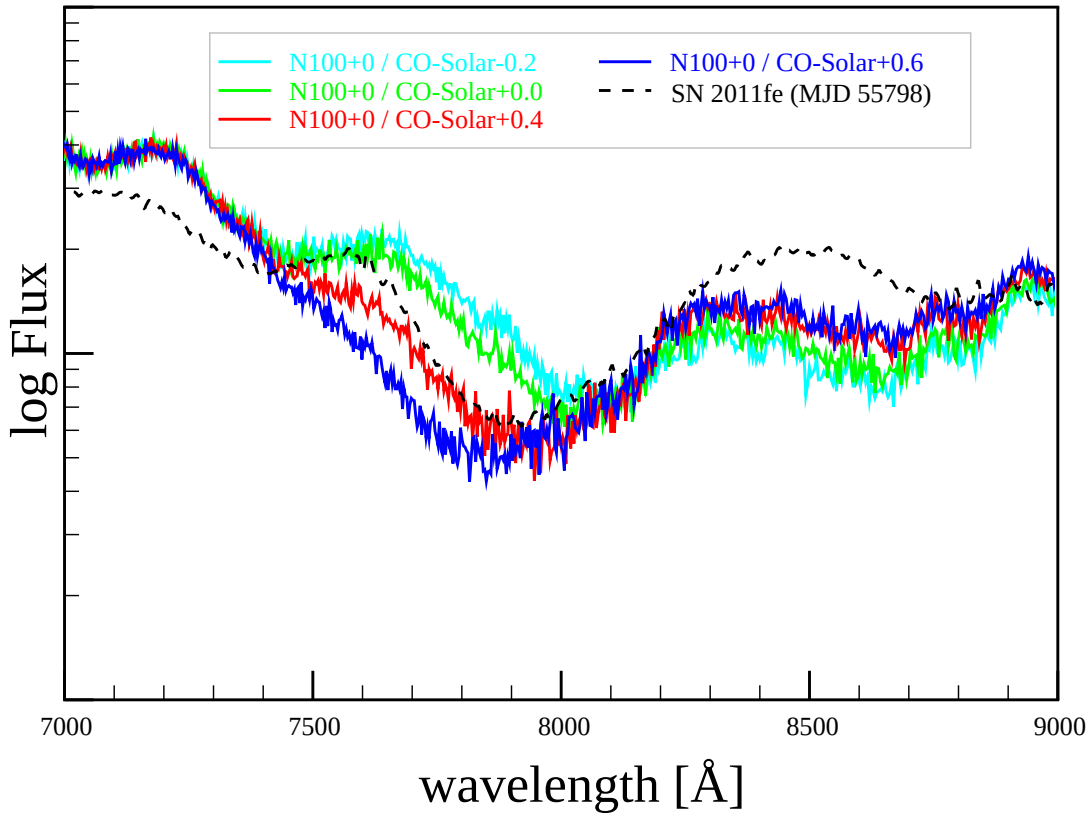

Figure 5.9: Like Figure 5.5 at 2 d after the explosion, but for a shell with a carbon-oxygen substrate and calcium enhancement or depletion ranging from $-0.2 - +0.6$ dex. These models tend to be very similar to those with a hydrogen substrate. An enhancement in calcium within the shell of $+0.2 - +0.4$ dex provides a reasonably good fit to the observed feature in SN 2011fe. A color figure is available online.

5.4.1.4 Shen & Moore-type envelopes

Figure 5.10 demonstrates the synthetic spectra resulting from Shen & Moore (2014) type abundances within the shell, as given in Table 5.2. Of the three models considered, that with a helium envelope of 0.005 $M_\odot$ fits the observed feature of SN 2011fe most closely. As this model does not include any calcium in the shell, the CaNIR feature is the result of only absorption within the ejecta and does not reproduce the high velocity wing of the feature. Despite the shell containing over 22 per cent silicon, there is no evidence of a HVF in the Si II 6355 Å or other silicon features. This is related in part to the lack of calcium HVF in the helium substrate — the helium does

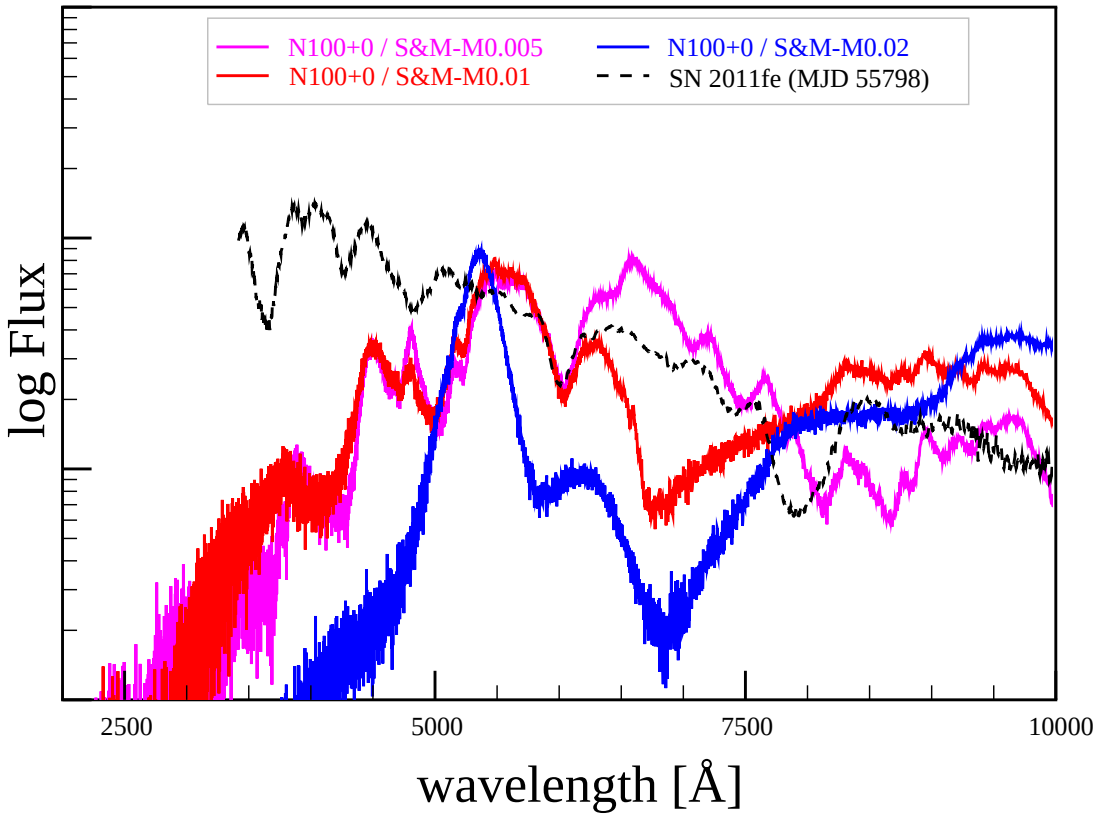

Figure 5.10: Like Figure 5.4 at 2 d after the explosion, but for a shell with Shen & Moore (2014) type abundances. The model with a 0.005 $M_\odot$ envelope is shown in magenta, the 0.01 $M_\odot$ envelope is shown in red, and the 0.02 $M_\odot$ envelope is shown in blue. The 0.01 $M_\odot$ model results in a deep and extended near-infrared feature; the 0.02 $M_\odot$ model results in an extremely extended feature that blends with the Si II 6355 Å feature. The 0.005 $M_\odot$ model does not contain calcium, so there is no calcium HVF; despite containing over 22 per cent silicon, there is also no evidence of a Si II HVF. A color figure is available online.

not ionize easily, leading to lower electron density and higher ionization state of the silicon within the shell.

The 0.01 $M_\odot$ envelope model is similar to that of the helium substrate model with 3 dex enhancement of calcium, with a CaNIR feature extending to about 6300 Å; the 0.02 $M_\odot$ envelope model generates a strong calcium feature between about 5000 – 7500 Å. These two models clearly can be ruled out at this epoch.

5.4.2 5 days after the explosion

5.4.2.1 Solar-type with hydrogen substrate

Figure 5.11 shows the spectra that result from abundance model N100+0 for the ejecta and the hydrogen substrate abundance models for the shell at 5 d after the explosion. There continues to be no evidence of hydrogen absorption or emission within the synthetic spectra at this epoch, nor any effect of the calcium within the shell upon the Ca II H&K feature. Figure 5.12 focuses on the CaNIR feature. At this epoch, an enhancement of near 1 dex of calcium within the shell, relative to a solar abundance, is required to match the CaNIR HVF of SN 2011fe. Enhancement of calcium by 2 dex within the shell causes an excessively strong feature. The blue edge of the feature is greatly softened by the material within the shell.

The Si II 6355 Å and O I 7773 Å features resulting from the models are stronger than the observed features at this epoch, with the O I feature being particularly enhanced. Both of these are associated with the ejecta rather than the shell and may represent an overabundance of silicon and oxygen at velocities higher than that of the photosphere within either the Gamezo et al. (2005) explosion model or an overabundance in the yields of oxygen and silicon within the Seitenzahl et al. (2013) N100 model.

Figure 5.13 shows the effect of calcium within the ejecta on the synthetic spectra, depleting the calcium yield relative to the Seitenzahl et al. (2013) N100 model with stable nuclides by -5 – 0 dex. The effect of the ejecta on the CaNIR feature is entirely redward of 7900 Å, with the minimum occurring near 8150 Å. There is a significant HVF between 7800 – 8000 Å that cannot be explained entirely by the ejecta at this epoch. It is again not clear that any one model of abundance in the ejecta results in the CaNIR feature better fitting the observed feature at this epoch, though a calcium yield within -3 – 0 dex of the Seitenzahl et al. (2013) N100 model is likely necessary to explain the PVF.

Figure 5.14 shows an effort to produce a best combination of ejecta and shell abundances to match the observed CaNIR feature of SN 2011fe. We select a depletion of 0.3 dex of calcium relative to the Seitenzahl et al. (2013) N100 model with stable nuclides, and 1.0 dex of enhancement of calcium within the shell, relative to a solar value. This model represents a balance between matching the depth of the feature blueward of 8000 Å, while avoiding excessive absorption blueward of 7800 Å. In this

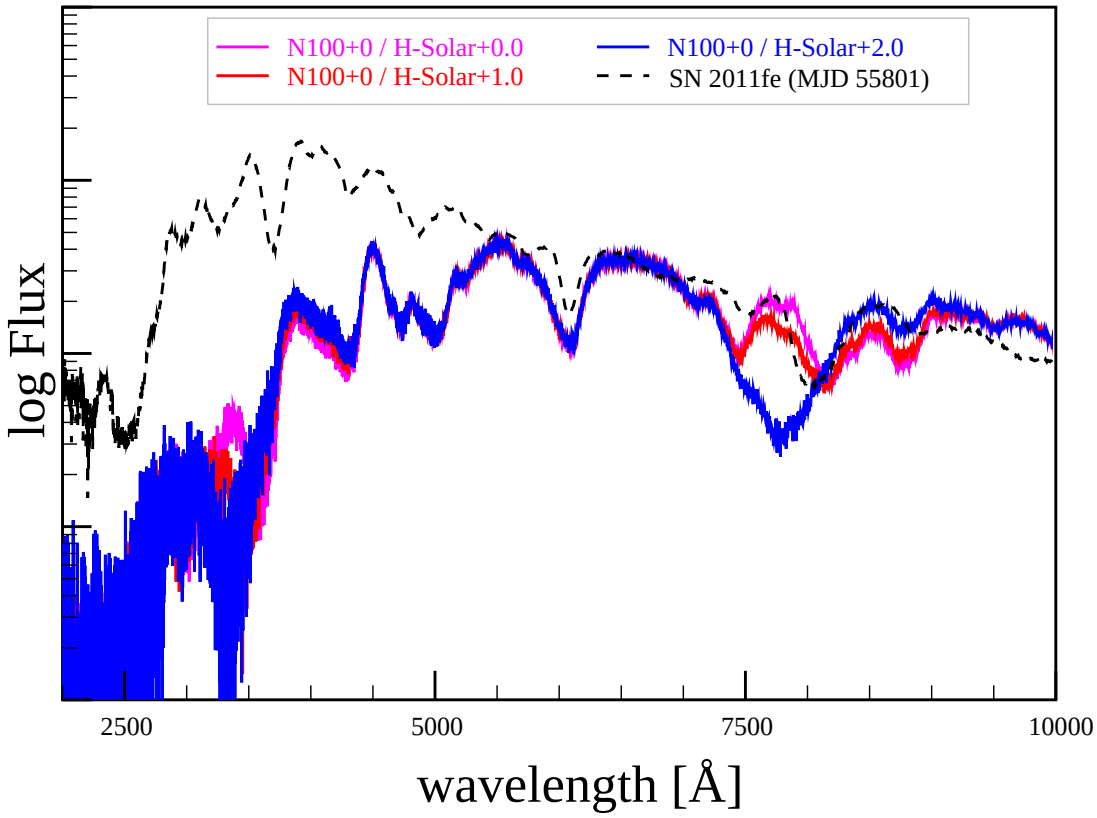

Figure 5.11: Like Figure 5.4 but at 5 d after the explosion, and with calcium enhancement in the shell ranging from 0 – +2 dex. At this epoch, the calcium in the shell continues to only affect the CaNIR feature. A color figure is available online.

model, the P Cygni emission is slightly too weak compared to the observed CaNIR feature.

5.4.2.2 Solar-type with helium substrate

Figure 5.15 shows the synthetic spectra at 5 d for the shells with a helium substrate. For calcium abundances in the shell at up to 3 dex above a solar value there is no effect upon the CaNIR feature, although there is a small effect upon the Ca II H&K feature, shown in Figure 5.16. An enhancement of 4 dex above a solar value results in an extremely strong and extended CaNIR feature.

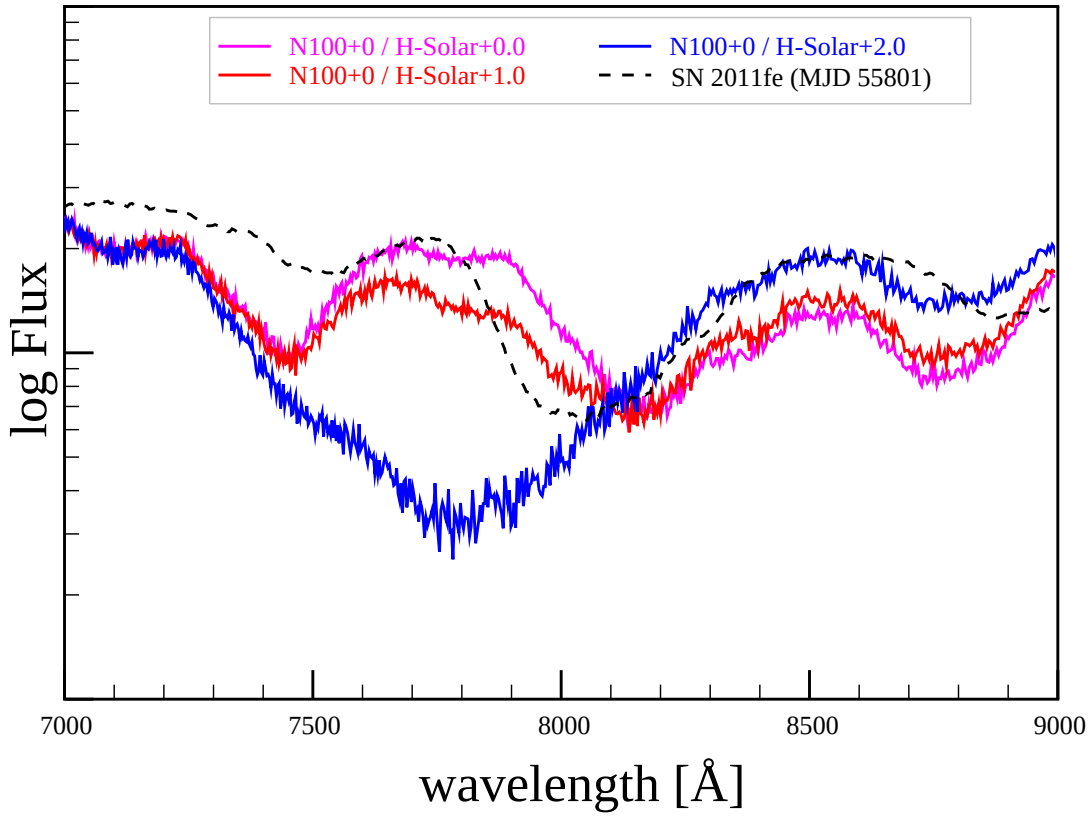

Figure 5.12: Like Figure 5.11 but focused on the CaNIR feature. The flattening of the P Cygni peak of the I I 7773 Å feature (near 7550 Å) for the shell with an enhancement of +1 dex of calcium is the HVF. The enhancement of calcium within the shell required to generate a HVF at this epoch is a factor of about 10 greater than the enhancement required at 2 d; we discuss the meaning and implications of this in Sec. 5.4.4. A color figure is available online.

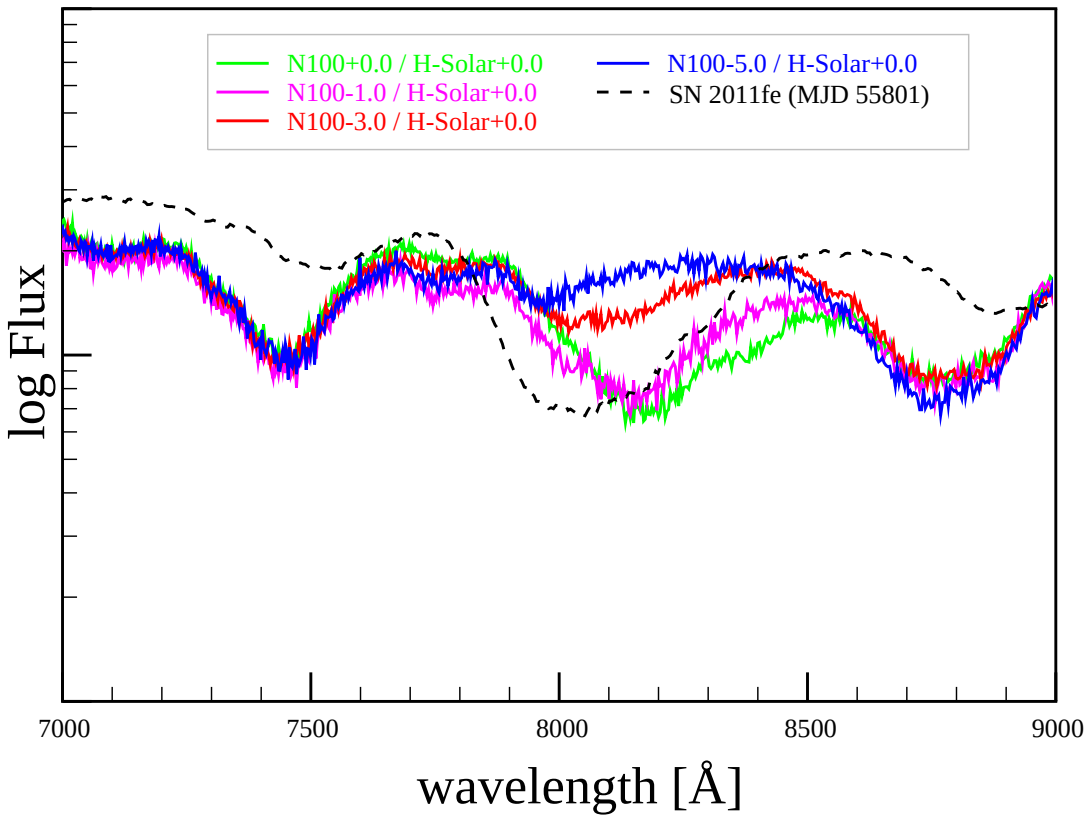

Figure 5.13: Like Figure 5.12 but at 5 d after the explosion and varying the calcium abundance in the ejecta. The calcium within the ejecta tends to affect only the appearance of the feature between 8000 – 8500 Å. A calcium depletion of -2 – -1 dex relative to the Seitenzahl et al. (2013) N100 model with stable nuclides may be the best approximation of the observed feature for a shell with a solar abundance of calcium. It is notable that there is a slight knee near 8300 Å that is visible in the observed feature as well as that associated with the Seitenzahl et al. (2013) abundance but is weaker or not apparent when the calcium is depleted. A color figure is available online.

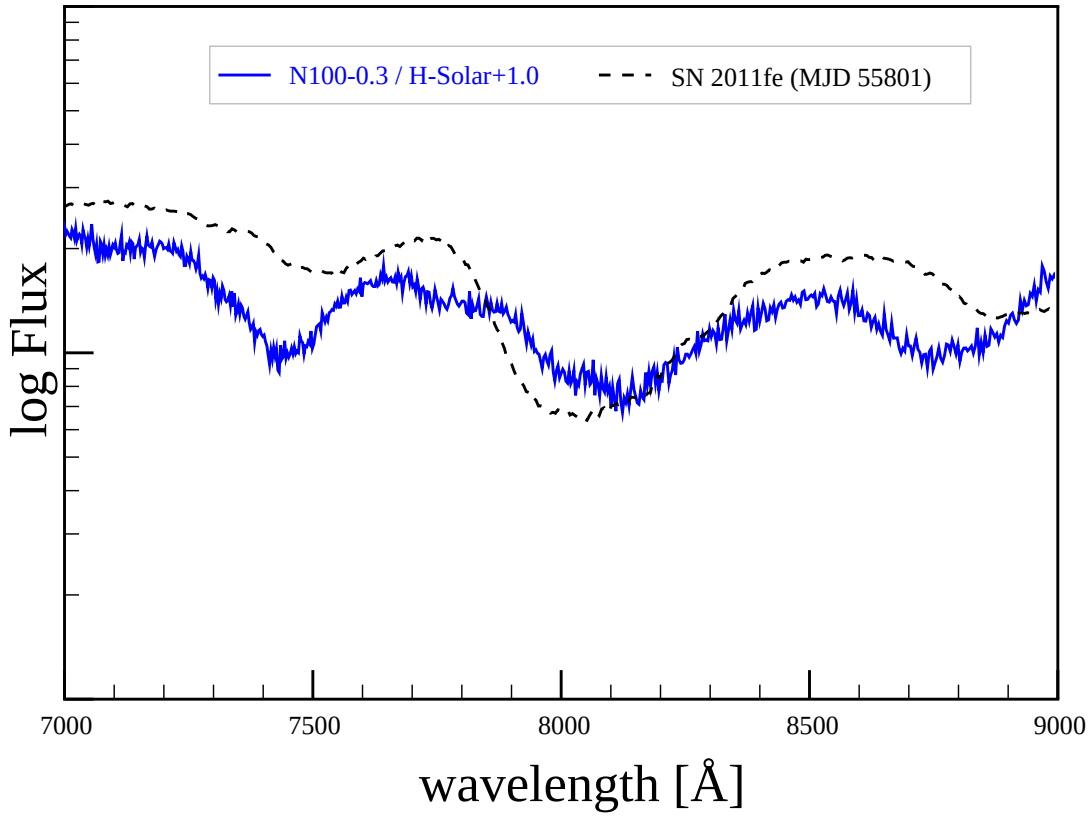

Figure 5.14: Same as Figure 5.12 at 5 d after the explosion, but using abundances that represents a combination of depletion of calcium in the ejecta and enhancement of calcium in shell that provides a better fit to the CaNIR feature. The abundance of calcium in the shell is a balance between attempting achieve the observed depth between 7900 – 8000 Å, and the peak near 7700 Å. The P Cygni emission near 8500 Å is slightly weaker than observed in SN 2011fe. A color figure is available online.

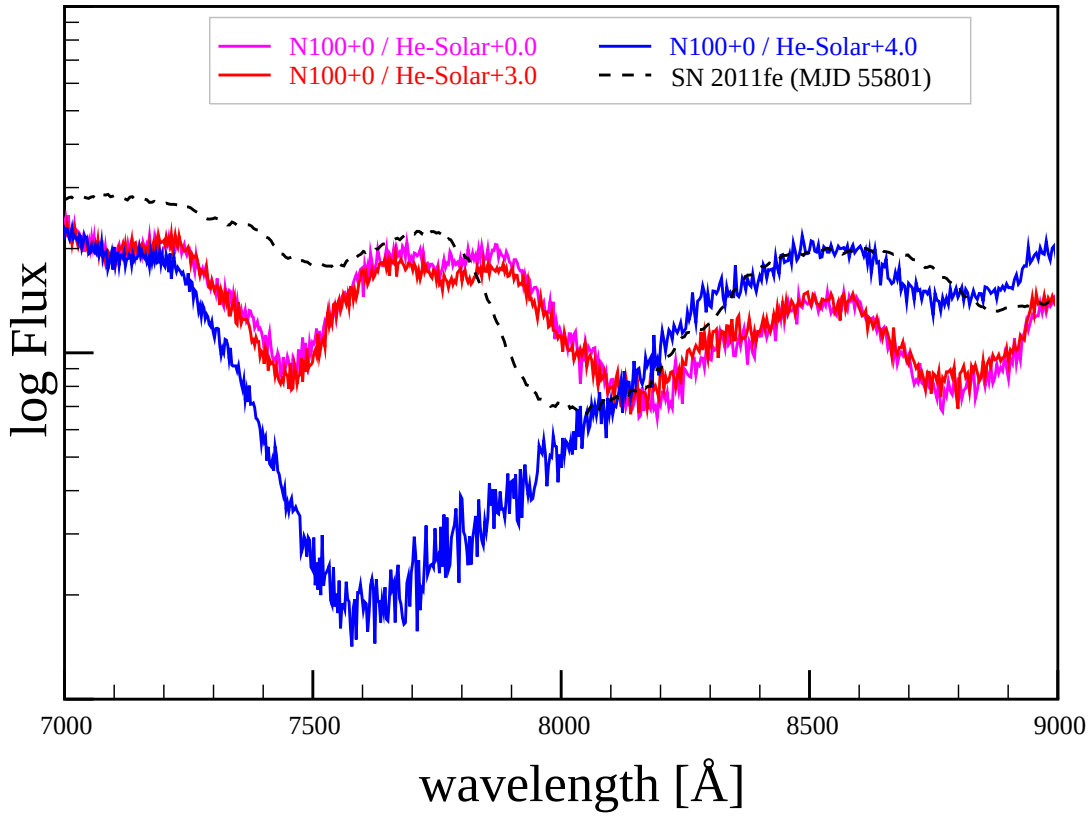

Figure 5.15: Like Figure 5.12 at 5 d after the explosion, but for a shell with a helium substrate and calcium enhancement in the shell, relative to a solar value, ranging from 0 – +4 dex, and focused on the CaNIR features. An abundance of +3 dex relative to solar is nearly indistinguishable from a purely solar abundance of helium at this epoch. Enhancement by an additional +1 dex results in an excessively strong feature. A color figure is available online.

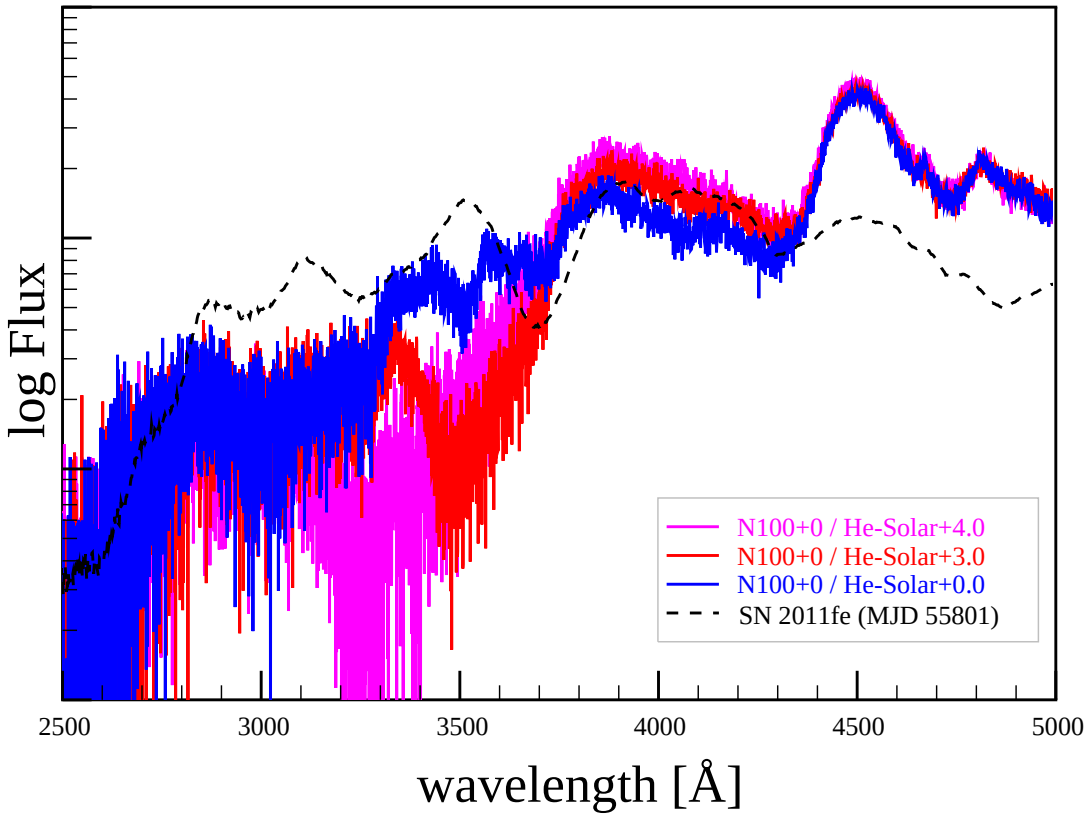

Figure 5.16: Like Figure 5.12 at 5 d after the explosion, but for a shell with a helium substrate and calcium enhancement in the shell, relative to a solar value, ranging from 0 – +4 dex, and focused on the Ca II H&K feature. There is some enhancement of the feature even at 3 dex above a solar abundance of calcium within the shell. A color figure is available online.

5.4.2.3 Solar-type with carbon-oxygen substrate

Figure 5.17 shows the synthetic spectra at 5 d for a shell with a carbon-oxygen substrate with an enhancement in calcium within the shell of 0 – 2 dex above solar value. For these models we see some evidence of a CaNIR HVF for all shells with solar abundance or more of calcium for the CaNIR feature. The CaNIR feature is clearly too strong for an abundance of 2 dex above a solar level of calcium. Like the models with a hydrogen substrate, the O I 7773 Å feature and Si II 6355 Å features are too strong due to the ejecta and are unaffected by material in the shell.

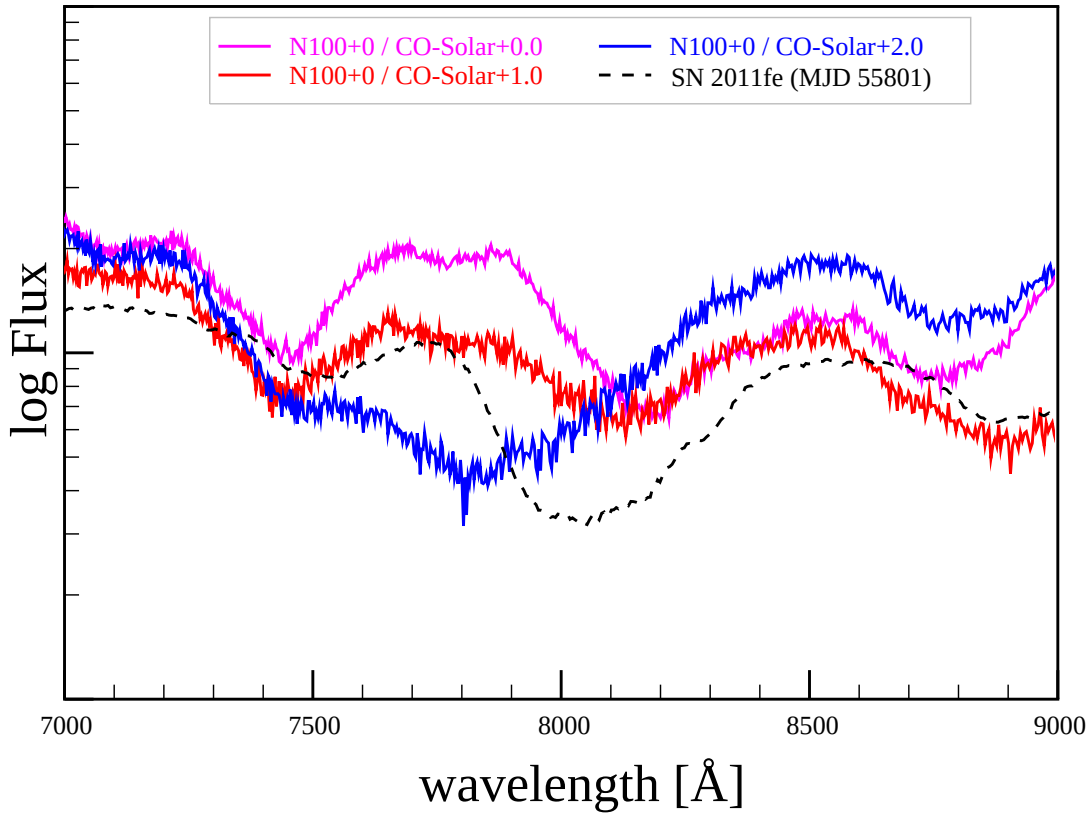

Figure 5.17: Like Figure 5.12 at 5 d after the explosion, but for a shell with a carbon-oxygen substrate and calcium enhancement within the shell ranging from $0 - +2$ dex. At $0 - +1$ dex of enhancement of calcium within the shell, the HVF tend to be weak and extended in range. For this composition of the ejecta, an enhancement of $+2$ dex of calcium within the shell causes excessive absorption. A color figure is available online.

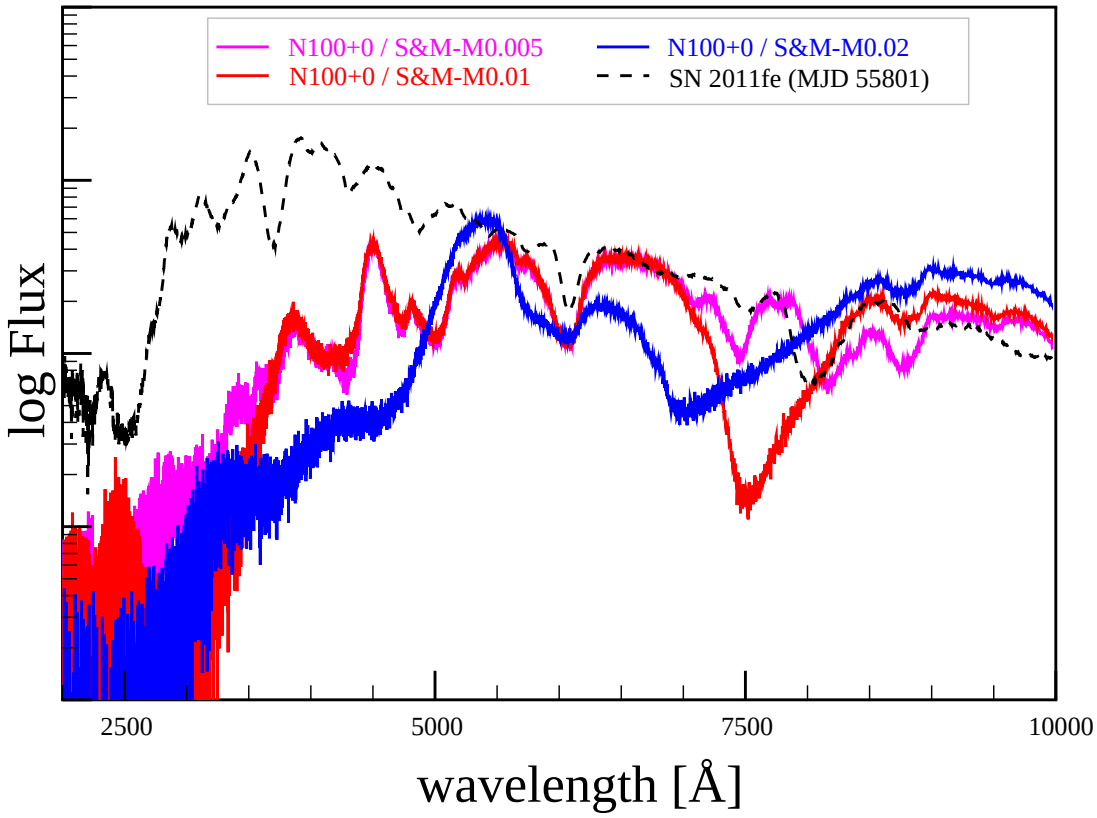

Figure 5.18: Like Figure 5.11 at 5 d after the explosion, but using Shen & Moore (2014) type abundances for the shell. The model with a 0.005 $M_\odot$ envelope is shown in magenta, the 0.01 $M_\odot$ envelope is shown in red, and the 0.02 $M_\odot$ envelope is shown in blue. The 0.01 and 0.02 $M_\odot$ models result in an extremely deep and extended CaNIR feature that does not match any observed features. A color figure is available online.

5.4.2.4 Shen & Moore-type envelopes

Figure 5.18 shows the synthetic spectra at 5 d for the Shen & Moore (2014) type abundance models. The models with an envelope of mass 0.01 $M_\odot$ and 0.02 $M_\odot$ have an excessively strong and extended CaNIR feature; the 0.02 $M_\odot$ model also shows evidence of an HVF for the Si II 6355 Å feature that is much stronger than those that are observed. The model with an envelope of mass 0.005 $M_\odot$ is very similar to that of the models with a helium substrate for the shell but does not have any enhancement of calcium features due a the absence of calcium in the envelope.

5.4.3 9 days after the explosion

At 9 d after the explosion, there appears a feature in the spectra of SN 2011fe at about 8240 Å that is clearly the HVF. As you will see in the following subsections and figure, it is difficult to reproduce this feature with our TARDIS models.

5.4.3.1 Solar-type with hydrogen substrate

Figure 5.19 shows the spectra that result from abundance model N100+0 for the ejecta and the hydrogen substrate abundance models for the shell at 9 d after the explosion. There continues to be no evidence of hydrogen absorption or emission within the synthetic spectra at this epoch, but the calcium within the shell does affect the Ca II H&K feature. The O I 7773 Å and Si II 6355 Å features better match the observed features in SN 2011fe, although both features have minima that are too blue by ∼100 Å. Figure 5.20 focuses on the CaNIR feature. Up to +3 dex of enhancement of calcium above solar value within the shell has little to no effect on the CaNIR feature. An enhancement of +4 dex produces a strong HVF between 7500 – 8000 Å. At this epoch, the calcium within the ejecta results in a feature that is too blue by about 200 Å, or at least is lacking absorption near 8300 Å. Figure 5.21 shows the Ca II H&K feature at this epoch. Enhancement of calcium within the shell leads to an overly deep and extended feature; this provides a constraint on the degree to which calcium can be enhanced in the shell without producing an overly strong Ca II H&K feature.

Figure 5.22 shows the effect of calcium within the ejecta on the synthetic spectra, depleting the calcium yield relative to the Seitenzahl et al. (2013) N100 model with stable nuclides from -5 – 0 dex. The CaNIR feature becomes noticeably weaker with even a modest depletion of calcium in the ejecta. At this epoch, the observed feature in SN 2011fe is better matched by little to no depletion of calcium within the ejecta.

Figure 5.23 shows an effort to produce a best combination of ejecta and shell abundances to match the observed CaNIR feature of SN 2011fe. We select an enhancement of +0.5 dex of calcium in the ejecta, relative to the Seitenzahl et al. (2013) N100 model with stable nuclides, and +3.0 dex of enhancement of calcium within the shell, relative to a solar value. This model results in slightly too much absorption near 8100 Å, due to absorption within the ejecta, but matches the red side of the feature reasonably well. Even with our best fitting model, we are unable to recreate

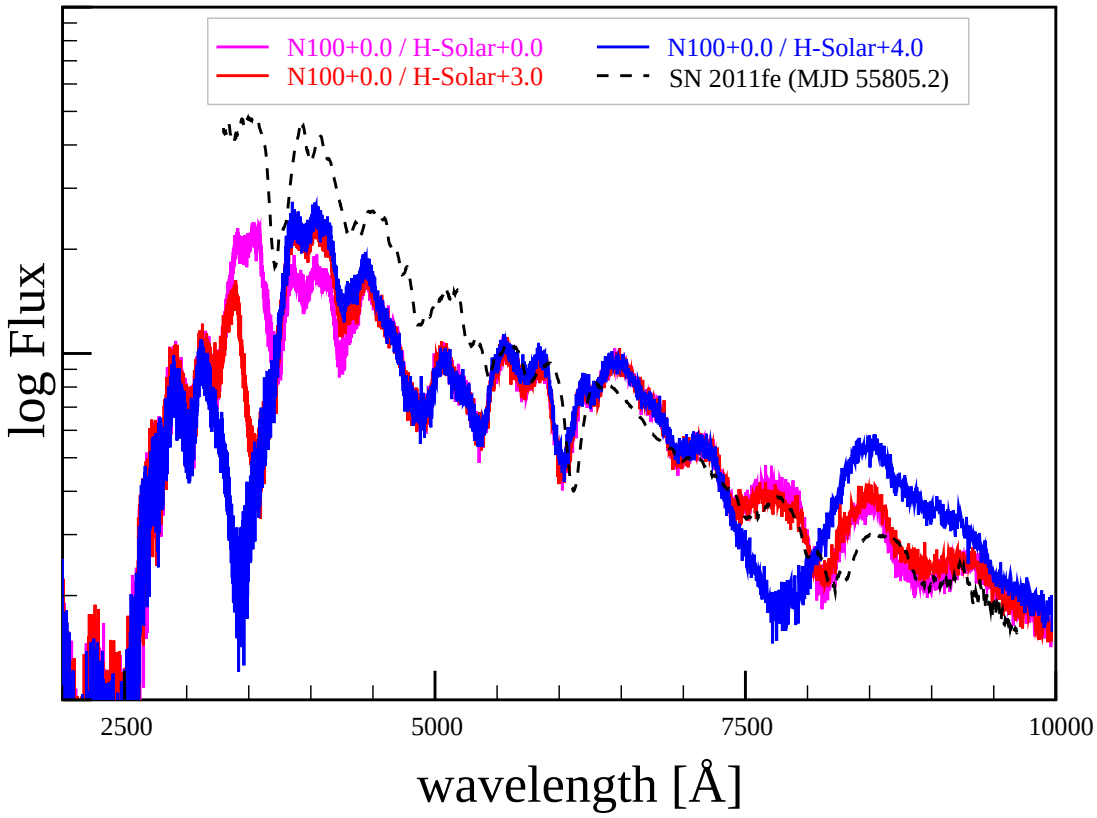

Figure 5.19: Like Figure 5.4 but at 9 d after the explosion, and for a shell with calcium enhancement between 0 – +4 dex. At this epoch, the calcium within the shell affects both the CaNIR and Ca II H&K features. There continues to be no evidence of absorption or emission due to the hydrogen in the shell. A color figure is available online.

the three components of the CaNIR feature seen in SN 2011fe at this epoch.

5.4.3.2 Solar-type with helium substrate

Figure 5.24 shows the synthetic spectra at 9 d for the helium substrate abundance models. At this epoch, the material within the shell requires an enhancement of over 5 dex above solar value in order to have a significant effect upon the CaNIR feature. Like the models with a hydrogen substrate, enhancement of calcium within the shell tends to produce an excessive HVF, though an enhancement of over 5 dex is required for this to occur with the helium substrate. The CaNIR PVF tends to be slightly too

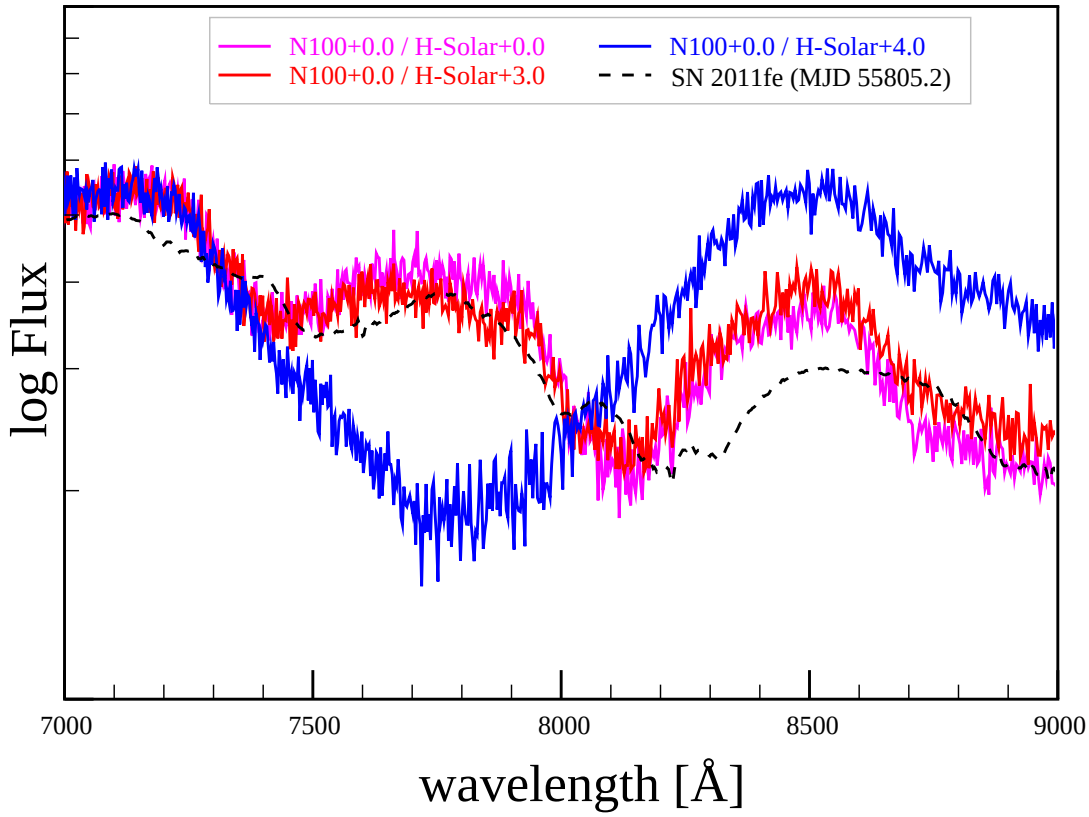

Figure 5.20: Like Figure 5.19 at 9 d after the explosion, but focused on the CaNIR feature. An enhancement of +4 dex results in a strong, broad CaNIR HVF, while there is little difference between the models with 0 – +3 dex of calcium enhancement. At this epoch, the feature resulting from the models produces an acceptable fit to the the blue side of the CaNIR feature, but performs poorly near 8200 Å. A color figure is available online.

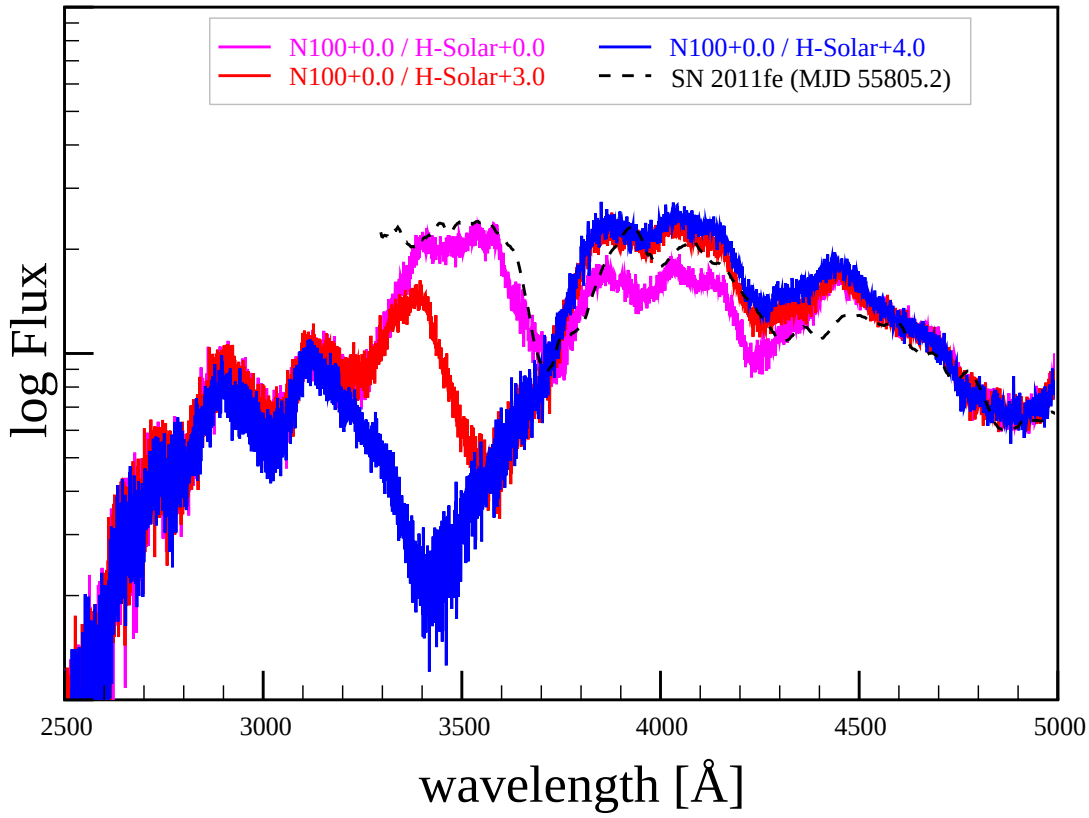

Figure 5.21: Like Figure 5.20 at 9 d after the explosion, but focused on the Ca II H & K feature. A calcium enhancement of +1 dex or more above solar value for material in the shell affects the strength of the feature and appears as a HVF. A calcium abundance near solar provides a better fit to this feature at this epoch. A color figure is available online.

blue. There is no evidence of helium absorption or emission features at this epoch.

5.4.3.3 Solar-type with carbon-oxygen substrate

Figure 5.25 shows the synthetic spectra at 9 d for the models with a carbon-oxygen substrate, focused on the CaNIR feature. At this epoch, the feature is only weakly affected by the calcium within the shell, as long as the enhancement of the calcium is less than ∼4 dex. At 5 dex of enhancement, an excessively strong HVF is produced. At a purely solar abundance of calcium within the shell, this model is indistinguishable from that of a hydrogen or helium substrate with an equivalent amount of calcium.

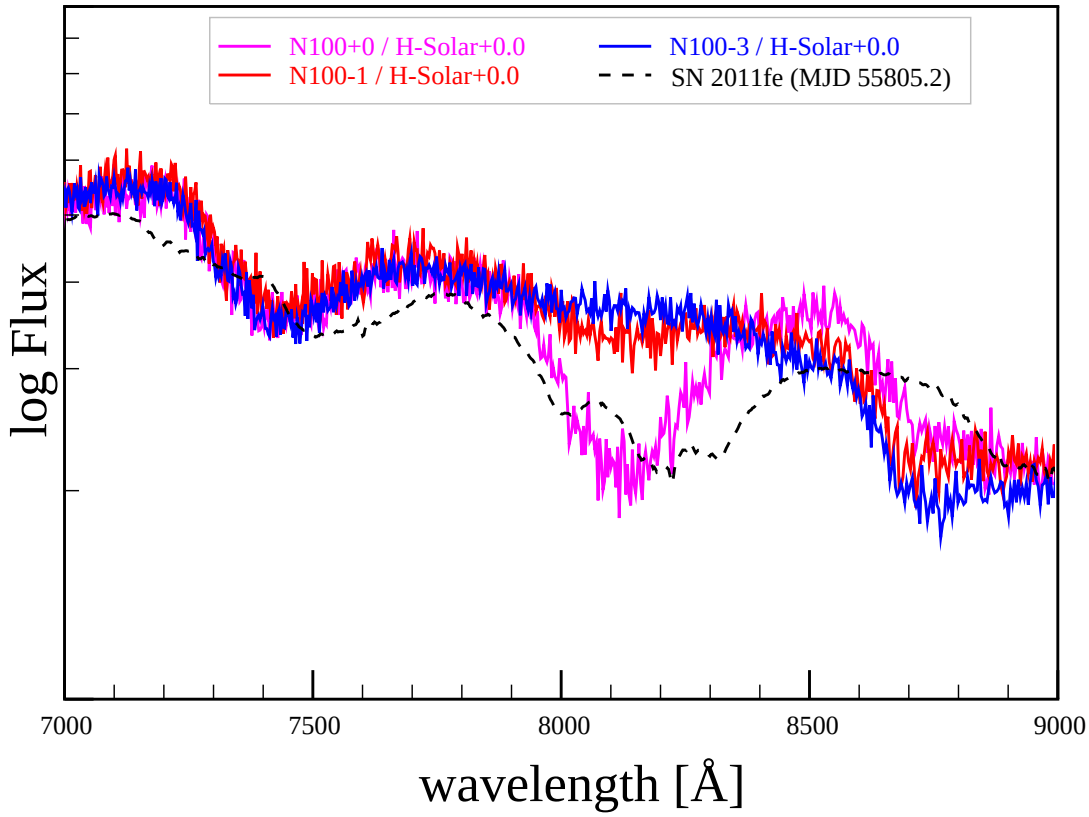

Figure 5.22: Like Figure 5.20 at 9 d after the explosion, but showing variation in the calcium abundance in the ejecta. A reduction of -1 dex of calcium within the ejecta notably reduces the strength of the PVF at this epoch, and does not do a good job of recreating the feature. An abundance of calcium that is near that of the Seitenzahl et al. (2013) N100 model with stable nuclides is likely the best match at this epoch. A color figure is available online.

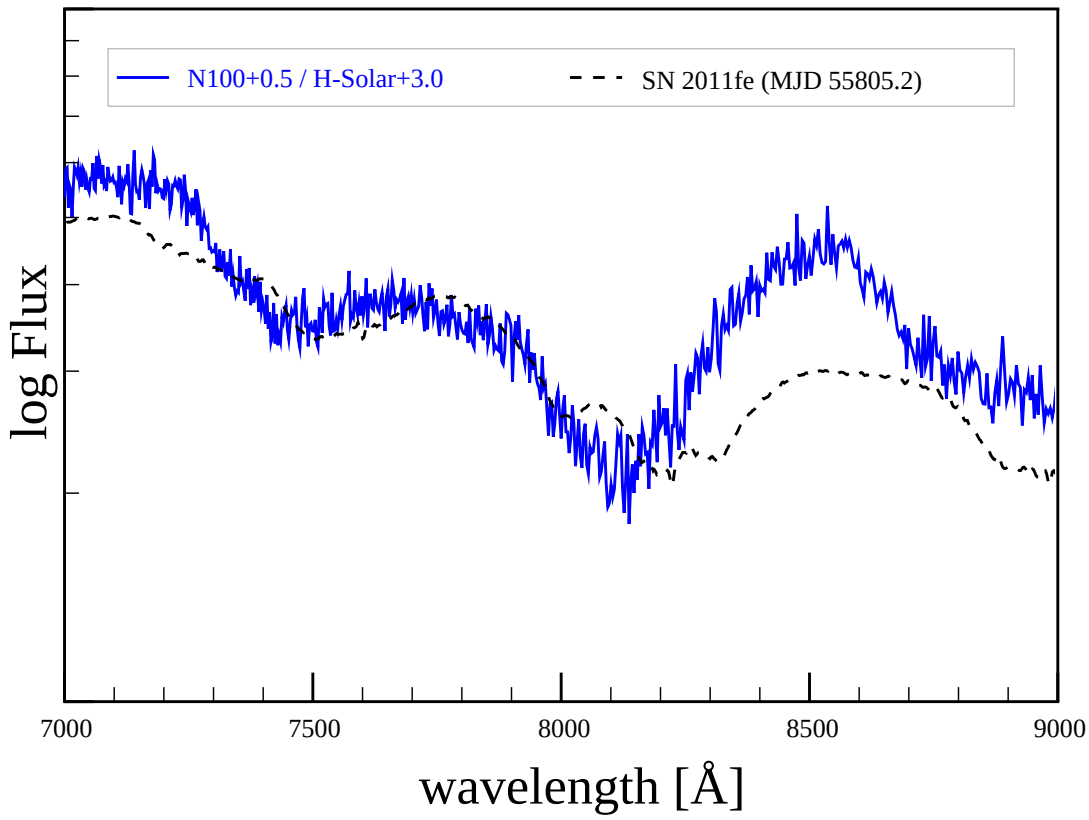

Figure 5.23: Same as Figure 5.20 at 9 d after the explosion, but using abundances that represent a combination of enhancement of +0.5 dex of calcium in the ejecta and +3 dex in the shell that provides a better fit to the CaNIR feature. At this epoch this fit fails to capture the absorption on the redward side of the feature. We were unable to reproduce the apparent multiple component nature of the feature at this epoch. The multiple components of the PVF may be a result of variations in calcium abundance within the ejecta not captured by the explosion models that we have used. A color figure is available online.

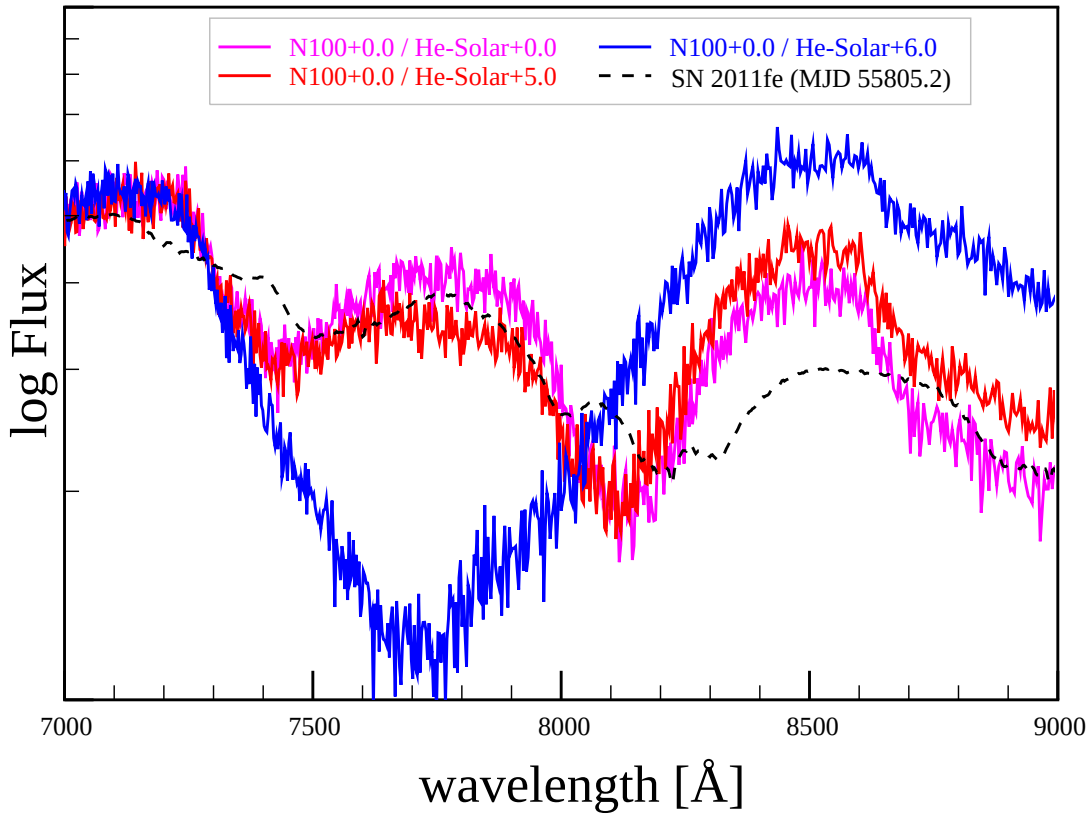

Figure 5.24: Like Figure 5.20 at 9 d after the explosion but for a shell with a helium substrate with calcium enhancement ranging from 0 – 6 dex in the shell. The material within the shell has little to no effect on the spectrum as epoch unless the calcium is enhanced by over 5 dex. Like the models with a hydrogen substrate, the PVF is slightly too blue. A color figure is available online.

5.4.3.4 Shen & Moore-type envelopes

Figure 5.26 shows the synthetic spectra at 9 d for the Shen & Moore (2014) abundance models. At this epoch, the spectra generated from the 0.005 $M_\odot$ and 0.01 $M_\odot$ envelope models match that of the solar-type abundance models. The 0.02 $M_\odot$ model results in the flux blueward of 3500 Å to be affected, chiefly depletion by the iron present in the shell, and making the Ca II H&K feature indistinct due to blending with absorption bands in the near-UV.

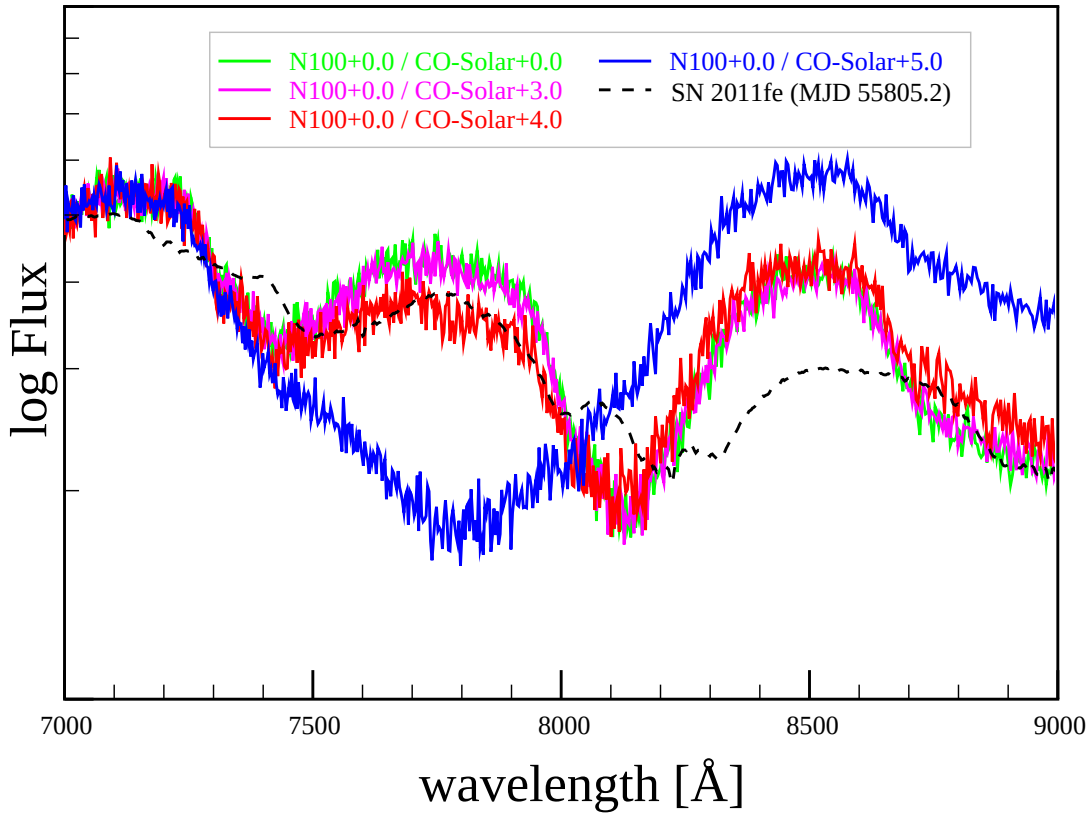

Figure 5.25: Like Figure 5.20 at 9 d after the explosion, but for a shell with a carbon-oxygen substrate and calcium enhancement ranging from 0 – 5 dex in the shell. At 3 dex of calcium enhancement or less, the material within the shell has little to no effect CaNIR feature at this epoch; there is slight evidence of a HVF with an enhancement of 4 dex, and a strong HVF at an enhancement of 5 dex. A color figure is available online.

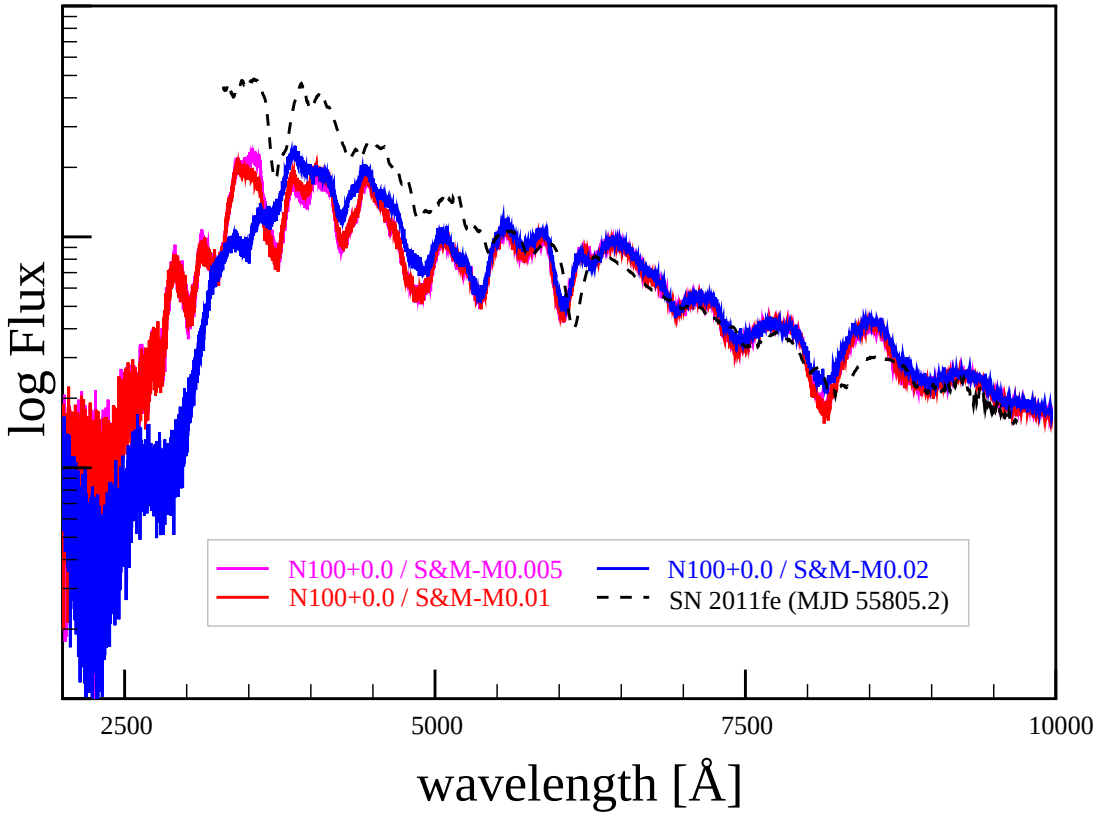

Figure 5.26: Like Figure 5.19 at 9 d after the explosion, but with Shen & Moore (2014) type abundances for the shell. The model with a 0.005 $M_\odot$ envelope is shown in magenta, the 0.01 $M_\odot$ envelope is shown in red, and the 0.02 $M_\odot$ envelope is shown in blue. The 0.01 and 0.005 $M_\odot$ models are nearly indistinguishable at this epoch, with the exception of some additional absorption by the 0.01 $M_\odot$ envelope on the blue side of the Ca II H&K feature. The 0.02 $M_\odot$ model results in a weaker CaNIR feature as well as weaker features blueward of ∼5000 Å, in addition to continued depletion of flux blueward of ∼4000 Å. A color figure is available online.

5.4.4 Discussion

In the prior subsections, we have considered shells with a mass of 0.005 $M_\odot$ with a hydrogen, helium, or carbon-oxygen substrate and varying levels of enhancement of depletion of calcium within the shell or ejecta. We find that the substrate has no effect on the spectrum, other than a higher abundance of calcium required in shells with a helium substrate due to the higher ionization potential (and hence lower electron density) of helium. We also considered shells with masses of 0.005, 0.01, and 0.02 $M_\odot$ and employing related abundances of the helium envelopes of Shen & Moore (2014). The envelopes with a mass of 0.005 $M_\odot$ do not contain calcium, so fail to produce an HVF; the envelopes of 0.01 and 0.02 $M_\odot$ result in overly broad and strong HVF.

Regarding shells with a mass of 0.005 $M_\odot$ with a hydrogen substrate, Shappee et al. (2013) and Botyánszki et al. (2018) find upper limits of 10^{-3} $M_\odot$ and 10^{-4} $M_\odot$, respectively, of hydrogen during the nebular phase of SN 2011fe. These limits are based on the assumption of the hydrogen being stripped from a companion and residing at relatively low velocities ($\sim$1,000–2,000 km s^{-1}) within the ejecta. It is not clear that this limit also applies to hydrogen that lies at the leading edge of the ejecta, well separated from the excitational radiation available from the nickel and cobalt decay nearer the centre of the supernova. For our solar-type abundance models, there is no observable absorption or emission features due to the substrate within the near-ultraviolet to far-infrared range at the epochs that we consider.

A common result for all composition models at 2 and 5 d is that the PVF is too strong using the Seitenzahl et al. (2013) N100 composition model. There are many possible reasons for this: the abundance of calcium as a function of velocity within the ejecta may not be correct due to the combination of elements of similar atomic mass into groups in the explosion models of Gamezo et al. (2005); the distribution of silicon group elements in the explosion models may not represent the real distribution of these elements within SN Ia; the Seitenzahl et al. (2013) N100 explosion model may have an overabundance of calcium relative to other silicon group elements, or the physics that is incorporated into TARDIS does not fully explain the state of calcium within the ejecta. All of these factors likely play some role in affecting the appearance of the feature.

We have not found a consistent abundance of calcium within the shell that can explain the observed HVF. In MW2, we noted that the evolution of the parameters

of the fit were inconsistent with the HVF fading solely due to the reduced density as the shell expands adiabatically. MW2 suggested that the ionization state of calcium within the shell (or ejecta) is likely not constant over the first few weeks after the explosion. While we expect that TARDIS does more accurately determine the ion state of calcium, it still relies on an incomplete approximation of the ionization state of all elements. The varying apparent abundance of calcium that is required may be the result of this approximation. We also note that we have assumed a uniform composition of the shell throughout; if the shell material is not homogeneous there may be less calcium required than we have found here. A non-homogeneous distribution of calcium within the shell may also explain why the blue side of the CaNIR feature for our best fit model has a shallower slope than is observed in SN 2011fe.

At 9 d after the explosion, the CaNIR feature is better explained by only the calcium within the ejecta, although the PVF resulting from our models tends to be too shallow, slightly blue, and does not show the three components of the feature seen in SN 2011fe. The lack of a HVF at this epoch is consistent with the findings of MW2. MW1 suggest that the strength of the PVF would overtake that of the HVF at about 8 d after the explosion, though we note that the photosphere velocity used in MW1 is much faster (by 5,000 – 14,000 km s^{-1}) than the velocities used in this work, leading to a much weaker PVF in MW1 at these early epochs. While Childress et al. (2014) and Silverman et al. (2015) both report a reasonably strong HVF component much later than 9 d after the explosion for SN 2011fe, we note that these works rely on fitting of multiple Gaussian features to an inherently non-Gaussian absorption feature. This fitting technique does not reliably capture the velocity or strength of the HVF once it blends with the PVF; see MW1 sec. 4.1 for further details.

5.4.4.1 Implications of super-solar calcium

In each of the solar-type compositions that we consider at 2 and 5 d, we need a super-solar abundance of calcium in the shell to generate the HVF. While this may be due to incorrect assumptions within TARDIS regarding the ionization or excitation state of calcium, it may accurately reflect the abundance of calcium in the shell. We can speculate on the source of this calcium by considering the possible sources of material for the shell.

If the source of the shell material is a companion star donating material, a super-

solar calcium content may be suggestive of a relatively young companion. The ubiquity of HVF in SN Ia and the expectation that there are likely both long-delay and short-delay SN Ia suggest that many should have older companions with sub-solar abundances of calcium. Post-main sequence stars with masses below $\sim$7 $M_{\odot}$ tend to be depleted in calcium within their atmospheres (Karakas & Lugaro, 2016; Pignatari et al., 2016), so these are less likely to be the source of such calcium.

If the donor star were instead a white dwarf, the average calcium abundance may be solar, but settling of metals toward the center of the white dwarf would deplete the calcium in the outer layers and enhance it within the inner layers (Schatzman, 1958). The details of the merger process then dictate the abundance of calcium within the shell: it could be depleted in calcium, if it forms from the outermost layers of the donor; enhanced in calcium, if it forms from material nearer the core of the companion; or near the original metallicity of the star, if the material of the companion is mixed during the merger or accretion process. The original metallicity of the system should determine the strength of the HVF, suggesting that any SN Ia that originate from population II systems should have weaker calcium HVF. The ubiquity of the CaNIR HVF again argues against this possibility.

Another implication of the calcium content of the shell material being related to the original metallicity of the system suggests that HVF should be weaker with increasing redshift. The comprehensive studies of HVF in SN Ia that have been done to date (Childress et al., 2014; Maguire et al., 2014; Silverman et al., 2015) consider only nearby redshifts and no attempts have been made to evaluate the trend of the strength of the HVF with the redshift of the host galaxy.

Given that the HVF are common, generally similar in strength, and that variations of less than 1 dex in the abundance of calcium within the shell do not have significant effect on the HVF at 5 d and 9 d after the explosion (as well as at 2 d in some cases), it is possible that the calcium that generates the HVF is newly synthesized. This could be explained by material ejected from the supernova at high velocity or by mixing of deeper layers of the supernova with the material in the shell. Our methodology here may be partially capturing that information, although it is unlikely that such ejected material would match our models in terms of density or kinematics.

One mechanism by which freshly synthesized calcium could be introduced into the shell without such models would be through the Rayleigh-Taylor instabilities that occur during the interaction between the shell and ejecta. If this were the source

of the enhanced calcium in the shell, however, there would be a relatively smooth gradient of calcium abundance from the ejecta to the shell material, resulting in an indistinct HVF, unless only the outermost layers of the ejecta are somehow enhanced in calcium due to or prior to the explosion. As the MW1 models were produced through 1-D simulations, they do not include such mixing.

The helium envelopes of Shen & Moore (2014) can also contain freshly formed calcium. We considered envelopes with a mass of 0.005, 0.01, and 0.02 $M_\odot$, none of which produce spectra that are a good match to SN 2011fe or any other SN Ia. We note that the 0.01 and 0.02 $M_\odot$ envelopes generate overly deep and extended calcium features; such features require correct handling of the Lorentzian wings and are not well approximated by TARDIS, but given that the spectra generated by these models are so different than observed spectra we rule these models out as possible explanations of SN Ia. An envelope with a mass near 0.008 $M_\odot$ or 0.09 $M_\odot$ may have the right abundance of calcium after the detonation to generate the observed HVF, though an envelope with a mass of 0.009 $M_\odot$ is likely excluded, as shells with such a high mass are likely to have a photosphere within the envelope at early epochs and result in an HVF that is too slow at later epochs. The calcium abundance as a function of the mass near 0.008 $M_\odot$ has a very steep slope of calcium abundance as a function of mass. While the models of MW1 and Shen & Moore (2014) are dynamically inconsistent, we take this an an indication that the mass of the envelope must be very fine-tuned to generate a calcium HVF that is comparable to those that have been observed. It is not clear why an envelope with such a finely-tuned mass would be favoured for that in which the detonation occurs. If this model is correct, identification of the ratio of calcium : helium required to generate the calcium HVF will provide a precise estimate of the mass of the envelope.

5.5 Conclusion

We have presented synthetic spectra at 2, 5, and 9 d after the explosion of a Type Ia supernova, generated using the Mulligan & Wheeler (2017) models of interaction between the supernova and a compact circumstellar shell using TARDIS (Kerzendorf & Sim, 2014). We apply abundance models to the shells that consist of either a hydrogen, helium, or carbon-oxygen substrate with overall solar abundance of metals

and depletion or enhancement in the calcium abundance, as well as abundance models matching the yields of the Shen & Moore (2014) helium envelope detonation models for envelopes with a mass of 0.005, 0.01, and 0.02 $M_\odot$. We use a Seitenzahl et al. (2013) model N100 stable nuclide yield for abundances within the ejecta, with variations in the calcium abundance to adjust for using an explosion model (Gamezo et al. (2005) model 'c') that groups nucleosynthetic products into five groups (carbon, oxygen, magnesium, silicon, and iron).

We find that solar to super-solar abundances of calcium may be required to generate a high velocity feature in the calcium near-infrared triplet, for models involving the hydrogen, helium, and carbon-oxygen substrates for the material within the shell. In all cases, the substrate leaves no imprint upon the spectra, although the models with a helium substrate require a greater enhancement of calcium than do the models with a hydrogen or carbon-oxygen. The need for super-solar abundance of calcium may be the result of the homogeneity of calcium within the shell, or approximations made within TARDIS regarding the ion- or excitation state of calcium.

The Shen & Moore (2014) models are extremely sensitive to the mass of the envelope in terms of generating spectra that are similar to those observed in SN 2011fe at equivalent epochs. An envelope of mass 0.005 $M_\odot$ does not contain calcium and therefore does not produce an HVF, but neither does it produce a Si II HVF despite containing 22 per cent silicon. An envelope of mass 0.01 $M_\odot$ produces an excessively deep and extended (both in wavelength and temporally) CaNIR absorption feature. Our methods suggest than an envelope with a mass near 0.008 $M_\odot$ would likely produce a HVF that is similar to those that have been observed; however, the models considered in Mulligan & Wheeler (2017) and Shen & Moore (2014) are not consistent so we take this only as indication that the mass of the envelope must be finely-tuned rather than having this precise mass. In the lower mass envelopes, the helium : calcium ratio is extremely sensitive to the mass of the envelope, so the ratio that is required to generate the observed HVF would be useful to constrain the mass of the envelope should the helium-envelope detonation model be found to be the cause of SN Ia.

Chapter Six: A simplified approach to determining the abundance of a single element in a supernova atmosphere

6.1 Prelude

In Chapters 4 and 5 we generated synthetic spectra to attempt to match the observed CaNIR feature of SN 2011fe at early epochs in order to evaluate the HVF resulting from the supernova-shell interaction models. In Chapter 5 we also attempted to constrain the abundance of calcium within the shell relative to the solar value, using TARDIS. This method is computationally expensive: each spectrum that is generated requires $\sim$2 – 4 hours to generate, depending on the number of particles used in the Monte Carlo routine of TARDIS. This makes use of TARDIS impractical to use at other than for a few selected epochs after the explosion. In contrast, SYN++ typically requires only $\sim$30 s to generate each spectrum, making it much more useful to rapidly evaluate and fit observed absorption features, but it cannot directly be used to derive the abundance of any particular element. We wish to make use of the information available from fitting an observed feature using SYN++ to estimate calcium abundance within the shell and / or the ejecta of a supernova.

In this chapter, we consider the physics of excitation and ionization of atoms and devise a method to estimate the relative population of atoms of a given element in a specified state. From these relative populations and the velocity and density information from the hydrodynamic simulations performed in Chapter 3, we can derive the abundance of an element within the atmosphere. This work was inspired by a comment from the anonymous referee of Mulligan & Wheeler (2018). The methods described herein are the work of this author, in consultation with J. Craig Wheeler. The writing and software that is in development to implement these methods are fully an effort of this author.

6.2 Introduction

Supernovae are responsible for generating and releasing a significant fraction of the metals within the universe. An understanding of the quantities of each element that is produced can lead to insight into the star formation history of galaxies as well as the physics of the explosion of the supernova. The quantity of a given element may be determined from nebular emission from the supernova remnant when observed well after the explosion when the nebular emission is sufficiently strong, i.e. the element of interest is either sufficiently spatially compact or otherwise sufficiently abundant that the emission can be observed. For supernovae that have not been or are unable to be observed during the nebular phase, or for elements that are not sufficiently abundant that the emission can be detected, it is necessary to determine the abundance from the depth of absorption features caused by the elements when the supernova material is still opaque. Spectral generation software can be used for this purpose.

Some spectral generation software used for spectral synthesis of supernovae, e.g. CMFGEN (Hillier & Miller, 1998) and TARDIS (Kerzendorf & Sim, 2014), make use of a user specified profile of density, abundance, and velocity of the expanding material, use nLTE methods to solve for the ion and excitation states of the elements that are included, then use radiative transfer to generate a spectrum for the supernova. It is not explicitly possible to find the abundance of an element in isolation, instead it is necessary to include a large group of elements and test a grid of possible compositions to identify the composition and profile that results in the best fit to an observed supernova. This process can be computationally expensive and time-consuming.

The alternative is a simplified method of performing spectral synthesis, such as that of SYNOW and SYN++ (Thomas et al., 2011a), allowing the user to specify ions in isolation if desired, then using a simplified approach to generating the spectra, namely the assumption that all material is in LTE. This allows for more rapid fitting of supernova spectra, but does not give reliable information about the abundance of the element.

When considering high-velocity features in SN Ia, we would like to understand the composition of the high-velocity material to help constrain its source. SYN++ is frequently used to identify high-velocity components of spectral features, so it would be most helpful to make use of the results of the fitting to derive abundances of the high-velocity material.

In this work we derive a method to determine the abundance of an element from the optical depth of a specific line of an ion at a specific velocity in the material with the assumption that the state populations of a given element (and all ions) are determined exclusively by radiative effects. We consider population of the configuration both by photo-excitation and -relaxation as well as entry into each configuration from photo-ionization and recombination. In Sec. 6.3 we describe the analytic method of determining the populations of each state of a single ion, then generalize this to include all ions of a given element. We also discuss the relevant sources of level, transition, and ionization information for each element and the discrepancies between them.

6.3 Methods

6.4 State populations of a single ion

For an ion with multiple electron configurations, in the complete absence of collisional excitation and de-excitation, the detailed balance may be written as

$$n_i\Bigg(\sum_{j:j<i}(A_{ij}+B_{ij}J_{ij})+\sum_{j:j>i}B_{ij}J_{ij}+\alpha_{i(k_i-1)}+\beta_{i(k_i+1)}\Bigg) = \sum_{j:j<i}n_jB_{ji}J_{ji}+\sum_{j:j>i}n_j(A_{ji}+B_{ji}J_{ij}) + n_{k_i+1}\alpha_{i(k_i+1)}+n_{k_i-1}\beta_{i(k_i-1)}, \quad (6.1)$$

where i and j are indices referring to each electron level (the unique set of quantum numbers n, l and associated coupling terms for each atomic state) of an ion k_i (k_i is an index referring to the ion state, i.e. $k_i \in$\{I,II,III,....\}), A_{ij}, A_{ji}, B_{ij}, and B_{ji} are the Einstein coefficients relating to levels i and j (B_{ji} and B_{ij} may refer to either the stimulated emission or absorption coefficients, depending on the relative values of i and j; e.g. in the $j > i$[1] term on the right hand side of the equation, B_{ji} is the stimulated emission coefficient), J_{ij} is a mean intensity over the line (described later in this section), $\alpha_{i(k-1)}$ is an Einstein-like coefficient that describes the recombination

[1]Here, and throughout this paper, the operators '<' and '>' compare the energy of the left and right operand levels, such that $j < i$ if and only if level j is less bound than level i, and $j > i$ if and only if level j is more bound than level i.

rate of free electrons for level i of ion k_i to ion $k_i - 1$ (e.g. k_i = II and $k_i - 1$ = I), $\beta_{i(k_i+1)}$ is an Einstein-like coefficient that describes the photo-ionization rate of electrons from configuration i of ion k_i to ion $k_i + 1$. Note that the Einstein-like recombination coefficients β are dependent on the radiation field and electron density. The details of the ionization and recombination terms are explained in Sec. 6.5. The left hand side of Eq. 6.1 consists of all transitions away from configuration i to other configurations, including other ion configurations, and the right hand side consists of all transitions to configuration i from other configurations.

The mean intensity terms describe the mean intensity of the radiation field for a particular transition; specifically

$$J_{ij} = \int_0^\infty j_\nu \phi_{ij}(\nu) d\nu, \tag{6.2}$$

where j_ν is the mean intensity of the radiation, $\phi_{ij}(\nu)$ is a line profile function for the transition, normalized such that $\int_0^\infty \phi_{ij}(\nu) d\nu = 1$. This line profile function may a Lorentzian, Gaussian, or a Voigt profile, with the width determined by either state lifetime or thermal motion of the gas. To reduce processing time, a delta function may also be used so long as the radiation field is reasonably flat for each transition being considered.

If we assume that all of the ionization terms are zero ($\alpha_{i(k-1)} \sim \alpha_{i(k+1)} \sim \beta_{i(k-1)} \sim \beta_{i(k+1)} \sim 0\,\mathrm{s}^{-1}$), such as may occur in a low density gas in a low temperature or weak radiation field, we can define

$$G_{ij} \equiv \begin{cases} B_{ji} J_{ji} & j < i \\ A_{ji} + B_{ji} J_{ji} & j > i \\ 0 & j = i \end{cases}. \tag{6.3}$$

and

$$Z_i \equiv \sum_j G_{ji} \left(= \sum_{j:j<i} (A_{ij} + B_{ij} J_{ij}) + \sum_{j:j>i} B_{ij} J_{ij} + \alpha_{if} - \beta_{if} J_{if} \right). \tag{6.4}$$

Then Eq. 6.1 then can be rewritten

$$n_i Z_i = \sum_j n_j G_{ij} + \alpha_{if}. \tag{6.5}$$

This leads to a system of equations

$$\boldsymbol{n} = \mathbf{A}\boldsymbol{n}, \tag{6.6}$$

where the vector $\boldsymbol{n}$ consists of elements $\boldsymbol{n}_i = n_i$, where i is a component of the vector and an index to a level, and matrix $\mathbf{A}$ consists of elements $\mathbf{A}_{ij} = G_{ij}/Z_i$. $\boldsymbol{n}$ is an eigenvector of $\mathbf{A}$. We define $\hat{n}$ as the unit eigenvector such that $\sum_i \hat{n}_i = 1$.

6.4.1 State populations of a set of ions of a given element

The ionization terms in Eq. 6.1 can be used to couple electron levels of different ions. We can expand the recombination term of electron level i of ion k_i to be

$$\alpha_{i(k_i-1)} = \sum_{j \in \mathbb{I}_{(k_i-1)}} \alpha_{ji}, \tag{6.7}$$

and

$$n_{k_i+1}\alpha_{i(k_i+1)} = \sum_{j \in \mathbb{I}_{(k_i-1)}} n_j \alpha_{ij}, \tag{6.8}$$

where $\mathbb{I}_{(k_i \pm 1)}$ is the set of electron level of ion $k_i \pm 1$. For the photo-ionization rate

$$\beta i(k_i+1) = \sum_{j \in \mathbb{I}_{(k_i+1)}} \beta_{ij}, \tag{6.9}$$

and

$$n_{k_i-1}\beta i(k_i-1) = \sum_{j \in \mathbb{I}_{(k_i-1)}} n_j \beta_{ij}, \tag{6.10}$$

where $\mathbb{I}_{k_i \pm 1}$ is the set of electron levels of ion $k_i \pm 1$. We will defer the definition of these terms to Sec. 6.5. Finally, we can expand the term in Eq. 6.1 that contains transitions into level i from other ions:

$$\alpha_{if} = \sum_{j \in \mathbb{I}_{k_i+1}} n_j \alpha_{ij} + \sum_{j \in \mathbb{I}_{k_i-1}} n_j \beta_{ij}. \tag{6.11}$$

We then define

$$H_{ij} \equiv \begin{cases} B_{ji}J_{ij} & j < i; j \in \mathbb{I}_{k_i} \\ A_{ji} + B_{ji}J_{ij} & j > i; j \in \mathbb{I}_{k_i} \\ 0 & i = j \\ \beta_{ij} & j \in \mathbb{I}_{k_i-1} \\ \alpha_{ji} & j \in \mathbb{I}_{k_i+1} \\ 0 & j \notin \mathbb{I}_{k_i-1} \cup \mathbb{I}_{k_i} \cup \mathbb{I}_{k_i+1} \end{cases}. \tag{6.12}$$

and restate Eq. 6.4 as

$$Z_i \equiv \sum_j H_{ji} \tag{6.13}$$

Eq. 6.1 then can be rewritten

$$n_i Z_i = \sum_j n_j H_{ij}. \tag{6.14}$$

This leads to a system of equations

$$\boldsymbol{n} = \mathsf{B}\boldsymbol{n}, \tag{6.15}$$

where matrix B has elements $\mathsf{B}_{ij} = H_{ij}/Z_i$, and vector $\boldsymbol{n}$ is the set of all levels of all ions. $\boldsymbol{n}$ is an eigenvector of B, and we define $\hat{n}$ as the unit eigenvector of B. $\hat{n}$ can be found numerically for any given radiation field.

6.5 Einstein-like coefficients for photo-ionization and recombination

The photo-ionization coefficients are related to the photo-ionization cross-section by

$$\beta_{ij} = 4\pi \int_{\nu_0}^{\nu_{max}} \frac{j_\nu}{h\nu} \sigma_{ij,\nu} d\nu, \tag{6.16}$$

where ν is the frequency, ν_0 is the frequency at the ionization threshold, $\sigma_{ij,\nu}$ is the specific cross-section of photo-ionization of level i to level j, and ν_{max} is a chosen maximum frequency for the integration. We make use of photo-ionization cross section data from the Opacity Project (Seaton, 1995), and assume that all available photo-ionization cross-sections for refer ionization from a singly excited state to the ground state of the subsequent ion. The Opacity Project does not include multi-excited atomic states in the database, e.g. for Ca I, $3p^6 4s^2$ is the ground state, $3p^6 4s4p$ is a singly excited state, and $3p^6 3d4p$ is a multi-excited state. In many cases the cross-section information is not available for known atomic levels (the Opacity Project was limited to $n, l \leq 10$), in which case we assume a cross-section of

$$\sigma_{ij,\nu} = A_{i,\min} \frac{\lambda_{i,\min}^2}{8\pi h} (x\Delta E_{ij} + y), \tag{6.17}$$

where $\lambda_{i,\max}$ is the minimum wavelength of a known transition from state i to a higher energy state, $A_{i,\min}$ is the associated Einstein coefficient for the transition, ΔE_{ij} is the total energy difference between states i and j, h is the Planck constant, and the factors x and y are arbitrary scalar factors.

The recombination cross-sections are related to the photo-ionization coefficients through the Milne relation for ionization:

$$\sigma_{ji} = \sigma_{ij} \frac{g_i}{g_j} \frac{h^2\nu^2}{4\pi^2 m_e^2 c^2 v^2}, \tag{6.18}$$

where σ_{ji} is the recombination cross-section, g_i and g_j are the statistical weights of levels i and j, and the velocity of the incident electron is $v = \sqrt{(h(\nu - \nu_I))/m_e}$, where m_e is the mass of an electron. The recombination rate is then

$$\alpha_{ji} = \int_0^{v_{\max}} \left(\frac{h\nu}{m_e c v}\right)^2 v f(v) \sigma_{ij} \frac{\Delta E_{i,0}}{\Delta E_{ij}} dv, \tag{6.19}$$

where n_e is the electron density, and $f(v)$ is the probability distribution function of velocities for the electrons, ΔE_{ij} is the actual energy difference between states i and j, and $\Delta E_{i,0}$ is the ionization potential of state i according to the Opacity Project database. We assume a Maxwellian velocity distribution. The maximum velocity for integration of the recombination cross section is determined in the same way as that for the photo-ionization cross section.

6.5.1 Identifying the ionized state of an excited state

We consider all ionization conditions from a particular state to any related ionized states that are not multiply excited. The simplest case is that of an excited state wherein the 'outermost' electron is freed; the ionized state is then the state of the remaining inner electrons, e.g. He I $1s^2$ and He I 1s1p both may ionize to He II 1s. This becomes slightly more complicated when LS-coupling terms are included and the ionized state has an unfilled outer shell. In these cases, we allow for the final coupling term to vary by $\Delta L \in \{-1, 0, 1\}$ and $\Delta J \in \{\pm 1/2\}$. An exception occurs in the event of J_1K-coupling, or LS-coupling wherein the inner shell is unfilled and the LS-coupling term of the inner shell is known. In these cases the L of the ionized state is already known, and only the J value varies by $\pm 1/2$.

We also consider the removal of an electron from an inner shell when this does not result in the ionized state being multiply excited. An example of this case is

ionization of the ground state of Ca II, $3p^6 4s$, to the excited $3p^5 4s$ state of Ca III. We again allow the final coupling term to vary by $\Delta L \in \{-1, 0, 1\}$ and $\Delta J \in \{\pm 1/2\}$.

For each of these cases, we assume the total energy required for ionization, ΔE_{ij}, is the energy difference between the states; i.e. $\Delta E_{ij} = \epsilon_j + \chi_{k_i} - \epsilon_i$, where ϵ is the energy of the state, χ_{k_i} is the ionization energy for the ground state of the ion, and subscripts j and i refer the the upper (i.e. ionized) state and lower states of the ionizing transition, respectively.

6.6 Radiation field and flux

We define a frequency-dependent radiation field at a given point in a expanding atmosphere of a supernova as $R(\nu, v)$, where ν is the frequency and v is the location within the atmosphere, described by the velocity. In general, $j_\nu = R(\nu, v)$. The most simple case for the radiation field is that of a blackbody ($B(\nu, T)$) with effective temperature T emanating from a photosphere with expansion velocity $v_{\rm PS}$. The resulting local flux at the specified location will then be

$$j_\nu = 2\pi B(\nu', T) \left(\frac{R_{\rm PS}}{R}\right)^2, \tag{6.20}$$

where $\nu' \approx (1 - (v - v_{\rm PS})/c)\nu$ is the redshifted frequency, $R_{\rm PS} = v_{\rm PS} t_{exp}$, t_{exp} is the time since the supernova exploded, and R is the radius of the location in the atmosphere being considered. If the velocities are non-relativistic, $R_{\rm PS}/R = v_{\rm PS}/v$.

For material in the outermost layers of a supernova, at velocities much larger than that of the photosphere, it may be desirable to instead incorporate a radiation field that has undergone processing when passing through layers slower than the material of interest.

6.7 Level, Transition, cross-section, and ionization energy data for ions

The Kurucz & Bell (1995) data are used for level data and oscillator strengths for each element, from which we derive the Einstein coefficients for each transition. We also develop a list of atomic levels from each level present in the transitions. The

levels are then coupled to those found in the Opacity Project data by the electron configuration and associated coupling terms. We take the energy of each level relative to the ground state from Kurucz & Bell (1995) rather than from the Opacity Project.

The ionization potentials used are taken from the NIST Atomic Spectra Database (Kramida et al., 2018). These potentials do not match those listed within the Opacity Project data. The values found in the NIST database are more accurate, so these potentials are used as the value of the ionization energy for the ground state for each ion (χ_{k_i}).

6.8 Abundance and optical depth

For a system with total density N and an abundance X_e of an element e,

$$X_e N = \mathcal{N} \sum_{l \in \mathbb{I}_e} \hat{n}_l, \tag{6.21}$$

where $\mathbb{I}_e$ is all configurations of all ions of element e. By definition, $\sum_{l \in \mathbb{I}_e} \hat{n}_l = 1$, thus $\mathcal{N} = X_e n$. The density of a given configuration l is then

$$N_l = X_e N \hat{n}_l. \tag{6.22}$$

The Sobolev optical depth for a line at a particular velocity v is

$$\tau_{luv} = hB_{lu} \left(N_l - N_u \frac{g_l}{g_u} \right) \frac{ds}{dv}, \tag{6.23}$$

where $ds/dv = t$ in a homologously expanding atmosphere, and l and u refer the the lower energy and upper energy states, respectively. Combining Eq 6.22 and Eq. 6.23, we can write this as

$$\tau_{luv} = hB_{lu} \left(\hat{n}_l - \hat{n}_u \frac{g_l}{g_u} \right) X_e N_v t, \tag{6.24}$$

where the subscript v refers to the velocity at which the optical depth and density are sampled.

If the optical depth and time after the explosion are known, then the abundance may be found by

$$X_{e,v} = \frac{\tau_{lu,v}}{hB_{lu} t N_v \left(\hat{n}_l - \hat{n}_u \frac{g_l}{g_u} \right)}. \tag{6.25}$$

6.8.1 Deriving the abundance using SYN++

If using SYN++, the optical depth can be found from the input parameters for a given ion. Within SYN++, the line optical depth at a specific velocity is

$$\tau_{luv} = S\mathcal{G}_v \frac{gf_{lu}\lambda_{lu}}{gf_{\rm ref}\lambda_{\rm ref}} e^{\left(0.011604506\ {\rm K\ eV^{-1}}\ \frac{E_{\rm ref}-E_l}{T_{\rm ion}}\right)}, \tag{6.26}$$

where subscript 'ref' refers to the reference line for a given ion, gf is the weighted oscillator strength, E refers to the energy of the level in eV (E_l is energy of the lower state, and $E_{\rm ref}$ that of the lower state of the reference line), T is the temperature specified for the ion (`temp`), S is a user specified scalar factor (the `log_tau` that is specified for the ion), and $\mathcal{G}_v$ is a velocity dependent factor that is specified by the user. Typically, $\mathcal{G}_v$ is

$$\mathcal{G}_v = e^{\left(\frac{v_{\rm ref}-v}{v_{\rm aux}}\right)}, \tag{6.27}$$

where $v_{\rm ref}$ is the user specified reference velocity (SYN++ parameter `v_ref`), and $v_{\rm aux}$ is the user specified e-folding factor (parameter `aux`) for the ion. Note that if two ions of the same type are specified, the factor $S\mathcal{G}_v$ is only that of the last instance of that ion for which `v_min` $< v <$ `v_max`, where `v_min` and `v_max` are the minimum and maximum velocity parameters specified for the ions. For example, if Ca II is specified twice, one with `v_min` = 10 and `v_max` = 30, and the second with `v_min` = 20 and `v_max` = 30, only the second instance affects the optical depth at velocities above 20,000 km s^{-1}.

6.9 Conclusion

We have described a method by which the relative population of any state of any ion of an element can be estimated by assuming and electron density and temperature and the radiation field in which that element lies. We allow for photo-excitation and -ionization, and simultaneously solve for both excitation and ionization. If the total ion number density and the optical depth of a specific line is known, the abundance of the element of interest may be determined.

Chapter Seven: Conclusion

In this work we have considered HVF of SN Ia and a model of a supernova interacting with a compact, circumstellar shell that may be one explanation of their cause. For SN Ia that are observed prior to peak brightness, HVF are nearly always observed in calcium or silicon. While the measured strength of the HVF when blended with PVF may be unclear due to the attempted use of fitting multiple Gaussians to observed features, the HVF have velocities consistently $\sim$7,000 km s^{-1} faster than the PVF, are a distinct feature, and are visible through to the time of peak brightness.

In Chapter 2 we investigated the evolution of the pEW and velocity of the PVF and HVF for CaNIR, Ca II H&K, and the Si II 6355 Å features, and found that the HVF, when it appears, is consistently $\sim$7,000 km s^{-1} faster than the PVF. The calcium HVFs have a velocity $\gtrsim$ 25,000 km s^{-1} in the first few days after the explosion, then slow to $\sim$20,000 km s^{-1} by the time of peak brightness. The silicon HVFs are less common, seem to start slightly slower, though still near 20,000 km s^{-1} at early epochs, and also slow to $\sim$20,000 km s^{-1}. The trend in pEW is not clear for either silicon or calcium, although the combined pEW of the HVF and PVF tend to decrease until about a week before peak brightness, then begin to slowly increase.

In Chapter 3, we describe simulations that we have run that explore the interaction between a SN Ia and a compact circumstellar shell. We consider shells with different radii, density profile, and mass. We conclude that for an initial radius $\lesssim$ 1 R$_\odot$, the resulting spectrum is unaffected by the radius. Shells that have a steep density gradient at the outer edge produce a distinctive shape that does not seem to match the observed shape of HVF, so a density profile of the shell that smoothly tapers off at the outer radius prior to interaction with the supernova is preferred. The mass of the shell seems to have the largest effect upon the velocity and presence of HVF due to the shell at epochs near peak brightness.

In Chapter 4, we used the supernova-shell interaction models that we developed in Chapter 3 to generate spectra using SYN++ in an attempt to fit the observed CaNIR feature of SN 2011fe at multiple epochs from $\sim$1 – 27 d after the explosion. From these results, we find that there is no clearly favored mass of the shell based upon the fit, although the shell with a mass of 0.005 M$_\odot$ does a slightly better job of recreating

the final velocity of the HVF. The optical depth within neither the shell nor the ejecta follows the expected trend of the inverse square of the time after the explosion, suggesting that if this model is the correct explanation for the HVF, the ionization and/or excitation state of the calcium within the shell is not constant; specifically, the quantity of calcium within the Ca II $3p^6 4p\ ^2P^o$ state must be increasing after $\sim$10 d after the explosion occurs. This may naturally occur as the gas and radiation temperature change as the supernova and shell expand.

In Chapter 5, we used TARDIS to generate synthetic spectra from the supernova-shell interaction models of Chapter 3, applying a variety of possible compositions to the shell and ejecta. We find that a solar or super-solar abundance of calcium is required within the shell in order to generate an HVF that is of similar strength to those that are observed for CaNIR. We test three possible substrates for the shell: hydrogen, helium, and carbon-oxygen, and find that the substrate has no effect upon spectra, other than to determine the quantity of calcium that is required to generate the HVF for CaNIR. The quantity of calcium within the shell that is required to best match the observed CaNIR feature increases between 2 – 9 d after the explosion. It is not clear if this is due to limitations of TARDIS, or a fault with the supernova-shell interaction model.

In Chapter 5, we also evaluate models corresponding to the Shen & Moore (2014) helium envelope detonation models for SN Ia, and find that only a very narrow range of mass near 0.008 $M_\odot$ could explain the observed HVF – a smaller mass will produce no HVF and a larger mass will produce an excessively strong HVF. There is no clear reason why the envelope might have this exact match.

In Chapter 6, we describe a method to attempt to derive the abundance of calcium or other elements within a supernova based upon the results of fitting observed supernova spectra with SYN++. This method attempts to solve both the ion state and excitation state of any element simultaneously in a radiation dominated environment. The computational effort to use the combination of SYN++ and this method represents a substantial savings of computing time relative to that of using TARDIS; specifically, approximately 40 CPU hours per model (with 81 samples) using SYN++ compared to 2-4 CPU hours per sample using TARDIS, a savings of up to about 80%. We look forward to completion and application of this software and method.

There is still much work to be done to complete evaluation of the supernova-shell interaction model. An important outstanding consideration is the effect that such

an interaction will have upon the light curve of the supernova, especially at early epochs. Preliminary work has suggested that the shell will have no effect upon the photometry of the supernova after 8 – 24 hours after the explosion. Use of software such as SNEC (Morozova et al., 2015) can allow a specific determination of the effect that the shell has upon the light curve, and potential observational signatures that could be caught using high-cadence surveys.

It is also important to evaluate the discrepancies between the observed HVF and those that we have generated within Chapters 4 and 5. The HVF produced by the shell especially at intermediate epochs (5 – 18 d after the explosion) tend to be more broad than observed HVF. This may be a result of a gradient within the calcium within the shell. We have assumed a constant calcium abundance throughout the shell; if the shell is the result of a helium envelope detonation or merger with a companion white dwarf, the material may not be so well mixed. Additionally, if the calcium within the shell is a result of mixing with the outer layers of the supernova, the calcium abundance would be higher near the contact discontinuity.

We also consider it important to evaluate more supernovae than just SN 2011fe using the methods that we have described within these works. If this model of supernova-shell interaction is correct, what differences in the mass of, or calcium content of, the shell are required to explain the HVF of other supernova, especially unusual cases such as SN 2010kg, that exhibits an unusually strong CaNIR HVF. We have also not attempted to evaluate the HVF of silicon, oxygen, or iron. While these HVF may not be as prevalent or strong, they may also provide clues to the source of the HVF material and must be explained by any source model.

All software used within this work is publicly available as the **s**uper**n**ova **a**nalysis **t**ool**k**it on github at `https://github.com/astrobit/snatk`, the software developed specifically for work associated with interaction between a supernova and shell are within the folder SuShI (**Su**pernova-**Sh**ell **I**nteraction).

Appendix A: Tables of Objects and Spectral Measurements

A.1 Prelude

Significant portions of this chapter have been published previously as an appendix to Silverman et al. (2015). This author was not involved in production of these tables. They are presented here exclusively for the completeness of Chapter 2.

A.2 Tables of Objects and Spectral Measurements

Table A.1 lists each SN Ia that we analyse herein and the (rest-frame) phases of their spectra. Also presented are published $\Delta m_{15}(B)$ and $(B-V)_0$ values, as well as spectral classifications based on various classification schemes.

Table A.1: Summary of SNe Ia

SN Name	Phase(s) (d)[a]	$\Delta m_{15}(B)$ (mag)[b]	$(B-V)_0$ (mag)[c]	SNID (Sub)Type[d]	Benetti Type[e]	Wang Type[f]
SN 1989M	2.5, 3.5	1.10 (20)	···	Ia-norm	HVG	HV
SN 1991T	−10.1, −9.1	0.92 (03)	0.090 (036)	Ia-91T	···	···
SN 1991bg	0.1, 1.1	1.89 (05)	0.714 (044)	Ia-91bg	FAINT	···
SN 1994D	−12.3, −11.3, −9.3, −7.7, −6.3, −5.3, −3.9, −3.3	1.36 (05)	−0.053 (035)	Ia-norm	LVG	N
SN 1994S	1.1	0.98 (04)	−0.090 (038)	Ia-norm	···	N
SN 1995D	3.8	1.03 (07)	−0.121 (033)	Ia-norm	···	N
SN 1995E	−2.5	0.98 (06)	0.668 (040)	Ia-norm	···	N
SN 1995ac	−6.3	0.93 (04)	−0.124 (036)	Ia-91T	···	···
SN 1997Y	1.3	1.25 (10)	−0.030 (000)	Ia-norm	···	N
SN 1997br	−4.8	1.08 (17)	0.160 (130)	Ia-91T	···	···
SN 1997do	−5.7	1.04 (05)	−0.019 (036)	Ia-norm	···	···
SN 1998dk	−7.2, −0.5	1.05 (10)	0.190 (000)	Ia-norm	···	HV
SN 1998dm	−12.5, −5.6	0.85 (05)	0.303 (034)	Ia-norm	···	···
SN 1998ef	−8.6	1.30 (05)	−0.072 (037)	Ia-norm	···	···
SN 1998es	0.3	0.98 (03)	0.056 (042)	Ia-99aa	···	···
SN 1999aa	−10.6, 0.2	0.79 (05)	−0.093 (033)	Ia-99aa	···	···
SN 1999ac	−3.7, −0.9	1.18 (03)	−0.038 (033)	Ia-norm	HVG	N
SN 1999cp	4.9	1.03 (03)	−0.047 (031)	Ia-norm	LVG	N

Continued on next page

Table A.1 — Continued

SN Name	Phase(s) (d)[a]	$\Delta m_{15}(B)$ (mag)[b]	$(B-V)_0$ (mag)[c]	SNID (Sub)Type[d]	Benetti Type[e]	Wang Type[f]
SN 1999da	−2.1	1.90 (17)	0.522 (037)	Ia-91bg	FAINT	···
SN 1999dk	−6.6	1.15 (03)	0.003 (037)	Ia-norm	···	···
SN 1999dq	−3.9, 3.0	0.97 (03)	0.050 (034)	Ia-99aa	HVG	···
SN 1999gd	−1.1	1.16 (06)	0.410 (000)	Ia-norm	···	N
SN 1999gh	4.1	1.69 (05)	0.190 (000)	Ia-norm	FAINT	N
SN 2000cp	2.9	···	···	Ia-norm	···	N
SN 2000cw	4.8	1.31 (04)	−0.072 (031)	Ia-norm	···	N
SN 2000dg	−5.1, 4.7	···	···	Ia-norm	···	N
SN 2000dk	1.0	1.64 (04)	−0.051 (032)	Ia-norm	FAINT	N
SN 2000dm	−1.6	1.56 (05)	−0.111 (037)	Ia-norm	HVG	N
SN 2000dn	−5.6, −0.9	1.12 (03)	−0.092 (036)	Ia-norm	LVG	N
SN 2000dx	−9.3	···	···	Ia-norm	···	···
SN 2000fa	−8.3	0.91 (03)	0.007 (037)	Ia-norm	···	N
SN 2001az	−3.2	···	···	Ia-norm	···	N
SN 2001ba	−4.6	0.99 (04)	−0.160 (033)	Ia-norm	···	···
SN 2001bf	1.2	0.93 (03)	−0.058 (034)	Ia-norm	···	N
SN 2001br	3.5, 3.5	1.35 (06)	0.067 (033)	Ia-norm	···	HV
SN 2001bp	0.5	···	···	Ia-norm	···	···
SN 2001cp	1.4	0.92 (04)	−0.035 (033)	Ia-norm	···	N

Continued on next page

Table A.1 — Continued

SN Name	Phase(s) (d)[a]	$\Delta m_{15}(B)$ (mag)[b]	$(B-V)_0$ (mag)[c]	SNID (Sub)Type[d]	Benetti Type[e]	Wang Type[f]
SN 2001da	−1.1	1.23 (05)	0.130 (032)	Ia-norm	HVG	N
SN 2001eh	−5.6, −4.5, 3.3	0.81 (04)	−0.110 (033)	Ia-99aa	···	···
SN 2001ep	2.8	1.49 (06)	0.027 (043)	Ia-norm	HVG	N
SN 2001ex	−1.8	···	···	Ia-91bg	···	···
SN 2001fe	−1.0	1.03 (17)	−0.014 (047)	Ia-norm	···	N
SN 2002aw	2.1	···	···	Ia-norm	···	N
SN 2002bf	3.0	···	···	Ia-norm	···	HV
SN 2002bo	−11.9, −1.1	1.15 (04)	0.315 (052)	Ia-norm	HVG	HV
SN 2002cd	1.1	0.96 (03)	0.576 (030)	Ia-norm	LVG	HV
SN 2002cf	−0.8	1.86 (06)	0.353 (047)	Ia-91bg	···	···
SN 2002ck	3.6	···	···	Ia-norm	···	N
SN 2002cr	−6.8, −5.8, −3.9	1.26 (05)	−0.102 (038)	Ia-norm	···	···
SN 2002cs	−7.8	1.03 (05)	−0.066 (034)	Ia-norm	···	···
SN 2002cu	−5.3	1.43 (04)	−0.016 (033)	Ia-norm	···	···
SN 2002de	−0.3	1.00 (03)	0.043 (031)	Ia-norm	HVG	HV
SN 2002dj	−8.0	1.09 (03)	0.053 (033)	Ia-norm	···	···
SN 2002dk	−1.2	···	···	Ia-91bg	···	···
SN 2002eb	1.7	0.99 (03)	−0.125 (031)	Ia-norm	···	N
SN 2002ef	4.7	1.04 (10)	0.309 (032)	Ia-norm	···	N

Continued on next page

Table A.1 — Continued

SN Name	Phase(s) (d)[a]	$\Delta m_{15}(B)$ (mag)[b]	$(B-V)_0$ (mag)[c]	SNID (Sub)Type[d]	Benetti Type[e]	Wang Type[f]
SN 2002er	−4.6	1.28 (05)	0.103 (034)	Ia-norm	···	HV
SN 2002eu	−0.1	···	···	Ia-norm	HVG	N
SN 2002fb	1.0	···	···	Ia-91bg	···	···
SN 2002ha	−0.9, 4.9	1.38 (06)	−0.093 (048)	Ia-norm	LVG	N
SN 2002he	−5.9, −1.0, 0.3, 3.2	1.49 (04)	−0.050 (037)	Ia-norm	HVG	HV
SN 2002hu	−5.8	1.02 (05)	−0.121 (035)	Ia-99aa	···	···
SN 2002hw	−6.3	1.53 (06)	0.558 (061)	Ia-norm	···	···
SN 2003U	−2.6	···	···	Ia-norm	···	N
SN 2003W	−7.0, −6.0, −5.1	1.10 (03)	0.106 (036)	Ia-norm	···	···
SN 2003Y	−1.7	1.73 (09)	0.830 (047)	Ia-91bg	···	···
SN 2003cq	−0.2	···	···	Ia-norm	···	HV
SN 2003fa	−8.2	0.98 (10)	−0.087 (098)	Ia-99aa	···	···
SN 2003gn	−5.4, 3.3	1.24 (08)	−0.011 (037)	Ia-norm	···	···
SN 2003gt	−5.1	1.06 (03)	−0.019 (032)	Ia-norm	···	···
SN 2003he	2.7	0.99 (03)	−0.010 (033)	Ia-norm	LVG	N
SN 2003hs	−5.5	···	···	Ia-norm	···	···
SN 2003iv	1.8	···	−0.100 (100)	Ia-norm	HVG	N
SN 2003kf	−7.5	0.93 (04)	−0.014 (039)	Ia-norm	···	···
SN 2004as	−4.4	1.11 (03)	0.021 (034)	Ia-norm	···	HV

Continued on next page

Table A.1 — Continued

SN Name	Phase(s) (d)[a]	$\Delta m_{15}(B)$ (mag)[b]	$(B-V)_0$ (mag)[c]	SNID (Sub)Type[d]	Benetti Type[e]	Wang Type[f]
SN 2004bl	4.6	···	···	Ia-norm	HVG	N
SN 2004br	3.5	0.68 (16)	−0.097 (046)	Ia-norm	···	N
SN 2004bv	−7.1	0.89 (04)	0.082 (033)	Ia-91T	···	···
SN 2004bw	−10.0, −7.1	1.31 (05)	−0.079 (034)	Ia-norm	···	N
SN 2004dt	−6.5, 1.4	1.29 (05)	−0.080 (034)	Ia-norm	HVG	HV
SN 2004ef	−5.5	1.38 (04)	0.048 (033)	Ia-norm	···	HV
SN 2004eo	−5.6	1.39 (03)	−0.042 (031)	Ia-norm	···	···
SN 2004ey	−7.6	0.96 (06)	−0.110 (039)	Ia-norm	···	···
SN 2004fu	−2.7, 2.4	···	···	Ia-norm	HVG	HV
SN 2004fz	−5.2	1.40 (05)	−0.127 (039)	Ia-norm	···	···
SN 2004gs	0.4	1.77 (04)	0.046 (032)	Ia-norm	···	N
SN 2004gu	−4.7	0.80 (04)	···	Ia-norm	···	···
SN 2005M	−1.4	0.83 (04)	−0.082 (032)	Ia-norm	HVG	N
SN 2005W	0.6	1.15 (06)	···	Ia-norm	···	N
SN 2005ag	0.5	0.86 (01)	···	Ia-norm	···	N
SN 2005am	4.5	1.71 (09)	−0.008 (062)	Ia-norm	FAINT	N
SN 2005ao	−1.3, 0.5	···	···	Ia	···	···
SN 2005bc	1.6	1.39 (05)	0.382 (033)	Ia-norm	LVG	N
SN 2005bl	−5.6	···	···	Ia-91bg	···	···

Continued on next page

Table A.1 — Continued

SN Name	Phase(s) (d)[a]	$\Delta m_{15}(B)$ (mag)[b]	$(B-V)_0$ (mag)[c]	SNID (Sub)Type[d]	Benetti Type[e]	Wang Type[f]
SN 2005cf	−10.9, −2.1, −1.2	1.08 (03)	−0.062 (031)	Ia-norm	HVG	N
SN 2005cg	−10.1, −9.1, −4.3, −0.4, 4.5	···	···	Ia-norm	HVG	HV
SN 2005de	−0.8	1.22 (03)	0.010 (032)	Ia-norm	HVG	N
SN 2005dv	−0.6	···	···	Ia-norm	···	HV
SN 2005el	−6.7, 1.2	1.31 (05)	−0.114 (035)	Ia-norm	LVG	N
SN 2005er	−0.3, 1.7	···	···	Ia-91bg	HVG	···
SN 2005eq	−6.0, −3.0, 0.7	0.88 (05)	−0.021 (034)	Ia-99aa	HVG	···
SN 2005eu	−10.1, −9.1, −5.5	0.94 (04)	−0.072 (040)	Ia-norm	···	···
SN 2005hj	−5.2, −4.3, 0.5, 2.4, 3.3	···	···	Ia-norm	LVG	N
SN 2005iq	−5.9	1.28 (05)	−0.116 (050)	Ia-norm	···	···
SN 2005ki	1.6	1.53 (05)	−0.160 (048)	Ia-norm	LVG	N
SN 2005lz	0.6	1.60 (05)	−0.071 (059)	Ia-norm	···	N
SN 2005ms	−1.9	0.99 (04)	−0.071 (048)	Ia-norm	HVG	N
SN 2005na	0.0, 1.0	1.24 (06)	−0.128 (042)	Ia-norm	HVG	N
SN 2006D	3.7	1.41 (08)	0.050 (039)	Ia-norm	···	N
SN 2006N	−1.9, −0.9	1.56 (04)	0.014 (042)	Ia-norm	HVG	N
SN 2006S	−3.9, 3.0	0.89 (06)	0.046 (046)	Ia-norm	LVG	N
SN 2006X	−11.2, −10.2, −9.2, −8.2, −7.2, −6.2, −5.2, −0.2, 0.8, 1.8, 2.8, 3.2	1.10 (04)	1.260 (034)	Ia-norm	HVG	HV

Continued on next page

Table A.1 — Continued

SN Name	Phase(s) (d)[a]	$\Delta m_{15}(B)$ (mag)[b]	$(B-V)_0$ (mag)[c]	SNID (Sub)Type[d]	Benetti Type[e]	Wang Type[f]
SN 2006ax	−10.1	1.03 (04)	−0.105 (038)	Ia-norm	···	···
SN 2006bt	−5.3, −4.5, 2.3	1.01 (07)	0.104 (034)	Ia-norm	HVG	N
SN 2006bu	4.2	···	···	Ia-norm	···	N
SN 2006bz	−2.4	2.22 (17)	0.575 (064)	Ia-91bg	···	···
SN 2006cj	3.4	···	···	Ia-norm	···	N
SN 2006cm	−1.2	1.14 (19)	1.055 (052)	Ia-norm	···	N
SN 2006cp	−5.3	0.99 (05)	0.063 (039)	Ia-norm	···	···
SN 2006cq	2.0	···	···	Ia-norm	···	N
SN 2006cs	2.3	···	···	Ia-91bg	···	···
SN 2006cz	1.1	···	···	Ia-99aa	···	···
SN 2006dm	−7.9	1.54 (03)	−0.022 (034)	Ia-norm	HVG	N
SN 2006ef	3.2	1.38 (05)	0.004 (034)	Ia-norm	···	HV
SN 2006ej	−3.7	1.40 (15)	−0.046 (062)	Ia-norm	HVG	HV
SN 2006em	4.2	···	···	Ia-91bg	···	···
SN 2006et	3.3	0.73 (03)	0.161 (064)	Ia-norm	LVG	N
SN 2006gt	3.1	···	···	Ia-91bg	···	···
SN 2006gj	4.7	1.39 (17)	0.340 (100)	Ia-norm	···	N
SN 2006gr	−8.7	0.81 (04)	0.059 (036)	Ia-norm	···	···
SN 2006ke	2.4	···	···	Ia-91bg	HVG	···

Continued on next page

Table A.1 — Continued

SN Name	Phase(s) (d)[a]	$\Delta m_{15}(B)$ (mag)[b]	$(B-V)_0$ (mag)[c]	SNID (Sub)Type[d]	Benetti Type[e]	Wang Type[f]
SN 2006kf	−9.0, −3.1	1.71 (10)	−0.081 (041)	Ia-norm	···	N
SN 2006lf	−6.3	1.31 (08)	−0.068 (052)	Ia-norm	···	···
SN 2006le	−8.7	0.90 (04)	−0.133 (034)	Ia-norm	···	···
SN 2006or	−2.8	···	···	Ia-norm	···	N
SN 2006os	−0.9	···	···	Ia-norm	···	N
SN 2006qo	−11.1	1.05 (10)	0.153 (042)	Ia	···	···
SN 2006sr	−2.3, 2.7	1.41 (13)	−0.017 (066)	Ia-norm	HVG	HV
SN 2007A	2.4	···	···	Ia-norm	LVG	N
SN 2007F	−9.4, 3.2	0.98 (03)	−0.060 (033)	Ia-norm	···	N
SN 2007N	0.4	···	···	Ia	···	···
SN 2007O	−0.3	···	···	Ia-norm	···	N
SN 2007S	−6.0	0.93 (04)	0.400 (032)	Ia-norm	···	N
SN 2007af	−9.8, −1.3, 0.2, 2.8, 3.8	1.22 (05)	−0.014 (036)	Ia-norm	HVG	N
SN 2007al	3.4	···	···	Ia-91bg	···	···
SN 2007ba	2.1	···	···	Ia-91bg	···	···
SN 2007bd	−5.8	···	−0.060 (040)	Ia-norm	···	N
SN 2007bc	0.6	1.37 (06)	−0.113 (036)	Ia-norm	···	N
SN 2007bm	−7.8	···	···	Ia-norm	···	···
SN 2007bz	1.7	···	···	Ia-norm	···	HV

Continued on next page

Table A.1 — Continued

SN Name	Phase(s) (d)[a]	$\Delta m_{15}(B)$ (mag)[b]	$(B-V)_0$ (mag)[c]	SNID (Sub)Type[d]	Benetti Type[e]	Wang Type[f]
SN 2007ca	−11.1	···	0.290 (050)	Ia-norm	···	···
SN 2007ci	−6.6, −1.7	1.74 (04)	0.003 (042)	Ia-norm	···	N
SN 2007co	−4.1, −0.6, 0.9	1.04 (10)	−0.008 (032)	Ia-norm	LVG	N
SN 2007cq	−5.8	1.12 (03)	0.004 (032)	Ia	···	···
SN 2007fb	2.0	···	···	Ia-norm	LVG	N
SN 2007fr	−5.8, −1.3	1.79 (04)	−0.095 (045)	Ia-norm	···	N
SN 2007gi	−7.3, −0.4	···	···	Ia-norm	HVG	HV
SN 2007gk	−1.7	···	···	Ia-norm	HVG	HV
SN 2007hj	−1.2	1.95 (06)	0.090 (038)	Ia-norm	FAINT	HV
SN 2007le	−10.3, −9.4	1.01 (04)	0.280 (039)	Ia-norm	HVG	HV
SN 2007s1[g]	−1.2	1.24 (05)	−0.066 (033)	Ia-norm	···	N
SN 2007on	−3.0, −3.0	···	···	Ia-norm	···	N
SN 2007qe	−8.2, −6.5, −2.5	1.01 (03)	−0.021 (038)	Ia-norm	···	HV
SN 2008Z	−2.3	0.91 (06)	0.109 (059)	Ia-99aa	···	···
SN 2008ar	−8.9, −5.6, 1.5, 2.8, 4.3	1.08 (05)	−0.101 (047)	Ia-norm	···	N
SN 2008bt	−1.1	···	···	Ia-91bg	···	···
SN 2008cl	4.2	···	···	Ia-norm	···	HV
SN 2008s1[h]	−6.4, −4.4, −3.4, 0.5, 4.4	1.39 (04)	−0.167 (037)	Ia-norm	···	N
SN 2008dx	2.5	···	···	Ia-91bg	FAINT	···

Continued on next page

Table A.1 — Continued

SN Name	Phase(s) (d)[a]	$\Delta m_{15}(B)$ (mag)[b]	$(B-V)_0$ (mag)[c]	SNID (Sub)Type[d]	Benetti Type[e]	Wang Type[f]
SN 2008ec	−9.8, −8.9, −6.0, −0.2, 1.0	1.36 (06)	0.081 (034)	Ia-norm	LVG	N
SN 2008ei	3.3	···	···	Ia-norm	HVG	HV
SN 2008s5[i]	1.3	···	···	Ia	LVG	···
SN 2008hm	1.3	0.80 (02)	···	Ia-norm	···	···
SN 2008hs	−8.9, −7.9, −6.3	···	···	Ia-norm	···	···
SN 2008hv	−11.7, −9.2, −6.6	1.25 (01)	0.039 (009)	Ia-norm	···	···
SN 2009F	−3.0	1.97 (05)	0.635 (036)	Ia-norm	···	···
SN 2009ad	−3.4	0.88 (17)	−0.006 (136)	Ia-norm	···	N
SN 2009an	−5.8, −3.8, −2.9	1.33 (01)	0.124 (009)	Ia-norm	HVG	HV
SN 2009fx	−2.2	···	···	Ia-norm	···	N
SN 2009ig	−14.4, −14.3, −14.2, −13.9, −13.3, −12.4, −12.3, −11.4, −11.3, −10.9, −10.9, −10.9, −10.3, −9.9, −9.4, −8.9, −8.4, −7.9, −6.9, −6.9, −6.0, −6.0, −4.0, −3.0, −2.0, −1.0, 3.4, 4.3	0.89 (02)	0.059 (033)	Ia-norm	LVG	HV
SN 2009no	2.1	···	···	Ia-norm	···	N
SN 2009nq	−3.1	1.11 (09)	0.106 (051)	Ia-norm	···	N
SN 2010Y	−7.2, −3.2	1.63 (01)	0.062 (019)	Ia-norm	···	N

Continued on next page

Table A.1 — Continued

SN Name	Phase(s) (d)[a]	$\Delta m_{15}(B)$ (mag)[b]	$(B-V)_0$ (mag)[c]	SNID (Sub)Type[d]	Benetti Type[e]	Wang Type[f]
PTF 10bjs	−9.8, −8.6, −7.4, −6.6, −5.5, −1.8, 0.2	0.88 (03)	−0.090 (020)	Ia-norm	···	HV
SN 2010ai	−10.5, −8.6, −3.7, −0.8	1.34 (01)	0.048 (015)	Ia-norm	HVG	N
PTF 10fps	0.0, 0.9, 3.9	1.62 (09)	0.140 (040)	Ia-norm	FAINT	N
SN 2010dm	−6.5	0.80 (01)	0.190 (040)	Ia-99aa	···	···
PTF 10icb	−9.8	1.02 (05)	0.060 (020)	Ia-norm	···	···
SN 2010ex	1.1	···	···	Ia-norm	···	N
PTF 10qjl	−3.0	1.12 (04)	−0.100 (020)	Ia-norm	···	N
SN 2010ii	−6.1, −0.5	···	···	Ia-norm	···	HV
SN 2010it	−9.5, −8.5, −6.6, −2.6, −0.6, 3.3	···	···	Ia-norm	HVG	HV
PTF 10ygu	−3.7	0.90 (03)	0.440 (030)	Ia-norm	···	HV
SN 2010iw	−4.9, −3.0, −0.1, 3.9	···	···	Ia-99aa	HVG	···
SN 2010kg	−9.9, −9.0, −8.0, −6.0, −5.0, −4.1, −3.1, −1.1, −0.1, 0.9, 2.8, 4.8	1.37 (06)	0.300 (085)	Ia-norm	HVG	HV
SN 2011ao	−7.5, −6.7, −5.8, −4.8, −1.8, −0.8, 0.2, 1.2, 2.2, 3.2	···	···	Ia-norm	HVG	N
SN 2011by	−11.7, −9.8, −5.7, −3.8, 0.2, 0.3, 2.3, 4.2	1.14 (03)	−0.061 (032)	Ia-norm	LVG	N
SN 2011dm	−5.5	···	···	Ia-norm	···	···

Continued on next page

Table A.1 — Continued

SN Name	Phase(s) (d)[a]	$\Delta m_{15}(B)$ (mag)[b]	$(B-V)_0$ (mag)[c]	SNID (Sub)Type[d]	Benetti Type[e]	Wang Type[f]
SN 2011ek	−6.0, −5.0, 3.0	1.19 (04)	0.180 (040)	Ia-norm	···	HV
SN 2011fe	−17.0, −16.0, −15.0, −15.0, −13.0, −12.0, −11.0, −10.0, −10.0, −9.0, −9.0, −7.0, −2.0, −1.0, 2.0, 3.0	1.07 (06)	−0.067 (085)	Ia-norm	LVG	N
SN 2011gy	−1.1	···	···	Ia-norm	···	HV
SN 2011hb	−5.8, −2.9, 3.0	···	···	Ia-norm	HVG	N
SN 2011ia	−3.0	···	···	Ia-norm	···	N
SN 2012I	−1.0	···	···	Ia-norm	···	N
SN 2012bh	0.0	···	···	Ia-norm	···	N
SN 2012cg	−14.7, −13.8, −12.8, −11.8, −10.5, −9.6, −7.8, −6.8, −4.8, −3.8, −3.8, −0.5	0.83 (05)	0.120 (050)	Ia-99aa	LVG	···
SN 2012da	−1.0	···	···	Ia-norm	···	N
SN 2012fr	−14.4, −14.1, −12.6, −12.4, −11.4, −9.3, −8.4, −8.2, −7.6, −7.5, −6.7, −6.6, −6.4, −5.6, −4.7, −4.6, −3.7, −3.6, −2.5, −2.4, −1.4, −1.3, −0.3, 0.4, 0.7, 1.3, 1.7, 2.3, 3.2, 4.5	0.85 (05)	···	Ia-norm	LVG	HV
SN 2013cs	−8.9, −3.0	···	···	Ia-norm	···	HV

Continued on next page

Table A.1 — Continued

SN Name	Phase(s) (d)[a]	$\Delta m_{15}(B)$ (mag)[b]	$(B-V)_0$ (mag)[c]	SNID (Sub)Type[d]	Benetti Type[e]	Wang Type[f]
SN 2013di	−1.6	···	···	Ia-norm	···	N

[a]Phases are in rest-frame days.

[b]Uncertainties are in parentheses, in units of 0.01 mag.

[c]Uncertainties are in parentheses, in units of 0.001 mag.

[d]Spectral classification using the SuperNova IDentification code (SNID; Blondin & Tonry, 2007) as implemented in BSNIP I (Silverman et al., 2012a).

[e]Classification based on the velocity gradient of the Si II λ6355 line (Benetti et al., 2005). "HVG" = high velocity gradient; "LVG" = low velocity gradient; "FAINT" = faint/underluminous.

[f]Classification based on the velocity of the Si II λ6355 line (Wang et al., 2009b). "HV" = high velocity; "N" = normal.

[g]Also known as SNF20071021-000.

[h]Also known as SNF20080514-002.

[i]Also known as SNF20080909-030.

Tables A.2, A.3, and A.4 list measured values of the Ca II H&K (CaHK), Si II 6355 Å, and Ca II near-IR triplet (CaNIR) features, respectively. The velocity for each component is displayed, as well as the pseudo-equivalent width (pEW; e.g., Garavini et al., 2007; Silverman et al., 2012b). Also shown for each feature is R, the ratio of the pEW of the HVF to the pEW of the PVF, as defined by Childress et al. (2014). Fits with no HVF have $R \equiv 0$ and fits with no PVF have undefined values of R.

Table A.2: CaHK Fit Results

SN Name	Phase (d)[a]	HVF v (10^3 km s^{-1})	HVF pEW (Å)	PVF v (10^3 km s^{-1})	PVF pEW (Å)	$R^{b}_{\rm CaHK}$	Si II λ3858 v (10^3 km s^{-1})	Si IIλ3858 pEW (Å)
SN 1989M	2.5	···	···	11.19 (0.05)	81.8 (0.8)	0	10.93 (0.05)	92.3 (0.4)
SN 1991bg	0.1	···	···	11.19 (0.05)	233.1 (2.4)	0	···	···
SN 1994D	−12.3	26.95 (0.07)	97.3 (1.2)	17.53 (0.07)	85.4 (1.1)	1.14 (0.02)	···	···
SN 1994D	−7.7	23.56 (0.05)	120.0 (0.8)	11.31 (0.05)	36.7 (0.6)	3.27 (0.05)	11.79 (0.05)	5.2 (0.2)
SN 1994D	−6.3	20.74 (0.12)	110.0 (1.2)	9.95 (0.05)	20.5 (0.9)	5.36 (0.24)	11.95 (0.05)	5.4 (0.3)
SN 1994D	−5.3	19.60 (0.14)	101.0 (1.4)	10.16 (0.05)	18.5 (0.9)	5.46 (0.28)	11.94 (0.05)	8.0 (0.3)
SN 1994D	−3.9	22.87 (0.10)	22.2 (0.6)	11.86 (0.05)	55.6 (0.2)	0.40 (0.01)	11.75 (0.05)	15.9 (0.5)
SN 1994D	−3.3	24.17 (0.09)	13.1 (0.4)	11.10 (0.05)	50.0 (0.2)	0.26 (0.01)	11.71 (0.05)	30.3 (0.4)
SN 1994S	1.1	18.62 (0.09)	54.8 (1.1)	10.54 (0.06)	56.0 (1.0)	0.98 (0.03)	···	···
SN 1995D	3.8	17.57 (0.05)	39.8 (0.3)	10.77 (0.05)	57.0 (0.3)	0.70 (0.01)	···	···
SN 1995E	−2.5	18.03 (0.14)	56.1 (1.6)	10.83 (0.12)	53.0 (1.6)	1.06 (0.04)	···	···
SN 1997Y	1.3	18.30 (0.05)	34.8 (0.6)	11.60 (0.05)	75.9 (0.8)	0.46 (0.01)	···	···
SN 1997do	−5.7	27.80 (0.05)	64.9 (1.2)	18.52 (0.08)	125.8 (1.3)	0.52 (0.01)	···	···
SN 1998dk	−7.2	27.00 (0.29)	100.7 (4.6)	16.64 (0.29)	101.5 (4.5)	0.99 (0.06)	···	···
SN 1998dk	−0.5	19.38 (0.05)	104.2 (0.8)	11.82 (0.05)	33.0 (0.7)	3.16 (0.07)	···	···
SN 1998dm	−12.5	22.63 (0.21)	70.5 (2.5)	12.82 (0.17)	65.7 (2.3)	1.07 (0.05)	···	···
SN 1998dm	−5.6	21.36 (0.16)	32.0 (1.2)	12.19 (0.05)	69.8 (0.7)	0.46 (0.02)	11.73 (0.05)	6.8 (0.7)
SN 1998ef	−8.6	22.10 (0.05)	127.5 (0.7)	12.72 (0.05)	18.7 (0.5)	6.83 (0.19)	···	···
SN 1999aa	−10.6	22.54 (0.19)	33.2 (4.9)	15.16 (1.33)	27.9 (4.8)	1.19 (0.27)	···	···

Continued on next page

Table A.2 — Continued

SN Name	Phase (d)[a]	HVF v (10^3 km s^{-1})	HVF pEW (Å)	PVF v (10^3 km s^{-1})	PVF pEW (Å)	R^{b}_{CaHK}	Si II λ3858 v (10^3 km s^{-1})	Si IIλ3858 pEW (Å)
SN 1999ac	−0.9	18.63 (0.05)	26.3 (0.8)	12.68 (0.05)	82.6 (0.9)	0.32 (0.01)	···	···
SN 1999cp	4.9	···	···	10.64 (0.05)	125.9 (1.0)	0	10.31 (0.05)	26.4 (0.4)
SN 1999da	−2.1	···	···	13.91 (0.05)	162.4 (1.5)	0	···	···
SN 1999dq	−3.9	22.30 (0.05)	19.0 (0.7)	11.32 (0.07)	38.8 (0.7)	0.49 (0.02)	11.44 (0.05)	9.7 (0.3)
SN 1999dq	3.0	19.27 (0.05)	51.8 (0.6)	10.97 (0.05)	42.5 (0.5)	1.22 (0.02)	···	···
SN 2000cp	2.9	···	···	11.19 (0.13)	171.4 (5.2)	0	10.90 (0.12)	58.6 (2.4)
SN 2000cw	4.8	···	···	14.45 (0.05)	304.9 (1.6)	0	···	···
SN 2000dg	−5.1	22.82 (0.43)	13.8 (1.4)	11.00 (0.05)	55.1 (0.7)	0.25 (0.03)	11.72 (0.05)	11.7 (0.7)
SN 2000dg	4.7	···	···	11.09 (0.05)	112.3 (1.8)	0	11.27 (0.05)	13.5 (0.5)
SN 2000dk	1.0	···	···	12.35 (0.05)	171.4 (1.9)	0	11.60 (0.05)	22.8 (0.7)
SN 2000dm	−1.6	24.10 (0.40)	10.1 (1.3)	12.03 (0.05)	72.3 (0.5)	0.14 (0.02)	11.98 (0.05)	19.8 (0.8)
SN 2000dn	−0.9	17.74 (0.06)	39.5 (1.4)	11.11 (0.07)	87.2 (1.3)	0.45 (0.02)	···	···
SN 2000dx	−9.3	22.28 (0.09)	179.6 (2.6)	···	···	···	···	···
SN 2000fa	−8.3	23.12 (0.09)	142.7 (1.6)	11.94 (0.25)	22.0 (1.4)	6.49 (0.42)	···	···
SN 2001az	−3.2	20.97 (0.10)	56.1 (1.3)	12.17 (0.10)	56.9 (1.6)	0.99 (0.04)	···	···
SN 2001bf	1.2	18.40 (0.05)	51.0 (0.4)	7.90 (0.05)	21.7 (0.3)	2.35 (0.04)	···	···
SN 2001bp	0.5	19.36 (0.32)	36.4 (4.7)	11.64 (0.26)	51.4 (5.1)	0.71 (0.12)	···	···
SN 2001cp	1.4	17.59 (0.10)	63.5 (1.5)	10.72 (0.07)	45.4 (1.2)	1.40 (0.05)	···	···
SN 2001da	−1.1	20.79 (0.07)	102.9 (1.5)	12.31 (0.09)	59.6 (1.4)	1.73 (0.05)	···	···

Continued on next page

Table A.2 — Continued

SN Name	Phase (d)[a]	HVF v (10^3 km s^{-1})	HVF pEW (Å)	PVF v (10^3 km s^{-1})	PVF pEW (Å)	R^{b}_{CaHK}	Si II λ3858 v (10^3 km s^{-1})	Si IIλ3858 pEW (Å)
SN 2001eh	−5.6	20.59 (0.14)	42.4 (4.6)	12.98 (0.83)	43.3 (5.1)	0.98 (0.16)	···	···
SN 2001eh	−4.5	20.11 (0.06)	33.0 (1.5)	12.51 (0.24)	46.1 (1.8)	0.72 (0.04)	···	···
SN 2001eh	3.3	18.30 (0.05)	73.1 (0.8)	10.51 (0.05)	27.5 (0.8)	2.66 (0.08)	···	···
SN 2001ep	2.8	···	···	12.93 (0.05)	204.6 (2.1)	0	11.01 (0.05)	9.9 (0.7)
SN 2001ex	−1.8	···	···	11.07 (0.06)	129.6 (3.3)	0	10.66 (0.09)	15.9 (1.0)
SN 2001fe	−1.0	18.96 (0.06)	30.6 (0.6)	11.53 (0.05)	54.9 (0.7)	0.56 (0.01)	···	···
SN 2002aw	2.1	···	···	11.61 (0.11)	139.6 (4.3)	0	11.16 (0.12)	24.2 (1.7)
SN 2002bo	−11.9	27.87 (0.67)	69.7 (8.4)	19.68 (0.47)	82.5 (8.5)	0.85 (0.13)	···	···
SN 2002bo	−1.1	18.45 (0.20)	104.1 (3.4)	11.51 (0.13)	32.4 (3.0)	3.21 (0.31)	···	···
SN 2002cd	1.1	17.77 (0.05)	133.5 (1.0)	···	···	···	···	···
SN 2002cf	−0.8	···	···	13.16 (0.05)	186.9 (2.1)	0	···	···
SN 2002ck	3.6	14.16 (0.08)	79.5 (1.6)	9.13 (0.05)	16.0 (1.0)	4.98 (0.34)	···	···
SN 2002cr	−6.8	16.88 (0.16)	84.9 (2.0)	10.33 (0.10)	19.2 (1.8)	4.43 (0.44)	···	···
SN 2002cs	−7.8	23.83 (0.05)	61.8 (0.8)	14.76 (0.05)	41.1 (0.6)	1.50 (0.03)	···	···
SN 2002de	−0.3	19.32 (0.15)	73.1 (2.9)	11.37 (0.11)	46.0 (2.4)	1.59 (0.10)	···	···
SN 2002dj	−8.0	24.57 (0.09)	140.6 (1.7)	15.38 (0.08)	40.5 (1.5)	3.47 (0.13)	···	···
SN 2002dk	−1.2	22.65 (0.97)	162.5 (15.0)	12.41 (0.23)	69.0 (13.2)	2.35 (0.50)	···	···
SN 2002eb	1.7	18.20 (0.05)	68.4 (0.6)	10.30 (0.05)	32.6 (0.5)	2.10 (0.04)	···	···
SN 2002ef	4.7	···	···	13.11 (0.11)	206.7 (6.6)	0	···	···

Continued on next page

Table A.2 — Continued

SN Name	Phase (d)[a]	HVF v (10^3 km s^{-1})	HVF pEW (Å)	PVF v (10^3 km s^{-1})	PVF pEW (Å)	R^{b}_{CaHK}	Si II λ3858 v (10^3 km s^{-1})	Si IIλ3858 pEW (Å)
SN 2002er	−4.6	18.73 (0.05)	127.6 (0.6)	11.58 (0.05)	25.0 (0.5)	5.11 (0.11)	···	···
SN 2002eu	−0.1	···	···	9.69 (0.07)	52.1 (3.2)	0	10.63 (0.11)	83.5 (1.8)
SN 2002fb	1.0	···	···	10.31 (0.05)	255.3 (2.1)	0	···	···
SN 2002ha	−0.9	17.16 (0.05)	72.3 (0.7)	10.33 (0.05)	39.1 (0.7)	1.85 (0.04)	···	···
SN 2002ha	4.9	···	···	11.81 (0.05)	157.2 (1.0)	0	10.80 (0.05)	15.6 (0.3)
SN 2002he	0.3	···	···	15.46 (0.05)	227.3 (0.5)	0	···	···
SN 2002he	3.2	···	···	14.71 (0.05)	218.1 (0.5)	0	···	···
SN 2002hu	−5.8	20.01 (0.05)	56.4 (0.5)	11.20 (0.06)	54.1 (0.6)	1.04 (0.01)	···	···
SN 2002hw	−6.3	···	···	13.73 (0.05)	172.1 (0.8)	0	···	···
SN 2003U	−2.6	···	···	10.35 (0.09)	80.9 (3.1)	0	10.43 (0.10)	89.4 (1.6)
SN 2003W	−5.1	23.01 (0.05)	158.7 (0.9)	···	···	···	···	···
SN 2003Y	−1.7	···	···	11.00 (0.06)	227.2 (3.1)	0	···	···
SN 2003cq	−0.2	18.70 (0.21)	107.6 (3.8)	11.38 (0.16)	37.2 (3.3)	2.89 (0.27)	···	···
SN 2003fa	−8.2	21.15 (0.10)	37.6 (2.7)	12.84 (0.63)	31.3 (3.1)	1.20 (0.15)	···	···
SN 2003gn	−5.4	24.65 (1.36)	81.8 (35.8)	16.93 (2.28)	93.1 (33.0)	0.88 (0.49)	···	···
SN 2003gt	−5.1	24.15 (0.17)	9.8 (1.8)	11.54 (0.05)	58.5 (0.9)	0.17 (0.03)	12.28 (0.05)	13.0 (0.6)
SN 2003he	2.7	17.77 (0.13)	92.8 (2.2)	10.46 (0.08)	30.8 (1.7)	3.01 (0.18)	···	···
SN 2003hs	−5.5	19.73 (0.17)	144.6 (5.8)	···	···	···	···	···
SN 2003kf	−7.5	23.49 (0.05)	73.2 (0.2)	13.17 (0.05)	66.1 (0.1)	1.11 (0.01)	12.20 (0.05)	4.8 (0.1)

Continued on next page

Table A.2 — Continued

SN Name	Phase (d)[a]	HVF v (10^3 km s^{-1})	HVF pEW (Å)	PVF v (10^3 km s^{-1})	PVF pEW (Å)	R^{b}_{CaHK}	Si II λ3858 v (10^3 km s^{-1})	Si IIλ3858 pEW (Å)
SN 2004ey	−7.6	22.82 (0.05)	91.9 (0.4)	13.13 (0.05)	56.4 (0.4)	1.63 (0.01)	···	···
SN 2004fu	−2.7	20.31 (0.05)	149.7 (0.4)	12.31 (0.05)	32.4 (0.4)	4.62 (0.05)	···	···
SN 2005er	1.7	···	···	10.91 (0.08)	251.2 (4.6)	0	···	···
SN 2005eq	−3.0	21.85 (0.05)	27.0 (0.6)	11.53 (0.08)	57.3 (0.8)	0.47 (0.01)	10.40 (0.05)	12.7 (0.3)
SN 2005eu	−9.1	21.79 (0.05)	24.2 (0.4)	11.51 (0.05)	37.1 (0.5)	0.65 (0.01)	···	···
SN 2006bt	−5.3	19.16 (0.06)	52.1 (0.8)	11.45 (0.07)	38.1 (0.9)	1.37 (0.04)	···	···
SN 2006or	−2.8	16.33 (0.05)	140.0 (0.6)	···	···	···	···	···
SN 2006sr	2.7	···	···	11.98 (0.08)	111.4 (2.3)	0	11.75 (0.09)	43.0 (1.0)
SN 2007A	2.4	17.91 (0.05)	33.3 (0.6)	11.07 (0.05)	60.8 (0.7)	0.55 (0.01)	···	···
SN 2007le	−10.3	32.19 (0.05)	53.8 (1.3)	21.67 (0.09)	164.3 (1.5)	0.33 (0.01)	···	···
SN 2007le	−9.4	31.57 (0.05)	36.0 (0.8)	22.08 (0.06)	170.8 (1.0)	0.21 (0.01)	···	···
SN 2007on	−3.0	18.44 (0.05)	41.8 (0.3)	12.09 (0.05)	59.7 (0.4)	0.70 (0.01)	···	···
SN 2008Z	−2.3	20.98 (0.14)	34.7 (2.2)	12.23 (0.12)	58.2 (2.1)	0.60 (0.04)	···	···
SN 2008ar	2.8	22.51 (0.22)	127.6 (4.6)	13.99 (0.15)	34.2 (3.4)	3.73 (0.39)	···	···
SN 2008s1[c]	−6.4	18.96 (0.17)	11.7 (1.9)	11.92 (0.11)	51.2 (1.6)	0.23 (0.04)	···	···
SN 2008s1[c]	−4.4	18.71 (0.54)	20.6 (5.0)	11.23 (0.41)	56.9 (6.2)	0.36 (0.10)	···	···
SN 2008s1[c]	−3.4	18.38 (0.11)	14.7 (1.9)	11.90 (0.12)	62.5 (2.0)	0.23 (0.03)	···	···
SN 2008s1[c]	0.5	···	···	11.41 (0.15)	118.9 (5.4)	0	10.56 (0.14)	20.4 (1.8)
SN 2008s1[c]	4.4	···	···	11.52 (0.06)	125.5 (2.3)	0	10.55 (0.06)	21.3 (0.9)

Continued on next page

Table A.2 — Continued

SN Name	Phase (d)[a]	HVF v (10^3 km s^{-1})	HVF pEW (Å)	PVF v (10^3 km s^{-1})	PVF pEW (Å)	R^{b}_{CaHK}	Si II λ3858 v (10^3 km s^{-1})	Si IIλ3858 pEW (Å)
SN 2008dx	2.5	···	···	11.61 (0.21)	170.9 (9.7)	0	···	···
SN 2008ec	−0.2	···	···	11.43 (0.05)	131.6 (1.6)	0	11.06 (0.05)	39.0 (0.7)
SN 2009ig	−14.3	37.16 (0.05)	24.4 (1.2)	27.86 (0.13)	117.2 (1.3)	0.21 (0.01)	···	···
SN 2009ig	−10.9	30.22 (0.08)	57.0 (2.5)	19.89 (0.16)	161.3 (2.3)	0.35 (0.02)	···	···
SN 2009ig	−9.9	28.48 (0.07)	99.3 (2.6)	19.57 (0.21)	87.5 (2.3)	1.14 (0.04)	···	···
SN 2009ig	−9.4	26.63 (0.05)	169.1 (0.6)	13.96 (0.05)	27.1 (0.5)	6.25 (0.11)	···	···
SN 2009ig	−8.9	25.47 (0.05)	148.1 (0.4)	13.99 (0.05)	29.9 (0.3)	4.95 (0.05)	···	···
SN 2009ig	−8.4	25.48 (0.05)	164.8 (0.6)	13.08 (0.05)	22.9 (0.4)	7.21 (0.13)	···	···
SN 2009ig	−7.9	24.75 (0.05)	147.0 (0.3)	13.46 (0.05)	24.8 (0.2)	5.94 (0.05)	···	···
SN 2009ig	−6.9	24.25 (0.05)	130.1 (0.3)	13.54 (0.05)	30.9 (0.2)	4.22 (0.03)	···	···
SN 2009ig	−6.0	23.43 (0.05)	119.1 (0.2)	13.58 (0.05)	26.8 (0.2)	4.44 (0.03)	···	···
SN 2011by	−11.7	22.58 (0.67)	31.8 (4.4)	13.61 (0.19)	68.2 (2.3)	0.47 (0.07)	12.96 (0.05)	14.9 (2.3)
SN 2011by	−5.7	24.13 (0.15)	7.8 (0.6)	11.97 (0.05)	68.7 (0.3)	0.11 (0.01)	12.17 (0.05)	21.7 (0.4)
SN 2011by	−3.8	19.29 (0.05)	31.8 (0.3)	11.52 (0.05)	65.5 (0.4)	0.49 (0.01)	···	···
SN 2011by	0.2	17.28 (0.08)	44.9 (0.8)	10.56 (0.05)	52.5 (0.8)	0.86 (0.02)	···	···
SN 2011by	4.2	16.55 (0.06)	30.5 (0.6)	10.64 (0.05)	55.1 (0.7)	0.55 (0.01)	···	···
SN 2011fe	−16.0	31.16 (0.10)	24.9 (1.3)	21.70 (0.11)	123.0 (1.6)	0.20 (0.01)	···	···
SN 2011fe	−15.0	24.05 (0.49)	95.2 (5.9)	16.06 (0.29)	51.6 (6.5)	1.84 (0.26)	···	···
SN 2011fe	−13.0	20.92 (0.24)	118.2 (4.2)	13.17 (0.15)	29.6 (3.7)	3.99 (0.51)	···	···

Continued on next page

Table A.2 — Continued

SN Name	Phase (d)[a]	HVF v (10^3 km s^{-1})	HVF pEW (Å)	PVF v (10^3 km s^{-1})	PVF pEW (Å)	R^{b}_{CaHK}	Si II λ3858 v (10^3 km s^{-1})	Si IIλ3858 pEW (Å)
SN 2011fe	−10.0	20.66 (0.05)	73.6 (0.2)	12.49 (0.05)	52.8 (0.2)	1.39 (0.01)	···	···
SN 2012cg	−11.8	23.79 (0.34)	76.6 (4.1)	14.85 (0.41)	48.4 (4.1)	1.58 (0.16)	···	···
SN 2012cg	−3.8	20.56 (0.05)	52.5 (0.3)	11.79 (0.05)	47.9 (0.4)	1.10 (0.01)	···	···
SN 2012fr	−6.7	24.89 (0.05)	167.5 (0.6)	11.95 (0.09)	12.9 (0.6)	13.04 (0.61)	···	···
SN 2012fr	−5.6	24.32 (0.05)	138.0 (0.6)	11.64 (0.05)	25.4 (0.4)	5.43 (0.09)	12.15 (0.05)	3.1 (0.1)
SN 2012fr	−4.7	23.84 (0.05)	141.2 (0.7)	11.59 (0.10)	26.0 (0.8)	5.44 (0.18)	···	···
SN 2012fr	−3.7	23.46 (0.05)	131.5 (0.7)	11.85 (0.09)	28.9 (0.9)	4.55 (0.14)	···	···
SN 2012fr	1.3	22.60 (0.06)	84.6 (1.1)	13.81 (0.11)	49.8 (1.3)	1.70 (0.05)	···	···
SN 2012fr	2.3	20.15 (0.10)	98.5 (2.1)	11.29 (0.07)	44.5 (1.4)	2.21 (0.08)	···	···
SN 2012fr	3.2	20.91 (0.05)	100.4 (0.8)	11.75 (0.05)	30.0 (1.1)	3.34 (0.12)	···	···
SN 2013cs	−8.9	21.49 (0.09)	125.5 (1.4)	13.74 (0.05)	35.7 (1.2)	3.52 (0.13)	···	···
SN 2013cs	−3.0	17.67 (0.06)	97.6 (1.0)	10.70 (0.05)	34.3 (0.9)	2.85 (0.08)	···	···

[a]Phases are in rest-frame days.

[b]R_{CaHK} is the ratio of the pEW of the HVF to the pEW of the PVF, as defined by Childress et al. (2014).

[c]Also known as SNF20080514-002.

Table A.3: Si II 6355 Å Fit Results

SN Name	Phase (d)[a]	HVF v (10^3 km s^{-1})	HVF pEW (Å)	PVF v (10^3 km s^{-1})	PVF pEW (Å)	$R^{b}_{\text{Si II6355 Å}}$
SN 1989M	2.5	···	···	12.33 (0.05)	132.9 (0.1)	0
SN 1989M	3.5	···	···	12.19 (0.05)	124.2 (0.1)	0
SN 1991T	−10.1	···	···	10.66 (0.06)	21.1 (0.3)	0
SN 1991T	−9.1	···	···	9.93 (0.09)	17.4 (0.4)	0
SN 1991bg	0.1	···	···	9.63 (0.05)	96.0 (0.6)	0
SN 1991bg	1.1	···	···	9.21 (0.05)	94.5 (0.9)	0
SN 1994D	−12.3	19.03 (0.05)	40.1 (0.9)	13.67 (0.05)	97.8 (0.6)	0.41 (0.01)
SN 1994D	−11.3	18.82 (0.06)	34.7 (1.5)	13.30 (0.08)	96.2 (0.5)	0.36 (0.02)
SN 1994D	−9.3	17.47 (0.10)	20.3 (0.7)	11.76 (0.05)	65.5 (0.6)	0.31 (0.01)
SN 1994D	−7.7	18.17 (0.06)	6.5 (0.2)	11.77 (0.05)	76.4 (0.6)	0.09 (0.01)
SN 1994D	−6.3	···	···	10.79 (0.05)	86.5 (0.2)	0
SN 1994D	−5.3	···	···	11.07 (0.05)	83.8 (0.2)	0
SN 1994D	−3.9	···	···	10.92 (0.05)	85.5 (0.1)	0
SN 1994D	−3.3	···	···	10.80 (0.05)	90.4 (0.1)	0
SN 1994S	1.1	···	···	10.40 (0.05)	85.6 (0.2)	0
SN 1995D	3.8	···	···	10.17 (0.05)	80.2 (0.1)	0
SN 1995E	−2.5	···	···	10.68 (0.05)	101.8 (0.1)	0
SN 1995ac	−6.3	···	···	10.16 (0.13)	20.0 (1.3)	0

Continued on next page

Table A.3 — Continued

SN Name	Phase (d)[a]	HVF v (10^3 km s^{-1})	HVF pEW (Å)	PVF v (10^3 km s^{-1})	PVF pEW (Å)	$R^{b}_{\text{Si II6355 Å}}$
SN 1997Y	1.3	···	···	10.51 (0.05)	110.6 (0.3)	0
SN 1997br	−4.8	···	···	10.77 (0.05)	23.0 (0.2)	0
SN 1997do	−5.7	···	···	13.96 (0.05)	110.6 (0.2)	0
SN 1998dk	−7.2	···	···	14.41 (0.05)	112.2 (0.2)	0
SN 1998dk	−0.5	···	···	12.38 (0.05)	108.0 (0.1)	0
SN 1998dm	−12.5	···	···	12.18 (0.05)	66.4 (0.1)	0
SN 1998dm	−5.6	···	···	10.86 (0.05)	66.2 (0.1)	0
SN 1998ef	−8.6	···	···	14.32 (0.05)	150.6 (0.3)	0
SN 1998es	0.3	···	···	10.24 (0.05)	59.5 (0.1)	0
SN 1999aa	−10.6	···	···	12.60 (0.07)	31.4 (0.5)	0
SN 1999aa	0.2	···	···	10.35 (0.05)	59.6 (0.2)	0
SN 1999ac	−3.7	···	···	11.19 (0.05)	76.7 (0.1)	0
SN 1999ac	−0.9	···	···	10.40 (0.05)	86.3 (0.2)	0
SN 1999cp	4.9	···	···	10.43 (0.05)	105.4 (0.1)	0
SN 1999da	−2.1	···	···	10.66 (0.05)	129.5 (0.2)	0
SN 1999dk	−6.6	···	···	14.55 (0.05)	134.8 (0.1)	0
SN 1999dq	−3.9	···	···	10.97 (0.05)	42.0 (0.2)	0
SN 1999dq	3.0	···	···	10.86 (0.05)	61.7 (0.1)	0
SN 1999gd	−1.1	···	···	10.42 (0.05)	116.5 (0.4)	0

Continued on next page

Table A.3 — Continued

SN Name	Phase (d)[a]	HVF v (10^3 km s^{-1})	HVF pEW (Å)	PVF v (10^3 km s^{-1})	PVF pEW (Å)	$R^{b}_{\text{Si II6355 Å}}$
SN 1999gh	4.1	···	···	10.58 (0.05)	164.5 (0.2)	0
SN 2000cp	2.9	···	···	11.00 (0.05)	145.1 (0.3)	0
SN 2000cw	4.8	···	···	9.91 (0.05)	111.8 (0.3)	0
SN 2000dg	−5.1	···	···	10.90 (0.05)	76.4 (0.2)	0
SN 2000dg	4.7	···	···	10.39 (0.05)	72.8 (0.3)	0
SN 2000dk	1.0	···	···	10.67 (0.05)	124.3 (0.1)	0
SN 2000dm	−1.6	···	···	11.08 (0.05)	106.9 (0.1)	0
SN 2000dn	−0.9	···	···	10.19 (0.05)	119.4 (0.4)	0
SN 2000dx	−9.3	···	···	15.11 (0.05)	151.2 (1.5)	0
SN 2000fa	−8.3	···	···	14.13 (0.05)	95.6 (0.6)	0
SN 2001az	−3.2	···	···	11.73 (0.05)	81.5 (0.6)	0
SN 2001ba	−4.6	···	···	12.77 (0.11)	144.2 (7.6)	0
SN 2001bf	1.2	···	···	11.75 (0.05)	130.0 (0.2)	0
SN 2001br	3.5	···	···	12.93 (0.05)	133.9 (1.3)	0
SN 2001br	3.5	···	···	12.56 (0.05)	152.5 (0.7)	0
SN 2001bp	0.5	···	···	10.86 (0.05)	75.4 (1.2)	0
SN 2001cp	1.4	···	···	10.61 (0.05)	81.2 (0.3)	0
SN 2001da	−1.1	···	···	11.35 (0.05)	121.4 (0.3)	0
SN 2001eh	−5.6	···	···	11.18 (0.05)	43.4 (0.7)	0

Continued on next page

Table A.3 — Continued

SN Name	Phase (d)[a]	HVF v (10^3 km s^{-1})	HVF pEW (Å)	PVF v (10^3 km s^{-1})	PVF pEW (Å)	$R^{b}_{\text{Si II6355 Å}}$
SN 2001eh	−4.5	···	···	11.05 (0.05)	42.2 (0.4)	0
SN 2001eh	3.3	···	···	10.84 (0.05)	61.1 (0.2)	0
SN 2001ep	2.8	···	···	10.16 (0.05)	120.9 (0.1)	0
SN 2001ex	−1.8	···	···	9.92 (0.05)	123.0 (0.6)	0
SN 2001fe	−1.0	···	···	11.07 (0.05)	73.2 (0.1)	0
SN 2002aw	2.1	···	···	10.21 (0.05)	99.9 (0.8)	0
SN 2002bf	3.0	18.48 (0.05)	38.5 (0.5)	13.68 (0.05)	133.4 (0.1)	0.29 (0.01)
SN 2002bo	−11.9	20.97 (0.07)	36.4 (2.3)	15.63 (0.11)	103.7 (0.2)	0.35 (0.02)
SN 2002bo	−1.1	···	···	13.07 (0.05)	156.5 (0.5)	0
SN 2002cd	1.1	···	···	15.23 (0.05)	121.9 (0.1)	0
SN 2002cf	−0.8	···	···	10.22 (0.05)	117.6 (0.4)	0
SN 2002ck	3.6	···	···	10.31 (0.05)	76.1 (0.6)	0
SN 2002cr	−6.8	···	···	11.08 (0.05)	105.5 (0.3)	0
SN 2002cs	−7.8	19.17 (0.05)	22.5 (1.0)	14.91 (0.05)	104.4 (0.1)	0.22 (0.01)
SN 2002cu	−5.3	19.51 (0.05)	20.0 (0.8)	13.24 (0.05)	123.6 (0.1)	0.16 (0.01)
SN 2002de	−0.3	···	···	11.59 (0.05)	102.8 (1.3)	0
SN 2002dj	−8.0	···	···	15.59 (0.05)	150.2 (0.3)	0
SN 2002dk	−1.2	···	···	10.43 (0.05)	116.8 (0.5)	0
SN 2002eb	1.7	···	···	10.23 (0.05)	72.7 (0.2)	0

Continued on next page

Table A.3 — Continued

SN Name	Phase (d)[a]	HVF v (10^3 km s^{-1})	HVF pEW (Å)	PVF v (10^3 km s^{-1})	PVF pEW (Å)	$R^{b}_{\text{Si II6355 Å}}$
SN 2002ef	4.7	···	···	11.43 (0.05)	108.4 (0.5)	0
SN 2002er	−4.6	···	···	12.05 (0.05)	112.6 (0.1)	0
SN 2002eu	−0.1	···	···	11.02 (0.05)	128.2 (0.5)	0
SN 2002fb	1.0	···	···	10.57 (0.05)	101.9 (0.3)	0
SN 2002ha	−0.9	···	···	10.93 (0.05)	106.7 (0.1)	0
SN 2002ha	4.9	···	···	10.38 (0.05)	106.2 (0.2)	0
SN 2002he	−5.9	···	···	13.30 (0.05)	110.1 (0.4)	0
SN 2002he	−1.0	···	···	12.52 (0.05)	123.2 (0.3)	0
SN 2002he	0.3	···	···	12.36 (0.05)	126.5 (0.2)	0
SN 2002he	3.2	···	···	12.07 (0.05)	127.7 (0.3)	0
SN 2002hu	−5.8	···	···	10.46 (0.05)	58.1 (0.3)	0
SN 2002hw	−6.3	···	···	11.25 (0.05)	94.4 (0.3)	0
SN 2003U	−2.6	···	···	11.30 (0.05)	130.1 (0.4)	0
SN 2003W	−5.1	20.77 (0.05)	31.5 (2.3)	15.07 (0.13)	118.8 (0.1)	0.27 (0.02)
SN 2003Y	−1.7	···	···	9.86 (0.05)	99.4 (0.5)	0
SN 2003cq	−0.2	···	···	12.08 (0.05)	129.2 (0.8)	0
SN 2003fa	−8.2	···	···	11.73 (0.06)	42.4 (0.8)	0
SN 2003gn	−5.4	···	···	13.39 (0.05)	154.1 (1.2)	0
SN 2003gn	3.3	···	···	10.99 (0.06)	194.3 (3.9)	0

Continued on next page

Table A.3 — Continued

SN Name	Phase (d)[a]	HVF v (10^3 km s^{-1})	HVF pEW (Å)	PVF v (10^3 km s^{-1})	PVF pEW (Å)	$R^{b}_{\text{Si II6355 Å}}$
SN 2003gt	−5.1	···	···	11.39 (0.05)	75.4 (0.3)	0
SN 2003he	2.7	···	···	11.31 (0.05)	103.2 (0.3)	0
SN 2003hs	−5.5	···	···	13.55 (0.05)	160.3 (1.3)	0
SN 2003iv	1.8	···	···	10.56 (0.05)	112.6 (0.2)	0
SN 2003kf	−7.5	···	···	12.07 (0.05)	68.4 (0.1)	0
SN 2004as	−4.4	17.14 (0.05)	12.2 (0.7)	12.33 (0.05)	120.6 (0.1)	0.10 (0.01)
SN 2004bl	4.6	···	···	10.72 (0.05)	98.3 (0.4)	0
SN 2004br	3.5	···	···	11.03 (0.05)	43.1 (0.6)	0
SN 2004bv	−7.1	···	···	11.05 (0.05)	40.8 (0.3)	0
SN 2004bw	−10.0	···	···	13.46 (0.05)	116.7 (2.1)	0
SN 2004dt	−6.5	19.18 (0.05)	56.2 (1.1)	13.20 (0.05)	117.5 (0.3)	0.48 (0.01)
SN 2004dt	1.4	···	···	13.54 (0.05)	182.5 (0.3)	0
SN 2004ef	−5.5	18.45 (0.05)	18.6 (0.8)	13.05 (0.05)	117.0 (3.7)	0.16 (0.01)
SN 2004eo	−5.6	···	···	11.07 (0.05)	105.4 (0.3)	0
SN 2004ey	−7.6	···	···	11.81 (0.05)	80.0 (0.1)	0
SN 2004fu	−2.7	···	···	12.90 (0.05)	133.5 (0.1)	0
SN 2004fu	2.4	···	···	11.98 (0.05)	137.4 (0.1)	0
SN 2004fz	−5.2	···	···	10.44 (0.05)	91.4 (0.2)	0
SN 2004gs	0.4	···	···	10.43 (0.05)	131.3 (0.3)	0

Continued on next page

Table A.3 — Continued

SN Name	Phase (d)[a]	HVF v (10^3 km s^{-1})	HVF pEW (Å)	PVF v (10^3 km s^{-1})	PVF pEW (Å)	$R^{b}_{\text{Si II6355 Å}}$
SN 2004gu	−4.7	···	···	10.89 (0.17)	31.4 (1.6)	0
SN 2005M	−1.4	···	···	10.67 (0.06)	70.6 (1.3)	0
SN 2005W	0.6	···	···	10.60 (0.05)	115.6 (0.3)	0
SN 2005ag	0.5	···	···	11.37 (0.05)	91.0 (1.8)	0
SN 2005am	4.5	···	···	11.15 (0.05)	116.7 (0.1)	0
SN 2005ao	−1.3	···	···	11.55 (0.05)	77.4 (0.5)	0
SN 2005ao	0.5	···	···	11.46 (0.05)	76.4 (0.4)	0
SN 2005bc	1.6	···	···	10.70 (0.05)	115.5 (0.2)	0
SN 2005bl	−5.6	···	···	10.69 (0.10)	54.5 (3.5)	0
SN 2005cf	−10.9	18.79 (0.05)	53.1 (0.6)	12.47 (0.05)	88.8 (0.1)	0.60 (0.01)
SN 2005cf	−2.1	···	···	10.23 (0.05)	84.3 (0.1)	0
SN 2005cf	−1.2	···	···	10.11 (0.05)	86.0 (0.1)	0
SN 2005cg	−10.1	20.83 (0.23)	21.2 (2.3)	13.51 (0.22)	59.3 (2.0)	0.36 (0.04)
SN 2005cg	−9.1	19.53 (0.09)	22.5 (0.8)	12.77 (0.06)	48.4 (0.2)	0.46 (0.02)
SN 2005cg	−4.3	···	···	12.11 (0.05)	67.2 (0.3)	0
SN 2005cg	−0.4	···	···	11.56 (0.05)	75.2 (0.3)	0
SN 2005cg	4.5	···	···	11.33 (0.05)	80.7 (0.3)	0
SN 2005de	−0.8	···	···	10.23 (0.05)	102.2 (0.4)	0
SN 2005dv	−0.6	···	···	12.55 (0.05)	153.7 (0.6)	0

Continued on next page

Table A.3 — Continued

SN Name	Phase (d)[a]	HVF v (10^3 km s^{-1})	HVF pEW (Å)	PVF v (10^3 km s^{-1})	PVF pEW (Å)	$R^{b}_{\text{Si II6355 Å}}$
SN 2005el	−6.7	···	···	11.33 (0.05)	67.3 (0.2)	0
SN 2005el	1.2	···	···	10.46 (0.05)	89.9 (0.2)	0
SN 2005er	−0.3	···	···	8.74 (0.05)	98.2 (0.3)	0
SN 2005er	1.7	···	···	9.35 (0.05)	65.9 (0.3)	0
SN 2005eq	−6.0	···	···	10.30 (0.09)	61.8 (1.7)	0
SN 2005eq	−3.0	···	···	10.20 (0.05)	44.3 (0.1)	0
SN 2005eq	0.7	···	···	10.09 (0.05)	53.3 (0.2)	0
SN 2005eu	−10.1	···	···	11.48 (0.05)	38.6 (0.2)	0
SN 2005eu	−9.1	···	···	11.26 (0.05)	36.3 (0.3)	0
SN 2005eu	−5.5	···	···	11.27 (0.05)	50.2 (0.6)	0
SN 2005hj	−5.2	···	···	10.35 (0.10)	29.6 (1.4)	0
SN 2005hj	−4.3	···	···	10.69 (0.06)	26.9 (0.9)	0
SN 2005hj	0.5	···	···	10.55 (0.05)	44.6 (0.6)	0
SN 2005hj	2.4	···	···	10.62 (0.05)	42.3 (0.7)	0
SN 2005hj	3.3	···	···	10.62 (0.05)	51.0 (0.5)	0
SN 2005iq	−5.9	···	···	11.60 (0.05)	91.9 (0.2)	0
SN 2005ki	1.6	···	···	11.03 (0.05)	106.7 (0.1)	0
SN 2005lz	0.6	···	···	10.11 (0.05)	112.5 (0.3)	0
SN 2005ms	−1.9	···	···	11.84 (0.05)	120.8 (0.8)	0

Continued on next page

Table A.3 — Continued

SN Name	Phase (d)[a]	HVF v (10^3 km s^{-1})	HVF pEW (Å)	PVF v (10^3 km s^{-1})	PVF pEW (Å)	$R^{b}_{\text{Si II6355 Å}}$
SN 2005na	0.0	···	···	10.55 (0.05)	72.2 (0.4)	0
SN 2005na	1.0	···	···	10.30 (0.05)	70.5 (0.6)	0
SN 2006D	3.7	···	···	10.42 (0.05)	99.3 (0.1)	0
SN 2006N	−1.9	···	···	11.39 (0.05)	99.2 (0.2)	0
SN 2006N	−0.9	···	···	11.30 (0.05)	111.6 (0.2)	0
SN 2006S	−3.9	···	···	11.08 (0.05)	48.6 (1.0)	0
SN 2006S	3.0	···	···	10.71 (0.05)	73.1 (0.5)	0
SN 2006X	−11.2	23.07 (0.05)	45.3 (1.0)	17.37 (0.05)	128.0 (16.3)	0.35 (0.01)
SN 2006X	−10.2	22.89 (0.05)	42.2 (1.0)	17.17 (0.05)	137.3 (0.6)	0.31 (0.01)
SN 2006X	−9.2	22.41 (0.05)	48.9 (1.2)	16.52 (0.05)	137.2 (30.5)	0.36 (0.01)
SN 2006X	−8.2	22.15 (0.05)	44.7 (0.7)	16.35 (0.05)	143.8 (3.9)	0.31 (0.01)
SN 2006X	−7.2	21.55 (0.05)	50.8 (0.6)	15.77 (0.05)	135.4 (4.5)	0.37 (0.01)
SN 2006X	−6.2	21.43 (0.05)	39.6 (0.6)	15.88 (0.05)	151.4 (0.8)	0.26 (0.01)
SN 2006X	−5.2	21.01 (0.05)	39.6 (0.7)	15.52 (0.05)	152.6 (10.4)	0.26 (0.01)
SN 2006X	−0.2	19.67 (0.05)	26.2 (0.8)	14.80 (0.05)	155.5 (9.5)	0.17 (0.01)
SN 2006X	0.8	19.29 (0.05)	22.3 (0.7)	14.59 (0.05)	158.6 (0.6)	0.14 (0.01)
SN 2006X	1.8	18.97 (0.05)	17.9 (0.5)	14.53 (0.05)	156.2 (2.3)	0.11 (0.01)
SN 2006X	2.8	···	···	14.57 (0.05)	179.4 (0.2)	0
SN 2006X	3.2	···	···	14.74 (0.05)	188.7 (0.1)	0

Continued on next page

Table A.3 — Continued

SN Name	Phase (d)[a]	HVF v (10^3 km s^{-1})	HVF pEW (Å)	PVF v (10^3 km s^{-1})	PVF pEW (Å)	$R^{b}_{\text{Si II6355 Å}}$
SN 2006ax	−10.1	···	···	12.25 (0.05)	87.4 (0.4)	0
SN 2006bt	−5.3	···	···	12.12 (0.05)	113.6 (0.3)	0
SN 2006bt	−4.5	···	···	11.88 (0.05)	111.7 (0.4)	0
SN 2006bt	2.3	···	···	10.51 (0.05)	131.8 (0.3)	0
SN 2006bu	4.2	···	···	11.18 (0.05)	81.8 (0.7)	0
SN 2006bz	−2.4	···	···	10.85 (0.05)	101.9 (0.8)	0
SN 2006cj	3.4	···	···	10.93 (0.05)	71.7 (0.7)	0
SN 2006cm	−1.2	···	···	11.15 (0.05)	48.3 (0.3)	0
SN 2006cp	−5.3	···	···	14.41 (0.05)	164.0 (0.3)	0
SN 2006cq	2.0	···	···	10.16 (0.05)	93.7 (0.8)	0
SN 2006cs	2.3	···	···	10.73 (0.05)	91.6 (0.5)	0
SN 2006cz	1.1	···	···	11.86 (0.05)	57.6 (0.4)	0
SN 2006dm	−7.9	···	···	12.25 (0.05)	103.0 (0.9)	0
SN 2006ef	3.2	···	···	11.81 (0.05)	140.1 (0.1)	0
SN 2006gr	−8.7	···	···	16.35 (0.05)	81.4 (0.6)	0
SN 2006ej	−3.7	···	···	12.40 (0.05)	114.9 (0.2)	0
SN 2006em	4.2	···	···	8.23 (0.05)	79.1 (0.3)	0
SN 2006et	3.3	···	···	9.91 (0.05)	73.4 (0.2)	0
SN 2006gj	4.7	···	···	9.91 (0.05)	123.0 (0.5)	0

Continued on next page

Table A.3 — Continued

SN Name	Phase (d)[a]	HVF v (10^3 km s^{-1})	HVF pEW (Å)	PVF v (10^3 km s^{-1})	PVF pEW (Å)	$\mathcal{R}^{b}_{\mathrm{Si\ II6355\ Å}}$
SN 2006gt	3.1	···	···	9.83 (0.05)	120.2 (0.8)	0
SN 2006ke	2.4	···	···	9.10 (0.05)	66.1 (0.4)	0
SN 2006kf	−9.0	···	···	13.31 (0.05)	129.1 (0.2)	0
SN 2006kf	−3.1	···	···	11.32 (0.05)	115.2 (0.1)	0
SN 2006le	−8.7	20.03 (0.05)	19.6 (0.2)	13.05 (0.05)	64.3 (0.2)	0.31 (0.01)
SN 2006lf	−6.3	···	···	11.72 (0.05)	95.6 (0.1)	0
SN 2006or	−2.8	···	···	11.34 (0.05)	112.8 (0.3)	0
SN 2006os	−0.9	···	···	12.20 (0.05)	131.5 (0.5)	0
SN 2006qo	−11.1	···	···	12.24 (0.10)	21.0 (0.8)	0
SN 2006sr	−2.3	···	···	12.47 (0.05)	111.2 (0.2)	0
SN 2006sr	2.7	···	···	11.73 (0.05)	116.0 (0.2)	0
SN 2007A	2.4	···	···	10.60 (0.05)	89.3 (0.1)	0
SN 2007F	−9.4	···	···	12.14 (0.05)	64.3 (0.3)	0
SN 2007F	3.2	···	···	10.60 (0.05)	86.7 (0.2)	0
SN 2007N	0.4	···	···	10.33 (0.05)	90.4 (0.2)	0
SN 2007O	−0.3	···	···	10.00 (0.05)	75.2 (0.2)	0
SN 2007S	−6.0	···	···	11.07 (0.05)	41.9 (0.4)	0
SN 2007af	−9.8	···	···	12.28 (0.05)	99.3 (0.2)	0
SN 2007af	−1.3	···	···	10.62 (0.05)	110.1 (0.1)	0

Continued on next page

Table A.3 — Continued

SN Name	Phase (d)[a]	HVF v (10^3 km s^{-1})	HVF pEW (Å)	PVF v (10^3 km s^{-1})	PVF pEW (Å)	$R^{b}_{\text{Si II6355 Å}}$
SN 2007af	0.2	···	···	10.56 (0.05)	108.4 (0.3)	0
SN 2007af	2.8	···	···	10.23 (0.05)	116.8 (0.1)	0
SN 2007af	3.8	···	···	10.08 (0.05)	111.2 (0.1)	0
SN 2007al	3.4	···	···	8.73 (0.05)	73.4 (0.5)	0
SN 2007ba	2.1	···	···	9.63 (0.05)	111.0 (0.7)	0
SN 2007bc	0.6	···	···	9.85 (0.05)	101.2 (0.2)	0
SN 2007bd	−5.8	···	···	13.36 (0.05)	108.7 (0.9)	0
SN 2007bm	−7.8	···	···	11.22 (0.05)	87.9 (0.2)	0
SN 2007bz	1.7	···	···	11.70 (0.05)	69.9 (0.4)	0
SN 2007ca	−11.1	···	···	12.44 (0.05)	54.9 (0.6)	0
SN 2007ci	−6.6	···	···	12.26 (0.05)	117.0 (0.5)	0
SN 2007ci	−1.7	···	···	11.83 (0.05)	122.7 (0.3)	0
SN 2007co	−4.1	···	···	12.50 (0.05)	124.1 (0.3)	0
SN 2007co	−0.6	···	···	11.73 (0.05)	114.4 (0.5)	0
SN 2007co	0.9	···	···	11.51 (0.05)	121.6 (0.2)	0
SN 2007cq	−5.8	···	···	10.48 (0.05)	40.2 (0.5)	0
SN 2007fb	2.0	···	···	10.80 (0.05)	117.3 (0.3)	0
SN 2007fr	−5.8	···	···	11.48 (0.05)	113.4 (0.8)	0
SN 2007fr	−1.3	···	···	10.74 (0.05)	118.2 (0.8)	0

Continued on next page

Table A.3 — Continued

SN Name	Phase (d)[a]	HVF v (10^3 km s^{-1})	HVF pEW (Å)	PVF v (10^3 km s^{-1})	PVF pEW (Å)	$R^{b}_{\mathrm{Si\ II6355\ Å}}$
SN 2007gi	−7.3	22.18 (0.05)	33.8 (0.3)	16.79 (0.05)	147.9 (1.4)	0.23 (0.01)
SN 2007gi	−0.4	20.05 (0.05)	32.9 (0.4)	14.87 (0.05)	151.6 (0.8)	0.22 (0.01)
SN 2007gk	−1.7	···	···	13.66 (0.05)	171.4 (0.2)	0
SN 2007hj	−1.2	···	···	11.71 (0.05)	149.3 (0.2)	0
SN 2007le	−10.3	21.47 (0.05)	33.6 (0.7)	15.00 (0.05)	138.8 (1.1)	0.24 (0.01)
SN 2007le	−9.4	21.38 (0.05)	21.3 (0.3)	14.52 (0.05)	113.1 (1.1)	0.19 (0.01)
SN 2007s1[c]	−1.2	···	···	11.37 (0.05)	125.1 (0.3)	0
SN 2007on	−3.0	···	···	11.46 (0.05)	117.2 (0.1)	0
SN 2007on	−3.0	···	···	11.52 (0.05)	119.8 (0.1)	0
SN 2007qe	−6.5	···	···	15.18 (0.05)	142.5 (0.3)	0
SN 2008Z	−2.3	···	···	11.46 (0.05)	55.8 (0.2)	0
SN 2008ar	−8.9	18.48 (0.11)	27.9 (1.6)	12.17 (0.09)	84.4 (0.2)	0.33 (0.02)
SN 2008ar	2.8	···	···	10.34 (0.05)	92.0 (0.8)	0
SN 2008bt	−1.1	···	···	9.75 (0.05)	97.6 (1.1)	0
SN 2008cl	4.2	···	···	10.95 (0.05)	108.9 (1.8)	0
SN 2008s1[d]	−6.4	···	···	11.03 (0.05)	69.1 (0.3)	0
SN 2008s1[d]	−4.4	···	···	10.86 (0.05)	71.9 (0.9)	0
SN 2008s1[d]	−3.4	···	···	10.76 (0.05)	82.1 (0.5)	0
SN 2008s1[d]	0.5	···	···	10.56 (0.05)	96.1 (0.5)	0

Continued on next page

Table A.3 — Continued

SN Name	Phase (d)[a]	HVF v (10^3 km s^{-1})	HVF pEW (Å)	PVF v (10^3 km s^{-1})	PVF pEW (Å)	$R^{b}_{\text{Si II6355 Å}}$
SN 2008s1[d]	4.4	···	···	10.39 (0.05)	96.0 (0.2)	0
SN 2008dx	2.5	···	···	8.85 (0.05)	90.8 (0.8)	0
SN 2008ec	−0.2	···	···	10.75 (0.05)	119.4 (0.2)	0
SN 2008ei	3.3	18.29 (0.05)	22.5 (0.9)	13.83 (0.05)	159.3 (0.2)	0.14 (0.01)
SN 2008s5[e]	1.3	···	···	9.13 (0.05)	53.6 (0.3)	0
SN 2008hs	−7.9	···	···	11.97 (0.05)	109.5 (0.4)	0
SN 2008hs	−6.3	···	···	11.55 (0.05)	112.4 (0.4)	0
SN 2008hv	−9.2	18.82 (0.08)	35.6 (1.2)	12.79 (0.07)	74.8 (0.7)	0.48 (0.02)
SN 2009ad	−3.4	···	···	10.79 (0.05)	61.0 (0.2)	0
SN 2009an	−5.8	···	···	13.98 (0.05)	149.2 (0.2)	0
SN 2009an	−3.8	···	···	13.01 (0.05)	140.2 (0.2)	0
SN 2009an	−2.9	···	···	12.68 (0.05)	137.2 (0.3)	0
SN 2009fx	−2.2	···	···	10.11 (0.05)	40.7 (0.7)	0
SN 2009ig	−14.4	25.10 (0.05)	59.1 (1.5)	19.06 (0.08)	97.5 (0.4)	0.61 (0.02)
SN 2009ig	−14.3	25.08 (0.05)	61.0 (1.0)	19.06 (0.06)	102.3 (1.1)	0.60 (0.01)
SN 2009ig	−14.2	25.21 (0.05)	43.3 (1.6)	19.66 (0.09)	122.6 (0.6)	0.35 (0.01)
SN 2009ig	−13.9	24.08 (0.05)	72.4 (0.9)	17.63 (0.05)	76.5 (1.2)	0.95 (0.02)
SN 2009ig	−13.3	24.33 (0.05)	45.6 (0.4)	18.13 (0.05)	110.1 (1.0)	0.41 (0.01)
SN 2009ig	−12.4	23.88 (0.05)	30.4 (0.5)	17.61 (0.05)	104.4 (0.5)	0.29 (0.01)

Continued on next page

Table A.3 — Continued

SN Name	Phase (d)[a]	HVF v (10^3 km s^{-1})	HVF pEW (Å)	PVF v (10^3 km s^{-1})	PVF pEW (Å)	$R^{b}_{\text{Si II6355 Å}}$
SN 2009ig	−12.3	24.02 (0.05)	28.9 (0.9)	17.57 (0.06)	108.6 (0.2)	0.27 (0.01)
SN 2009ig	−11.4	23.62 (0.05)	21.3 (0.2)	16.72 (0.05)	95.9 (0.2)	0.22 (0.01)
SN 2009ig	−11.3	23.55 (0.05)	19.4 (0.2)	16.60 (0.05)	96.9 (0.1)	0.20 (0.01)
SN 2009ig	−10.9	23.14 (0.05)	14.4 (0.3)	15.80 (0.05)	86.4 (0.7)	0.17 (0.01)
SN 2009ig	−10.3	23.13 (0.05)	13.3 (0.3)	15.76 (0.05)	77.0 (0.1)	0.17 (0.01)
SN 2009ig	−9.9	22.96 (0.05)	10.4 (0.3)	15.08 (0.05)	82.7 (0.7)	0.13 (0.01)
SN 2009ig	−9.4	22.90 (0.05)	9.8 (0.1)	14.96 (0.05)	80.8 (1.5)	0.12 (0.01)
SN 2009ig	−8.9	22.70 (0.05)	7.8 (0.3)	14.56 (0.05)	79.9 (0.4)	0.10 (0.01)
SN 2009ig	−8.4	22.40 (0.05)	4.4 (0.2)	14.89 (0.05)	87.3 (3.4)	0.05 (0.01)
SN 2009ig	−7.9	···	···	14.46 (0.05)	80.9 (0.2)	0
SN 2009ig	−6.9	···	···	14.30 (0.05)	77.6 (0.2)	0
SN 2009ig	−6.9	···	···	14.21 (0.05)	75.9 (0.2)	0
SN 2009ig	−6.0	···	···	13.87 (0.05)	78.6 (0.1)	0
SN 2009ig	−6.0	···	···	13.83 (0.05)	73.0 (0.1)	0
SN 2009ig	−4.0	···	···	13.56 (0.05)	77.7 (0.2)	0
SN 2009ig	−3.0	···	···	13.60 (0.05)	77.7 (0.2)	0
SN 2009ig	−2.0	···	···	13.65 (0.05)	80.7 (0.2)	0
SN 2009ig	−1.0	···	···	13.66 (0.05)	81.6 (0.2)	0
SN 2009ig	3.4	···	···	13.59 (0.05)	84.2 (0.2)	0

Continued on next page

Table A.3 — Continued

SN Name	Phase (d)[a]	HVF v (10^3 km s^{-1})	HVF pEW (Å)	PVF v (10^3 km s^{-1})	PVF pEW (Å)	$R^{b}_{\text{Si II6355 Å}}$
SN 2009ig	4.3	···	···	13.73 (0.05)	81.5 (0.3)	0
SN 2009no	2.1	···	···	10.03 (0.05)	63.5 (0.3)	0
SN 2009nq	−3.1	···	···	10.19 (0.05)	88.7 (0.1)	0
SN 2010Y	−7.2	···	···	11.03 (0.05)	90.1 (0.4)	0
SN 2010Y	−3.2	···	···	10.54 (0.05)	104.8 (0.2)	0
PTF 10bjs	−9.8	···	···	14.02 (0.06)	40.4 (1.1)	0
PTF 10bjs	−8.6	···	···	14.09 (0.06)	38.3 (1.0)	0
PTF 10bjs	−7.4	···	···	14.02 (0.05)	40.0 (0.5)	0
PTF 10bjs	−6.6	···	···	13.96 (0.05)	46.4 (0.6)	0
PTF 10bjs	−5.5	···	···	14.03 (0.05)	44.7 (0.8)	0
PTF 10bjs	−1.8	···	···	13.79 (0.05)	55.6 (0.3)	0
PTF 10bjs	0.2	···	···	13.79 (0.05)	60.3 (0.3)	0
SN 2010ai	−10.5	···	···	13.60 (0.05)	94.1 (0.8)	0
SN 2010ai	−8.6	···	···	12.44 (0.05)	89.6 (0.3)	0
SN 2010ai	−3.7	···	···	11.34 (0.05)	99.8 (0.2)	0
SN 2010ai	−0.8	···	···	11.08 (0.05)	104.0 (0.2)	0
PTF 10fps	0.0	···	···	9.93 (0.05)	105.8 (0.4)	0
PTF 10fps	0.9	···	···	9.90 (0.05)	103.6 (0.6)	0
PTF 10fps	3.9	···	···	9.56 (0.05)	105.9 (0.6)	0

Continued on next page

Table A.3 — Continued

SN Name	Phase (d)[a]	HVF v (10^3 km s^{-1})	HVF pEW (Å)	PVF v (10^3 km s^{-1})	PVF pEW (Å)	$\mathcal{R}^{b}_{\mathrm{Si\ II6355\ Å}}$
SN 2010dm	−6.5	17.73 (0.11)	3.6 (0.5)	11.78 (0.07)	35.9 (0.6)	0.10 (0.01)
PTF 10icb	−9.8	···	···	12.00 (0.05)	62.7 (0.3)	0
SN 2010ex	1.1	···	···	10.89 (0.05)	80.3 (0.3)	0
PTF 10qjl	−3.0	···	···	11.01 (0.05)	59.9 (0.5)	0
SN 2010ii	−6.1	···	···	14.16 (0.05)	108.5 (0.3)	0
SN 2010ii	−0.5	···	···	12.24 (0.05)	105.7 (0.2)	0
SN 2010it	−9.5	···	···	15.10 (0.05)	131.8 (0.4)	0
SN 2010it	−8.5	···	···	14.29 (0.05)	105.0 (0.3)	0
SN 2010it	−6.6	···	···	13.45 (0.05)	89.8 (0.4)	0
SN 2010it	−2.6	···	···	12.20 (0.05)	80.2 (0.3)	0
SN 2010it	−0.6	···	···	12.13 (0.05)	107.4 (0.4)	0
SN 2010it	3.3	···	···	11.55 (0.05)	100.7 (0.3)	0
PTF 10ygu	−3.7	20.73 (0.14)	43.8 (3.4)	14.43 (0.20)	87.7 (2.7)	0.50 (0.04)
SN 2010iw	−4.9	17.16 (0.07)	4.4 (0.2)	10.50 (0.05)	37.6 (0.2)	0.12 (0.01)
SN 2010iw	−3.0	···	···	10.39 (0.05)	44.3 (0.4)	0
SN 2010iw	−0.1	···	···	10.36 (0.05)	53.3 (0.3)	0
SN 2010iw	3.9	···	···	10.22 (0.05)	63.3 (0.2)	0
SN 2010kg	−9.9	21.98 (0.05)	56.6 (1.8)	16.68 (0.09)	96.2 (0.7)	0.59 (0.02)
SN 2010kg	−9.0	21.84 (0.05)	30.4 (1.6)	17.05 (0.09)	126.4 (3.1)	0.24 (0.01)

Continued on next page

Table A.3 — Continued

SN Name	Phase (d)[a]	HVF v (10^3 km s^{-1})	HVF pEW (Å)	PVF v (10^3 km s^{-1})	PVF pEW (Å)	$R^{b}_{\text{Si II6355 Å}}$
SN 2010kg	−8.0	20.95 (0.05)	48.4 (1.2)	15.70 (0.06)	103.8 (2.0)	0.47 (0.01)
SN 2010kg	−6.0	20.52 (0.05)	33.1 (0.9)	15.32 (0.05)	120.3 (4.1)	0.28 (0.01)
SN 2010kg	−5.0	19.81 (0.05)	43.4 (1.0)	14.30 (0.05)	107.1 (21.3)	0.40 (0.01)
SN 2010kg	−4.1	19.77 (0.05)	36.8 (0.6)	14.22 (0.05)	114.2 (17.6)	0.32 (0.01)
SN 2010kg	−3.1	19.64 (0.05)	32.7 (0.7)	14.09 (0.05)	118.2 (24.5)	0.28 (0.01)
SN 2010kg	−1.1	19.17 (0.05)	28.2 (0.4)	13.58 (0.05)	122.2 (0.9)	0.23 (0.01)
SN 2010kg	−0.1	19.17 (0.05)	28.6 (0.4)	13.51 (0.05)	122.8 (3.1)	0.23 (0.01)
SN 2010kg	0.9	18.72 (0.05)	28.1 (0.8)	13.08 (0.05)	128.2 (5.4)	0.22 (0.01)
SN 2010kg	2.8	18.45 (0.05)	30.7 (0.4)	12.71 (0.05)	124.8 (91.4)	0.25 (0.01)
SN 2010kg	4.8	18.16 (0.05)	32.4 (0.5)	12.49 (0.05)	123.1 (1.5)	0.26 (0.01)
SN 2011ao	−7.5	17.52 (0.11)	38.8 (1.4)	11.71 (0.14)	41.4 (4.2)	0.94 (0.05)
SN 2011ao	−6.7	17.35 (0.09)	32.9 (0.9)	11.37 (0.09)	40.2 (9.5)	0.82 (0.03)
SN 2011ao	−5.8	17.40 (0.07)	27.2 (0.6)	11.21 (0.06)	42.4 (1.2)	0.64 (0.02)
SN 2011ao	−4.8	17.19 (0.06)	22.1 (0.5)	10.88 (0.05)	45.0 (1.0)	0.49 (0.01)
SN 2011ao	−1.8	16.99 (0.05)	9.0 (0.2)	10.41 (0.05)	57.1 (1.0)	0.16 (0.01)
SN 2011ao	−0.8	16.68 (0.05)	6.2 (0.2)	10.28 (0.05)	60.2 (21.3)	0.10 (0.01)
SN 2011ao	0.2	17.35 (0.11)	4.4 (0.3)	10.34 (0.05)	66.4 (0.6)	0.07 (0.01)
SN 2011ao	1.2	···	···	10.36 (0.05)	70.2 (0.3)	0
SN 2011ao	2.2	···	···	10.16 (0.05)	72.2 (0.2)	0

Continued on next page

Table A.3 — Continued

SN Name	Phase (d)[a]	HVF v (10^3 km s^{-1})	HVF pEW (Å)	PVF v (10^3 km s^{-1})	PVF pEW (Å)	$R^{b}_{\text{Si II6355 Å}}$
SN 2011ao	3.2	···	···	10.02 (0.05)	73.9 (0.4)	0
SN 2011by	−11.7	···	···	11.95 (0.05)	75.3 (0.1)	0
SN 2011by	−9.8	···	···	11.42 (0.05)	68.0 (0.1)	0
SN 2011by	−5.7	···	···	10.81 (0.05)	70.6 (0.1)	0
SN 2011by	−3.8	···	···	10.55 (0.05)	78.2 (0.1)	0
SN 2011by	0.2	···	···	10.27 (0.05)	88.6 (0.1)	0
SN 2011by	0.3	···	···	10.29 (0.05)	90.3 (0.2)	0
SN 2011by	2.3	···	···	10.20 (0.05)	92.7 (0.2)	0
SN 2011by	4.2	···	···	10.02 (0.05)	93.6 (0.1)	0
SN 2011dm	−5.5	···	···	13.62 (0.05)	104.7 (0.1)	0
SN 2011ek	−6.0	···	···	13.75 (0.05)	145.2 (0.1)	0
SN 2011ek	−5.0	···	···	13.36 (0.05)	148.2 (0.1)	0
SN 2011ek	3.0	···	···	11.75 (0.05)	150.7 (0.1)	0
SN 2011fe	−16.0	20.16 (0.05)	22.7 (0.9)	15.53 (0.06)	69.1 (6.0)	0.33 (0.01)
SN 2011fe	−15.0	···	···	14.73 (0.05)	101.0 (0.4)	0
SN 2011fe	−15.0	···	···	15.20 (0.05)	103.8 (0.3)	0
SN 2011fe	−13.0	···	···	13.14 (0.05)	98.3 (0.2)	0
SN 2011fe	−12.0	···	···	13.01 (0.05)	107.5 (0.1)	0
SN 2011fe	−11.0	···	···	12.09 (0.05)	98.7 (0.2)	0

Continued on next page

Table A.3 — Continued

SN Name	Phase (d)[a]	HVF v (10^3 km s^{-1})	HVF pEW (Å)	PVF v (10^3 km s^{-1})	PVF pEW (Å)	$R^{b}_{\text{Si II6355 Å}}$
SN 2011fe	−10.0	···	···	11.77 (0.05)	96.9 (0.1)	0
SN 2011fe	−10.0	···	···	11.68 (0.05)	87.9 (0.2)	0
SN 2011fe	−9.0	···	···	11.23 (0.05)	85.7 (0.3)	0
SN 2011fe	−9.0	···	···	11.34 (0.05)	95.1 (0.1)	0
SN 2011fe	−7.0	···	···	11.21 (0.05)	85.0 (0.1)	0
SN 2011fe	−2.0	···	···	10.53 (0.05)	97.0 (0.1)	0
SN 2011fe	−1.0	···	···	10.58 (0.05)	98.7 (0.1)	0
SN 2011fe	2.0	···	···	10.44 (0.05)	103.2 (0.1)	0
SN 2011fe	3.0	···	···	10.26 (0.05)	103.1 (0.1)	0
SN 2011gy	−1.1	···	···	11.41 (0.05)	105.5 (0.1)	0
SN 2011hb	−5.8	17.77 (0.13)	23.8 (1.4)	11.90 (0.10)	61.7 (1.2)	0.39 (0.02)
SN 2011hb	−2.9	···	···	11.80 (0.05)	78.8 (0.4)	0
SN 2011hb	3.0	···	···	10.74 (0.05)	86.4 (0.4)	0
SN 2011ia	−3.0	···	···	10.68 (0.05)	63.2 (0.2)	0
SN 2012I	−1.0	···	···	10.95 (0.05)	102.1 (0.2)	0
SN 2012bh	0.0	···	···	10.36 (0.05)	85.5 (0.2)	0
SN 2012cg	−14.7	22.27 (0.14)	47.8 (1.9)	17.22 (0.19)	3.3 (5.1)	14.54 (4.88)
SN 2012cg	−13.8	22.07 (0.05)	15.9 (0.9)	17.05 (0.09)	61.5 (3.7)	0.26 (0.02)
SN 2012cg	−12.8	19.02 (0.13)	47.2 (1.8)	13.48 (0.13)	46.7 (4.8)	1.01 (0.06)

Continued on next page

Table A.3 — Continued

SN Name	Phase (d)[a]	HVF v (10^3 km s^{-1})	HVF pEW (Å)	PVF v (10^3 km s^{-1})	PVF pEW (Å)	$\mathcal{R}^{b}_{\mathrm{Si\ II6355\ Å}}$
SN 2012cg	−11.8	18.92 (0.06)	32.2 (0.8)	13.21 (0.06)	59.5 (0.8)	0.54 (0.02)
SN 2012cg	−10.5	17.85 (0.17)	31.0 (1.6)	12.27 (0.11)	43.7 (8.7)	0.71 (0.04)
SN 2012cg	−9.6	18.07 (0.17)	15.3 (1.1)	12.21 (0.10)	45.2 (21.4)	0.34 (0.03)
SN 2012cg	−7.8	···	···	11.88 (0.05)	24.7 (0.2)	0
SN 2012cg	−6.8	···	···	11.34 (0.05)	50.4 (0.2)	0
SN 2012cg	−4.8	···	···	10.94 (0.05)	53.8 (0.1)	0
SN 2012cg	−3.8	···	···	10.89 (0.05)	51.9 (0.1)	0
SN 2012cg	−3.8	···	···	11.04 (0.05)	55.7 (0.2)	0
SN 2012cg	−0.5	···	···	10.58 (0.05)	63.2 (0.2)	0
SN 2012da	−1.0	···	···	11.11 (0.05)	79.5 (0.2)	0
SN 2012fr	−14.4	23.61 (0.05)	159.8 (1.0)	···	···	···
SN 2012fr	−14.1	23.67 (0.05)	192.8 (0.1)	···	···	···
SN 2012fr	−12.6	22.43 (0.05)	124.6 (0.4)	14.00 (0.05)	26.0 (40.1)	4.79 (0.06)
SN 2012fr	−12.4	22.26 (0.05)	119.1 (0.4)	13.80 (0.05)	24.6 (0.1)	4.85 (0.07)
SN 2012fr	−11.4	21.91 (0.05)	94.3 (0.3)	13.22 (0.05)	26.7 (2.2)	3.53 (0.03)
SN 2012fr	−9.3	21.25 (0.05)	38.2 (0.3)	13.12 (0.05)	44.6 (0.2)	0.86 (0.01)
SN 2012fr	−8.4	21.13 (0.05)	32.0 (0.3)	12.92 (0.05)	45.3 (0.2)	0.71 (0.01)
SN 2012fr	−8.2	20.93 (0.05)	29.9 (0.2)	12.87 (0.05)	45.4 (0.3)	0.66 (0.01)
SN 2012fr	−7.6	20.58 (0.05)	24.1 (0.1)	12.46 (0.05)	47.9 (0.8)	0.50 (0.01)

Continued on next page

Table A.3 — Continued

SN Name	Phase (d)[a]	HVF v (10^3 km s^{-1})	HVF pEW (Å)	PVF v (10^3 km s^{-1})	PVF pEW (Å)	$\mathcal{R}^{b}_{\mathrm{Si\ II6355\ Å}}$
SN 2012fr	−7.5	20.60 (0.05)	25.2 (0.2)	12.75 (0.05)	46.8 (0.6)	0.54 (0.01)
SN 2012fr	−6.7	20.38 (0.06)	17.2 (0.4)	12.64 (0.05)	52.8 (8.7)	0.33 (0.01)
SN 2012fr	−6.6	20.11 (0.05)	15.1 (0.1)	12.28 (0.05)	53.8 (4.5)	0.28 (0.01)
SN 2012fr	−6.4	20.50 (0.05)	17.9 (0.4)	12.70 (0.05)	53.2 (0.1)	0.34 (0.01)
SN 2012fr	−5.6	20.63 (0.05)	16.1 (0.2)	12.58 (0.05)	55.9 (11.7)	0.29 (0.01)
SN 2012fr	−4.7	19.69 (0.07)	9.8 (0.3)	12.49 (0.05)	56.9 (4.1)	0.17 (0.01)
SN 2012fr	−4.6	19.85 (0.05)	8.5 (0.1)	12.33 (0.05)	57.7 (3.2)	0.15 (0.01)
SN 2012fr	−3.7	19.00 (0.11)	7.7 (0.4)	12.40 (0.05)	57.9 (1.9)	0.13 (0.01)
SN 2012fr	−3.6	18.76 (0.05)	4.7 (0.1)	12.06 (0.05)	56.7 (1.0)	0.08 (0.01)
SN 2012fr	−2.5	···	···	12.41 (0.05)	64.0 (0.2)	0
SN 2012fr	−2.4	···	···	12.53 (0.05)	61.4 (0.2)	0
SN 2012fr	−1.4	···	···	12.48 (0.05)	59.7 (0.1)	0
SN 2012fr	−1.3	···	···	12.42 (0.05)	59.2 (0.1)	0
SN 2012fr	−0.3	···	···	12.42 (0.05)	60.8 (0.1)	0
SN 2012fr	0.4	···	···	12.15 (0.05)	63.4 (0.1)	0
SN 2012fr	0.7	···	···	12.51 (0.05)	62.3 (0.1)	0
SN 2012fr	1.3	···	···	12.48 (0.05)	63.6 (0.3)	0
SN 2012fr	1.7	···	···	12.36 (0.05)	61.1 (0.1)	0
SN 2012fr	2.3	···	···	12.29 (0.05)	61.1 (0.1)	0

Continued on next page

Table A.3 — Continued

SN Name	Phase (d)[a]	HVF v (10^3 km s^{-1})	HVF pEW (Å)	PVF v (10^3 km s^{-1})	PVF pEW (Å)	$R^{b}_{\mathrm{Si\ II6355\ Å}}$
SN 2012fr	3.2	···	···	12.52 (0.05)	64.9 (0.3)	0
SN 2012fr	4.5	···	···	12.48 (0.05)	62.1 (0.1)	0
SN 2013cs	−8.9	···	···	14.03 (0.05)	142.9 (0.2)	0
SN 2013cs	−3.0	···	···	12.81 (0.05)	146.3 (0.1)	0
SN 2013di	−1.6	···	···	11.46 (0.05)	85.6 (0.3)	0

[a]Phases are in rest-frame days.

[b]R_{Si} is the ratio of the pEW of the HVF to the pEW of the PVF, as defined by Childress et al. (2014).

[c]Also known as SNF20071021-000.

[d]Also known as SNF20080514-002.

[e]Also known as SNF20080909-030.

Table A.4: CaNIR Fit Results

SN Name	Phase (d)[a]	HVF v (10^3 km s^{-1})	HVF pEW (Å)	PVF v (10^3 km s^{-1})	PVF pEW (Å)	R^{b}_{CaNIR}
SN 1989M	2.5	···	···	13.33 (0.05)	197.1 (0.2)	0
SN 1989M	3.5	···	···	13.00 (0.05)	209.9 (0.2)	0
SN 1991bg	1.1	···	···	11.84 (0.05)	268.8 (1.2)	0
SN 1994D	−7.7	20.85 (0.05)	41.7 (0.2)	10.01 (0.05)	37.7 (0.8)	1.11 (0.02)
SN 1994D	−3.9	20.37 (0.05)	21.5 (0.2)	10.22 (0.05)	48.4 (1.9)	0.44 (0.02)
SN 1994D	−3.3	20.77 (0.05)	21.3 (0.2)	10.51 (0.05)	64.1 (2.2)	0.33 (0.01)
SN 1994S	1.1	18.12 (0.06)	31.3 (1.2)	10.14 (0.06)	109.1 (6.9)	0.29 (0.02)
SN 1995D	3.8	17.73 (0.05)	55.0 (0.3)	10.06 (0.05)	104.8 (2.0)	0.52 (0.01)
SN 1995E	−2.5	19.22 (0.05)	56.2 (0.3)	10.48 (0.05)	91.0 (1.3)	0.62 (0.01)
SN 1997Y	1.3	16.50 (0.13)	28.1 (2.0)	10.10 (0.10)	94.3 (10.5)	0.30 (0.04)
SN 1997do	−5.7	23.78 (0.05)	164.5 (0.3)	12.69 (0.05)	36.0 (0.6)	4.57 (0.07)
SN 1998dk	−7.2	25.15 (0.05)	155.6 (1.1)	14.12 (0.21)	94.2 (10.5)	1.65 (0.18)
SN 1998dk	−0.5	18.21 (0.05)	30.8 (0.5)	12.08 (0.05)	103.5 (2.8)	0.30 (0.01)
SN 1998dm	−12.5	21.63 (0.05)	97.8 (0.2)	11.46 (0.05)	51.7 (0.9)	1.89 (0.03)
SN 1998dm	−5.6	20.18 (0.05)	32.1 (0.2)	10.97 (0.05)	47.3 (0.7)	0.68 (0.01)
SN 1998ef	−8.6	21.51 (0.08)	147.2 (2.1)	12.62 (0.10)	79.9 (6.9)	1.84 (0.16)
SN 1998es	0.3	19.80 (0.05)	40.1 (0.2)	9.93 (0.05)	40.6 (0.9)	0.99 (0.02)
SN 1999aa	0.2	18.91 (0.05)	37.8 (0.4)	10.22 (0.05)	31.2 (1.7)	1.21 (0.07)
SN 1999ac	−0.9	17.71 (0.05)	106.2 (0.3)	9.62 (0.05)	58.6 (1.5)	1.81 (0.05)

Continued on next page

Table A.4 — Continued

SN Name	Phase (d)[a]	HVF v (10^3 km s^{-1})	HVF pEW (Å)	PVF v (10^3 km s^{-1})	PVF pEW (Å)	R^{b}_{CaNIR}
SN 1999cp	4.9	···	···	10.61 (0.05)	184.7 (0.2)	0
SN 1999da	−2.1	···	···	14.48 (0.05)	377.7 (0.4)	0
SN 1999dk	−6.6	22.06 (0.05)	109.3 (0.3)	13.05 (0.05)	113.9 (2.0)	0.96 (0.02)
SN 1999dq	−3.9	23.01 (0.05)	15.6 (0.6)	11.71 (0.16)	25.1 (2.5)	0.62 (0.07)
SN 1999dq	3.0	19.76 (0.05)	57.7 (0.2)	10.61 (0.05)	49.4 (1.0)	1.17 (0.02)
SN 1999gd	−1.1	···	···	11.42 (0.05)	165.0 (1.0)	0
SN 1999gh	4.1	···	···	10.76 (0.05)	303.3 (0.6)	0
SN 2000cp	2.9	···	···	11.56 (0.05)	281.5 (2.0)	0
SN 2000cw	4.8	···	···	11.72 (0.05)	302.4 (1.4)	0
SN 2000dg	−5.1	21.68 (0.07)	24.7 (0.3)	10.47 (0.08)	69.7 (4.9)	0.35 (0.03)
SN 2000dg	4.7	···	···	10.65 (0.05)	106.3 (1.1)	0
SN 2000dk	1.0	···	···	11.90 (0.05)	249.3 (0.5)	0
SN 2000dm	−1.6	17.35 (0.05)	36.9 (0.7)	10.27 (0.05)	102.2 (3.3)	0.36 (0.01)
SN 2000dn	−5.6	18.21 (0.32)	49.7 (6.2)	9.53 (0.44)	90.6 (31.0)	0.55 (0.20)
SN 2000dn	−0.9	16.28 (0.07)	81.1 (2.5)	9.49 (0.08)	138.4 (8.5)	0.59 (0.04)
SN 2000dx	−9.3	23.35 (0.05)	367.1 (5.4)	···	···	···
SN 2000fa	−8.3	23.85 (0.05)	158.5 (0.7)	12.62 (0.07)	35.4 (2.4)	4.47 (0.30)
SN 2001az	−3.2	20.98 (0.08)	32.2 (1.2)	9.76 (0.13)	82.9 (8.7)	0.39 (0.04)
SN 2001bf	1.2	14.97 (0.05)	36.4 (0.4)	7.57 (0.05)	40.8 (1.7)	0.89 (0.04)

Continued on next page

Table A.4 — Continued

SN Name	Phase (d)[a]	HVF v (10^3 km s^{-1})	HVF pEW (Å)	PVF v (10^3 km s^{-1})	PVF pEW (Å)	R^{b}_{CaNIR}
SN 2001br	3.5	···	···	12.88 (0.05)	239.6 (4.0)	0
SN 2001cp	1.4	18.20 (0.06)	43.0 (0.9)	10.62 (0.06)	84.5 (5.2)	0.51 (0.03)
SN 2001da	−1.1	19.90 (0.05)	113.5 (1.0)	10.89 (0.11)	138.2 (7.3)	0.82 (0.04)
SN 2001eh	−4.5	20.70 (0.05)	31.8 (1.0)	8.57 (0.12)	18.8 (3.0)	1.69 (0.28)
SN 2001eh	3.3	17.81 (0.05)	69.9 (0.7)	10.13 (0.05)	48.1 (1.9)	1.45 (0.06)
SN 2001ep	2.8	···	···	11.51 (0.05)	249.6 (0.3)	0
SN 2001ex	−1.8	···	···	11.21 (0.05)	335.0 (2.4)	0
SN 2001fe	−1.0	17.02 (0.08)	10.9 (0.6)	10.96 (0.06)	46.7 (4.1)	0.23 (0.02)
SN 2002aw	2.1	···	···	8.77 (0.09)	122.8 (3.0)	0
SN 2002bf	3.0	17.36 (0.05)	152.2 (0.5)	10.67 (0.05)	96.7 (2.1)	1.57 (0.03)
SN 2002bo	−11.9	24.88 (0.09)	246.7 (4.2)	16.01 (0.10)	123.9 (19.2)	1.99 (0.31)
SN 2002bo	−1.1	16.52 (0.05)	130.2 (1.5)	10.13 (0.09)	109.6 (4.9)	1.19 (0.05)
SN 2002cd	1.1	15.28 (0.05)	158.2 (0.3)	···	···	···
SN 2002cf	−0.8	···	···	12.18 (0.05)	275.9 (0.6)	0
SN 2002ck	3.6	17.01 (0.06)	50.6 (1.1)	10.26 (0.05)	96.5 (8.6)	0.52 (0.05)
SN 2002cr	−6.8	17.97 (0.05)	58.5 (0.8)	9.59 (0.07)	92.3 (3.5)	0.63 (0.03)
SN 2002cr	−5.8	16.67 (0.23)	44.8 (5.1)	8.62 (0.55)	76.5 (26.8)	0.59 (0.22)
SN 2002cr	−3.9	15.85 (0.36)	46.4 (6.3)	8.81 (0.38)	71.4 (24.0)	0.65 (0.24)
SN 2002cs	−7.8	21.12 (0.05)	31.8 (0.5)	14.08 (0.05)	79.8 (2.9)	0.40 (0.02)

Continued on next page

Table A.4 — Continued

SN Name	Phase (d)[a]	HVF v (10^3 km s^{-1})	HVF pEW (Å)	PVF v (10^3 km s^{-1})	PVF pEW (Å)	$R^{b}_{\rm CaNIR}$
SN 2002dj	−8.0	24.19 (0.05)	149.3 (0.9)	14.57 (0.09)	127.4 (6.3)	1.17 (0.06)
SN 2002dk	−1.2	19.50 (0.05)	101.4 (3.8)	12.61 (0.43)	264.4 (24.5)	0.38 (0.04)
SN 2002eb	1.7	19.58 (0.05)	56.1 (0.5)	9.49 (0.05)	55.5 (1.5)	1.01 (0.03)
SN 2002ef	4.7	···	···	11.94 (0.05)	192.8 (1.7)	0
SN 2002er	−4.6	20.07 (0.05)	105.7 (0.2)	11.32 (0.05)	118.8 (0.9)	0.89 (0.01)
SN 2002eu	−0.1	···	···	11.63 (0.05)	214.8 (1.2)	0
SN 2002fb	1.0	···	···	11.65 (0.05)	270.2 (0.7)	0
SN 2002ha	−0.9	17.17 (0.05)	49.4 (0.8)	10.28 (0.05)	94.6 (2.7)	0.52 (0.02)
SN 2002ha	4.9	···	···	10.99 (0.05)	236.7 (0.6)	0
SN 2002he	−5.9	20.77 (0.07)	30.7 (1.2)	12.43 (0.14)	105.5 (8.7)	0.29 (0.03)
SN 2002he	−1.0	18.40 (0.07)	28.0 (1.5)	11.77 (0.11)	126.0 (9.3)	0.22 (0.02)
SN 2002he	0.3	···	···	12.40 (0.05)	194.0 (0.6)	0
SN 2002he	3.2	···	···	12.02 (0.05)	226.6 (0.6)	0
SN 2002hu	−5.8	20.13 (0.05)	80.2 (0.7)	9.32 (0.06)	41.1 (2.2)	1.95 (0.11)
SN 2002hw	−6.3	···	···	12.64 (0.05)	175.6 (0.6)	0
SN 2003U	−2.6	···	···	12.39 (0.05)	192.2 (1.3)	0
SN 2003W	−7.0	21.87 (0.07)	202.8 (4.1)	···	···	···
SN 2003W	−6.0	20.57 (0.06)	178.6 (3.7)	···	···	···
SN 2003W	−5.1	20.15 (0.05)	257.0 (1.4)	···	···	···

Continued on next page

Table A.4 — Continued

SN Name	Phase (d)[a]	HVF v (10^3 km s^{-1})	HVF pEW (Å)	PVF v (10^3 km s^{-1})	PVF pEW (Å)	R^{b}_{CaNIR}
SN 2003Y	−1.7	···	···	12.87 (0.05)	291.7 (1.0)	0
SN 2003cq	−0.2	18.53 (0.13)	51.9 (3.6)	10.71 (0.31)	124.2 (21.7)	0.42 (0.08)
SN 2003gn	−5.4	21.66 (0.05)	181.0 (3.1)	11.55 (0.19)	76.2 (11.6)	2.38 (0.36)
SN 2003gn	3.3	···	···	10.48 (0.16)	338.1 (16.0)	0
SN 2003gt	−5.1	22.23 (0.05)	26.4 (0.5)	11.02 (0.05)	57.0 (2.6)	0.46 (0.02)
SN 2003he	2.7	17.58 (0.06)	49.1 (1.9)	10.15 (0.14)	158.7 (13.0)	0.31 (0.03)
SN 2003hs	−5.5	16.12 (0.06)	307.6 (4.1)	···	···	···
SN 2003iv	1.8	···	···	10.47 (0.05)	213.4 (0.8)	0
SN 2003kf	−7.5	22.94 (0.05)	89.9 (0.1)	11.39 (0.05)	41.8 (0.6)	2.15 (0.03)
SN 2004as	−4.4	20.43 (0.05)	111.9 (2.1)	12.59 (0.17)	128.5 (11.6)	0.87 (0.08)
SN 2004bl	4.6	···	···	11.80 (0.05)	166.6 (1.7)	0
SN 2004bw	−7.1	21.35 (0.22)	115.0 (7.6)	11.79 (0.49)	65.4 (21.8)	1.76 (0.60)
SN 2004dt	−6.5	20.54 (0.05)	44.1 (0.6)	11.69 (0.08)	53.8 (3.7)	0.82 (0.06)
SN 2004dt	1.4	···	···	10.96 (0.05)	130.3 (1.1)	0
SN 2004ef	−5.5	22.24 (0.05)	101.7 (1.6)	11.95 (0.49)	99.2 (19.2)	1.03 (0.20)
SN 2004eo	−5.6	18.20 (0.05)	102.2 (0.7)	9.68 (0.05)	76.2 (1.9)	1.34 (0.03)
SN 2004ey	−7.6	21.93 (0.05)	90.1 (0.2)	10.91 (0.05)	46.3 (0.7)	1.95 (0.03)
SN 2004fu	−2.7	19.54 (0.05)	89.6 (0.5)	12.00 (0.05)	115.0 (2.3)	0.78 (0.02)
SN 2004fu	2.4	···	···	12.50 (0.05)	230.3 (0.2)	0

Continued on next page

Table A.4 — Continued

SN Name	Phase (d)[a]	HVF v (10^3 km s^{-1})	HVF pEW (Å)	PVF v (10^3 km s^{-1})	PVF pEW (Å)	R^{b}_{CaNIR}
SN 2004fz	−5.2	18.59 (0.05)	36.7 (0.5)	10.39 (0.05)	75.6 (2.1)	0.49 (0.01)
SN 2004gs	0.4	···	···	11.43 (0.05)	249.1 (1.0)	0
SN 2005W	0.6	···	···	11.70 (0.05)	212.6 (0.7)	0
SN 2005am	4.5	···	···	11.41 (0.05)	223.2 (0.2)	0
SN 2005ao	−1.3	16.62 (0.16)	22.8 (2.9)	11.48 (0.13)	72.7 (12.5)	0.31 (0.07)
SN 2005ao	0.5	19.61 (0.10)	32.1 (1.9)	11.36 (0.14)	118.7 (14.4)	0.27 (0.04)
SN 2005bc	1.6	···	···	11.79 (0.05)	205.1 (0.4)	0
SN 2005cf	−10.9	25.12 (0.05)	216.5 (4.1)	16.01 (0.09)	189.9 (13.3)	1.14 (0.08)
SN 2005cf	−2.1	20.66 (0.05)	141.9 (0.3)	9.80 (0.05)	67.3 (1.6)	2.11 (0.05)
SN 2005cf	−1.2	20.13 (0.05)	125.3 (0.4)	9.92 (0.05)	62.6 (1.2)	2.00 (0.04)
SN 2005cg	−10.1	24.56 (0.18)	108.3 (17.9)	11.66 (5.94)	78.2 (0.1)	1.38 (1.94)
SN 2005cg	−9.1	23.46 (0.05)	109.8 (1.2)	10.63 (0.32)	32.5 (6.2)	3.38 (0.64)
SN 2005cg	−4.3	21.91 (0.05)	78.9 (0.9)	10.79 (0.21)	35.8 (5.1)	2.21 (0.32)
SN 2005cg	−0.4	20.45 (0.05)	65.3 (0.9)	11.03 (0.09)	49.6 (3.9)	1.32 (0.10)
SN 2005cg	4.5	19.20 (0.06)	59.5 (1.4)	11.02 (0.10)	95.6 (7.3)	0.62 (0.05)
SN 2005de	−0.8	17.97 (0.05)	65.9 (1.6)	10.16 (0.08)	113.7 (5.9)	0.58 (0.03)
SN 2005dv	−0.6	···	···	13.34 (0.05)	258.8 (1.3)	0
SN 2005el	−6.7	20.77 (0.05)	45.3 (0.3)	11.23 (0.06)	52.2 (2.0)	0.87 (0.03)
SN 2005el	1.2	17.77 (0.05)	36.5 (0.7)	10.11 (0.05)	93.2 (4.2)	0.39 (0.02)

Continued on next page

Table A.4 — Continued

SN Name	Phase (d)[a]	HVF v (10^3 km s^{-1})	HVF pEW (Å)	PVF v (10^3 km s^{-1})	PVF pEW (Å)	R^{b}_{CaNIR}
SN 2005er	−0.3	···	···	13.42 (0.05)	396.9 (0.3)	0
SN 2005er	1.7	···	···	12.83 (0.05)	358.2 (0.4)	0
SN 2005eq	−3.0	20.58 (0.05)	37.5 (0.2)	9.31 (0.05)	13.3 (0.7)	2.82 (0.16)
SN 2005eq	0.7	19.24 (0.05)	46.5 (0.5)	9.53 (0.07)	34.2 (2.3)	1.36 (0.09)
SN 2005eu	−10.1	23.59 (0.05)	18.4 (0.2)	···	···	···
SN 2005hj	3.3	16.63 (0.31)	26.5 (3.0)	9.86 (0.39)	48.1 (18.5)	0.55 (0.22)
SN 2005iq	−5.9	19.54 (0.05)	63.5 (0.5)	10.78 (0.05)	80.6 (2.1)	0.79 (0.02)
SN 2005ki	1.6	18.36 (0.05)	23.0 (0.2)	10.65 (0.05)	72.5 (1.7)	0.32 (0.01)
SN 2005lz	0.6	···	···	10.42 (0.05)	159.5 (0.7)	0
SN 2005ms	−1.9	···	···	13.58 (0.05)	205.6 (3.1)	0
SN 2005na	0.0	19.20 (0.17)	16.2 (1.0)	10.04 (0.11)	45.6 (7.4)	0.36 (0.06)
SN 2005na	1.0	···	···	10.27 (0.11)	158.0 (4.1)	0
SN 2006D	3.7	···	···	12.20 (0.05)	207.9 (0.3)	0
SN 2006N	−1.9	···	···	11.89 (0.05)	85.4 (0.6)	0
SN 2006N	−0.9	···	···	11.74 (0.05)	153.0 (0.7)	0
SN 2006S	−3.9	20.05 (0.26)	96.6 (5.7)	9.37 (0.96)	49.2 (42.4)	1.96 (1.70)
SN 2006S	3.0	18.68 (0.05)	83.0 (1.1)	9.76 (0.08)	96.0 (6.7)	0.87 (0.06)
SN 2006X	−11.2	32.29 (0.05)	270.2 (1.6)	19.92 (0.07)	287.7 (9.9)	0.94 (0.03)
SN 2006X	−10.2	31.74 (0.05)	253.0 (2.5)	19.82 (0.11)	283.4 (14.4)	0.89 (0.05)

Continued on next page

Table A.4 — Continued

SN Name	Phase (d)[a]	HVF v (10^3 km s^{-1})	HVF pEW (Å)	PVF v (10^3 km s^{-1})	PVF pEW (Å)	R^{b}_{CaNIR}
SN 2006X	−9.2	29.84 (0.05)	242.2 (2.1)	18.57 (0.10)	252.8 (12.7)	0.96 (0.05)
SN 2006X	−8.2	28.29 (0.05)	232.5 (2.1)	17.54 (0.10)	225.5 (13.0)	1.03 (0.06)
SN 2006X	−7.2	26.34 (0.05)	255.1 (1.5)	15.99 (0.05)	170.6 (7.7)	1.50 (0.07)
SN 2006X	−6.2	20.86 (0.05)	210.9 (1.0)	14.57 (0.18)	16.9 (1.9)	12.52 (1.43)
SN 2006X	−5.2	20.84 (0.50)	191.1 (22.6)	13.72 (0.92)	31.6 (40.2)	6.04 (7.72)
SN 2006X	−0.2	19.02 (0.05)	150.4 (1.6)	12.28 (0.09)	131.9 (8.1)	1.14 (0.07)
SN 2006X	0.8	18.71 (0.05)	149.6 (1.2)	11.95 (0.06)	141.9 (6.0)	1.05 (0.05)
SN 2006X	1.8	18.65 (0.05)	147.6 (0.9)	11.60 (0.06)	166.6 (5.3)	0.89 (0.03)
SN 2006X	2.8	18.50 (0.05)	152.9 (1.3)	11.17 (0.08)	179.8 (8.0)	0.85 (0.04)
SN 2006X	3.2	18.51 (0.05)	131.2 (0.4)	11.13 (0.05)	175.2 (1.9)	0.75 (0.01)
SN 2006ax	−10.1	20.11 (0.05)	112.5 (0.9)	11.31 (0.08)	79.0 (4.0)	1.42 (0.07)
SN 2006bt	−5.3	19.42 (0.05)	62.7 (3.7)	12.44 (0.45)	150.3 (18.0)	0.42 (0.06)
SN 2006bt	−4.5	17.97 (0.05)	58.4 (3.2)	12.17 (0.66)	151.5 (18.6)	0.39 (0.05)
SN 2006bt	2.3	17.02 (0.05)	122.8 (4.1)	9.20 (0.19)	141.4 (14.8)	0.87 (0.10)
SN 2006bu	4.2	···	···	13.64 (0.06)	206.5 (4.2)	0
SN 2006bz	−2.4	···	···	13.23 (0.05)	352.6 (2.2)	0
SN 2006cm	−1.2	···	···	11.08 (0.05)	41.1 (0.6)	0
SN 2006cp	−5.3	21.07 (0.05)	123.4 (2.4)	12.47 (0.25)	151.0 (15.7)	0.82 (0.09)
SN 2006cq	2.0	19.33 (0.11)	77.6 (7.2)	11.36 (2.39)	168.8 (115.7)	0.46 (0.32)

Continued on next page

Table A.4 — Continued

SN Name	Phase (d)[a]	HVF v (10^3 km s^{-1})	HVF pEW (Å)	PVF v (10^3 km s^{-1})	PVF pEW (Å)	R^{b}_{CaNIR}
SN 2006cs	2.3	···	···	12.06 (0.05)	232.2 (2.2)	0
SN 2006cz	1.1	18.38 (0.71)	52.5 (19.4)	10.46 (1.59)	54.3 (73.3)	0.97 (1.35)
SN 2006dm	−7.9	22.01 (0.14)	58.6 (5.7)	12.86 (1.28)	185.2 (64.9)	0.32 (0.12)
SN 2006ef	3.2	···	···	11.24 (0.05)	180.8 (0.4)	0
SN 2006gr	−8.7	23.53 (0.05)	150.1 (1.1)	···	···	···
SN 2006ej	−3.7	18.96 (0.05)	28.4 (0.7)	11.84 (0.09)	110.6 (5.0)	0.26 (0.01)
SN 2006em	4.2	···	···	12.48 (0.05)	291.4 (0.6)	0
SN 2006et	3.3	17.46 (0.05)	90.6 (0.6)	9.22 (0.05)	44.2 (2.7)	2.05 (0.13)
SN 2006gj	4.7	···	···	10.78 (0.05)	265.5 (1.1)	0
SN 2006gt	3.1	···	···	10.97 (0.05)	270.1 (2.4)	0
SN 2006ke	2.4	···	···	12.16 (0.05)	175.4 (1.0)	0
SN 2006kf	−9.0	19.49 (0.13)	79.7 (2.9)	11.58 (0.27)	67.7 (14.3)	1.18 (0.25)
SN 2006kf	−3.1	···	···	11.78 (0.05)	145.1 (0.5)	0
SN 2006le	−8.7	25.46 (0.05)	140.2 (0.6)	14.52 (0.09)	37.0 (2.4)	3.79 (0.24)
SN 2006lf	−6.3	18.47 (0.05)	59.1 (0.2)	10.77 (0.05)	67.5 (0.5)	0.87 (0.01)
SN 2006or	−2.8	···	···	12.03 (0.05)	207.0 (0.7)	0
SN 2006os	−0.9	18.49 (0.10)	70.2 (3.6)	10.80 (0.25)	115.8 (16.5)	0.61 (0.09)
SN 2006sr	−2.3	···	···	12.59 (0.05)	116.5 (0.6)	0
SN 2006sr	2.7	···	···	11.83 (0.05)	165.2 (0.6)	0

Continued on next page

Table A.4 — Continued

SN Name	Phase (d)[a]	HVF v (10^3 km s^{-1})	HVF pEW (Å)	PVF v (10^3 km s^{-1})	PVF pEW (Å)	R^{b}_{CaNIR}
SN 2007A	2.4	17.02 (0.05)	32.9 (0.5)	8.94 (0.05)	78.1 (2.8)	0.42 (0.02)
SN 2007F	−9.4	24.20 (0.05)	110.2 (0.4)	11.14 (0.05)	43.9 (1.4)	2.51 (0.08)
SN 2007F	3.2	16.19 (0.05)	36.0 (1.0)	10.88 (0.05)	80.0 (4.5)	0.45 (0.03)
SN 2007N	0.4	19.73 (0.05)	234.2 (0.4)	10.93 (0.05)	172.5 (2.5)	1.36 (0.02)
SN 2007O	−0.3	19.17 (0.05)	86.9 (0.3)	9.30 (0.05)	41.4 (0.7)	2.10 (0.04)
SN 2007S	−6.0	19.83 (0.05)	42.7 (0.8)	10.33 (0.32)	15.5 (4.4)	2.75 (0.78)
SN 2007af	−9.8	20.52 (0.05)	128.3 (0.8)	11.59 (0.07)	85.4 (4.3)	1.50 (0.08)
SN 2007af	−1.3	17.86 (0.05)	42.7 (0.8)	10.77 (0.05)	137.2 (3.4)	0.31 (0.01)
SN 2007af	0.2	···	···	11.43 (0.05)	164.9 (1.0)	0
SN 2007af	2.8	···	···	10.87 (0.05)	232.0 (0.1)	0
SN 2007af	3.8	···	···	10.93 (0.05)	229.2 (0.3)	0
SN 2007al	3.4	···	···	12.05 (0.05)	291.2 (0.8)	0
SN 2007ba	2.1	···	···	11.77 (0.05)	324.2 (2.1)	0
SN 2007bc	0.6	···	···	10.96 (0.05)	158.1 (0.7)	0
SN 2007bd	−5.8	···	···	14.64 (0.06)	161.3 (2.4)	0
SN 2007bm	−7.8	19.30 (0.05)	61.8 (0.3)	10.29 (0.05)	70.6 (1.7)	0.88 (0.02)
SN 2007bz	1.7	···	···	12.31 (0.05)	94.3 (1.3)	0
SN 2007ca	−11.1	22.86 (0.05)	110.8 (1.1)	11.75 (0.35)	69.2 (12.1)	1.60 (0.28)
SN 2007ci	−6.6	17.38 (0.14)	114.4 (3.8)	11.12 (0.17)	69.9 (7.8)	1.64 (0.19)

Continued on next page

Table A.4 — Continued

SN Name	Phase (d)[a]	HVF v (10^3 km s^{-1})	HVF pEW (Å)	PVF v (10^3 km s^{-1})	PVF pEW (Å)	R^{b}_{CaNIR}
SN 2007ci	−1.7	···	···	12.24 (0.05)	132.6 (0.9)	0
SN 2007co	−4.1	20.13 (0.05)	135.4 (1.0)	11.32 (0.09)	109.8 (5.0)	1.23 (0.06)
SN 2007co	−0.6	18.54 (0.05)	110.2 (1.6)	10.37 (0.12)	108.1 (6.6)	1.02 (0.06)
SN 2007co	0.9	18.05 (0.05)	101.0 (1.1)	10.75 (0.06)	133.3 (3.9)	0.76 (0.02)
SN 2007cq	−5.8	···	···	12.43 (0.05)	68.2 (1.0)	0
SN 2007fb	2.0	···	···	11.40 (0.05)	157.5 (0.6)	0
SN 2007fr	−5.8	···	···	13.08 (0.05)	203.8 (1.9)	0
SN 2007fr	−1.3	···	···	12.36 (0.05)	246.0 (2.2)	0
SN 2007gi	−7.3	20.44 (0.05)	287.6 (0.2)	···	···	···
SN 2007gi	−0.4	18.46 (0.05)	146.1 (0.4)	12.12 (0.05)	105.1 (1.4)	1.39 (0.02)
SN 2007gk	−1.7	19.82 (0.05)	96.7 (1.5)	12.01 (0.13)	199.0 (7.2)	0.49 (0.02)
SN 2007hj	−1.2	···	···	12.98 (0.05)	283.1 (0.4)	0
SN 2007le	−10.3	28.99 (0.05)	370.5 (3.2)	20.31 (0.05)	146.5 (12.9)	2.53 (0.22)
SN 2007le	−9.4	27.75 (0.05)	231.0 (15.0)	19.77 (0.43)	121.0 (25.2)	1.91 (0.42)
SN 2007s1[c]	−1.2	···	···	14.23 (0.05)	291.5 (1.3)	0
SN 2007on	−3.0	17.23 (0.05)	87.9 (1.6)	10.61 (0.07)	134.9 (5.7)	0.65 (0.03)
SN 2007qe	−8.2	29.17 (0.27)	279.3 (17.1)	17.32 (0.58)	107.1 (70.3)	2.61 (1.72)
SN 2007qe	−6.5	28.33 (0.05)	154.0 (6.0)	18.83 (0.35)	198.4 (25.5)	0.78 (0.10)
SN 2007qe	−2.5	25.21 (0.63)	117.0 (16.2)	14.04 (2.67)	115.3 (161.9)	1.01 (1.43)

Continued on next page

Table A.4 — Continued

SN Name	Phase (d)[a]	HVF v (10^3 km s^{-1})	HVF pEW (Å)	PVF v (10^3 km s^{-1})	PVF pEW (Å)	$R^{b}_{\rm CaNIR}$
SN 2008ar	−8.9	23.65 (0.05)	212.3 (1.9)	12.17 (0.11)	34.9 (3.6)	6.08 (0.63)
SN 2008ar	−5.6	22.20 (0.15)	146.5 (9.6)	11.35 (0.69)	32.7 (18.7)	4.48 (2.57)
SN 2008ar	1.5	17.98 (0.23)	70.0 (6.2)	9.68 (0.56)	70.5 (25.5)	0.99 (0.37)
SN 2008ar	2.8	18.07 (0.11)	65.9 (3.2)	8.84 (0.39)	108.8 (23.8)	0.61 (0.14)
SN 2008ar	4.3	15.81 (0.18)	67.7 (6.5)	8.49 (0.43)	107.5 (28.7)	0.63 (0.18)
SN 2008bt	−1.1	···	···	12.11 (0.05)	177.3 (1.9)	0
SN 2008cl	4.2	···	···	10.50 (0.10)	251.2 (9.9)	0
SN 2008s1[d]	−6.4	21.61 (0.08)	19.5 (0.5)	11.05 (0.34)	90.2 (12.8)	0.22 (0.03)
SN 2008s1[d]	−4.4	22.82 (0.11)	40.6 (2.4)	10.51 (8.36)	176.2 (277.9)	0.23 (0.36)
SN 2008s1[d]	−3.4	22.86 (0.09)	46.1 (1.0)	11.39 (0.33)	78.9 (12.8)	0.58 (0.10)
SN 2008s1[d]	0.5	···	···	11.20 (0.05)	135.9 (1.6)	0
SN 2008s1[d]	4.4	···	···	11.00 (0.05)	191.3 (0.8)	0
SN 2008dx	2.5	···	···	11.45 (0.05)	275.9 (1.4)	0
SN 2008ec	−9.8	···	···	13.27 (0.06)	132.4 (3.4)	0
SN 2008ec	−8.9	···	···	12.70 (0.07)	117.3 (3.4)	0
SN 2008ec	−6.0	···	···	11.99 (0.10)	95.6 (4.3)	0
SN 2008ec	−0.2	···	···	11.05 (0.05)	141.0 (0.4)	0
SN 2008ec	1.0	···	···	10.88 (0.08)	127.1 (6.1)	0
SN 2008ei	3.3	19.00 (0.05)	64.8 (4.1)	13.52 (0.42)	217.7 (24.4)	0.30 (0.04)

Continued on next page

Table A.4 — Continued

SN Name	Phase (d)[a]	HVF v (10^3 km s^{-1})	HVF pEW (Å)	PVF v (10^3 km s^{-1})	PVF pEW (Å)	R^{b}_{CaNIR}
SN 2008s5[e]	1.3	18.61 (0.05)	57.3 (0.5)	8.52 (0.05)	44.0 (2.0)	1.30 (0.06)
SN 2008hm	1.3	18.90 (0.11)	78.4 (3.5)	10.48 (0.30)	89.1 (15.7)	0.88 (0.16)
SN 2008hs	−8.9	···	···	13.33 (0.08)	174.0 (5.9)	0
SN 2008hs	−7.9	···	···	13.77 (0.05)	215.4 (0.8)	0
SN 2008hs	−6.3	···	···	12.79 (0.05)	182.3 (1.0)	0
SN 2008hv	−11.7	24.96 (0.52)	218.1 (35.1)	16.01 (1.02)	130.0 (134.1)	1.68 (1.75)
SN 2008hv	−9.2	25.27 (0.05)	78.1 (3.3)	13.79 (0.89)	97.4 (23.2)	0.80 (0.19)
SN 2008hv	−6.6	22.48 (0.15)	73.1 (5.3)	11.20 (0.57)	22.6 (13.7)	3.23 (1.97)
SN 2009F	−3.0	···	···	11.84 (0.09)	181.7 (8.0)	0
SN 2009ad	−3.4	19.87 (0.07)	22.2 (0.7)	9.12 (0.14)	38.7 (3.9)	0.57 (0.06)
SN 2009an	−5.8	22.83 (0.05)	123.3 (0.9)	12.19 (0.17)	98.9 (9.3)	1.25 (0.12)
SN 2009an	−3.8	20.83 (0.05)	83.0 (0.8)	11.49 (0.11)	103.3 (5.9)	0.80 (0.05)
SN 2009an	−2.9	19.39 (0.06)	75.8 (1.6)	11.33 (0.14)	112.7 (8.3)	0.67 (0.05)
SN 2009ig	−14.4	35.15 (0.05)	138.7 (2.7)	25.52 (0.30)	287.0 (19.5)	0.48 (0.03)
SN 2009ig	−13.9	32.82 (0.11)	157.5 (19.1)	24.63 (0.23)	198.1 (43.6)	0.79 (0.20)
SN 2009ig	−12.4	30.87 (0.10)	219.6 (16.9)	23.16 (0.52)	109.6 (26.7)	2.00 (0.51)
SN 2009ig	−11.4	29.13 (0.05)	213.5 (4.2)	18.32 (0.31)	66.1 (8.2)	3.23 (0.41)
SN 2009ig	−10.9	27.50 (0.05)	152.4 (1.9)	15.82 (0.13)	7.7 (3.0)	19.78 (7.57)
SN 2009ig	−9.4	26.35 (0.05)	130.7 (0.3)	13.63 (0.05)	33.2 (1.3)	3.94 (0.15)

Continued on next page

Table A.4 — Continued

SN Name	Phase (d)[a]	HVF v (10^3 km s^{-1})	HVF pEW (Å)	PVF v (10^3 km s^{-1})	PVF pEW (Å)	$R^{b}_{\rm CaNIR}$
SN 2009ig	−8.4	25.65 (0.05)	112.1 (0.8)	14.73 (0.05)	10.2 (0.9)	11.04 (0.99)
SN 2009ig	−6.9	24.05 (0.05)	69.4 (0.5)	13.46 (0.08)	33.5 (2.0)	2.07 (0.12)
SN 2009ig	−6.0	23.18 (0.05)	36.3 (0.2)	12.92 (0.08)	39.8 (2.0)	0.91 (0.05)
SN 2009ig	−4.0	21.99 (0.05)	22.6 (0.4)	12.72 (0.09)	52.6 (3.4)	0.43 (0.03)
SN 2009ig	−3.0	21.94 (0.05)	19.6 (0.5)	12.91 (0.09)	70.2 (5.1)	0.28 (0.02)
SN 2009ig	−2.0	21.65 (0.11)	19.5 (0.9)	13.52 (0.14)	78.2 (9.1)	0.25 (0.03)
SN 2009ig	−1.0	20.97 (0.05)	21.5 (0.5)	13.39 (0.07)	88.5 (4.5)	0.24 (0.01)
SN 2009ig	3.4	···	···	13.63 (0.05)	124.1 (0.9)	0
SN 2009ig	4.3	···	···	13.66 (0.05)	135.2 (0.7)	0
SN 2009no	2.1	···	···	9.10 (0.05)	97.9 (1.1)	0
SN 2009nq	−3.1	18.26 (0.05)	65.3 (0.6)	9.60 (0.05)	63.1 (1.8)	1.03 (0.03)
SN 2010Y	−7.2	18.03 (0.23)	65.3 (3.7)	10.54 (0.31)	99.3 (16.5)	0.66 (0.12)
SN 2010Y	−3.2	···	···	11.06 (0.05)	155.2 (0.6)	0
PTF 10bjs	−9.8	25.34 (0.08)	63.2 (2.1)	14.74 (0.66)	16.8 (9.5)	3.77 (2.14)
PTF 10bjs	−8.6	25.01 (0.07)	70.1 (2.2)	15.25 (0.47)	13.2 (6.7)	5.33 (2.70)
PTF 10bjs	−7.4	24.85 (0.06)	72.0 (1.9)	14.63 (0.28)	18.6 (5.2)	3.86 (1.09)
PTF 10bjs	−6.6	25.07 (0.06)	60.6 (1.2)	15.12 (0.32)	21.3 (5.5)	2.84 (0.73)
PTF 10bjs	−5.5	23.82 (0.06)	49.7 (1.3)	13.00 (0.27)	31.8 (6.3)	1.56 (0.31)
PTF 10bjs	−1.8	22.20 (0.07)	24.9 (0.7)	12.92 (0.14)	33.6 (3.2)	0.74 (0.07)

Continued on next page

Table A.4 — Continued

SN Name	Phase (d)[a]	HVF v (10^3 km s^{-1})	HVF pEW (Å)	PVF v (10^3 km s^{-1})	PVF pEW (Å)	$R^{b}_{\rm CaNIR}$
PTF 10bjs	0.2	20.84 (0.09)	20.9 (1.4)	12.08 (0.23)	42.3 (5.8)	0.49 (0.07)
SN 2010ai	−10.5	···	···	14.72 (0.05)	176.4 (3.0)	0
SN 2010ai	−8.6	···	···	13.62 (0.05)	150.8 (0.8)	0
SN 2010ai	−3.7	···	···	12.61 (0.05)	101.9 (0.6)	0
SN 2010ai	−0.8	···	···	11.60 (0.05)	150.8 (0.9)	0
PTF 10fps	0.0	17.27 (0.10)	60.1 (3.1)	9.10 (0.23)	121.4 (13.3)	0.49 (0.06)
PTF 10fps	0.9	17.67 (0.15)	45.5 (4.5)	9.68 (0.45)	126.9 (25.3)	0.36 (0.08)
PTF 10fps	3.9	···	···	10.51 (0.05)	189.2 (1.4)	0
SN 2010dm	−6.5	20.90 (0.05)	46.1 (1.5)	9.86 (0.33)	21.7 (5.4)	2.13 (0.53)
PTF 10icb	−9.8	19.72 (0.05)	61.3 (0.6)	10.47 (0.11)	47.1 (3.6)	1.30 (0.10)
SN 2010ex	1.1	18.53 (0.07)	39.4 (0.9)	10.29 (0.09)	77.6 (5.9)	0.51 (0.04)
PTF 10qjl	−3.0	20.95 (0.08)	42.7 (1.2)	10.66 (0.11)	33.9 (4.3)	1.26 (0.16)
SN 2010ii	−6.1	···	···	14.91 (0.05)	130.8 (1.1)	0
SN 2010ii	−0.5	···	···	11.28 (0.05)	80.9 (1.0)	0
SN 2010it	−9.5	25.86 (0.05)	161.4 (0.6)	13.75 (0.17)	73.7 (6.1)	2.19 (0.18)
SN 2010it	−8.5	24.61 (0.05)	98.9 (0.5)	13.22 (0.11)	56.3 (3.6)	1.76 (0.11)
SN 2010it	−6.6	22.27 (0.05)	58.8 (0.8)	12.63 (0.28)	75.1 (10.4)	0.78 (0.11)
SN 2010it	−2.6	···	···	12.57 (0.05)	73.0 (1.5)	0
SN 2010it	−0.6	···	···	11.93 (0.05)	106.9 (0.6)	0

Continued on next page

Table A.4 — Continued

SN Name	Phase (d)[a]	HVF v (10^3 km s^{-1})	HVF pEW (Å)	PVF v (10^3 km s^{-1})	PVF pEW (Å)	R^{b}_{CaNIR}
SN 2010it	3.3	···	···	11.15 (0.05)	101.4 (0.7)	0
PTF 10ygu	−3.7	21.21 (0.07)	90.4 (2.0)	13.72 (0.19)	47.9 (9.3)	1.89 (0.37)
SN 2010iw	−4.9	20.80 (0.05)	50.7 (0.5)	10.39 (0.16)	39.5 (3.8)	1.28 (0.12)
SN 2010iw	−3.0	20.13 (0.05)	37.6 (0.6)	8.99 (0.19)	17.9 (2.6)	2.10 (0.30)
SN 2010iw	−0.1	20.31 (0.05)	32.7 (0.6)	9.41 (0.14)	34.5 (4.4)	0.95 (0.12)
SN 2010iw	3.9	19.98 (0.05)	26.6 (0.5)	9.65 (0.05)	45.7 (2.9)	0.58 (0.04)
SN 2010kg	−9.9	37.20 (0.05)	130.5 (8.1)	24.64 (1.66)	358.3 (0.1)	0.36 (0.08)
SN 2010kg	−9.0	32.95 (0.07)	221.3 (4.5)	21.41 (0.22)	187.3 (23.0)	1.18 (0.15)
SN 2010kg	−8.0	29.20 (0.06)	288.8 (2.9)	17.54 (0.06)	102.5 (10.5)	2.82 (0.29)
SN 2010kg	−6.0	26.17 (0.28)	109.9 (18.8)	17.45 (0.83)	150.6 (69.0)	0.73 (0.36)
SN 2010kg	−5.0	21.89 (0.13)	112.1 (5.3)	14.14 (0.28)	94.4 (23.2)	1.19 (0.30)
SN 2010kg	−4.1	19.77 (0.05)	130.9 (1.0)	11.68 (0.06)	60.6 (3.3)	2.16 (0.12)
SN 2010kg	−3.1	19.94 (0.05)	101.3 (0.8)	12.40 (0.06)	97.0 (3.8)	1.04 (0.04)
SN 2010kg	−1.1	17.98 (0.05)	124.6 (0.5)	10.83 (0.05)	82.1 (2.4)	1.52 (0.05)
SN 2010kg	−0.1	18.03 (0.05)	120.6 (0.9)	10.55 (0.06)	99.0 (4.0)	1.22 (0.05)
SN 2010kg	0.9	17.61 (0.05)	102.9 (2.1)	10.84 (0.24)	121.3 (13.2)	0.85 (0.09)
SN 2010kg	2.8	16.90 (0.05)	123.8 (1.2)	9.91 (0.08)	106.3 (5.4)	1.16 (0.06)
SN 2010kg	4.8	16.90 (0.05)	127.8 (1.3)	9.00 (0.08)	130.0 (5.2)	0.98 (0.04)
SN 2011ao	−7.5	20.89 (0.05)	113.1 (0.5)	10.96 (0.05)	44.3 (1.6)	2.55 (0.09)

Continued on next page

Table A.4 — Continued

SN Name	Phase (d)[a]	HVF v (10^3 km s^{-1})	HVF pEW (Å)	PVF v (10^3 km s^{-1})	PVF pEW (Å)	R^{b}_{CaNIR}
SN 2011ao	−6.7	21.49 (0.05)	80.4 (1.9)	12.88 (0.24)	59.3 (8.1)	1.36 (0.19)
SN 2011ao	−5.8	21.63 (0.05)	77.2 (2.0)	11.43 (0.74)	76.1 (20.6)	1.01 (0.28)
SN 2011ao	−4.8	20.62 (0.05)	80.2 (0.3)	10.96 (0.07)	37.6 (1.7)	2.13 (0.10)
SN 2011ao	−1.8	20.00 (0.05)	76.2 (0.4)	10.07 (0.05)	36.3 (1.4)	2.10 (0.08)
SN 2011ao	−0.8	19.58 (0.05)	79.1 (0.5)	10.59 (0.12)	44.0 (2.6)	1.80 (0.11)
SN 2011ao	0.2	19.85 (0.05)	72.9 (0.5)	9.95 (0.14)	42.1 (3.3)	1.73 (0.14)
SN 2011ao	1.2	19.53 (0.05)	78.5 (0.6)	9.74 (0.07)	43.4 (2.6)	1.81 (0.11)
SN 2011ao	2.2	18.94 (0.05)	74.3 (0.5)	9.55 (0.05)	47.0 (2.3)	1.58 (0.08)
SN 2011ao	3.2	18.56 (0.05)	88.1 (0.6)	9.23 (0.06)	54.3 (2.6)	1.62 (0.08)
SN 2011by	−11.7	19.65 (0.05)	94.6 (0.3)	11.39 (0.05)	58.4 (1.3)	1.62 (0.04)
SN 2011by	−9.8	19.41 (0.05)	50.1 (0.3)	10.64 (0.05)	64.0 (1.9)	0.78 (0.02)
SN 2011by	−5.7	19.30 (0.05)	34.7 (0.2)	9.55 (0.05)	50.5 (1.0)	0.69 (0.01)
SN 2011by	−3.8	20.08 (0.05)	26.1 (0.1)	10.02 (0.05)	70.3 (1.1)	0.37 (0.01)
SN 2011by	0.2	17.74 (0.05)	27.2 (0.3)	10.15 (0.05)	83.0 (2.5)	0.33 (0.01)
SN 2011by	0.3	17.28 (0.05)	29.9 (0.6)	10.31 (0.05)	99.2 (3.8)	0.30 (0.01)
SN 2011by	2.3	17.45 (0.05)	30.5 (0.9)	10.02 (0.07)	116.6 (6.6)	0.26 (0.02)
SN 2011by	4.2	17.26 (0.05)	36.3 (0.3)	10.17 (0.05)	133.4 (2.5)	0.27 (0.01)
SN 2011dm	−5.5	22.09 (0.05)	90.3 (0.2)	13.00 (0.05)	88.2 (1.0)	1.02 (0.01)
SN 2011ek	−6.0	···	···	14.54 (0.05)	218.1 (0.3)	0

Continued on next page

Table A.4 — Continued

SN Name	Phase (d)[a]	HVF v (10^3 km s^{-1})	HVF pEW (Å)	PVF v (10^3 km s^{-1})	PVF pEW (Å)	$R^{b}_{\rm CaNIR}$
SN 2011ek	−5.0	···	···	14.13 (0.05)	218.8 (0.3)	0
SN 2011ek	3.0	···	···	11.96 (0.05)	272.9 (0.6)	0
SN 2011fe	−17.0	28.26 (0.35)	197.5 (36.5)	15.92 (2.17)	327.3 (0.1)	0.60 (0.36)
SN 2011fe	−16.0	26.90 (0.05)	176.5 (2.2)	16.70 (0.15)	181.1 (14.7)	0.97 (0.08)
SN 2011fe	−15.0	24.35 (0.05)	122.5 (1.3)	14.93 (0.20)	225.6 (11.8)	0.54 (0.03)
SN 2011fe	−13.0	21.39 (0.05)	169.4 (0.7)	12.51 (0.05)	149.4 (4.7)	1.13 (0.04)
SN 2011fe	−12.0	20.97 (0.05)	107.4 (0.2)	12.23 (0.05)	193.1 (1.7)	0.56 (0.01)
SN 2011fe	−11.0	19.22 (0.05)	110.4 (0.5)	10.66 (0.06)	98.7 (3.3)	1.12 (0.04)
SN 2011fe	−10.0	19.48 (0.05)	77.0 (0.2)	10.35 (0.05)	96.5 (2.0)	0.80 (0.02)
SN 2011fe	−10.0	19.22 (0.05)	89.0 (0.1)	10.71 (0.05)	93.0 (0.4)	0.96 (0.01)
SN 2011fe	−9.0	19.16 (0.05)	57.2 (0.3)	10.46 (0.05)	76.7 (2.3)	0.75 (0.02)
SN 2011fe	−9.0	19.94 (0.05)	58.5 (0.2)	10.20 (0.05)	128.4 (2.0)	0.46 (0.01)
SN 2011fe	−7.0	20.24 (0.05)	40.8 (0.3)	10.91 (0.05)	63.3 (1.4)	0.64 (0.02)
SN 2011fe	−2.0	19.27 (0.05)	27.2 (0.1)	9.86 (0.05)	135.4 (1.4)	0.20 (0.01)
SN 2011fe	−1.0	18.73 (0.05)	28.6 (0.1)	9.76 (0.05)	137.2 (1.2)	0.21 (0.01)
SN 2011fe	2.0	16.33 (0.05)	38.1 (0.2)	9.55 (0.05)	141.3 (1.0)	0.27 (0.01)
SN 2011fe	3.0	15.98 (0.05)	41.7 (0.2)	9.54 (0.05)	148.6 (1.0)	0.28 (0.01)
SN 2011gy	−1.1	···	···	12.01 (0.05)	103.0 (0.5)	0
SN 2011hb	−5.8	22.86 (0.05)	83.7 (2.6)	12.14 (0.85)	75.0 (17.2)	1.12 (0.26)

Continued on next page

Table A.4 — Continued

SN Name	Phase (d)[a]	HVF v (10^3 km s^{-1})	HVF pEW (Å)	PVF v (10^3 km s^{-1})	PVF pEW (Å)	R^{b}_{CaNIR}
SN 2011hb	−2.9	21.47 (0.05)	70.5 (0.4)	10.50 (0.08)	31.6 (2.1)	2.23 (0.15)
SN 2011hb	3.0	19.51 (0.05)	74.9 (1.7)	9.64 (0.17)	67.3 (7.2)	1.11 (0.12)
SN 2011ia	−3.0	···	···	9.99 (0.05)	65.5 (1.0)	0
SN 2012I	−1.0	···	···	11.87 (0.05)	152.4 (0.6)	0
SN 2012bh	0.0	19.71 (0.05)	25.6 (0.5)	9.46 (0.10)	68.9 (6.2)	0.37 (0.03)
SN 2012cg	−12.8	24.21 (0.05)	86.6 (2.4)	16.42 (0.19)	101.3 (9.0)	0.85 (0.08)
SN 2012cg	−11.8	22.30 (0.05)	140.1 (0.7)	13.67 (0.06)	76.6 (3.3)	1.83 (0.08)
SN 2012cg	−10.5	21.32 (0.05)	122.7 (0.9)	11.88 (0.08)	50.7 (4.2)	2.42 (0.20)
SN 2012cg	−9.6	21.11 (0.05)	88.4 (1.2)	11.88 (0.10)	42.6 (3.9)	2.07 (0.19)
SN 2012cg	−7.8	21.43 (0.05)	55.3 (0.3)	11.86 (0.05)	29.7 (1.2)	1.86 (0.08)
SN 2012cg	−3.8	21.11 (0.05)	56.7 (0.1)	10.40 (0.05)	26.5 (0.4)	2.14 (0.03)
SN 2012cg	−3.8	21.07 (0.05)	48.2 (0.4)	10.56 (0.10)	33.0 (2.6)	1.46 (0.12)
SN 2012cg	−0.5	20.28 (0.05)	39.4 (0.3)	10.44 (0.05)	43.2 (1.9)	0.91 (0.04)
SN 2012da	−1.0	18.56 (0.05)	75.8 (1.2)	9.16 (0.14)	54.6 (5.6)	1.39 (0.14)
SN 2012fr	−14.4	32.78 (0.05)	450.1 (2.7)	···	···	···
SN 2012fr	−12.4	30.67 (0.05)	395.0 (0.4)	···	···	···
SN 2012fr	−11.4	30.17 (0.05)	330.7 (0.3)	···	···	···
SN 2012fr	−9.3	27.24 (0.05)	135.8 (0.9)	···	···	···
SN 2012fr	−8.4	26.00 (0.05)	110.1 (0.3)	···	···	···

Continued on next page

Table A.4 — Continued

SN Name	Phase (d)[a]	HVF v (10^3 km s^{-1})	HVF pEW (Å)	PVF v (10^3 km s^{-1})	PVF pEW (Å)	$R^{b}_{\rm CaNIR}$
SN 2012fr	−8.2	25.80 (0.05)	97.4 (0.3)	···	···	···
SN 2012fr	−7.5	25.33 (0.05)	95.9 (0.3)	···	···	···
SN 2012fr	−6.7	25.17 (0.05)	96.1 (1.3)	12.72 (0.23)	5.9 (2.1)	16.37 (5.76)
SN 2012fr	−6.4	24.80 (0.05)	98.2 (1.1)	11.84 (0.17)	26.7 (3.1)	3.67 (0.43)
SN 2012fr	−5.6	24.46 (0.05)	100.3 (0.2)	11.42 (0.05)	12.8 (0.4)	7.84 (0.26)
SN 2012fr	−4.7	24.14 (0.05)	99.4 (0.3)	11.30 (0.05)	13.1 (0.7)	7.60 (0.38)
SN 2012fr	−3.7	23.87 (0.05)	84.3 (0.4)	11.26 (0.05)	35.6 (1.9)	2.37 (0.13)
SN 2012fr	−2.5	22.96 (0.05)	90.7 (0.4)	11.58 (0.05)	31.9 (1.0)	2.85 (0.09)
SN 2012fr	−2.4	23.33 (0.05)	105.7 (1.9)	11.44 (0.09)	32.0 (3.2)	3.30 (0.33)
SN 2012fr	−1.4	22.67 (0.05)	86.0 (0.2)	12.15 (0.05)	39.8 (1.1)	2.16 (0.06)
SN 2012fr	−1.3	22.32 (0.05)	80.9 (0.1)	12.13 (0.05)	35.6 (0.9)	2.27 (0.06)
SN 2012fr	−0.3	21.65 (0.05)	80.8 (0.2)	12.03 (0.05)	49.8 (0.7)	1.62 (0.02)
SN 2012fr	0.7	21.56 (0.05)	82.0 (0.3)	12.22 (0.05)	68.3 (1.3)	1.20 (0.02)
SN 2012fr	1.3	20.61 (0.05)	82.6 (0.5)	11.68 (0.05)	62.3 (2.9)	1.33 (0.06)
SN 2012fr	1.7	21.02 (0.05)	79.7 (0.3)	12.32 (0.05)	85.8 (2.0)	0.93 (0.02)
SN 2012fr	2.3	20.92 (0.05)	71.2 (0.2)	11.98 (0.05)	67.5 (1.2)	1.05 (0.02)
SN 2012fr	3.2	19.42 (0.05)	86.6 (0.5)	11.91 (0.05)	63.7 (2.1)	1.36 (0.04)
SN 2012fr	4.5	19.58 (0.05)	57.9 (0.9)	11.60 (0.05)	133.2 (4.3)	0.43 (0.02)
SN 2013cs	−8.9	21.39 (0.05)	61.4 (0.8)	13.69 (0.08)	99.0 (4.2)	0.62 (0.03)

Continued on next page

Table A.4 — Continued

SN Name	Phase (d)[a]	HVF v (10^3 km s^{-1})	HVF pEW (Å)	PVF v (10^3 km s^{-1})	PVF pEW (Å)	R^{b}_{CaNIR}
SN 2013cs	−3.0	16.47 (0.05)	32.1 (0.7)	10.65 (0.39)	135.4 (8.2)	0.24 (0.02)
SN 2013di	−1.6	20.42 (0.05)	104.5 (0.5)	10.28 (0.06)	47.0 (2.1)	2.22 (0.10)

[a]Phases are in rest-frame days.

[b]R_{CaNIR} is the ratio of the pEW of the HVF to the pEW of the PVF, as defined by Childress et al. (2014).

[c]Also known as SNF20071021-000.

[d]Also known as SNF20080514-002.

[e]Also known as SNF20080909-030.

Appendix B: Fitting spectral features using a sparsely sampled multidimensional parameter space

B.1 Prelude

Significant portions of this appendix have been published previously as an appendix to Mulligan & Wheeler (2018). In this chapter we discuss the challenges of fitting an absorption feature in supernova spectra using synthetic spectra generated from a supernova model, especially when each spectrum is generated from a sparsely sampled parameter space in which it is computationally expensive to generate spectra and analytic derivatives of the parameters used in generating the spectra are not available.

B.2 Optimizing the quality of fit in 4-D parameter space

The fitting method that we employ — a refined grid search using variance as the distinguishing parameter — presents challenges in ensuring that the parameters that result in the best fit of the observed spectra are the most representative of the physical conditions. There are two problems that we encounter when fitting spectra in such a parameter space. The first is that variance (or χ-square) can be a poor indicator of the quality of fit of a spectrum when the resulting fit is not exact. There may be minima or maxima that occur in the feature of interest that are washed out by differences between the model and observed spectra on a larger scale. For example, consider absorption by a doublet in a typical absorption line in a star. A fit to such a feature by a single Gaussian would manage to capture the relative broadness and average depth of the absorption features, but would fail to capture the presence of two minima. Higher order statistical moments or "χ-by-eye" may help discern the failure of the fundamental model. We investigated use of moments up to the 6^{th} order but did not find any improvement in the fit for our models — the variance was the best predictor of the quality of the fit.

The second problem that we encounter is that we do not know the topography of the parameter space. Use of a grid search may lead to choice of a local minima as the best fit, rather than a nearby global minima that resides over a narrow, nearby ridge. Is is not computationally practical to sample the parameter space at high enough resolution to ensure that we have truly reached a global minimum. Furthermore, because the model is not expected to perfectly replicate the physical characteristics of the supernova, and because there is some degeneracy between the parameters (i.e. there is overlap in the absorption due to the shell and ejecta that can make them individually difficult to distinguish, and there is also degeneracy between the different models due to the effects of velocity of the photosphere and the relative strength of absorption by the shell or ejecta components) we expect the best fit within the available space to lie in a valley that is somewhat broad in those parameters that are degenerate. We do see this in the relatively small difference between the best quality of fit of the various models at a given epoch (c.f. Table 4.2). One of the ways to overcome this is through the choice of starting point of the search. By initially fitting by eye we can have some confidence that one point within our initial grid is likely to be within the deepest valley within the space.

To investigate the topography of the parameter space of an individual model presents its own challenge — visualizing a non-uniformly sampled parameter space. The method that we use to refine the grid results in sub-grid refinement during each refinement step. For example, consider a 2-D parameter space with an evenly spaced grid of points for which we wish to visualize the quality of fit along only one axis. If the parameters at the central point of the grid fit the data the best, then the next refinement step would be a grid centered about that central point with half the size of the original grid. If one of the corners of the refined grid then fit the data best, the next refinement would be a grid with one-fourth the size of the original grid and centered on the corner of the second grid. Such a method of refinement is demonstrated in Figure B.1. In the figure, three cases are presented, all of which show the second level of refinement centered on the central parameter sample in the first level or refinement, and the third level or refinement centered on the sample at the top corner of the second level of refinement. The only difference in the three cases shown in Figure B.1 are which parameter sample at the third level of refinement has the highest quality of fit. In case 'a' (Fig. B.1a) the best parameter sample is co-linear with the middle row of the grid at the second refined parameter level, in

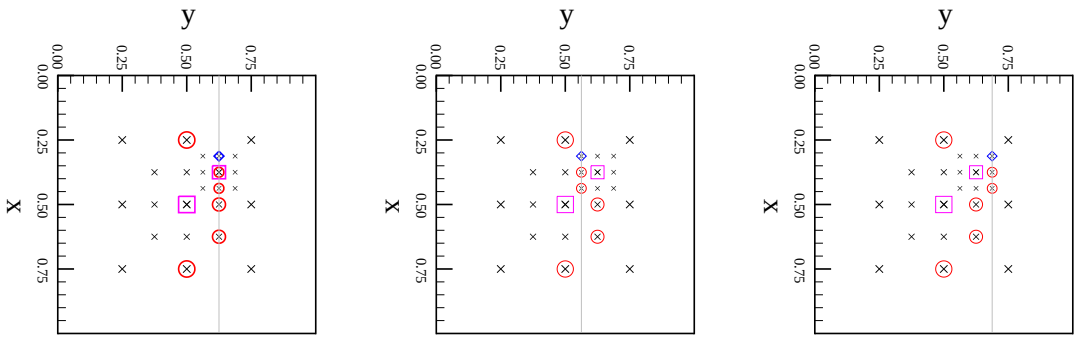

(a) Case ‘a’ (b) Case ‘b’ (c) Case ‘c’

Figure B.1: Three cases of sampling an arbitrary 2-D parameter space using our refined grid method. The locations of the samples are each shown as an ‘X’, with the size of the symbol indicating the refinement level — the most coarse samples are larger than the most refined samples. The best parameter sample is indicated with a blue diamond; the gray line indicates its y-coordinate. The magenta squares indicate the parameter samples that were the best at prior levels of refinement that are also the central point of the later level of refinement. The red circles indicate the points in each level of the grid that are co-linear (or, in a higher dimensional space, co-planar) with the best fitting samples at each level. The latter are also the points chosen for visualization of the quality of fit along the gray line. The three panels are identical except for the location of the parameter sample that is the best fit. Case ’a’ maximizes the number of points that are co-linear along the horizontal axis that are used for the visualization. Case ‘b’ demonstrates the case wherein the best fit is between the samples in the first and second level of refinement and it seems natural to use the samples from the middle row of the first level for demonstrating the quality of fit near $x = 0.25$ and $x = 0.75$. Case ’c’ demonstrates the case of the best sample lying closer to the first level row of samples (the top row) that did not include the best sample at that level of refinement. In this case, we still use the middle row of samples at the lowest level of refinement for visualization of the quality of the fit because of the use of the central sample of the middle row of the first level for the subsequent refinement.

case ‘b’ (Fig. B.1b) the best parameter sample lies between the middle row of the first refined parameter level and the top row of the second refined parameter level, and in case ‘c’ (Fig. B.1c) the best parameter sample lies between the top rows of both the first and second refined parameter levels.

When attempting to visualize the quality of fit, we select a plane in the parameter space that includes the parameters that result in the best fit overall. Only a few

other parameters will lie in a plane with this sample — those in the same plane of the most refined grid and perhaps a subset of parameter samples in the previous level of refinement. Interpolation between points, especially at the lowest level of refinement (most coarse grid), will result in substantial loss of information, especially in a non-linear space as we expect this to be. Therefore we select the parameter samples in each level of refinement that are co-planar with the best sample in that level for use in visualizing the topography.

Figure B.1 also shows the parameter samples at each level of refinement that would be selected for visualization in this simple example of visualization along a line in a 2-D parameter space. In case 'a' (Fig. B.1a), there are eight unique parameter samples that are co-linear with the best sample (one sample is duplicated in two levels). Of these eight parameter samples, five of them are co-linear and one sample is ignored ($x = 0.5, y = 0.5$), because there is a sample closer to or co-linear with the best sample. In cases 'b' and 'c' (Fig. B.1b and B.1c, respectively), there are nine total parameter samples, though only seven would be used for visualization due to samples at higher levels of refinement being closer to the line on which the best sample lies. Of those seven, only three are co-linear with the best parameter sample. In case 'c' (Fig. B.1c) the best parameter sample lies between samples at the first and second level, but lies further from the sample that was the best of the first level. In this case, the middle row of the first level of refinement is still used for purposes of visualization because it included the best parameter sample at that level. Figure B.2 shows an example of a 1-D visualization of the quality of fit of the parameter space for case 'a', using the x values of the selected samples, i.e. the samples circled in red in Figure B.1. Figure B.3 shows a 2-D visualization of the quality of fit for the entire parameter space of case 'a'. Both the 1-D and 2-D visualizations suggest that there is a smooth distribution in quality of fit with a minimum near the sample that result in the best quality of fit.

In Figure B.4 we present the result of such a visualization for the model with a shell of mass 0.003 $M_\odot$ at 4.47 d after the explosion for the temperature - velocity plane, where darker shades indicate better quality of fit. We find that there is a a bowl near $T_{\rm PS} \sim 15{,}000$ K and $v_{\rm PS} \sim 14{,}000$ km s^{-1}. The bowl appears relatively smooth, but it is possible that our result lies within a local, rather than global, minimum. Figure B.5 shows the visualization of the quality of fit in the scalar parameter $(S^{\rm E}, S^{\rm S})$ axes. In these axes there is a bowl near $\log S^{\rm E} \sim 1.5, \log S^{\rm S} \sim 1.75$. This bowl also appears

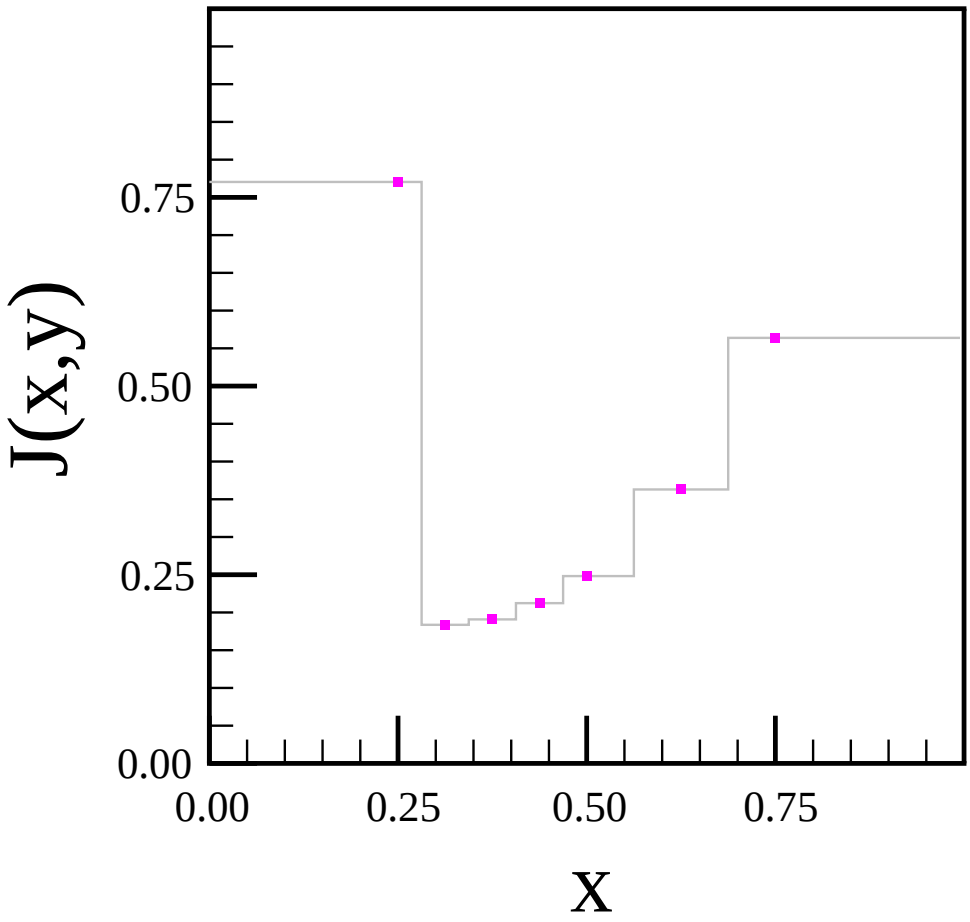

Figure B.2: A sample visualization of the quality of fit in the horizontal axis and sampled along the gray line for case 'a' in figure B.1. The samples are taken at $x = 0.25, 0.31, 0.38, 0.44, 0.50, 0.62$, and 0.75. Note that the samples are not co-linear in y — see text and Fig B.1 for details. The segments are not centered at the x values of the samples due to the non-uniform sampling; instead, the edges of the segments are halfway between samples. In this space, there is a steep dropoff somewhere between $x = 0.25$ and $x = 0.31$. The best fit identified is at $x = 0.31$, though there may be a better fit between $x = 0.25$ and $x \simeq 0.42$. Additionally, if the quality of fit topography is very hilly, it is possible that samples are catching the crests of the hills and therefore a global minimum is missed. That the quality of fit monotonically decreases leftward from $x = 0.75$, the largest sampled value in this example, suggests that there are probably not additional minima; i.e. the probability of catching only crests in the samples between $x = 0.3$ and $x = 0.75$ is small.

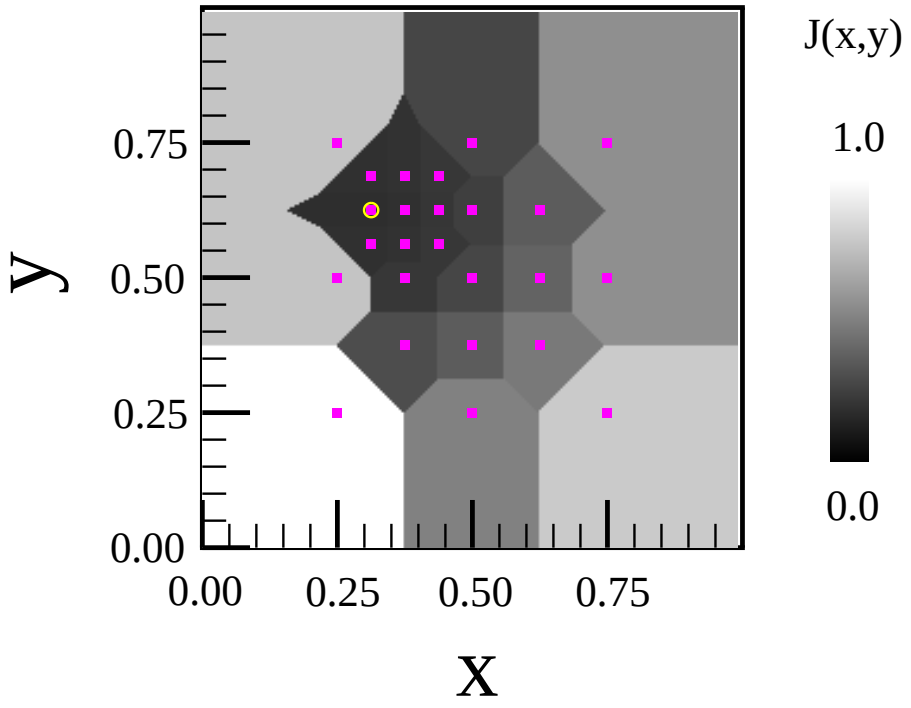

Figure B.3: A 2-D visualization of an example quality of fit of a parameter space that results in case 'a' (See text and Fig. B.1a). Here, shading is used to indicate quality of fit, with darker shades representing a better fit. The magenta points represent the locations of samples in the parameter space. The space in between samples is shaded based upon the nearest sample. The sample that resulted in the best fit is circled in yellow. This visualization suggests there is a bowl centered near the sample with the best fit and is in agreement with the 1-D visualization presented in Figure B.2.

smooth, and seems to be slightly elongated in the S^{S} axis.

Increasing the number of parameter samples taken at each level of grid refinement could increase the probability of finding a global minimum, though the computational workload scales as N^4, where N is the number of samples taken in each axis. Using a suggested starting point for the grid requires use of an odd number of samples in each axis in order for the central point of the grid to lie at the starting point; therefore increasing the sampling in each axis from three points to five increases the number of samples from 81 per grid refinement level to 625 per refinement level, a factor of 7.7 larger. A grid with three samples in each axis requires approximately 240 CPU hours on Stampede2 at the Texas Advanced Computing Center to perform fitting at a single epoch for all six models that we have considered.

Overall, the method employed is a balance between computational effort and thorough sampling of the parameter space. The relative smoothness of the bowl in which the best samples lie suggest that the grid refinement method is reasonable for the space that we are sampling. Due to sparse sampling, however, uncertainties may still be larger than the spacing between points at the most-refined level of the grid.

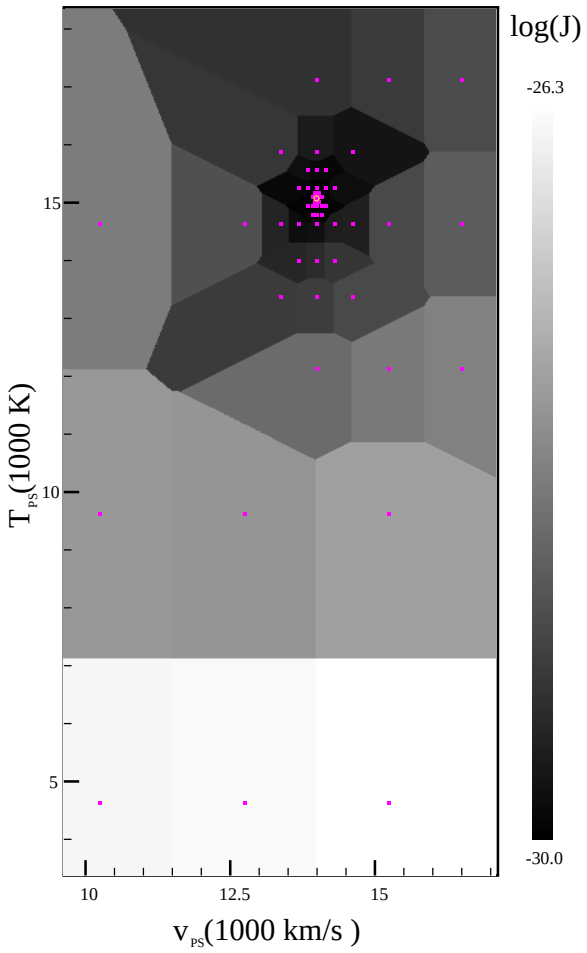

Figure B.4: The quality of fit space for the model with a shell of mass 0.003 $M_\odot$ at 7.55 d after the explosion in the photospheric temperature ($T_{\rm PS}$) and velocity ($v_{\rm PS}$) plane. Magenta points indicate the position in ($T_{\rm PS}, v_{\rm PS}$) space of the samples, and the yellow circle indicates the sample that results in the best fit in the space. The shade indicates the variance (J) in units of erg^2 cm^{-4} sec^{-2}, with darker shades indicating better a quality of fit. The shading is in log scale, as shown on the plot, with the worst fits having a variance of $\log J \sim -26.3$ and the best having a variance of $\log J \sim -30$. Due to sparse sampling, the shading is based upon the nearest sample on the plane. In this space, there is a bowl near $T_{\rm PS} \sim 15,000$ K and $v_{\rm PS}$ ~14,000 km s^{-1}. The first grid point selected for further refinement for this model is at the corner of the samples in the initial plane, with $T_{\rm PS} \sim 14,500$ K and $v_{\rm PS}$ ~15,500 km s^{-1}.

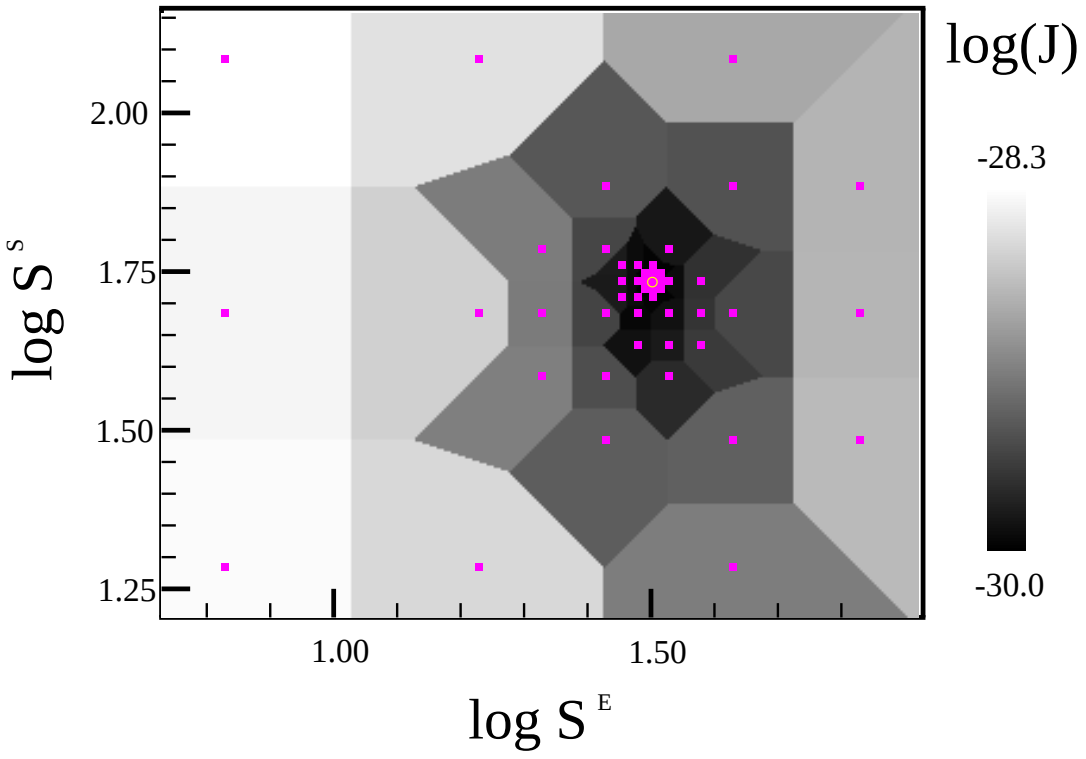

Figure B.5: A visualization of the space for the model with a shell of mass 0.003 $M_\odot$ at 7.55 d after the explosion in the plane of the scalars for the ejecta ($S^{\rm E}$) and shell ($S^{\rm S}$). Magenta points indicate the position in ($S^{\rm E}, S^{\rm S}$) space of the samples. The shade indicates the variance (J) in units of erg^2 cm^{-4} sec^{-2}, with darker shades indicating better a quality of fit. The shading is in log scale, as shown on the plot, with the worst fits having a variance of $\log J \sim -26.3$ and the best having a variance of $\log J \sim -30$. Due to sparse sampling, the shading is based upon the nearest sample on the plane. There is a bowl near $\log S^{\rm E} \sim 1.5$ and $\log S^{\rm S} \sim 1.75$. The bowl appears slightly elongated in the $S^{\rm S}$ axis.

Bibliography

Asplund M., Grevesse N., Sauval A. J., Scott P., 2009, ARA&A, 47, 481

Barbon R., Benetti S., Rosino L., Cappellaro E., Turatto M., 1990, A&A, 237, 79

Benetti S., et al., 2004, MNRAS, 348, 261

Benetti S., et al., 2005, ApJ, 623, 1011

Betoule M., et al., 2014, A&A, 568, A22

Blondin S., Tonry J. L., 2007, ApJ, 666, 1024

Blondin S., Mandel K. S., Kirshner R. P., 2011, A&A, 526, A81

Blondin S., Dessart L., Hillier D. J., Khokhlov A. M., 2013, MNRAS, 429, 2127

Bloom J. S., et al., 2012, ApJ, 744, L17

Bongard S., Baron E., Smadja G., Branch D., Hauschildt P. H., 2006, ApJ, 647, 513

Botyánszki J., Kasen D., Plewa T., 2018, ApJ, 852, L6

Brahe T., 1572, De Nova stella, anni 1572

Branch D., 1986, ApJ, 300, L51

Branch D., van den Bergh S., 1993, AJ, 105, 2231

Branch D., et al., 2006, PASP, 118, 560

Branch D., Dang L. C., Baron E., 2009, PASP, 121, 238

Bronder T. J., et al., 2008, A&A, 477, 717

Cardelli J. A., Clayton G. C., Mathis J. S., 1989, ApJ, 345, 245

Castor J. I., 1970, MNRAS, 149, 111

Childress M. J., et al., 2013a, ApJ, 770, 29

Childress M. J., et al., 2013b, ApJ, 770, 29

Childress M. J., Filippenko A. V., Ganeshalingam M., Schmidt B. P., 2014, MNRAS, 437, 338

Chiosi E., Chiosi C., Trevisan P., Piovan L., Orio M., 2015, MNRAS, 448, 2100

Chomiuk L., et al., 2012, ApJ, 750, 164

Chornock R., Filippenko A. V., 2008, AJ, 136, 2227

Colgate S. A., McKee C., 1969, ApJ, 157, 623

Di Stefano R., Kilic M., 2012, ApJ, 759, 56

Di Stefano R., Voss R., Claeys J. S. W., 2011, ApJ, 738, L1

Elias J. H., Frogel J. A., Hackwell J. A., Persson S. E., 1981, ApJ, 251, L13

Filippenko A. V., et al., 1992a, AJ, 104, 1543

Filippenko A. V., et al., 1992b, ApJ, 384, L15

Fink M., Röpke F. K., Hillebrandt W., Seitenzahl I. R., Sim S. A., Kromer M., 2010, A&A, 514, A53

Fisher A., Branch D., Nugent P., Baron E., 1997, ApJ, 481, L89

Folatelli G., 2004, New A Rev., 48, 623

Folatelli G., et al., 2012, ApJ, 745, 74

Folatelli G., et al., 2013, ApJ, 773, 53

Foley R. J., 2013, MNRAS, 435, 273

Foley R. J., Kasen D., 2011, ApJ, 729, 55

Foley R. J., Filippenko A. V., Jha S. W., 2008, ApJ, 686, 117

Foley R. J., Sanders N. E., Kirshner R. P., 2011, ApJ, 742, 89

Foley R. J., et al., 2012a, ApJ, 744, 38

Foley R. J., et al., 2012b, ApJ, 752, 101

Foley R. J., et al., 2013, ApJ, 767, 57

Fryxell B., et al., 2000, ApJS, 131, 273

Gamezo V. N., Khokhlov A. M., Oran E. S., 2005, ApJ, 623, 337

Ganeshalingam M., et al., 2010, ApJS, 190, 418

Ganeshalingam M., Li W., Filippenko A. V., 2011, MNRAS, 416, 2607

Garavini G., et al., 2004, AJ, 128, 387

Garavini G., et al., 2007, A&A, 470, 411

Gerardy C. L., et al., 2004, ApJ, 607, 391

Guillochon J., Parrent J., Kelley L. Z., Margutti R., 2017, ApJ, 835, 64

Hachinger S., Mazzali P. A., Benetti S., 2006, MNRAS, 370, 299

Hamuy M., Phillips M. M., Maza J., Suntzeff N. B., Schommer R. A., Aviles R., 1995, AJ, 109, 1

Harkness R. P., et al., 1987, ApJ, 317, 355

Harris C. E., Nugent P. E., Kasen D. N., 2016, ApJ, 823, 100

Hatano K., Branch D., Fisher A., Baron E., Filippenko A. V., 1999, ApJ, 525, 881

Hatano K., Branch D., Lentz E. J., Baron E., Filippenko A. V., Garnavich P. M., 2000, ApJ, 543, L49

Hicken M., et al., 2009, ApJ, 700, 331

Hicken M., et al., 2012, ApJS, 200, 12

Hill G. J., Nicklas H. E., MacQueen P. J., Tejada C., Cobos Duenas F. J., Mitsch W., 1998, in Optical Astronomical Instrumentation. pp 375–386, doi:10.1117/12.316773

Hillebrandt W., Niemeyer J. C., 2000, Annual Review of Astronomy and Astrophysics, 38, 191

Hillier D. J., Miller D. L., 1998, ApJ, 496, 407

Howell D. A., 2011, Nature Communications, 2, 350

Howell D. A., et al., 2006, Nature, 443, 308

Hoyle F., Fowler W. A., 1960a, ApJ, 132, 565

Hoyle F., Fowler W. A., 1960b, ApJ, 132, 565

Iben I., Tutukov A., 1984, ApJS, 54, 335

Iwamoto K., Brachwitz F., Nomoto K., Kishimoto N., Umeda H., Hix W. R., Thielemann F.-K., 1999, ApJS, 125, 439

Jeffery D. J., 1989, ApJS, 71, 951

Jha S., et al., 2006a, AJ, 131, 527

Jha S., Branch D., Chornock R., Foley R. J., Li W., Swift B. J., Casebeer D., Filippenko A. V., 2006b, AJ, 132, 189

Justham S., 2011, ApJ, 730, L34

Karakas A. I., Lugaro M., 2016, ApJ, 825, 26

Kasen D., et al., 2003, ApJ, 593, 788

Kepler J., 1606, De Stella nova in pede serpentarii

Kerzendorf W. E., Sim S. A., 2014, MNRAS, 440, 387

Konishi K., et al., 2011, AJ, submitted (arXiv:1103.2497),

Kramida A., Yu. Ralchenko Reader J., and NIST ASD Team 2018, NIST Atomic Spectra Database (ver. 5.5.6), [Online]. Available: `https://physics.nist.gov/asd` [2018, June 7]. National Institute of Standards and Technology, Gaithersburg, MD.

Kurucz R. L., Bell B., 1995, Atomic line list

Leibundgut B., et al., 1993, AJ, 105, 301

Leonard D. C., Li W., Filippenko A. V., Foley R. J., Chornock R., 2005, ApJ, 632, 450

Li W., et al., 2001a, PASP, 113, 1178

Li W., Filippenko A. V., Treffers R. R., Riess A. G., Hu J., Qiu Y., 2001b, ApJ, 546, 734

Li W., et al., 2003, PASP, 115, 453

Li W., et al., 2011, MNRAS, 412, 1441

Maeda K., et al., 2010, Nature, 466, 82

Maguire K., et al., 2012a, MNRAS, 426, 2359

Maguire K., et al., 2012b, MNRAS, 426, 2359

Maguire K., et al., 2013, MNRAS, 436, 222

Maguire K., et al., 2014, MNRAS, 444, 3258

Maoz D., Mannucci F., Nelemans G., 2014, ARA&A, 52, 107

Marion G. H., Höflich P., Gerardy C. L., Vacca W. D., Wheeler J. C., Robinson E. L., 2009, AJ, 138, 727

Marion G. H., et al., 2012, The Astronomer's Telegram, 4215, 1

Marion G. H., et al., 2013, ApJ, 777, 40

Maund J. R., et al., 2013, MNRAS, 433, L20

Mazzali P. A., Benetti S., Stehle M., Branch D., Deng J., Maeda K., Nomoto K., Hamuy M., 2005a, MNRAS, 357, 200

Mazzali P. A., et al., 2005b, ApJ, 623, L37

Mazzali P. A., et al., 2014, MNRAS, 439, 1959

Miller J. S., Stone R. P. S., 1993, Lick Obs. Tech. Rep. 66. Santa Cruz: Lick Obs.

Milne P. A., Foley R. J., Brown P. J., Narayan G., 2014, ApJ, submitted (arXiv:1408.1706),

Morozova V., Piro A. L., Renzo M., Ott C. D., Clausen D., Couch S. M., Ellis J., Roberts L. F., 2015, ApJ, 814, 63

Mulligan B. W., Wheeler J. C., 2017, MNRAS, 467, 778

Mulligan B. W., Wheeler J. C., 2018, MNRAS, 476, 1299

Nomoto K., Thielemann F. K., Yokoi K., 1984, ApJ, 286, 644

Nordin J., et al., 2011, A&A, 526, A119

Nordsieck K. H., Burgh E. B., Kobulnicky H. A., Williams T. B., O'Donoghue D., Percival J. W., Smith M. P., 2001, in American Astronomical Society Meeting Abstracts. p. 102.04

Nugent P., Phillips M., Baron E., Branch D., Hauschildt P., 1995, ApJ, 455, L147

Nugent P. E., et al., 2011, Nature, 480, 344

O'Donnell J. E., 1994, ApJ, 422, 158

Pan Y.-C., et al., 2014, MNRAS, 438, 1391

Pan Y.-C., Sullivan M., Maguire K., Gal-Yam A., Hook I. M., Howell D. A., Nugent P. E., Mazzali P. A., 2015, MNRAS, 446, 354

Parrent J. T., et al., 2011, ApJ, 732, 30

Parrent J. T., et al., 2012, ApJ, 752, L26

Patat F., Baade D., Höflich P., Maund J. R., Wang L., Wheeler J. C., 2009, A&A, 508, 229

Pereira R., et al., 2013, A&A, 554, A27

Perlmutter S., et al., 1999, ApJ, 517, 565

Phillips M. M., 1993, ApJ, 413, L105

Phillips M. M., Wells L. A., Suntzeff N. B., Hamuy M., Leibundgut B., Kirshner R. P., Foltz C. B., 1992, AJ, 103, 1632

Pignatari M., et al., 2016, ApJS, 225, 24

Piro A. L., Nakar E., 2013, ApJ, 769, 67

Piro A. L., Nakar E., 2014, ApJ, 784, 85

Quimby R., Höflich P., Kannappan S. J., Rykoff E., Rujopakarn W., Akerlof C. W., Gerardy C. L., Wheeler J. C., 2006, ApJ, 636, 400

Rayner J. T., et al., 2003, PASP, 115, 362

Rest A., et al., 2014, ApJ, 795, 44

Riess A. G., et al., 1998, AJ, 116, 1009

Scalzo R. A., et al., 2010, ApJ, 713, 1073

Schatzman E. L., 1958, White dwarfs

Schlegel D. J., Finkbeiner D. P., Davis M., 1998, ApJ, 500, 525

Seaton M. J., 1995, The opacity project

Seitenzahl I. R., et al., 2013, MNRAS, 429, 1156

Shappee B. J., Stanek K. Z., Pogge R. W., Garnavich P. M., 2013, ApJ, 762, L5

Shen K. J., Moore K., 2014, ApJ, 797, 46

Shen K. J., Kasen D., Weinberg N. N., Bildsten L., Scannapieco E., 2010, ApJ, 715, 767

Silverman J. M., Filippenko A. V., 2012, MNRAS, 425, 1917

Silverman J. M., Ganeshalingam M., Li W., Filippenko A. V., Miller A. A., Poznanski D., 2011, MNRAS, 410, 585

Silverman J. M., et al., 2012a, MNRAS, 425, 1789

Silverman J. M., Kong J. J., Filippenko A. V., 2012b, MNRAS, 425, 1819

Silverman J. M., et al., 2012c, ApJ, 756, L7

Silverman J. M., Ganeshalingam M., Filippenko A. V., 2013a, MNRAS, 430, 1030

Silverman J. M., et al., 2013b, MNRAS, 436, 1225

Silverman J. M., Vinkó J., Marion G. H., Wheeler J. C., Barna B., Szalai T., Mulligan B. W., Filippenko A. V., 2015, MNRAS, 451, 1973

Sobolev V. V., 1960, Moving envelopes of stars. Cambridge: Harvard University Press

Sternberg A., et al., 2011, Science, 333, 856

Stritzinger M. D., et al., 2011, AJ, 142, 156

Strolger L., et al., 2002, AJ, 124, 2905

Sullivan M., et al., 2006, ApJ, 648, 868

Suzuki N., et al., 2012, ApJ, 746, 85

Tanaka M., Mazzali P. A., Maeda K., Nomoto K., 2006, ApJ, 645, 470

Tanaka M., et al., 2008, ApJ, 677, 448

Thomas R. C., Branch D., Baron E., Nomoto K., Li W., Filippenko A. V., 2004, ApJ, 601, 1019

Thomas R. C., Nugent P. E., Meza J. C., 2011a, PASP, 123, 237

Thomas R. C., et al., 2011b, ApJ, 743, 27

Timmes F. X., Swesty F. D., 2000, ApJS, 126, 501

Tsujimoto T., Shigeyama T., 2012, ApJ, 760, L38

Vinkó J., et al., 2012, A&A, 546, A12

Walker E. S., et al., 2011, MNRAS, 410, 1262

Wang L., Wheeler J. C., 2008, ARA&A, 46, 433

Wang L., et al., 2003, ApJ, 591, 1110

Wang L., Baade D., Höflich P., Wheeler J. C., Kawabata K., Khokhlov A., Nomoto K., Patat F., 2006, ApJ, 653, 490

Wang X., et al., 2008, ApJ, 675, 626

Wang X., et al., 2009a, ApJ, 697, 380

Wang X., et al., 2009b, ApJ, 699, L139

Wang X., Wang L., Filippenko A. V., Zhang T., Zhao X., 2013, Science, 340, 170

Webbink R. F., 1984, ApJ, 277, 355

Wheeler J. C., Harkness R. P., 1990, Reports on Progress in Physics, 53, 1467

Whelan J., Iben Icko J., 1973, ApJ, 186, 1007

Woosley S. E., Kasen D., 2011, ApJ, 734, 38

Zhang J.-J., Wang X.-F., Bai J.-M., Zhang T.-M., Wang B., Liu Z.-W., Zhao X.-L., Chen J.-C., 2014, AJ, 148, 1

Zhang K., et al., 2016, ApJ, 820, 67

Zhao X., et al., 2015, ApJS, 220, 20

Zhao X., et al., 2016, ApJ, 826, 211

Zwicky F., 1938, ApJ, 88, 522